Numerical Simulation of Multi-Fluid Flows with the Particle Finite Element Method

M. De Mier
S. Idelsohn
E. Oñate

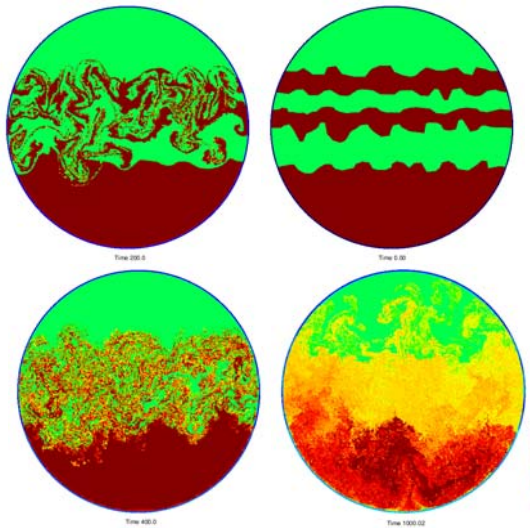

Monograph CIMNE Nº-115, March 2010

Numerical Simulation of Multi-Fluid Flows with the Particle Finite Element Method

M. De Mier
S. Idelsohn
E. Oñate

Monograph CIMNE Nº-115, March 2010

International Center for Numerical Methods in Engineering
Gran Capitán s/n, 08034 Barcelona, Spain

INTERNATIONAL CENTER FOR NUMERICAL METHODS IN ENGINEERING
Edificio C1, Campus Norte UPC
Gran Capitán s/n
08034 Barcelona, Spain

Primera edición: Marzo 2010

NUMERICAL SIMULATION OF MULTI-FLUID FLOWS WITH THE PARTICLE FINITE ELEMENT METHOD
Monografía CIMNE M115

ISBN: 978-84-96736-87-0

Depósito legal: B-19256-2010

Abstract

The simultaneous presence of multiple fluids with different properties in external or internal flows is found in daily life, environmental problems, and numerous industrial processes, among many other practical situations. Examples are fluid-fuel interaction in enhanced oil recovery, blending of polymers, emulsions in food manufacturing, rain droplet formation in clouds, fuel injection in engines, and bubble column reactors, to name only a few. Although multi-fluid flows occur frequently in nature and engineering practice, they still pose a major research challenge from both theoretical and computational points of view. In the case of immiscible fluids, the dynamics of the interface between fluids plays a dominant role. The success of the simulation of such flows will depend on the ability of the numerical method to model accurately the interface and the phenomena taking place on it.

In this work we have focused on understanding the basic physical principles of multi-fluid flows and the difficulties that arise in their numerical simulation. We have extended the Particle Finite Element Method to problems involving several different fluids with the aim of exploiting the fact that Lagrangian methods are specially well suited for tracking any kind of interfaces. We have developed a numerical scheme able to deal with large jumps in the physical properties (density and viscosity), include surface tension, and accurately represent all types of discontinuities in the flow variables at the interface. The scheme is based on decoupling the nodes position, velocity and pressure variables through the Picard linearization and a pressure segregation method which takes into account the interface conditions. The interface has been defined to be aligned with the moving mesh, so that it remains sharp along time. Furthermore, pressure degrees of freedom have been duplicated at the interface nodes to represent the discontinuity of this variable due to surface tension and variable viscosity, and the mesh has been refined in the vicinity of the interface to improve the accuracy of the computations. We have applied the resulting scheme to several academic and geological problems, such as the two-fluid sloshing, extrusion of viscous fluids, bubble rise and breakup, mixing of magmatic liquids and negatively buoyant jets.

Keywords: Particle Finite Element Method, multi-fluid flow, moving interface, surface tension, Lagrangian mesh, pressure segregation, bubble dynamics, mixing, magmatic processes.

Resumen

La presencia simultánea de múltiples fluidos con diferentes propiedades ocurre en numerosos problemas medioambientales, procesos industriales y situaciones de la vida diaria. Algunos ejemplos son la interacción fluido-combustible en la extracción mejorada de petróleo, mezcla de polímeros, emulsiones en productos alimentarios, formación de gotas de lluvia en nubes, inyección en motores de combustión o reactores de columna de burbujas. A pesar de que los flujos de multi-fluidos son muy frecuentes, todavía suponen un reto tanto desde el punto de vista teórico como computacional. En el caso de fluidos inmiscibles, la dinámica de la interfase entre fluidos juega un papel determinante. El éxito en la simulación de estos flujos dependerá de la capacidad del método numérico de modelar con precisión la interfase y los fenómenos que tienen lugar en ella.

En este trabajo nos hemos centrado en entender la principios físicos básicos de los multi-fluidos y las dificultades que aparecen en su simulación numérica. Hemos extendido el Particle Finite Element Method (PFEM) a problemas de varios fluidos diferentes con el objetivo de explotar el hecho de que los métodos lagrangianos son especialmente adecuados para el seguimiento de todo tipo de interfases. Hemos desarrollado un esquema numérico capaz de tratar grandes saltos en las propiedades físicas (densidad y viscosidad), de incluir la tensión superficial y de representar las discontinuidades de las variables del flujo. El esquema se basa en desacoplar las variables de posición de los nodos, velocidad y presión a través de la linearización de Picard y un método de segregación de la presión que tiene en cuenta las condiciones de interfase. La interfase se ha definido alineada con la malla móvil, de forma que se mantiene el salto de propiedades físicas sin suavizar a lo largo del tiempo. Además, los grados de libertad de la presión han sido duplicados en los nodos de interfase para representar la discontinuidad de esta variable debido a la tensión superficial y a la viscosidad variable, y la malla ha sido refinada cerca de la interfase para mejorar la precisión de la simulación. Hemos aplicado el esquema resultante a diversos problemas académicos y geológicos, como el sloshing de dos fluidos, extrusión de fluidos viscosos, ascensión y rotura de una burbuja dentro de una columna de líquido, mezcla de magmas y fuentes invertidas (negatively buoyant jet).

Palabras clave: Particle Finite Element Method, flujo de multi-fluidos, interfase móvil, tensión superficial, malla lagrangiana, segregación de la presión, dinámica de burbujas, mezclas, procesos magmáticos.

Contents

Index iv

Introduction **1**

1 Multi-fluid flows **3**
1.1 Interfacial physics 4
1.2 Governing equations of multi-fluid flows 9
1.3 Discontinuities at the interface 14

2 Lagrangian methods **19**
2.1 Lagrangian description 19
2.2 State of the art 21
2.3 Particle methods 22
2.4 Particle Finite Element Method 26

3 PFEM for multi-fluid flows **41**
3.1 Interface description 42
3.2 Main difficulties in the numerical solution of multi-fluid flows 47
3.3 Meshing procedure 49
3.3.1 Adaptive mesh refinement close to the interfaces 51
3.4 Discretization of the governing equations 53
3.4.1 Weak form 54
3.4.2 Lagrangian non-linearity and time integration 55
3.4.3 Pressure segregation 58
3.4.4 Spatial discretization 60
3.4.5 Pressure stabilization 62
3.4.6 Treatment of pressure on free surfaces and internal interfaces 64
3.4.7 Predictor-corrector scheme 67
3.5 Numerical results for variable density 67
3.5.1 Two-fluid sloshing 67
3.5.2 Heterogeneous flow with several materials 71
3.6 Numerical results for variable viscosity 71

3.6.1 Two-fluid dam break . . . 73
3.6.2 Extrusion . . . 77
3.7 Treatment of surface tension . . . 84
3.7.1 Curvature calculation . . . 85
3.7.2 Static bubble . . . 86
3.8 Application: Rising Bubble . . . 89
3.8.1 Numerical tests . . . 91
3.8.2 Results . . . 93
3.8.3 Topology changes of the interface: bubble breakup and coalescence . . . 100
3.9 Conclusions . . . 105

4 Geological applications **118**
4.1 Internal magmatic processes . . . 119
4.2 Characterization of mixing . . . 121
4.3 Thermal models . . . 124
4.3.1 Natural convection in a square cavity . . . 127
4.4 Magmatic Overturn . . . 127
4.4.1 Numerical example . . . 129
4.4.2 Quantification of mixing . . . 130
4.4.3 Conclusions . . . 130
4.5 Mixing of magmatic liquids . . . 130
4.5.1 San Pedro volcano . . . 134
4.5.2 Quantification of mixing and comparison with natural rocks . 135
4.5.3 Model equations and parameters . . . 136
4.5.4 Physical properties of silicate melts . . . 137
4.5.5 Numerical settings, initial and boundary conditions . . . 140
4.5.6 Results . . . 143
4.5.7 Conclusions . . . 147
4.6 Negatively buoyant jets: experimental and numerical study . . . 149
4.6.1 Numerical results . . . 156
4.6.2 Comparison between numerical and experimental data . . . 163
4.6.3 Conclusions . . . 166

Introduction

Flows involving several fluids with different physical properties are common in nature and technology. In the case of immiscible fluids, the dynamics of the interface between fluids plays a dominant role. In order to describe quantitatively these flows, the understanding of physical processes taking place on the interface is essential, and the successful simulation depends on the ability of the numerical method to model the interface accurately. Therefore, the computation of multi-fluid flows requires to solve, in addition to the governing equations in each fluid, all the physical phenomena the interface is subject to, such as jumps in density and viscosity, thermal diffusion, chemical diffusion, surface tension, phase change, or chemical reactions, and to take into account that the interface can move, bend and reconnect in arbitrary ways.

The objective of this work is to extend the Particle Finite Element Method (PFEM) to multi-fluid flow problems for both miscible and immiscible fluids. PFEM combines the flexibility of particle methods with the advantages of the finite element discretization, and has been developed for modeling and analysis of complex multidisciplinary problems in fluid and solid mechanics. We want to exploit the fact that Lagrangian methods are specially well suited for tracking interfaces.

Furthermore, we are interested in simulating geological processes in the Earth's interior, which typically involve a large variety of materials and phases. Most of these processes are not directly observable, and although they can be experimentally investigated, it is in general not possible to quantitatively extrapolate the results to the natural reality. The numerical modeling of heterogeneous flows allows to gain insight about these processes and their flow dynamics, mainly driven by gravitational instabilities caused by gradients in the physical properties due to composition, temperature or pressure. In particular, we are interested in understanding the processes occurring inside the magma chamber, as a first step towards being able to predict volcanic eruptions.

Most of the developments of PFEM presented here have been motivated by the collaboration with the Volcanology Group of the Institute of Earth Sciences Jaume Almera at the Spanish National Research Council (CSIC). This work is based on the

first author's doctoral thesis *Numerical simulation of multi-fluid flows with the Particle Finite Element Method* [1].

Outline

Chapter 1 introduces the theory of multi-fluid flows and the main physical phenomena that may occur at the interface, focusing specially on the surface tension. The chapter also presents the governing equations, together with the boundary and interface conditions, and describes the possible discontinuities of the flow variables.

Chapter 2 is devoted to Lagrangian methods for fluid flow simulations. It presents the Lagrangian description in continuum mechanics, briefly reviews the state of the art of finite element methods using this description, and introduces the particle-based approach. The chapter closes with an overview of the Particle Finite Element Method (PFEM).

Chapter 3 explains the numerical scheme developed to solve multi-fluid flows using the PFEM. Details are given about the interface representation, the remeshing procedure, the discretization of the governing equations, and the treatment of the surface tension. Finally, the method is tested in some academic examples.

In Chapter 4, the PFEM is applied to three geological problems related to the fluid dynamics and mixing inside the magma chamber. This chapter introduces the basic concepts in volcanology and internal magmatic processes, the characterization of mixing, and the most extended thermal models in geophysics. The numerical results are compared with field observations and experimental data.

Acknowledgments

This work has been financially supported by the Agencia de Gestio d'Ajuts Universitaris i de Recerca of the Generalitat de Catalunya, the European Social Fund, and CIMNE. Support from the European Commission and the European Research Council through the "Real Time Computational Techniques for Multi-Fluid Problems" project is also gratefully acknowledged.

References

[1] Mier-Torrecilla, M., 2010. Numerical simulation of multi-fluid flows with the Particle Finite Element Method. Ph.D. thesis, Technical University of Catalonia.

Chapter 1

Multi-fluid flows

The simultaneous presence of multiple fluids with different properties in external or internal flows is found in daily life, environmental problems, and numerous industrial processes, among many other practical situations. These types of flow are labeled “multi-phase”, ”multi-fluid” or simply ”heterogeneous”. Examples are fluid-fuel interaction in enhanced oil recovery, blending of polymers, emulsions in food manufacturing, rain droplet formation in clouds, fuel injection in engines, and bubble column reactors, to name only a few. Although heterogeneous fluid flows occur frequently in nature and engineering practice, they still pose a major research challenge from both theoretical and computational points of view (Sommerfeld et al. [27]). Contrary to heterogeneous solid materials where the main cause of variation in the physical properties are the Young modulus or the anisotropy of the different materials involved, in fluids the main reasons for the heterogeneity are the variations of the density and the viscosity. These property variations for incompressible flows may be due to a change in the temperature field or due to the presence of several fluids (Idelsohn et al. [10]).

Multiphase flows in general involve a combination of phases: gas, liquid, and solid. In most cases only a mixture of two phases is considered. Ishii & Hibiki [11] classify two-phase flows into: gas-liquid, gas-solid, liquid-solid and immiscible liquid-liquid mixtures. Although the latter is technically not a two-phase mixture, it shares a number of characteristics with multiphase flows. A boundary may separate two different phases or two media of the same phase but different constitution. To avoid ambiguity we will use the following terminology:

- phase: gas, liquid and solid,
- interface: boundary between phases but specifically used for liquid-liquid boundaries,
- free surface: liquid-gas boundary.

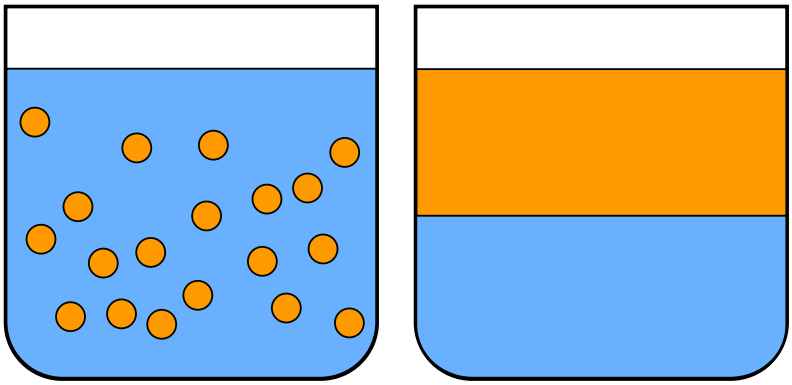

Figure 1.1: Multi-fluid flow topologies: (a) disperse and (b) separated.

Ishii & Hibiki [11] also classify multiphase flows regarding the interface topology in dispersed and separated flows (see Figure 1.1):

- Disperse flows consist of finite particles, drops or bubbles (disperse phase) distributed in a connected volume of the continuous phase. For example, water droplets in air, air bubbles in water or sand grains in water.
- Separated flows consist of two or more continuous fluids separated by interfaces.

While in separated flows the interface between the two phases is important and significant, in dispersed flows the interface position is difficult to track and usually not relevant, only some average or homogenized quantity is needed for the fluid flow analysis.

In this work we focus on multi-fluid separated flows, and therefore, on the interfaces between fluids. To explain the different physical theories for representing the interface and the phenomenon of surface tension is the objective of Section 1.1. The governing equations of multi-fluid flows and their interface conditions are described in Section 1.2, together with other phenomena that may occur at the interface, such as phase change, thermal and compositional diffusion, and variable surface tension. Finally, Section 1.3 describes the possible discontinuities of the flow variables across the interface.

1.1 Interfacial physics

The nature of the interface has been subject of extensive investigation. Young, Laplace, and Gauss, in the early 1800s, considered the interface between two fluids to be represented as a surface of zero thickness endowed with physical properties such as surface tension. They assumed that physical quantities

(e.g. density, viscosity) were discontinuous across the interface and phenomena such as capillarity occurring at the interface were represented by boundary conditions.

Later Poisson, Maxwell, and Gibbs represented the interface like a rapid but smooth transition of physical quantities between the bulk fluid values. Gibbs [8] introduced the notion of a surface of discontinuity and surface excess quantities in order to develop the equilibrium thermodynamics of interfaces. The idea that the interface has a non-zero thickness (i.e. it is diffuse) was developed in detail by Rayleigh [20] and by van der Waals [28], who proposed gradient theories for the interface based on thermodynamic principles. Korteweg [14] built on these ideas and proposed a constitutive law for the capillary stress tensor in terms of the density and its spatial gradients. Extensive reviews about molecular theory of interfaces and diffuse-interface models can be found in Rowlinson & Widom [22], Joseph [12] and Anderson & McFadden [1].

Although the interface between two fluids is a thin layer, typically a few molecular dimensions thick (its micrometric thickness is not well defined since physical properties vary continuously from the values of one phase to the other), the classical sharp-interface/zero thickness macroscopic approach fails only when the interfacial thickness is comparable to the length scale of the physical mechanism being examined, for example near the critical point of phase change or in situations involving changes in the topology of the interface like the breakup of a liquid droplet.

In the case of fluids with similar properties and negligible surface tension, the interface is called *passive* (Aref & Tryggvason [2]). A passive interface is convected by the flow without affecting it. On the other hand, *active* interfaces modify the surrounding flow through capillary effects, and thus their behavior is determined by the surface tension.

Surface tension

Surface tension is a property of a fluid-fluid interface whose origins lie in the different intermolecular attractive forces that act in the two fluid phases (Rowlinson & Widom [22] and Bush [6]) (see Figure 1.2). The result is an interfacial energy per area that acts to resist the creation of new interface and the interface behaves like a stretched membrane trying to minimize its area. Thus, capillary force drives the interface towards a minimal energy state characterized by a configuration of minimum surface area. Fluids between which no surface tension arises are said to be *miscible*. For example, salt molecules diffuse freely across a boundary between fresh and saltwater; consequently these fluids are miscible and there is no surface tension between them.

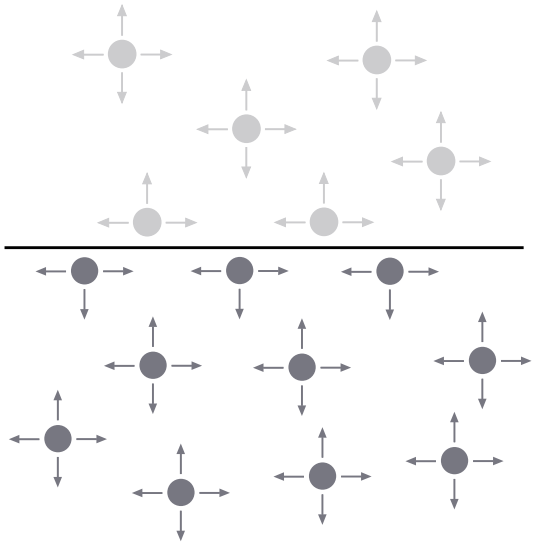

Figure 1.2: The molecules of a fluid in a thin layer on the interface experience nonsymmetric action of intermolecular forces from the two bulk fluids, and this asymmetry gives rise to the surface tension force.

In the absence of viscous, gravitational or external forces, surface tension causes a static fluid bubble to become spherical. A curved interface can be in equilibrium only if the effective pressure due to surface tension is balanced by an equal and opposite difference between the pressures in the fluids on the two sides of the interface. Thus at any point of the interface there must be a jump in pressure of magnitude (Landau & Lifshitz [15])

$$\Delta p = \gamma\kappa = \gamma(\frac{1}{R_1} + \frac{1}{R_2}) \tag{1.1}$$

where γ is the surface tension coefficient, and κ is the interface curvature, which can be written in terms of the principal radii of curvature R_1 and R_2. Equation (1.1) is called the *Young-Laplace equation* for capillary pressure. If $R_1 = R_2 = \infty$, i.e. the interface is plane, the pressure is the same in both fluids. For most processes, at a given temperature the surface tension coefficient γ is a constant value that characterizes the pair of contacting materials.

Some dimensionless numbers relevant in capillary flows are:

$$\text{Weber number} \qquad We = \frac{\rho U^2 L}{\gamma} = \frac{\text{inertia}}{\text{surface tension}} \tag{1.2}$$

$$\text{Bond (or Eötvös) number} \qquad Bo = Eo = \frac{\rho g L^2}{\gamma} = \frac{\text{gravity}}{\text{surface tension}} \tag{1.3}$$

$$\text{Capillary number} \qquad Ca = \frac{\mu U}{\gamma} = \frac{\text{viscosity}}{\text{surface tension}} \tag{1.4}$$

where ρ denotes the density (or sometimes the density difference $\Delta\rho$ between fluids), L a characteristic length scale (e.g. radius of a drop), U a characteristic velocity and μ the dynamic viscosity. The Bond number indicates the relative importance of forces induced by gravity and surface tension. These two forces are comparable when $Bo = 1$, which arises on a lengthscale corresponding to the capillary wavelength $\lambda_{ca} = \sqrt{\frac{\gamma}{\rho g}}$. These waves traveling along the interface between two fluids whose dynamics are dominated by the effects of surface tension are known as *capillary waves*. As a fluid system becomes progressively smaller, the relative importance of surface tension over gravity increases, and therefore surface tension effects are dominant in microscale engineering processes.

Surface tension is also responsible for topology changes in the flow domain, such as breakup of liquid threads and jets (see Figure 1.3), coalescence of drops and bubbles, rupture of films, evolution of foams, or nucleation of bubbles. The two basic mechanisms are the ones present in the breakup of a liquid thread into droplets, and the coalescence of two drops to form a larger one.

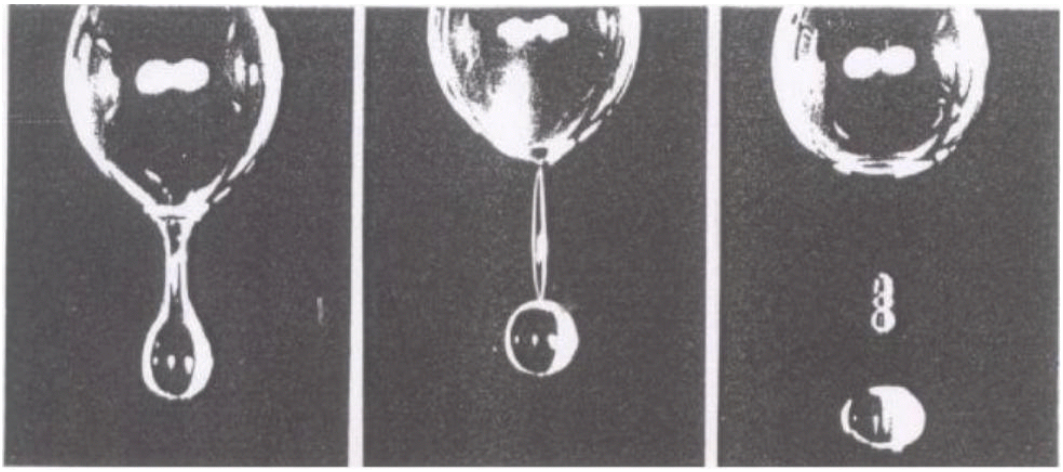

Figure 1.3: Breakup of a liquid thread (from Shikhmurzaev [25]).

Breakup is based on the Plateau-Rayleigh instability (Plateau [18], Rayleigh [21]), which causes the pinch-off of thin liquid threads. It is an instability driven by the surface tension and begins with the existence of small perturbations on the thread surface. Although the longitudinal curvature of the thread opposes the growth of the instability, if the curvature associated with the cross-sectional area is larger than the longitudinal curvature (see Figure 1.4), it will cause the instability to grow. Due to the Young-Laplace equation (1.1), pressure is higher in the troughs than in the crests. Liquid then is pushed into the lower pressure region in the crest, the perturbation grows in amplitude over time and thus the instability can develop.

Coalescence of two fluid drops is a more complex phenomenon. Bremond et al.

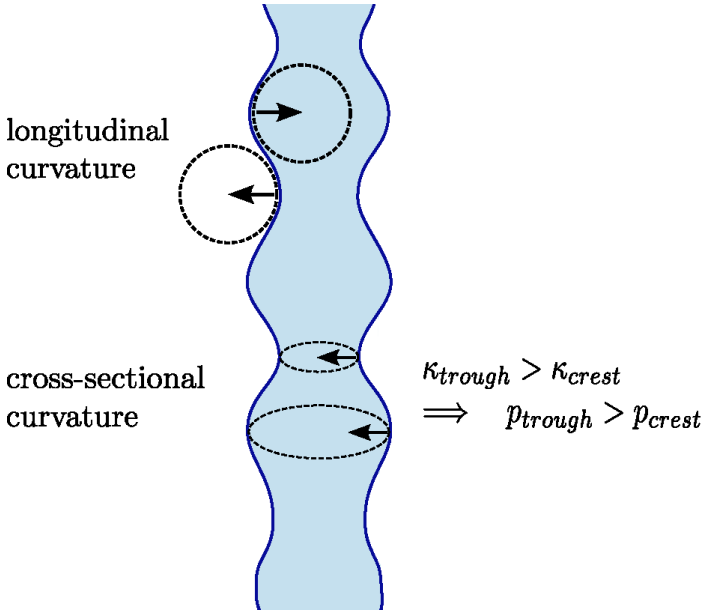

Figure 1.4: Curvatures in a three-dimensional fluid thread.

[5] describes it as follows: when the drops approach each other, they get flattened as the pressure increases in the contact area, and the thin film between the drops drains until the two interfaces interact via van der Waals forces. These forces hasten the film draining and amplify the fluctuations of the interfaces, that eventually merge leading to the coalescence of the two droplets. Coalescence occurs during the separation and not during the impact, because separation momentarily reduces the fluid pressure between the droplets and induces the formation of two facing nipples in the contact area (see Figure 1.5) that produces the connection of the interfaces prior to merge.

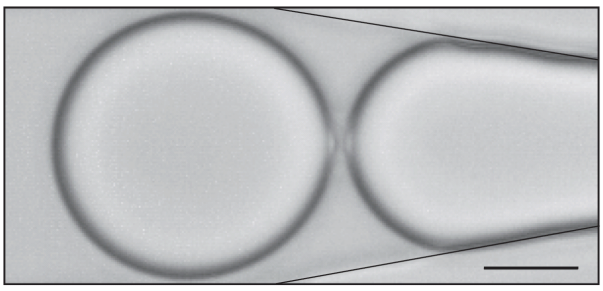

Figure 1.5: Formation of two facing nipples in the contact area prior to coalescence induced by separating the droplets. The scale bar is 20 μm (from Bremond et al. [5]).

1.2 Governing equations of multi-fluid flows

Let $\Omega \subset \boldsymbol{R}^d$, $d \in \{2, 3\}$, be a bounded domain containing two different fluids (see Fig. 1.6). We denote time by t, the Cartesian spatial coordinates by $\boldsymbol{x} = \{x_i\}_{i=1}^d$, and the vectorial operator of spatial derivatives by $\boldsymbol{\nabla} = \{\partial_{x_i}\}_{i=1}^d$. We consider a viscous flow where the density ρ and the dynamic viscosity μ depend on space and time. The evolution of the velocity $\boldsymbol{u} = \boldsymbol{u}(\boldsymbol{x}, t)$ and the pressure $p = p(\boldsymbol{x}, t)$ is governed by the Navier-Stokes equations:

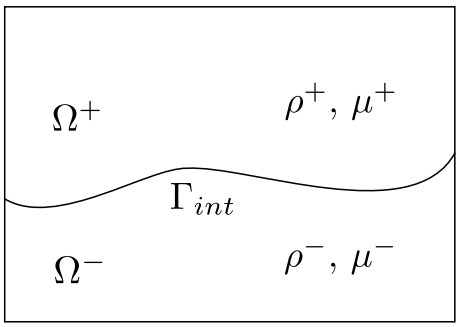

Figure 1.6: Two-fluid flow configuration.

$$\rho \frac{\mathrm{d}\boldsymbol{u}}{\mathrm{d}t} = \boldsymbol{\nabla} \cdot \boldsymbol{\sigma} + \rho \boldsymbol{g} \quad \text{in } \Omega \times (0, T) \qquad \text{Momentum conservation} \tag{1.5a}$$

$$\frac{\mathrm{d}\rho}{\mathrm{d}t} + \rho \boldsymbol{\nabla} \cdot \boldsymbol{u} = 0 \quad \text{in } \Omega \times (0, T) \qquad \text{Mass conservation} \tag{1.5b}$$

where $\boldsymbol{\sigma}$ is the Cauchy stress tensor, $\boldsymbol{g}$ the vector of gravity acceleration, and $\dfrac{\mathrm{d}\phi}{\mathrm{d}t}$ represents the total or material derivative of a function ϕ. Further notation can be found in Table 1.1.

The constitutive equation for a Newtonian and isotropic fluid takes the form

$$\boldsymbol{\sigma} = -p\boldsymbol{I} + 2\mu(\boldsymbol{D} - \frac{1}{3}\varepsilon_V \boldsymbol{I}) \tag{1.6}$$

with $\boldsymbol{I}$ the identity tensor, $\boldsymbol{D} = \frac{1}{2}(\boldsymbol{\nabla u} + \boldsymbol{\nabla}^T \boldsymbol{u})$ the strain rate tensor, and $\varepsilon_V = \boldsymbol{\nabla} \cdot \boldsymbol{u}$ the volumetric strain rate.

Let $\Gamma_{int}(t)$ be the interface that cuts the domain Ω in two open subdomains, $\Omega^+(t)$ and $\Omega^-(t)$, which satisfy: $\Omega^+ \cap \Omega^- = \emptyset$, $\Omega = \bar{\Omega}^+ \cup \bar{\Omega}^-$, and $\Gamma_{int} = \bar{\Omega}^+ \cap \bar{\Omega}^- = \partial\Omega^+ \cap \partial\Omega^-$. In each subdomain, the physical properties are defined as:

$$\rho = \rho(\boldsymbol{x}, t) = \begin{cases} \rho^+ & \text{if } \boldsymbol{x} \in \Omega^+(t) \\ \rho^- & \text{if } \boldsymbol{x} \in \Omega^-(t) \end{cases}, \qquad \mu = \mu(\boldsymbol{x}, t) = \begin{cases} \mu^+ & \text{if } \boldsymbol{x} \in \Omega^+(t) \\ \mu^- & \text{if } \boldsymbol{x} \in \Omega^-(t) \end{cases} \tag{1.7}$$

Table 1.1: Notation

Symbol	Description	Units	
$\boldsymbol{u}$	Velocity	$m\,s^{-1}$	
p	Pressure	Pa	
ρ	Density	$kg\,m^{-3}$	
μ	Dynamic viscosity	$Pa\,s$	
ν	Kinematic viscosity	$m^2\,s^{-1}$	
ε_V	Volumetric strain rate	s^{-1}	$\varepsilon_V = \boldsymbol{\nabla}\cdot\boldsymbol{u}$
$\boldsymbol{D}$	Strain rate tensor	s^{-1}	$\boldsymbol{D} = \frac{1}{2}(\boldsymbol{\nabla u} + \boldsymbol{\nabla}^T\boldsymbol{u})$
$\boldsymbol{\tau}$	Viscous stress tensor	Pa	$\boldsymbol{\tau} = 2\mu(\boldsymbol{D} - \frac{1}{3}\varepsilon_V\boldsymbol{I})$
$\boldsymbol{\sigma}$	Stress tensor	Pa	$\boldsymbol{\sigma} = -p\boldsymbol{I} + \boldsymbol{\tau}$
$\boldsymbol{f}$	External volume force	N	$\boldsymbol{f} = \rho\boldsymbol{g}$
$\boldsymbol{g}$	Gravity force	$m\,s^{-2}$	
$\boldsymbol{n}$	Normal direction		
$\boldsymbol{t}$	Tangential direction		
γ	Surface tension coefficient	$N\,m^{-1}$	
κ	Curvature	m^{-1}	
$[\![\cdot]\!]$	Jump operator		$[\![A]\!] = A^+ - A^-$

If density and viscosity are assumed to remain constant in each fluid (i.e. fluids are incompressible, immiscible, and isothermal), we have that $\frac{\mathrm{d}\rho}{\mathrm{d}t} = 0$ and $\frac{\mathrm{d}\mu}{\mathrm{d}t} = 0$. Consequently, we have on the one side that $\varepsilon_V = \boldsymbol{\nabla}\cdot\boldsymbol{u} = 0$, this is the mass conservation equation for incompressible flows; and on the other side, that $\frac{\mathrm{d}}{\mathrm{d}t}\Gamma_{int} = 0$. This latter consequence means that interfaces are material surfaces, which move with the fluid velocity $\boldsymbol{u}$, and therefore, they are naturally tracked in Lagrangian formulations.

The incompressible Navier-Stokes equations are written as

$$\rho\frac{\mathrm{d}\boldsymbol{u}}{\mathrm{d}t} = -\boldsymbol{\nabla}p + \boldsymbol{\nabla}\cdot\mu(\boldsymbol{\nabla u} + \boldsymbol{\nabla}^T\boldsymbol{u}) + \rho\boldsymbol{g} \tag{1.8a}$$

$$\boldsymbol{\nabla}\cdot\boldsymbol{u} = 0 \tag{1.8b}$$

or in index notation

$$\rho\frac{\mathrm{d}u_i}{\mathrm{d}t} = -\frac{\partial p}{\partial x_i} + \frac{\partial}{\partial x_j}\mu(\frac{\partial u_i}{\partial x_j} + \frac{\partial u_j}{\partial x_i}) + \rho g_i \tag{1.9a}$$

$$\frac{\partial u_i}{\partial x_i} = 0 \tag{1.9b}$$

Boundary and interface conditions

In order for the Navier-Stokes problem (1.8) to be well-posed, suitable boundary conditions need to be specified (see e.g. Quarteroni & Valli [19]). On the external boundary $\partial\Omega = \Gamma_D \cup \Gamma_N$, such that $\Gamma_D \cap \Gamma_N = \emptyset$, we consider the following:

$$\boldsymbol{u} = \bar{\boldsymbol{u}} \quad \text{on } \Gamma_D \qquad \text{Dirichlet BC} \tag{1.10}$$

$$\boldsymbol{\sigma} \cdot \boldsymbol{n} = \bar{\boldsymbol{\sigma}}_n \quad \text{on } \Gamma_N \qquad \text{Neumann BC} \tag{1.11}$$

$\bar{\boldsymbol{u}}$ is the prescribed velocity, $\boldsymbol{n}$ the outer unit normal to Γ_N, and $\bar{\boldsymbol{\sigma}}_n$ the prescribed traction vector. When Dirichlet boundary conditions are specified on the entire boundary $\partial\Omega$, pressure is not uniquely defined. In this case $\bar{\boldsymbol{u}}$ has to satisfy the compatibility condition $\int_{\partial\Omega} \bar{\boldsymbol{u}} \cdot \boldsymbol{n}\, d\Gamma = 0$.

A Neumann boundary Γ_N with $\bar{\boldsymbol{\sigma}}_n = \boldsymbol{0}$ is called *free surface*. For vanishing velocity gradients, the force $\bar{\boldsymbol{\sigma}}_n$ corresponds to the pressure on the boundary.

On the internal interfaces Γ_{int}, the coupling conditions are (Batchelor [3], Davies & Rideal [7]):

$$[\![\boldsymbol{u}]\!] = \boldsymbol{0} \qquad \text{on } \Gamma_{int} \tag{1.12}$$

$$[\![\boldsymbol{\sigma}]\!] \cdot \boldsymbol{n} = \gamma\kappa\boldsymbol{n} \qquad \text{on } \Gamma_{int} \tag{1.13}$$

with $\boldsymbol{n}$ now the unit normal to Γ_{int}, γ the surface tension coefficient, κ the interface curvature, and $[\![\phi]\!]$ represents the jump of a quantity ϕ across the interface

$$\begin{aligned} [\![\phi]\!] &= \lim_{\varepsilon \to 0} (\phi(\boldsymbol{x} + \varepsilon\boldsymbol{n}) - \phi(\boldsymbol{x} - \varepsilon\boldsymbol{n})) \\ &= \phi^+(\boldsymbol{x}) - \phi^-(\boldsymbol{x}) \qquad \forall \boldsymbol{x} \in \Gamma_{int} \end{aligned} \tag{1.14}$$

We denote by $\boldsymbol{n}$ both the outer unit normal to Γ_N and the unit normal to Γ_{int}. The meaning of $\boldsymbol{n}$ will be clear from the context.

Equation (1.12) expresses the continuity of all velocity components. The normal component has to be continuous when there is no mass flow through the interface, and the tangential components have to be continuous when both fluids are viscous ($\mu^+, \mu^- > 0$), similar to a no-slip condition.

Equation (1.13) expresses that the jump in the normal stresses is balanced with the surface tension force. This force is proportional to the interface curvature and points to the center of the osculating circle that approximates Γ_{int}. The surface tension coefficient γ is assumed constant and its value depends on the two fluids at the interface. Projecting Eq. (1.13) along the unit normal $\boldsymbol{n}$ and unit tangent $\boldsymbol{t}$ vectors attached to the interface results in the following scalar interface conditions:

$$n_i \cdot [\![\sigma_{ij}]\!] \cdot n_j = \gamma\kappa \qquad \text{on } \Gamma_{int} \tag{1.15}$$

$$t_i \cdot [\![\sigma_{ij}]\!] \cdot n_j = 0 \qquad \text{on } \Gamma_{int} \tag{1.16}$$

and we have that

$$n_i \cdot [\![\sigma_{ij}]\!] \cdot n_j = -(p^+ - p^-) + n_i \left(\mu^+ (\frac{\partial u_i}{\partial x_j} + \frac{\partial u_j}{\partial x_i})^+ - \mu^- (\frac{\partial u_i}{\partial x_j} + \frac{\partial u_j}{\partial x_i})^- \right) n_j \tag{1.17}$$

$$t_i \cdot [\![\sigma_{ij}]\!] \cdot n_j = t_i \left(\mu^+ (\frac{\partial u_i}{\partial x_j} + \frac{\partial u_j}{\partial x_i})^+ - \mu^- (\frac{\partial u_i}{\partial x_j} + \frac{\partial u_j}{\partial x_i})^- \right) n_j \tag{1.18}$$

We show next that the pressure field may have a jump at the interface between two fluids with different viscosities. In the analysis we consider only the case of a flat interface in order to avoid tedious computations accounting for a moving frame when the interface is curved. Nevertheless, the results are general for any interface boundary. Applying the mass conservation equation (1.9b) on both sides of the interface in the local coordinate system $\{\xi_i\}$ we have:

$$(\frac{\partial \mathrm{v}_i}{\partial \xi_i})^+ = 0, \quad (\frac{\partial \mathrm{v}_i}{\partial \xi_i})^- = 0 \tag{1.19}$$

where ξ_1 represents the coordinate in the perpendicular direction to the interface, ξ_2 and ξ_3 are the coordinates in two directions that span the tangential space (in the three-dimensional case), and v_i are the velocity components in this system.

From the interface condition (1.12), we have that $[\![u_i t_i]\!] = 0$, and thus, ${\mathrm{v}_2}^+ = {\mathrm{v}_2}^-$ and ${\mathrm{v}_3}^+ = {\mathrm{v}_3}^-$ for $\forall \boldsymbol{x} \in \Gamma_{int}$. This implies:

$$[\![\frac{\partial \mathrm{v}_2}{\partial \xi_2}]\!] = 0 \quad \text{and} \quad [\![\frac{\partial \mathrm{v}_3}{\partial \xi_3}]\!] = 0 \tag{1.20}$$

From Eq. (1.19) we also deduce:

$$[\![\frac{\partial \mathrm{v}_1}{\partial \xi_1}]\!] = 0 \tag{1.21}$$

Thus, the continuity of the normal velocity gradient at the interface is a consequence of the incompressibility.

The normal projections of the viscous stress tensor used in Eq. (1.17) may be written in the new Cartesian coordinates ξ_i as:

$$n_i [\![2\mu \boldsymbol{D}_{ij}(\mathbf{v})]\!] n_j = n_i [\![\mu (\frac{\partial \mathrm{v}_i}{\partial \xi_j} + \frac{\partial \mathrm{v}_j}{\partial \xi_i})]\!] n_j \tag{1.22}$$

The unit normal to the interface in the ξ_i system is $\boldsymbol{n} = (\ 1 \quad 0 \quad 0\ )^T$, which gives

$$n_i [\![2\mu \boldsymbol{D}_{ij}(\mathbf{v})]\!] n_j = [\![2\mu \frac{\partial \mathrm{v}_1}{\partial \xi_1}]\!] \tag{1.23}$$

and taking into account Eq. (1.21):

$$n_i [\![2\mu \boldsymbol{D}_{ij}(\mathbf{v})]\!] n_j = 2 [\![\mu]\!] \frac{\partial \mathrm{v}_1}{\partial \xi_1} \tag{1.24}$$

Replacing this expression in Eq. (1.17) gives:

$$-[\![p]\!] + 2[\![\mu]\!]\frac{\partial \mathrm{v}_1}{\partial \xi_1} = \gamma\kappa \tag{1.25}$$

which shows that the jump in the pressure field is not only a consequence of the surface tension, but also occurs in cases where surface tension is neglected. The jump in the pressure field in these cases is a function of the viscosity jump and the derivative of the normal velocity to the interface, i.e.

$$p^+ - p^- = 2(\mu^+ - \mu^-)\frac{\partial u_n}{\partial n} \tag{1.26}$$

where we use the notation $u_n = \mathrm{v}_1$ and $n = \xi_1$ to be more clear.

Thus in the case $\gamma \neq 0$, the interfacial condition (1.15) takes the full form (Kang et al. [13], Idelsohn et al. [9])

$$[\![\sigma_{nn}]\!] = \gamma\kappa \quad \Longrightarrow \quad \boxed{p^+ - p^- + \gamma\kappa = 2(\mu^+ - \mu^-)\frac{\partial u_n}{\partial n}} \tag{1.27}$$

and Eq. (1.16) reads

$$\mu^+\left(\frac{\partial u_t}{\partial n} + \frac{\partial u_n}{\partial s}\right)^+ - \mu^-\left(\frac{\partial u_t}{\partial n} + \frac{\partial u_n}{\partial s}\right)^- = 0 \tag{1.28}$$

where $\dfrac{\partial}{\partial s} = \boldsymbol{t}\cdot\boldsymbol{\nabla}$ is the surface derivative.

Equations (1.12) and (1.13) can be supplemented by appropriate conditions describing phase change, heat and mass transfer, chemical reactions and other phenomena taking place at the interface.

Phase change

Without phase change, one assumes continuity of fluid velocity $\boldsymbol{u}^+ = \boldsymbol{u}^-$, and the interface velocity V_Γ is then the normal velocity, the same on both sides of the interface, $V_\Gamma = \boldsymbol{u}^+\cdot\boldsymbol{n} = \boldsymbol{u}^-\cdot\boldsymbol{n}$.

In the case of phase change, there may be a mass flow q from one phase to the other. This mass flow is connected to the velocities on both sides of the interface in the way described next (Scardovelli & Zaleski [23]). Consider again the frame of reference attached to the interface, i.e. where the interface is at rest. The normal velocities in that frame of reference are $\mathrm{v} = \boldsymbol{u}\cdot\boldsymbol{n} - V_\Gamma$. The mass flow is the amount of mass that goes from phase + to phase -, and it must be the same on both sides of the interface by conservation of mass: $\rho^+\mathrm{v}^+ = \rho^-\mathrm{v}^- = q$. Then, in the general frame of reference,

$$\rho^+(\boldsymbol{u}^+\cdot\boldsymbol{n} - V_\Gamma) = \rho^-(\boldsymbol{u}^-\cdot\boldsymbol{n} - V_\Gamma) = q \tag{1.29}$$

Thermal and compositional diffusion

Diffusive heat transfer is described by the first law of thermodynamics applied to incompressible Newtonian fluids

$$\rho C_0 \frac{\mathrm{d}T}{\mathrm{d}t} = \boldsymbol{\nabla} \cdot (k \boldsymbol{\nabla} T) + \Phi \tag{1.30}$$

where T is the temperature, ρ the density, C_0 the specific heat, k thermal diffusion coefficient, and Φ the viscous dissipation (important only in high-speed flows and in fluids with extremely large viscosities).

Analogously, the conservation of mass in a binary system consisting of non-reactive incompressible fluids yields

$$\frac{\mathrm{d}c}{\mathrm{d}t} = \boldsymbol{\nabla} \cdot (\mathcal{D} \boldsymbol{\nabla} c) \tag{1.31}$$

where c is the composition field, and $\mathcal{D}$ the mass diffusivity coefficient.

Variable surface tension

The interfacial tension coefficient may vary along the interface due to a non-uniform temperature or to the presence of a non-uniform distribution of surfactants (Scriven [24], Levich & Krylov [16]). For problems with variable surface tension coefficient, $\gamma = \gamma(\boldsymbol{x})$, one has to include $\boldsymbol{\nabla}\gamma$ in the normal stress interfacial condition, Eq. (1.27):

$$p^+ - p^- + \gamma\kappa = 2(\mu^+ - \mu^-)\frac{\partial u_n}{\partial n} + \frac{\partial \gamma}{\partial n} \tag{1.32}$$

and the tangent stress condition, Eq. (1.28), is now

$$\mu^+ \left(\frac{\partial u_t}{\partial n} + \frac{\partial u_n}{\partial s} \right)^+ - \mu^- \left(\frac{\partial u_t}{\partial n} + \frac{\partial u_n}{\partial s} \right)^- = \frac{\partial \gamma}{\partial s} \tag{1.33}$$

Spatial variations in the surface tension coefficient along the interface cause fluid to flow from regions of lower to higher surface tension.

In summary, there are three interfacial conditions, namely continuity of velocity; continuity of tangential stresses; and balance of the normal stress contributions caused by pressure, viscous and capillary forces. Viscous and pressure stresses generated by the fluid motion tend to deform the interface while surface tension stresses tend to resist deformation.

Good references on the multi-fluid flow equations are Landau & Lifshitz [15], Davies & Rideal [7], Batchelor [3], Levich & Krylov [16], Brackbill et al. [4], Scardovelli & Zaleski [23], Smolianski [26] and Winkelmann [29].

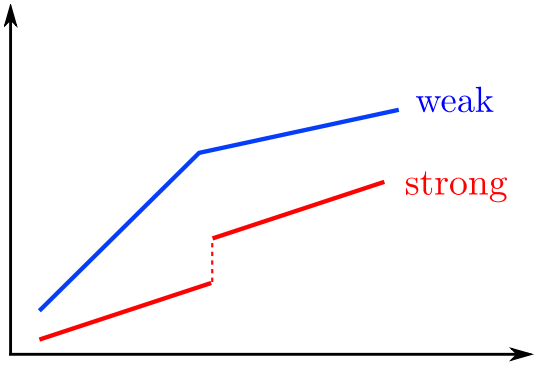

Figure 1.7: Weak and strong discontinuities.

1.3 Discontinuities at the interface

Discontinuities at the interface can be of two types (see Figure 1.7):

- *weak discontinuity*, when the flow variable has a kink (i.e. the gradient has a jump), and
- *strong discontinuity*, when the flow variable itself has a jump.

Differences in density at the interface cause a kink in the hydrostatic pressure profile, leading to a jump in the pressure gradient, and thus to a weak discontinuity in the pressure field (Fig. 1.8a).

If surface tension is not taken into account, both the normal and shear stresses have to be continuous across the interface (continuity of stresses). When there is a viscosity jump at the interface, it can be deduced from Eq. (1.28) that this leads to discontinuous components of the strain rate tensor $D_{ij} = \frac{1}{2}\left(\frac{\partial u_i}{\partial x_j} + \frac{\partial u_j}{\partial x_i}\right)$, and therefore the velocity field has a weak discontinuity at the interface (Fig. 1.8b). In fact, the viscosity jump results in the discontinuity of the tangential velocity gradient across the interface (Yih [30]) and drives an interfacial instability that can be thought of as the viscous counterpart of the Kelvin-Helmholtz instability (Li & Renardy [17]).

Differences in viscosity and the presence of surface tension cause a strong discontinuity in the pressure field, as expressed in Eq. (1.27) (Figs. 1.8b and 1.8c).

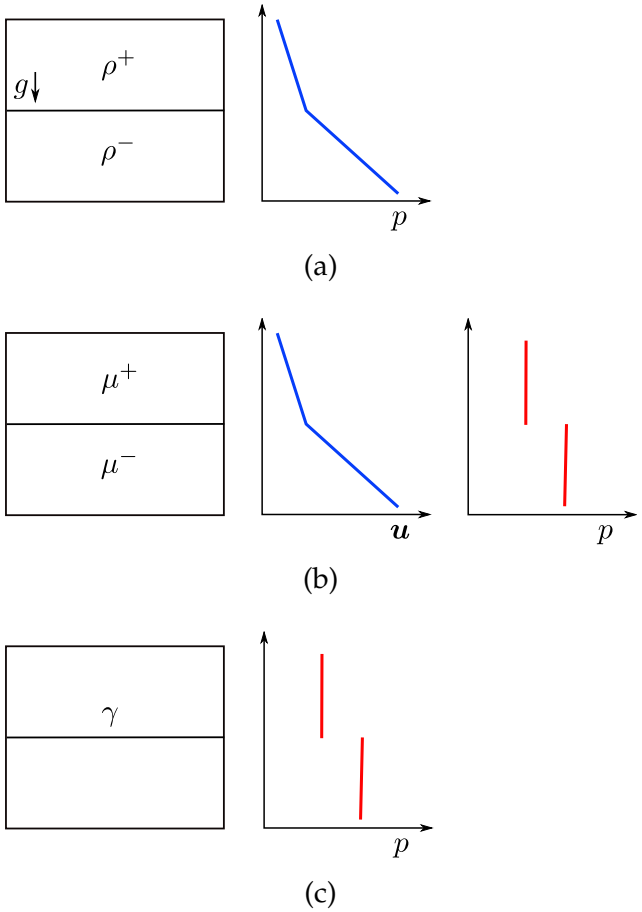

Figure 1.8: Flow discontinuities for: (a) density jump, (b) viscosity jump, and (c) surface tension.

References

[1] Anderson, D., and G. McFadden, 1998. Diffuse-interface methods in fluid mechanics. Annual Reviews of Fluid Mechanics 30, 139–165.

[2] Aref, H., and G. Tryggvason, 1984. Vortex dynamics of passive and active interfaces. Physica D: Nonlinear Phenomena 12, 59–70.

[3] Batchelor, G., 1967. An introduction to fluid dynamics. Cambridge University Press.

[4] Brackbill, J., D. Kothe, and C. Zemach, 1992. A continuum method for modeling surface tension. Journal of Computational Physics 100, 335–354.

[5] Bremond, N., A. Thiam, and J. Bibette, 2008. Decompressing emulsion droplets favors coalescence. Physical Review Letters 100.

[6] Bush, J., 2004. Surface tension module. MIT lecture notes.
URL http://web.mit.edu/1.63/www/Lec-notes/Surfacetension

[7] Davies, J., and E. Rideal, 1963. Interfacial phenomena. Academic Press.

[8] Gibbs, J., 1876. On the equilibrium of heterogeneous substances. Transactions of the Connecticut Academy 3.

[9] Idelsohn, S., M. Mier-Torrecilla, N. Nigro, and E. Oñate, 2009. On the analysis of heterogeneous fluids with jumps in the viscosity using a discontinuous pressure field. Computational Mechanics In press.

[10] Idelsohn, S., M. Mier-Torrecilla, and E. Oñate, 2009. Multi-fluid flows with the Particle Finite Element Method. Computer Methods in Applied Mechanics and Engineering 198, 2750–2767.

[11] Ishii, M., and T. Hibiki, 2005. Thermo-fluid dynamics of two-phase flow. Springer–Verlag.

[12] Joseph, D., 1990. Fluid mechanics of two miscible liquids with diffusion and gradient stresses. European Journal of Mechanics B 9, 565–596.

[13] Kang, M., R. Fedkiw, and X. Liu, 2000. A boundary condition capturing method for multiphase incompressible flow. Journal of Scientific Computing 15, 323–360.

[14] Korteweg, D., 1901. Sur la forme que prennent les equations du mouvements des fluides si l'on tient compte des forces capillaires causees par des variations de densite considerables mais continues et sur la theorie de la capillarite dans l'hypothese d'une variation continue de la densite. Arch. Neerl. Sci. Exactes Nat. Ser. II 6, 1–24.

[15] Landau, L., and E. Lifshitz, 1959. Fluid mechanics. Pergamon.

[16] Levich, V., and V. Krylov, 1969. Surface-tension-driven phenomena. Annual Reviews of Fluid Mechanics 1, 293–316.

[17] Li, J., and Y. Renardy, 2000. Numerical study of flows of two immiscible liquids at low Reynolds number. SIAM Review 42, 417–439.

[18] Plateau, J., 1873. Statique experimentale et theorique des liquides soumis aux seules forces moleculaire. Gauthier-Villars.

[19] Quarteroni, A., and A. Valli, 1997. Numerical approximation of partial differential equations. Springer–Verlag.

[20] Rayleigh, L., 1892. On the theory of surface forces-II. Compressible fluids. Philosophical Magazine 33, 209–20.

[21] Rayleigh, L., 1902. Scientific Papers. Cambridge University Press.

[22] Rowlinson, J., and B. Widom, 1982. Molecular theory of capillarity. Dover.

[23] Scardovelli, R., and S. Zaleski, 1999. Direct Numerical Simulation of free-surface and interfacial flow. Annual Reviews of Fluid Mechanics 31, 567–603.

[24] Scriven, L., 1960. Dynamics of a fluid interface. Equations of motion for Newtonian surface fluids. Chemical Engineering Science 12, 98–108.

[25] Shikhmurzaev, Y., 2007. Capillary flows with forming interfaces. Taylor & Francis.

[26] Smolianski, A., 2001. Numerical modeling of two fluid interfacial flows. Ph.D. thesis, University of Jyväskylä, Finnland.

[27] Sommerfeld, M., B. van Wachem, and R. Oliemans (Eds.), 2007. Best Practice Guidelines for Computational Fluid Dynamics of Dispersed Multiphase Flows. ERCOFTAC.

[28] van der Waals, J., 1893. The thermodynamic theory of capillarity under the hypothesis of a continuous density variation. Journal of Statistical Physics 20, 197–244.

[29] Winkelmann, C., 2007. Interior penalty finite element approximation of Navier-Stokes equations and application to free surface flows. Ph.D. thesis, Ecole Polytechnique Federale de Lausanne.

[30] Yih, C., 1967. Instability due to viscosity stratification. Journal of Fluid Mechanics 27, 337–352.

Chapter 2

Lagrangian methods

Over the last thirty years, computer simulation of incompressible fluid flow has been based on the Eulerian formulation of the fluid mechanics equations on continuous domains. However, it is still difficult to analyze problems in which the shape of the free surfaces or internal interfaces changes continuously or in fluid-structure interactions where complicated contact problems are involved.

Alternatively, particle methods in which each fluid particle is followed in a Lagrangian manner have been used. The first ideas on this approach were proposed by Gingold & Monaghan [24] for the treatment of astrophysical hydrodynamic problems with the so called Smoothed Particle Hydrodynamics method (SPH) and later generalized to fluid mechanics problems. SPH uses kernel approximations to interpolate the unknowns. More particle methods have been developed based on similar ideas and applied to multiphase flows. The combination of the particle approach with the finite element method has given rise to the Particle Finite Element Method (PFEM) (Idelsohn et al. [41], Oñate et al. [62]) used in this work.

This chapter introduces the Lagrangian methods for fluid flow simulations. First we present the governing equations in the Lagrangian description, and briefly review the state of the art of finite element methods using this description. Mesh-based methods are in general limited in the amount of mesh deformation they are able to simulate with accuracy. Other option are the particle methods and, in particular, the meshless subfamily. Finally, we focus on the Particle Finite Element Method and explain its main features.

2.1 Lagrangian description

The governing equations in fluids have been commonly formulated in a spatial or Eulerian description, where the frame of reference is fixed. Lagrangian methods make use of the material formulation, in which the frame of reference coincides

with the particles of the medium and thus, it is convected with the fluid.

While in the kinetic theory of fluids particles represent molecules in random motion, in the continuum mechanics theory molecules are replaced by a continuum whose behavior at any point is the average behavior of the molecules in a suitable neighborhood of the point. It is assumed that one can associate to any fluid particle the macroscopic properties of the bulk fluid.

Let $\Omega(t)$ denote again a material domain in $\boldsymbol{R}^d$. The initial coordinates $\boldsymbol{X}$ of a particle at time t^0 are called *material coordinates* and $\Omega_0 = \Omega(t^0)$ is the *reference configuration*. The position $\boldsymbol{x}$ of the particle at a later time t will be referred as the *spatial coordinates*. The motion of $\Omega(t)$ can be described by a mathematical transformation φ such that $\boldsymbol{x} = \varphi(\boldsymbol{X}, t)$. The current configuration is then $\Omega_t = \varphi(\Omega_0, t)$. It is assumed that φ is continuous, one-to-one and invertible. The deformation gradient is defined by

$$\boldsymbol{F}(\boldsymbol{X}, t) = \frac{\partial \varphi}{\partial \boldsymbol{X}} = \frac{\partial \boldsymbol{x}}{\partial \boldsymbol{X}} \tag{2.1}$$

φ^{-1} exists if and only if the Jacobian $J = \det(\boldsymbol{F}) \neq 0$. The condition $J > 0$ avoids a change of orientation in the reference axes.

The transformation φ also can be viewed as the parametric equation of a curve in space and parameter t, that goes through the point $\boldsymbol{X}$ at $t = 0$. These curves are called *particle paths* or *trajectories*. Any property of the fluid may be followed along the particle path, e.g. $\rho(\boldsymbol{X}, t)$ means the density that an observer located on the particle $\boldsymbol{X}$ would see through time. This material description of a property $G(\boldsymbol{X}, t)$ can be changed into a spatial description $g(\boldsymbol{x}, t)$ by $g(\boldsymbol{x}, t) = G(\varphi^{-1}(\boldsymbol{x}, t), t)$. It means that the value of a property at position $\boldsymbol{x}$ at time t is the value corresponding to the particle which is at $\boldsymbol{x}$ at time t. Conversely, the material description can be derived from the spatial one: $G(\boldsymbol{X}, t) = g(\varphi(\boldsymbol{X}, t), t)$, meaning that the property value as seen by the particle at time t is the value at the position it occupies at that time.

The material derivative $\dfrac{\mathrm{d}G}{\mathrm{d}t}$ is by definition the temporal variation of G evaluated in the material frame of reference (i.e. holding $\boldsymbol{X}$ fixed). Applying the chain rule, the material derivative can be expressed in the spatial frame of reference as

$$\begin{aligned} \frac{\mathrm{d}G}{\mathrm{d}t}(\boldsymbol{X}, t) &= \frac{\partial}{\partial t}(g \circ \varphi)(\boldsymbol{X}, t) = \frac{\partial g}{\partial t}(\varphi(\boldsymbol{X}, t)) + \frac{\partial g}{\partial \varphi}\frac{\partial \varphi}{\partial t}(\boldsymbol{X}, t) \\ &= \frac{\partial g}{\partial t}(\boldsymbol{x}, t) + \big(\boldsymbol{u}(\boldsymbol{x}, t) \cdot \boldsymbol{\nabla}_x\big) g(\boldsymbol{x}, t) \end{aligned} \tag{2.2}$$

where $\boldsymbol{u}(\boldsymbol{x}, t) = \dfrac{\partial \varphi}{\partial t}(\boldsymbol{X}, t)$ is the spatial velocity.

In the classical conservation of momentum equation,

$$\rho\big(\frac{\partial \boldsymbol{u}}{\partial t} + \boldsymbol{u} \cdot \boldsymbol{\nabla}_x \boldsymbol{u}\big) = \boldsymbol{\nabla}_x \cdot \boldsymbol{\sigma} + \rho \boldsymbol{g} \tag{2.3}$$

the Cauchy stress tensor $\boldsymbol{\sigma}(\boldsymbol{x},t)$ relates forces in the current configuration to areas in the current configuration. In terms of the coordinates $\boldsymbol{X}$, Eq. (2.3) becomes

$$\rho_0 \frac{\mathrm{d}\boldsymbol{u}}{\mathrm{d}t} = \boldsymbol{\nabla}_X \cdot \hat{\boldsymbol{\sigma}} + \rho_0 \boldsymbol{g} \tag{2.4}$$

where the first Piola-Kirchhoff stress tensor $\hat{\boldsymbol{\sigma}}$,

$$\hat{\boldsymbol{\sigma}} = J(\boldsymbol{X},t)\,\boldsymbol{\sigma}(\boldsymbol{x},t)\cdot\boldsymbol{F}^{-T}(\boldsymbol{X},t) = -Jp\boldsymbol{F}^{-T} + J\mu(\boldsymbol{\nabla}_X\boldsymbol{u}\boldsymbol{F}^{-1} + \boldsymbol{F}^{-T}\boldsymbol{\nabla}_X^T\boldsymbol{u})\boldsymbol{F}^{-T} \tag{2.5}$$

relates forces in the current configuration with areas in the reference configuration, and ρ_0 is the density in the reference configuration.

The classical incompressibility condition

$$\boldsymbol{\nabla}_x \cdot \boldsymbol{u} = 0 \tag{2.6}$$

may be reformulated in the Lagrangian description as

$$\frac{\mathrm{d}\rho}{\mathrm{d}t} = 0, \quad J = 1 \quad \text{or} \quad \boldsymbol{\nabla}_X \cdot (J\boldsymbol{F}^{-1}\boldsymbol{u}) = 0 \tag{2.7}$$

Whereas in the Eulerian description the acceleration is nonlinear with respect to the velocity $\boldsymbol{u}(\boldsymbol{x},t)$ and the deformation gradient is the identity tensor ($\boldsymbol{F} = \boldsymbol{I}$), in the Lagrangian description the material acceleration $\dfrac{\mathrm{d}\boldsymbol{u}}{\mathrm{d}t}$ is linear with respect to velocity but the Piola-Kirchhoff tensor $\hat{\boldsymbol{\sigma}}$ depends on the current coordinates of the material points, which are computed by solving the trajectories equation

$$\frac{\mathrm{d}\boldsymbol{x}}{\mathrm{d}t} = \boldsymbol{u}(\boldsymbol{x},t) \tag{2.8}$$

Therefore, the convective non-linearity of Eq. (2.3) transforms into a geometrical non-linearity in Eq. (2.4). Moreover, the governing equations in Lagrangian description present an initial value problem, and one is forced to include time as an independent variable even for steady flows.

2.2 State of the art

The Lagrangian description is the most natural approach to transient flow problems which involve free surfaces, interfaces or sharp boundaries, since: (i) the interface representation is naturally embedded in the material description of the flow, (ii) the boundary conditions are easy to apply and (iii) the convective term does not appear in the momentum equations. For these reasons, the Lagrangian formulation happens to be the standard one in structural mechanics (Belytschko et al. [7]). However, in fluid mechanics it has been applied much more rarely.

In a method based on a mesh representation of the flow solution, the main difficulty of the Lagrangian approach is the severe deformation of the

original domain that will occur during the computation and affect the numerical accuracy. To overcome this mesh distortion two approaches have been mainly used: remeshing algorithms and meshless methods. The remeshing approach introduces a new mesh and transfers the information from the old distorted mesh to the new one. Nodes may be added, deleted or reconnected to maintain the mesh as regular as possible. When the remeshing is just local, the method is called *free-Lagrange* (e.g. Crowley [17], Fritts & Boris [23]).

The idea of using a Lagrangian flow formulation dates from the work of Hirt et al. [32]. Since then, several authors have investigated this formulation. Examples within the context of FEM include the work of Bach & Hassager [5] with an application to small amplitude sloshing wave analysis, or Kawahara and collaborators (Ramaswamy et al. [70], Ramaswamy & Kawahara [69], Okamoto & Kawahara [59], Hayashi et al. [30]), who applied the fractional step to free surface problems including dam break simulation and large amplitude of liquids in containers. Because these methods were implemented on a mesh with fixed connectivities, they were limited in the extent of mesh deformation they could account for. Kawahara & Anjyu [45] were the first to introduce a mesh rezoning technique and applied it to the simulation of solitary wave propagation. Another example of a free-Lagrange finite element method is the work of Hansbo [29]. Recently, Radovitzky & Ortiz [68] and Malcevic & Ghattas [53] have developed Lagrangian methods based on a continuous and adaptive remeshing of the entire mesh. In all cases with remeshing, the transfer of data between different meshes (i.e. the interpolation of the flow variables to the quadrature points of the new mesh) may be a source of numerical diffusion.

The second approach allowing to overcome the problem of mesh distortion is to use meshless methods, which abandon the mesh completely. These methods represent the problem domain by a finite number of interacting particles.

2.3 Particle methods

Particle methods aim to represent the behavior of a physical problem by a collection of particles. Each particle moves accordingly to its own mass, and the internal and external forces applied on it. External forces are evaluated by the interaction with the neighbor particles. All physical and mathematical properties are attached to the particle itself and not to the elements as in FE methods. For instance, physical properties like viscosity or density, physical variables like velocity, temperature or pressure and also mathematical variables like gradients or volumetric deformations are assigned to each particle and they represent an average of the property around the particle position.

Particle methods are advantageous to treat discrete problems such as granular

materials but also to treat continuous problems with internal interfaces, frictional contact in fluid-solid interactions or free surfaces with breaking waves. Particles are associated the different materials and thus the interfaces can be easily followed. The most relevant characteristic of particle methods is that there is not a specified solution domain. The problem domain is defined by the particle positions and hence, there is not a boundary contour. This is the reason why, when a differential equation is to be solved in order to evaluate the forces, the boundary needs to be identified to impose the boundary conditions.

It must be noted that in order to evaluate the interacting forces between particles any classical approximation method may be used, including FEM, finite difference, meshless methods, etc. This means that a particle method may be used with or without a mesh, depending on the method chosen to evaluate the interacting forces.

Particle methods can be roughly classified in two types: (a) those based on probabilistic models, such as molecular dynamics, direct simulation Monte Carlo and lattice-gas automata; and (b) those based on deterministic models, such as SPH or other meshless methods, particle-mesh hybrid methods and the Particle Finite Element Method. The first class of methods represents macroscopic properties as statistical behavior of microscopic particles, so that a huge number of particles should be simulated for a long time to obtain accurate average values, while the second class of methods relies on the macroscopic Navier-Stokes equations. In this section we focus on the deterministic methods except for a brief introduction to the lattice-Boltzmann method, an improvement of the lattice-gas automata.

The lattice-Boltzmann method

While FEM is based on the numerical solution of a macroscopic description of the fluid flow, namely the Navier-Stokes equations, the lattice-Boltzmann method (LBM) (McNamara & Zanetti [55], Higuera & Jimenez [31], Chen et al. [13]) is a mesoscopic approach where the fluid dynamics is approximated by interactions between fictitious particles on a regular lattice. The key idea is to construct simplified kinetic models that incorporate the essential physics of microscopic processes so that the averaged properties obey the macroscopic equations. The fluid flow is modeled by the collective behavior of many molecules, not by individual molecules as in molecular dynamics simulations.

The computational grid consists of a number of lattice nodes which are connected with their neighbors by a bond. At each time step, particles move along the bonds of the lattice and interact locally according to a given set of rules:

1. Propagation. Particles move along lattice bonds from one lattice node to one of its neighbors.

2. Collision. Particles on the same lattice node redistribute their velocities locally, subject to mass and momentum conservation.

In the two dimensional model of Figure 2.1, a square lattice with a space increment Δx is used in which each node has eight nearest neighbors connected by bonds. Particles positions are confined to the nodes of the lattice and, in one time step Δt, the movement is restricted to a nearest neighbor along these bonds. Particles may move along the axes with velocity $|\boldsymbol{e}_i| = c := \Delta x/\Delta t$, move along the diagonal directions with velocity $|\boldsymbol{e}_i| = \sqrt{2}c$ or rest at the node with zero velocity. The single-particle distribution function $f_i(\boldsymbol{x}, t)$ is the probability of finding a particle at node $\boldsymbol{x}$ and time t with velocity $\boldsymbol{e}_i$. In total, nine values describe the particle distribution function at a node. $f_i(\boldsymbol{x}, t)$ has to satisfy the lattice Boltzmann equation

$$f_i(\boldsymbol{x} + \boldsymbol{e}_i, t + \Delta t) - f_i(\boldsymbol{x}, t) = \Omega_i \tag{2.9}$$

where $i = 0, ..., 8$ and Ω_i is the collision operator representing the rate of change of the particle distribution due to collisions. Bhatnagar, Gross and Krook (BGK) [9] simplified the collision operator by assuming that the momenta of the interacting particles will be redistributed at some constant rate towards a local equilibrium distribution $f_i^{eq}(\boldsymbol{x}, t)$. This simplification is called the single-time relaxation approximation:

$$\Omega_i = \frac{1}{\tau}\left(f_i^{eq}(\boldsymbol{x}, t) - f_i(\boldsymbol{x}, t)\right) \tag{2.10}$$

and τ is the relaxation time which controls the rate of approach to equilibrium. With the appropriate equilibrium distribution, and defining the speed of sound as $c_s^2 = c^2/3$, one can recover the continuity and Navier-Stokes equations through a Chapman-Enskog expansion (Qian et al. [67]). Accordingly, the pressure p is identified with $p = \rho c_s^2$ and the kinematic viscosity (in lattice units) is defined by $\nu = c_s^2 \Delta t(\tau - 0.5)$, with $\tau > 0.5$. The macroscopic flow variables are obtained through moment integration of the distribution functions:

$$\rho = \sum_{i=0}^{8} f_i, \quad \text{and} \quad \boldsymbol{u} = \frac{1}{\rho}\sum_{i=0}^{8} f_i\, \boldsymbol{e}_i \tag{2.11}$$

In the field of multi-fluid flows, Rothman & Keller [72] introduced the first lattice-gas automata model for simulation immiscible fluids. Since then several LB models have been constructed for simulating flows with immiscible components and multiple phases, e.g. Gunstensen et al. [28], Chen et al. [15], Shan & Chen [74], Rothman & Zaleski [73], Takada et al. [79], Inamuro et al. [43], most usually together with the diffuse-interface model (see Section 1.1). General references are the review by Chen & Doolen [14] and the books by Succi [76] and Sukop & Thorne [77].

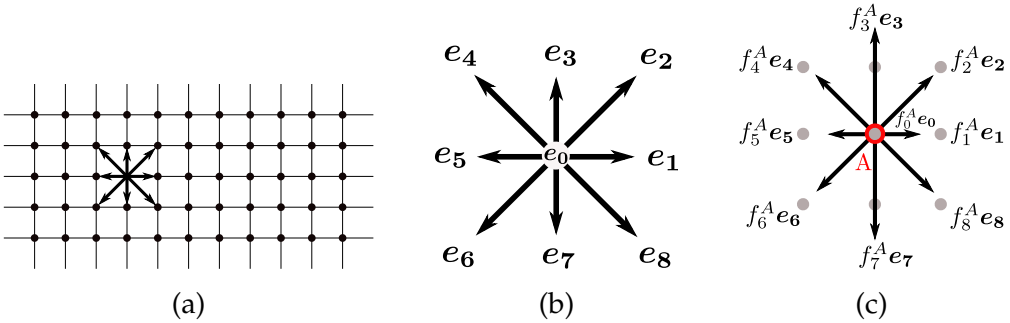

(a) (b) (c)

Figure 2.1: D2Q9 scheme (Dn stands for n dimensions and Qm for m velocities): (a) lattice, (b) velocities, and (c) momentum distribution. The total momentum at lattice node A is $\rho \boldsymbol{u} = \sum_i f_i^A \boldsymbol{e}_i$.

Meshless methods

Meshless methods do not rely on a mesh to approximate the equations, they just need the node connectivity to define the interpolations of the variables. Over the last decades a number of meshless methods have been proposed (see Table 2.1). They can be subdivided in accordance with the definition of the shape functions and the minimization method of the approximation. This minimization may be via a strong form (as in point collocation) or a weak form (as in Galerkin methods) approach. The first meshless method proposed was the Smoothed Particle Hydrodynamics (SPH) (Lucy [52], Gingold & Monaghan [24]), motivated by ideas from statistical theory and Monte Carlo integration. SPH introduces a smoothing kernel to approximate the functions and their spatial derivatives that model the interactions carried by neighboring particles. It was originally developed for compressible, inviscid flows and used for astrophysical problems (Gingold & Monaghan [25]). Koshizuka & Oka [46] have adapted and improved SPH for incompressible viscous flows and called it Moving Particle Semi-implicit (MPS) method. It uses a modified kernel function and a semi-implicit algorithm to incorporate the incompressibility condition. SPH, together with wavelet theory, is also the basis for a more general method known as the Reproducing Kernel Particle Method (RPKM), used by Liu et al. [51] and Aluru [1] in a weak and a strong form respectively.

Starting from a completely different idea, the Moving Least-Squares (MLS) approximation (Lancaster & Salkauskas [47]) became very popular in the meshless community for constructing shape functions. MLS is based on a polynomial interpolant that fits a number of points minimizing the distance between the interpolated function and the value of the unknown point. Recently, the equivalence between MLS and RPKM for polynomial basis has been proven (Jin et al. [44]), so that both approaches may now be considered to rely on the same

shape functions. MLS shape functions have been successfully used by Nayroles et al. [57] in a weak Galerkin form with a background grid for integration (in the so called Diffuse Element method) and, in a more accurate way, by Belytschko et al. [8] (Element-Free Galerkin method). Oñate et al. [63, 64, 66] used MLS and point collocation in the Finite Point method, avoiding the background integration grid.

Other possible choice for the shape function is the natural neighbor or Sibson function. This interpolation is based on the Voronoi diagram of the particles and is used as test and shape functions in the Natural Element Method (NEM) (Sukumar et al. [78]). Similarly, the Meshless FEM (MFEM) (Idelsohn et al. [40]) uses non-Sibsonian shape functions, which have almost the same properties than the Sibson interpolant but may be constructed with considerably less computing time. In the MFEM, the domain is uniquely divided into polyhedra elements with the Extended Delaunay Tessellation. Shape functions inside each polyhedron are determined using non-Sibsonian interpolation. They are simple and reduce to the standard linear FEM shape functions in case of triangles and tetrahedra. Consequently, only low-order quadrature rules are necessary in the MFEM leading to a very efficient method.

SPH shape functions do not form a partition of unity, in contrast to MLS and RKPM functions. Drawbacks of SPH are the lack of accuracy and stability. The major problem of MLS approximation is that the shape functions do not possess the Kronecker delta function property, what makes difficult the imposition of Dirichlet boundary conditions. Furthermore, the evaluation of MLS shape functions require the inversion of a matrix at every integration point. Thus, Galerkin methods based on MLS shape functions, such as DEM and EFGM, have a large computational cost associated with the numerical evaluation of the integrals in the weak form. In contrast, Sibson and non-Sibsonian interpolants build a partition of unit with linear consistency, are strictly positive and have Kronecker delta property. Some classical shape functions are illustrated in Figure 2.2.

Meshless methods have been applied to the solution of multi-fluid flows in e.g. Monaghan & Kocharyan [56], Koshizuka & Oka [46], Shirakawa et al. [75], Nomura et al. [58], Colagrossi & Landrini [16] and Hu & Adams [33]. Extensive reviews about meshless methods can be found in Duarte [20], Belytschko et al. [6], Li & Liu [49], Liu [50], Fries & Matthies [22], Brackbill [10], Babuska et al. [4] and Gu [27].

2.4 Particle Finite Element Method

The Particle Finite Element Method (PFEM) (Idelsohn et al. [40, 34], Oñate et al. [62]) is a numerical technique for modeling and analysis of complex multidisciplinary problems in fluid and solid mechanics involving thermal effects,

Method	References	System equation to be solved	Method of function approximation
Diffuse Element	Nayroles et al. [57]	Weak form	Moving Least-Squares approx, Galerkin method
Element Free Galerkin	Belytschko et al. [8]	Weak form	Moving Least-Squares approx, Galerkin method
Finite Point	Oñate et al. [63, 64]	Strong form	Fixed Least-Squares approx, point collocation
Smoothed Particle Hydrodynamics	Lucy [52], Gingold & Monaghan [24]	Strong form	Integral representation, point collocation
Reproducing Kernel Particle	Liu et al. [51], Aluru [1]	Strong or weak form	Integral representation, point collocation
Natural Element	Sukumar et al. [78]	Weak form	Galerkin method
Meshless FEM	Idelsohn et al. [40]	Weak form	Galerkin method
Moving Particle Semi-implicit	Koshizuka & Oka [46]	Strong form	Integral representation

Table 2.1: Some of the most relevant meshless methods and their features (from Liu [50]).

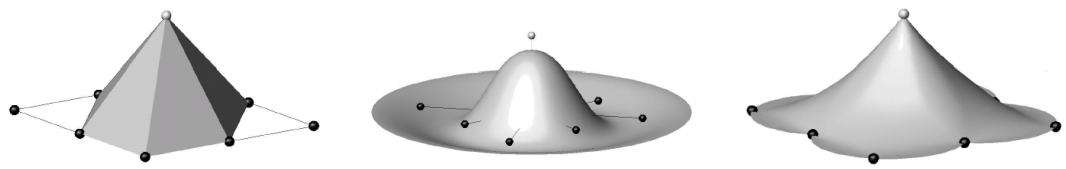

(a) (b) (c)

Figure 2.2: Some 2D shape functions for a regular node distribution: (a) linear Finite Element shape function, (b) MLS approximation function, and (c) natural neighbor shape function (from Del Pin [18]).

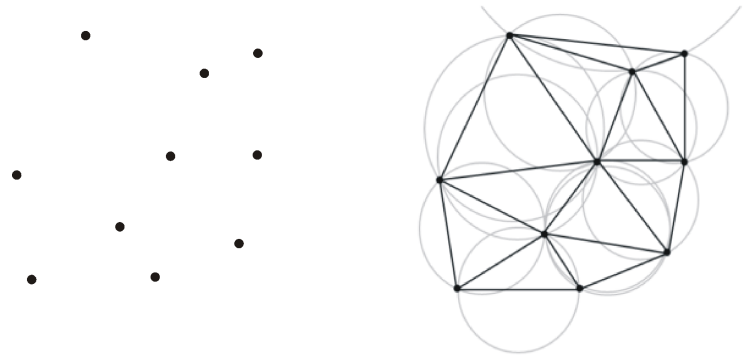

Figure 2.3: Delaunay triangulation of a cloud of nodes.

interfacial and free-surface flows, and fluid-structure interaction, among others.

PFEM is a particle method in the sense that the domain is defined by a collection of particles that move in a Lagrangian manner according to the calculated velocity field, transporting their momentum and physical properties (e.g. density, viscosity). The interacting forces between particles are evaluated with the help of a mesh. Mesh nodes coincide with the particles, so that when the particles move so does the mesh. On this moving mesh, the governing equations are discretized using the standard finite element method (FEM) (Zienkiewicz & Taylor [80]). The possible large distortion of the mesh is avoided through remeshing of the computational domain. Due to the fact that all the hydrodynamical information is stored in the nodes, remeshing does not introduce numerical diffusion as in the Lagrangian FE methods mentioned before. A robust and efficient Delaunay triangulation algorithm (Calvo [11], Fig. 2.3) allows frequent remeshing. This gives the method excellent capabilities for modeling large displacement and large deformation problems.

The particles are used to generate a discrete domain within which the integral form of the governing differential equations are solved. An algorithm is needed to define the boundary contours from the collection of particles. PFEM uses the alpha-shape technique (Edelsbrunner & Mücke [21]) to recognize the external boundary after the Delaunay triangulation of the domain convex hull (see Figure 2.4): All nodes defining an empty sphere with a radius $r(\boldsymbol{x})$ larger than $\alpha h(\boldsymbol{x})$ are considered to be boundary nodes. $h(x)$ is the distance between two neighboring nodes and the parameter α is chosen so that $\alpha \gtrsim 1$. Large values of α result in the convex hull of the collection, while small values return a boundary constituted just by the nodes. The error in the boundary surface definition is proportional to h. One of the advantages of the alpha-shape technique is the easy way to determine when particles separate from the fluid domain, as may happen in free surface problems (e.g. splashing).

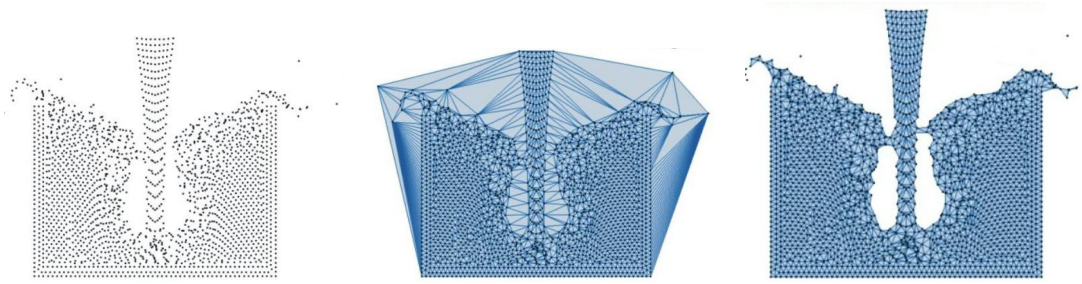

(a) (b) (c)

Figure 2.4: Alpha-shape: (a) collection of nodes, (b) Delaunay triangulation of the convex hull, (c) mesh after alpha-shape (from Calvo [11]).

The method is based on the following features:

- the information is particle-based, i.e. all the geometrical and mechanical information is attached to the nodes,
- the Lagrangian point of view for describing the motion,
- the governing equations are discretized and solved on a finite element mesh that is constructed at every time step,
- the boundaries of the domain are defined via the alpha-shape technique.

The use of a Lagrangian formulation eliminates the standard convection terms present in Eulerian formulations. The convection terms are responsible for non-linearity, non-symmetry and non-self-adjoin operators, which require the introduction of stabilization terms to avoid numerical oscillations. All these problems are absent in the Lagrangian formulation. Only the nonlinearity remains due to the unknown of the final particle position. The resulting systems of equations are solved with a symmetric iterative scheme, such as the conjugate gradient method. Linear shape functions ($\mathbb{P}_1/\mathbb{P}_1$) are used for all unknowns. This equal order approximation for both the velocity and the pressure variables introduces numerical instabilities in the pressure field that need to be stabilized.

A typical solution with the PFEM involves the following steps (illustrated in Figure 2.5):

(1) The starting point at each time step is the cloud of nodes in the fluid and solid domains.

(2) Identification of the external boundary and the internal interfaces. The alpha-shape method is used for boundary definition.

(3) Discretization of the domain with a finite element mesh generated by Delaunay triangulation.

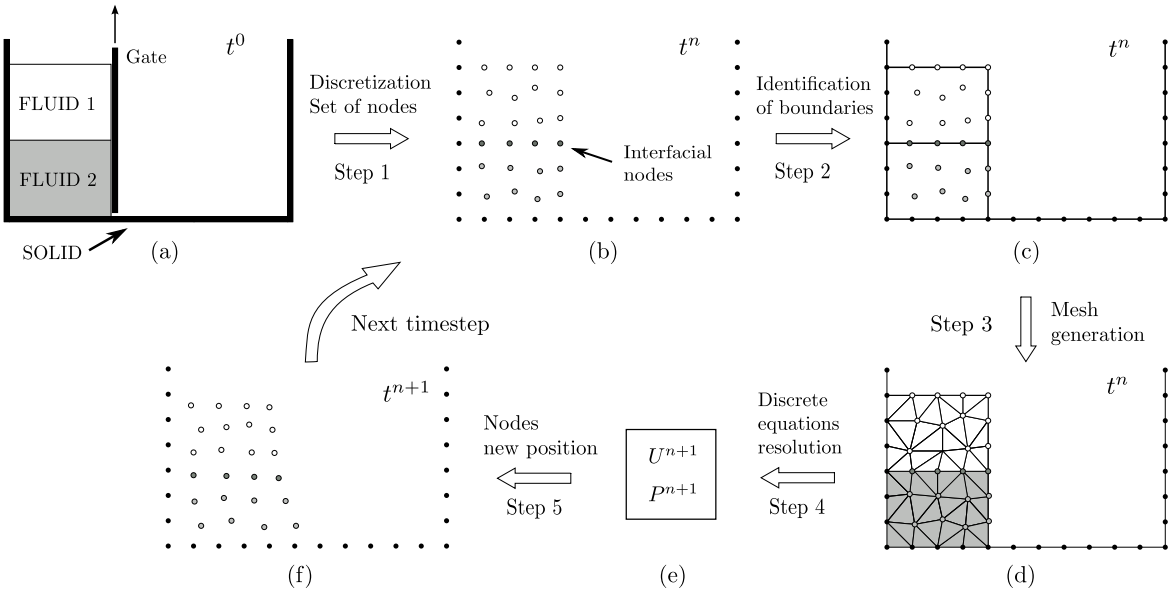

Figure 2.5: PFEM solution steps illustrated in a simple dam break example. As the gate of the dam is removed the water begins to flow. (a) Continuous problem (b) Step 1, discretization in cloud of nodes at time t^n; (c) Step 2, boundary and interface recognition; (d) Step 3, mesh generation; (e) Step 4, resolution of the discrete governing equations; (f) Step 5, nodes moved to new position for time t^{n+1}.

(4) Solution of the Lagrangian governing equations of motion for the fluid domain together with the boundary and interface conditions. Computing the relevant state variables at each time step: velocities, pressure, temperature, and concentration.

(5) Moving the mesh nodes to a new position in terms of the time increment and the velocity field computed in step (4).

(6) Back to step (1) and repeat the solution process for the next time step.

Thus PFEM combines the advantages of particle methods (namely only the "wet" domain considered, it is appropriate for changing domains, allows fluid fragmentation, tracks interfaces accurately, and does not introduce numerical diffusion when solving convection) with the accuracy of the finite element method.

Up to now, the method has been successfully applied to naval and coastal engineering (Oñate et al. [62, 61], Idelsohn et al. [41], Del Pin et al. [19], Larese et al. [48]), fluid-structure interaction (Idelsohn et al. [42, 36, 37, 35], Rossi et al. [71]), mould filling with solidification (Aubry et al. [3]), melting of polymers in fire (Oñate et al. [65]), excavation problems (Carbonell [12]), forming processes (Oliver et al. [60], Gonzalez-Ferrari [26]) and multi-fluid flows (Idelsohn et al. [38, 39]).

Previous theses on the PFEM for fluids include the works by Del Pin [18], Aubry [2] and Marti [54]. Del Pin [18] (2003) applied the method to incompressible flows with free surface and fluid-rigid solid interaction problems, such as dam break, sloshing, breaking wave, and floating bodies. The solver used a fractional step scheme with all the velocity components decoupled. Later Aubry [2] (2006) extended the method to viscous flow problems with heat transfer and solidification, such as the Rayleigh-Benard instability and mould filling. A generalized Stokes solver was implemented based on the Preconditioned Conjugate Gradient Uzawa, the compatible mini-element, and the Boussinesq approximation for thermal coupling. Finally, Marti [54] (2008) applied the PFEM to fluid-structure interaction problems using the same Lagrangian formulation for the fluid and the hypoelastic solid domains. The materials were modeled as compressible (solved with a penalty method) and incompressible (solved with a pressure segregation scheme specifically developed to overcome the added mass effect).

In the present work, the Particle Finite Element Method (PFEM) is used to solve the incompressible Navier-Stokes equations for multi-fluid flows. The motivation is to exploit the capability of the Lagrangian description to track the interfaces between different fluids. The very first example we ran consisted in an impinging jet (light fluid poured into a heavier fluid, see Figures 2.6 and 2.7), and the goal was to follow the movement of one fluid inside the other. Here we realized the numerical difficulties of simulating different materials and sharp interfaces. We have developed a numerical scheme able to deal with large jumps in the physical properties, include surface tension, and accurately represent the weak and strong discontinuities in the flow variables. The scheme is based on decoupling the nodes position, velocity and pressure variables through the Picard linearization and a pressure segregation method which takes into account the interface conditions. The interface has been defined to be aligned with the moving mesh, so that it remains sharp along time. Furthermore, pressure degrees of freedom have been duplicated at the interface nodes to represent the discontinuity of this variable due to surface tension and variable viscosity, and the mesh has been refined in the vicinity of the interface to improve the accuracy of the computations. We have applied the resulting scheme to several academic and geological problems, such as the two-fluid sloshing, extrusion of viscous fluids, bubble rise and breakup, mixing of magmatic liquids and negatively buoyant jets.

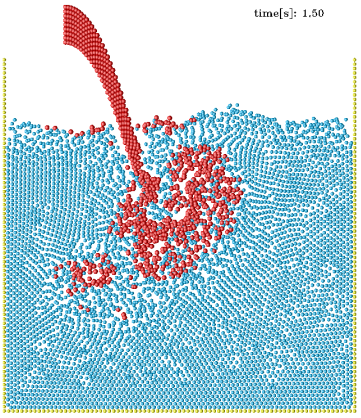

(a) $t = 1.5$ s

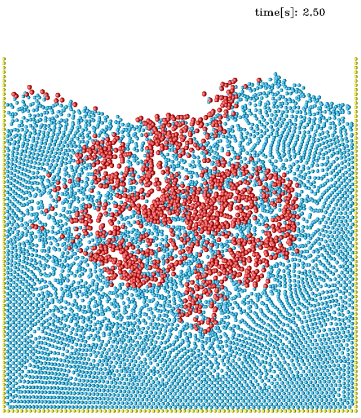

(b) $t = 2.5$ s

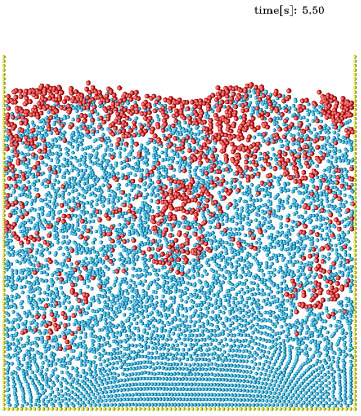

(a) $t = 5.5$ s

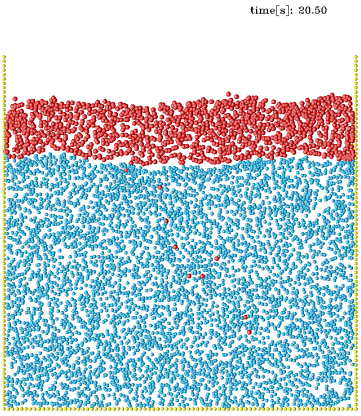

(b) $t = 20.5$ s

Figure 2.6: Impinging jet in 2D. A fluid of density $\rho = 800$ kg m^{-3} is poured into a 2×2 m container filled $3/4$ with water ($\rho = 1000$ kg m^{-3}). Both fluid have the same viscosity, $\mu = 10^{-3}$ Pa s, and the inflow jet velocity is 1 m s^{-1}. The jet generates some mixing, but at the end fluids separate due to their different densities.

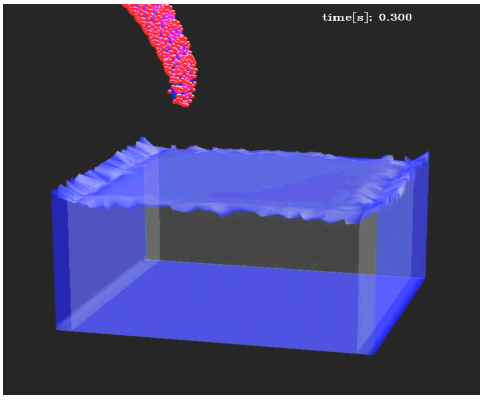

(a) $t = 0.3$ s

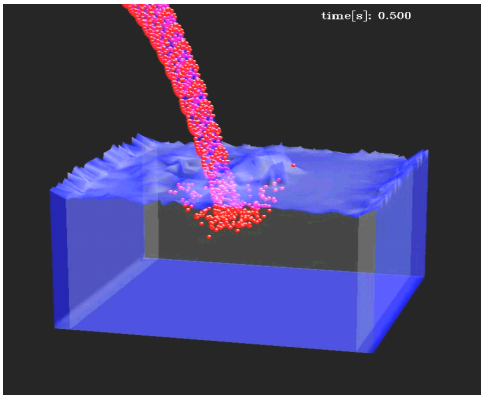

(b) $t = 0.5$ s

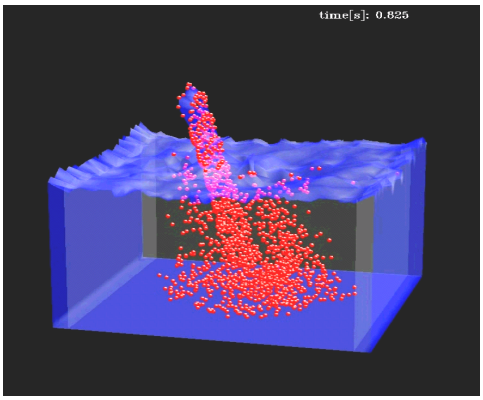

(a) $t = 0.8$ s

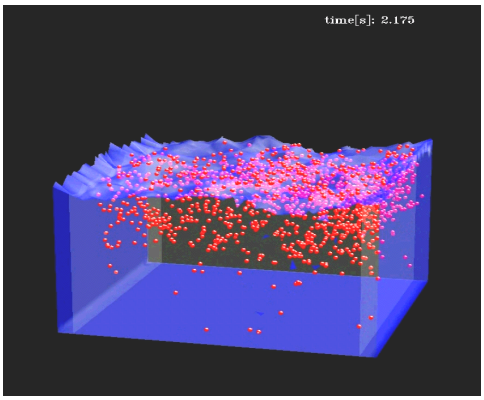

(b) $t = 2.2$ s

Figure 2.7: Impinging jet in 3D. Same settings than in the 2D case.

References

[1] Aluru, N., 2000. A point collocation method based on reproducing kernel approximations. International Journal for Numerical Methods in Engineering 47, 1083–1121.

[2] Aubry, R., 2006. Three dimensional Lagrangian fluid flow with thermal coupling. Ph.D. thesis, Universitat Politècnica de Catalunya, Barcelona (Spain).

[3] Aubry, R., S. Idelsohn, and E. Oñate, 2005. Particle Finite Element Method in fluid mechanics incluiding thermal convection-diffusion. Computers and Structures 83, 1459–1475.

[4] Babuska, I., U. Banerjee, and J. Osborn, 2005. Survey of meshless and generalized finite element methods: a unified approach. Tech. rep., Office of Naval Research.

[5] Bach, P., and O. Hassager, 1984. A Lagrangian finite element method for the simulation of flow of Newtonian liquids. AIChE Journal 30, 507–509.

[6] Belytschko, T., Y. Krongauz, D. Organ, M. Fleming, and P. Krysl, 1996. Meshless methods: An overview and recent developments. Computer Methods in Applied Mechanics and Engineering 139, 3–47.

[7] Belytschko, T., W. Liu, and B. Moran, 2000. Nonlinear Finite Elements for Continua and Structures. Wiley & Sons.

[8] Belytschko, T., Y. Lu, and L. Gu, 1994. Element-free Galerkin methods. International Journal for Numerical Methods in Engineering 37, 229–256.

[9] Bhatnagar, P., E. Gross, and M. Krook, 1954. A model for collision processes in gases. I. Small amplitude processes in charged and neutral one-component systems. Physical Review 94, 511–525.

[10] Brackbill, J., 2005. Particle methods. International Journal for Numerical Methods in Fluids 47, 693–705.

[11] Calvo, N., 2005. Generación de mallas tridimensionales por métodos duales. Ph.D. thesis, Universidad Nacional del Litoral, Santa Fe (Argentina).

[12] Carbonell, J., 2009. Modeling of ground excavation with the Particle Finite Element Method. Ph.D. thesis, Universitat Politècnica de Catalunya, Barcelona (Spain).

[13] Chen, H., S. Chen, and W. Matthaeus, 1992. Recovery of the Navier-Stokes equations using a lattice-gas Boltzmann method. Physical Review A 45, 5339.

[14] Chen, S., and G. Doolen, 1998. Lattice Bolzmann method for fluid flows. Annual Reviews of Fluid Mechanics 30, 329–64.

[15] Chen, S., G. Doolen, K. Eggert, D. Grunau, and E. Loh, 1991. Local lattice-gas model for immiscible fluids. Physical Review A 43, 7053–7056.

[16] Colagrossi, A., and M. Landrini, 2003. Numerical simulation of interfacial flows by smoothed particle hydrodynamics. Journal of Computational Physics 191, 448–475.

[17] Crowley, W., 1970. Flag: A free-Lagrange method for numerically simulating hydrodynamic flows in two dimensions. In: Lecture notes in physics. Vol. 8. pp. 37–43.

[18] Del Pin, F., 2003. The meshless finite element method applied to a lagrangian particle formulation of fluid flows. Ph.D. thesis, Universidad Nacional del Litoral, Santa Fe (Argentina).

[19] Del Pin, F., S. Idelsohn, E. Oñate, and R. Aubry, 2007. The ALE/Lagrangian Particle Finite Element Method: A new approach to computation of free-surfaces flows and fluid-object interactions. Computers and Fluids 36 (1), 27–38.

[20] Duarte, C., 1995. A review of some meshless methods to solve partial differential equations. TICAM Report 95-06, Texas Institute for Computational and Applied Mathematics.

[21] Edelsbrunner, H., and E. Mücke, 1994. Three-dimensional alpha shapes. ACM Transactions on Graphics 13, 43–72.

[22] Fries, T., and H. Matthies, 2004. Classification and overview of meshfree methods. Tech. rep., Technical University Braunschweig.

[23] Fritts, M. J., and J. P. Boris, 1979. The Lagrangian solution of transient problems in hydrodynamics using a triangular mesh. Journal of Computational Physics 31, 173–215.

[24] Gingold, R., and J. Monaghan, 1977. Smoothed particle hydrodynamics: theory and applications to non-spherical stars. Mon. Not. R. astr. Soc. 181, 375–389.

[25] Gingold, R., and J. Monaghan, 1982. Kernel estimates as a basis for general particle methods in hydrodynamics. Journal of Computational Physics 46, 429–453.

[26] Gonzalez-Ferrari, C., 2009. El Método de los Elementos Finitos de Partículas: Aplicaciones a la pulvimetalurgia industrial. Ph.D. thesis, Universitat Politécnica de Catalunya.

[27] Gu, Y., 2005. Meshfree methods and their comparisons. International Journal of Computational Methods 4, 477–515.

[28] Gunstensen, A., D. Rothman, S. Zaleski, and G. Zanetti, 1991. Lattice boltzmann model of immiscible fluids. Physical Review A 43, 4320–4327.

[29] Hansbo, P., 2000. A free-lagrange finite element method using space-time elements. Computer Methods in Applied Mechanics and Engineering 188, 347–361.

[30] Hayashi, M., K. Hatanaka, and M. Kawahara, 1991. Lagrangian finite element method for free surface Navier-Stokes flow using fractional step methods. International Journal for Numerical Methods in Fluids 13, 805–840.

[31] Higuera, F., and J. Jimenez, 1989. Boltzmann approach to lattice gas simulations. Europhysics Letters 9, 663–668.

[32] Hirt, C., J. Cook, and T. Butler, 1970. A Lagrangian method for calculating the dynamics of an incompressible fluid with free surface. Journal of Computational Physics 5, 103–124.

[33] Hu, X., and N. Adams, 2006. A multi-phase SPH method for macroscopic and mesoscopic flows. Journal of Computational Physics 213, 844–861.

[34] Idelsohn, S., N. Calvo, and E. Oñate, 2003. Polyhedrization of an arbitrary 3D point set. Computer Methods in Applied Mechanics and Engineering 192, 2649–2667.

[35] Idelsohn, S., F. Del Pin, R. Rossi, and E. Oñate, 2009. Fluid-structure interaction problems with strong added-mass effect. International Journal for Numerical Methods in Engineering 80, 1261–1294.

[36] Idelsohn, S., J. Marti, A. Limache, and E. Oñate, 2008. Unified Lagrangian formulation for elastic solids and incompressible fluids: Application to fluid-structure interaction problems via the PFEM. Computer Methods in Applied Mechanics and Engineering 197, 1762–1776.

[37] Idelsohn, S., J. Marti, A. Souto-Iglesias, and E. Oñate, 2008. Interaction between an elastic structure and free-surface flows: experimental versus numerical comparisons using the PFEM. Computational Mechanics 43, 125–132.

[38] Idelsohn, S., M. Mier-Torrecilla, N. Nigro, and E. Oñate, 2009. On the analysis of heterogeneous fluids with jumps in the viscosity using a discontinuous pressure field. Computational Mechanics In press.

[39] Idelsohn, S., M. Mier-Torrecilla, and E. Oñate, 2009. Multi-fluid flows with the Particle Finite Element Method. Computer Methods in Applied Mechanics and Engineering 198, 2750–2767.

[40] Idelsohn, S., E. Oñate, N. Calvo, and F. Del Pin, 2003. The meshless finite element method. International Journal for Numerical Methods in Engineering 58 (6), 893–912.

[41] Idelsohn, S., E. Oñate, and F. Del Pin, 2004. The Particle Finite Element Method: A powerful tool to solve incompressible flows with free-surfaces and breaking waves. International Journal for Numerical Methods in Engineering 61 (7), 964–989.

[42] Idelsohn, S., E. Oñate, F. Del Pin, and N. Calvo, 2006. Fluid-structure interaction using the Particle Finite Element Method. Computer Methods in Applied Mechanics and Engineering 195 (17–18), 2100–2123.

[43] Inamuro, T., T. Ogata, S. Tajima, and N. Konishi, 2004. A lattice Boltzmann method for incompressible two-phase flows with large density differences. Journal of Computational Physics 198, 628–644.

[44] Jin, X., G. Li, and N. Aluru, 2001. On the equivalence between least-squares and kernel approximations in meshless methods. Computer Modeling in Engineering and Sciences 2, 447–462.

[45] Kawahara, M., and A. Anjyu, 1988. Lagrangian finite element method for solitary wave propagation. Computational Mechanics Journal 3, 299–307.

[46] Koshizuka, S., and Y. Oka, 1996. Moving Particle Semi-Implicit method for fragmentation of incompressible fluid. Nuclear Engineering Science 123, 421–434.

[47] Lancaster, P., and K. Salkauskas, 1981. Surfaces generated by moving least squares methods. Mathematics of Computation 37, 141–158.

[48] Larese, A., R. Rossi, E. Oñate, and S. Idelsohn, 2008. Validation of the Particle Finite Element Method (PFEM) for simulation of free surface flows. Engineering Computations 25, 385–425.

[49] Li, S., and W. Liu, 2002. Meshfree and particle methods and their applications. Applied Mechanics Reviews 55, 1–34.

[50] Liu, G., 2003. Mesh free methods. CRC Press.

[51] Liu, W., S. Jun, and Y. Zhang, 1995. Reproducing kernel particle methods. International Journal for Numerical Methods in Fluids 20, 1081–1106.

[52] Lucy, L., 1977. A numerical approach to the testing of the fission hypothesis. Astronomical Journal 82, 1013–1024.

[53] Malcevic, I., and O. Ghattas, 2002. Dynamic-mesh finite element method for Lagrangian computational fluid dynamics. Finite Elements in Analysis and Design 38, 965–982.

[54] Marti, J., 2008. El método de elementos finitos de partículas en interacción fluido-estructura. Ph.D. thesis, Universidad Nacional del Litoral, Santa Fe (Argentina).

[55] McNamara, G., and G. Zanetti, 1988. Use of the Boltzmann equation to simulate lattice-gas automata. Physical Review Letters 61, 2332–2335.

[56] Monaghan, J., and A. Kocharyan, 1995. SPH simulation of multi-phase flow. Computer Physics Communications 87, 225–235.

[57] Nayroles, B., G. Touzot, and P. Villon, 1992. Generalizing the finite element method: diffuse approximation and diffuse elements. Computational Mechanics 10, 307–318.

[58] Nomura, K., S. Koshizuka, and Y. Oka, 2001. Numerical analysis of droplet breakup behavior using particle method. Journal of Nuclear Science and Technology 38, 1057–1064.

[59] Okamoto, T., and M. Kawahara, 1990. Two-dimensional sloshing analysis by Lagrangian finite element method. International Journal for Numerical Methods in Fluids 11, 453–477.

[60] Oliver, J., J. Cante, R. Weyler, C. González, and J. Hernández, 2007. Computational Plasticity. Vol. 1. Springer Verlag, Ch. Particle finite element methods in solid mechanics problems, pp. 87–103.

[61] Oñate, E., S. Idelsohn, M. Celigueta, and R. Rossi, 2008. Advances in the Particle Finite Element Method for the analysis of fluid-multibody interaction and bed erosion in free surface flows. Computer Methods in Applied Mechanics and Engineering 197, 1777–1800.

[62] Oñate, E., S. Idelsohn, F. Del Pin, and R. Aubry, 2004. The Particle Finite Element Method: An Overview. International Journal of Computational Methods 1 (2), 267–307.

[63] Oñate, E., S. Idelsohn, and O. Zienkiewicz, 1996. A finite point method in computational mechanics: Applications to convective transport and fluid flow. International Journal for Numerical Methods in Engineering 39, 3839–3866.

[64] Oñate, E., S. Idelsohn, O. Zienkiewicz, R. Taylor, and C. Sacco, 1996. A stabilized finite point method for analysis of fluid mechanics problems. Computer Methods in Applied Mechanics and Engineering 139, 315–346.

[65] Oñate, E., R. Rossi, S. Idelsohn, and K. Butler, 2009. Melting and spread of polymers in fire with the Particle Finite Element Method. International Journal for Numerical Methods in Engineering 81, 1046 – 1072.

[66] Oñate, E., C. Sacco, and S. Idelsohn, 2000. A finite point method for incompressible flow problems. Computing and Visualization in Science 2, 67–75.

[67] Qian, Y., D. D'Humieres, and P. Lallemand, 1992. Lattice BGK models for Navier-Stokes equation. Europhysics Letters 17, 479.

[68] Radovitzky, R., and M. Ortiz, 1998. Lagrangian finite element analysis of newtonian fluid flows. International Journal for Numerical Methods in Engineering 43, 607–619.

[69] Ramaswamy, B., and M. Kawahara, 1987. Lagrangian finite element analysis applied to viscous free surface fluid flow. International Journal for Numerical Methods in Fluids 7, 953–984.

[70] Ramaswamy, B., M. Kawahara, and T. Nakayama, 1986. Lagrangian finite element method for the analysis of two-dimensional sloshing problems. International Journal for Numerical Methods in Fluids 6, 659–670.

[71] Rossi, R., P. Ryzhakov, and E. Oñate, 2009. A monolithic FE formulation for the analysis of membranes in fluids. International Journal of Space Structures 24, 205–210.

[72] Rothman, D., and J. Keller, 1988. Immiscible cellular-automaton fluids. Journal of Statistical Physics 52, 1119–1127.

[73] Rothman, D., and S. Zaleski, 1994. Lattice-gas models of phase separation: interfaces, phase transitions, and multiphase flow. Reviews of Modern Physics 66, 1417–1481.

[74] Shan, X., and H. Chen, 1993. Lattice boltzmann model for simulating flows with multiple phases and components. Physical Review E 47, 1815–1820.

[75] Shirakawa, N., H. Horie, Y. Yamamoto, Y. Okano, and A. Yamaguchi, 2001. Analysis of jet flows with the two-fluid particle interaction method. Journal of Nuclear Science and Technology 38, 729–738.

[76] Succi, S., 2001. The Lattice Boltzmann Equation for Fluid Dynamics and Beyond. Clarendon Press.

[77] Sukop, M., and D. Thorne, 2006. Lattice Boltzmann modeling: an introduction for geoscientists and engineers. Springer.

[78] Sukumar, N., B. Moran, and T. Belytschko, 1998. The natural element method in solid mechanics. International Journal for Numerical Methods in Engineering 43, 839–887.

[79] Takada, N., M. Misawa, A. Tomiyama, and S. Fujiwara, 2000. Numerical simulation of two- and three-dimensional two-phase fluid motion by Lattice Boltzmann method. Computer Physics Communications 129, 233–246.

[80] Zienkiewicz, O., and R. Taylor, 2005. The Finite Element Method, 6th Edition. Vol. 3, Fluid Mechanics. Butterworth-Heinemann.

Chapter 3

PFEM for multi-fluid flows

This chapter is devoted to the computational treatment of the multi-fluid flow governing equations, and in particular to the numerical simulation of two immiscible, viscous, incompressible fluids separated by a moving interface.

The main difference between a homogeneous (single-fluid) flow and a heterogeneous one is the presence of internal interfaces. Well-known difficulties in the simulation of homogeneous flows are the coupling of pressure and velocity through the incompressibility constraint, the need of the discretization spaces to satisfy the inf-sup condition, and the non-linearity of the governing equations. In addition to these difficulties, any numerical scheme for heterogeneous flows needs to be able to follow the interface evolution, and model the jumps in the fluid properties and the discontinuities of the flow variables across the interface. Therefore, most schemes for single-fluid flows cannot be directly extended to multi-fluids.

In the case of immiscible multi-fluid flows, the governing equations can be solved for each fluid separately, with the different fluids coupled by suitable interface conditions, or equivalently, multi-fluids can be modeled as one heterogeneous fluid (i.e. with variable properties) and one set of equations is solved for the whole computational domain (Ishii [76]). The latter approach requires to account for interfacial phenomena such as surface tension by adding the appropriate interface terms to the governing equations, and since the material properties and the flow field are, in general, discontinuous across the interface, the differential form of the governing equations must be interpreted as a weak form, satisfied only in an integral sense.

The chapter is organized as follows: First we review the most used interface models proposed in the literature and the main difficulties that appear in the numerical simulation of heterogeneous flows, to focus then in the Particle Finite Element Method. We will describe its approach to model the interface,

the remeshing procedure, the treatment of the Lagrangian non-linearity, the discretization of the governing equations, and the modeling of the surface tension force. Finally, some numerical results will be presented to show the capabilities of the proposed scheme.

3.1 Interface description

A major challenge in the simulation of interfaces between different fluids is the accurate description of the interface evolution. The location of the interface is in general unknown and coupled to the local flow field which transports the interface. It is essential that the interface remains sharp and is able to fold, break and merge. In the past decades a number of techniques have been developed to model interfaces in multi-fluid flow problems, each technique with its own particular advantages and disadvantages. Comprehensive reviews can be found in e.g. Hyman [62], Floryan & Rasmussen [39], Unverdi & Tryggvason [135], Shyy [121], Rudman [115], Puckett et al. [109], Scardovelli & Zaleski [117], Tezduyar [129], Smolianski [123], Minev et al. [91], Caboussat [13] and Van Sint Annaland et al. [139].

A first classification of interface descriptions regarding the physical model used (see also Section 1.1) is:

- *Sharp-interface models*: In the classical fluid mechanical approach, the interface between two immiscible fluids is modeled as a zero-thickness boundary that evolves in time. The Navier-Stokes equations are supplemented with interface conditions that take into account interfacial physics like surface tension.

- *Diffuse-interface models*: These models are based on the diffuse-interface theory and use thermodynamic quantities distributed throughout the interfacial region to model microscopic interface physics (Anderson & McFadden [1], Chella & Viñals [16], Nadiga & Zaleski [95]). The model is built by adding a term to the stress tensor in the Navier-Stokes equations that is derived from the Korteweg postulates [80] and the van der Waals-Cahn-Hilliard [137, 14] free energy: $\boldsymbol{\sigma} = -p\boldsymbol{I} + \boldsymbol{\tau} - \boldsymbol{K}$, where $\boldsymbol{K} = \delta(\boldsymbol{\nabla}^T c \ \boldsymbol{\nabla} c)$, and c is the chemical composition. This term results in spontaneous phase separation and surface tension.

Most approaches for moving boundaries are based on the sharp-interface model and one set of governing equations. Another main classification, regarding the reference frame adopted (see Fig. 3.1), is:

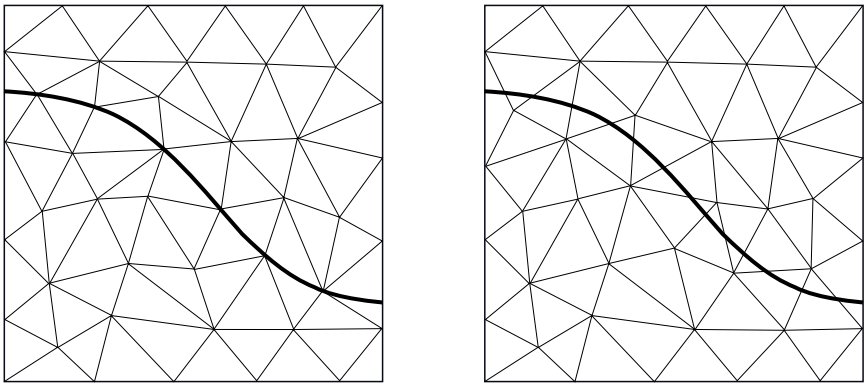

(a) (b)

Figure 3.1: (a) Moving mesh adapted to the interface, and (b) fixed mesh, where interface moves through the elements.

- *Moving mesh methods*: In these methods the mesh is deformable and adapted to the interface, which is explicitly tracked along the trajectories of the fluid particles. For example, methods based on the Arbitrary Lagrangian-Eulerian (ALE) formulation (e.g. Hirt et al. [54], Hughes et al. [59], Ramaswamy & Kawahara [111], Szabo & Hassager [127]); the deformable-spatial-domain/stabilized space-time deformation (DSD/SST) method (Tezduyar et al. [130, 131]); or the fully Lagrangian formulation such as in Hirt et al. [55], Ramaswamy & Kawahara [112], Hayashi et al. [53] (see Section 2.2), and the Particle Finite Element Method (Idelsohn et al. [75, 73, 74, 68, 70], Oñate et al. [103], Del Pin et al. [36]).
- *Fixed mesh methods*: These methods use a separate procedure to describe the position of the interface. They can be further grouped in
  - *Front-tracking methods*, which use massless marker points to follow the fluid interface while the Navier-Stokes equations are solved on a fixed mesh. The interface location is defined by the position of the markers, which are advected by the flow without modifying it. The advection velocity is interpolated from the fixed background mesh.

    In the first front-tracking methods, Particle-In-Cell (Harlow [51]) and Marker-And-Cell (Harlow & Welch [52]), the marker points were distributed throughout the whole domain. Later Glimm et al. [44], Unverdi & Tryggvason [136], Esmaeeli & Tryggvason [37, 38], Tryggvason et al. [133] and Bunner & Tryggvason [12] considered marker points only on the interface.
  - *Front-capturing methods*, which introduce a new variable ψ in the model to describe the presence or not of a fluid in a position of the domain. The

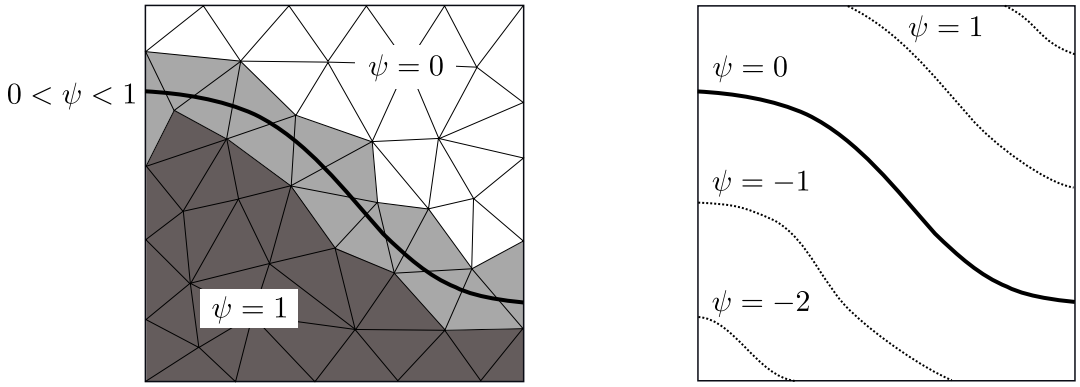

(a) (b)

Figure 3.2: Fixed mesh, front-capturing methods: (a) Volume-Of-Fluid and (b) Level Set.

interface is captured within the fixed mesh.

The most extended front-capturing methods are the Volume-Of-Fluid (VOF), originally developed by Noh & Woodward [97] and Hirt & Nichols [56], and the Level Set method by Osher & Sethian [105], Sussman et al. [126] and Sethian [118].

For the Volume-Of-Fluid method, ψ represents the percentage (or volume fraction) of each fluid in an element (see Fig. 3.2a). The interface is reconstructed based on these percentages. Although VOF possesses excellent mass conservation properties, it is difficult to calculate geometrical features of the interface, such as the curvature, because ψ is a non-smooth function. Density and viscosity are defined as $\rho = \psi\rho_1 + (1-\psi)\rho_2$ and $\mu = \psi\mu_1 + (1-\psi)\mu_2$ respectively, and the evolution of ψ is given by the advection equation

$$\frac{\partial \psi}{\partial t} + \boldsymbol{u} \cdot \boldsymbol{\nabla}\psi = 0, \tag{3.1}$$

where $\boldsymbol{u}$ is the flow velocity.

On the other hand, for the level set method ψ represents the signed distance to the interface (see Fig. 3.2b). Unfortunately, ψ may not remain a distance function after solving the evolution equation (3.1), and therefore, a redistanciation (or reinitialization) technique is needed to enforce the condition $||\boldsymbol{\nabla}\psi|| = 1$ (Sussman et al. [126]). Density and viscosity are defined as $\rho_\varepsilon = \rho_1 + (\rho_2 - \rho_1)H_\varepsilon(\psi)$ and $\mu_\varepsilon = \mu_1 + (\mu_2 - \mu_1)H_\varepsilon(\psi)$, where H_ε is a smoothed Heaviside function, e.g.

$$H_\varepsilon(\psi) = \begin{cases} 1 & \text{if } \psi > \varepsilon \\ 0 & \text{if } \psi < -\varepsilon \\ \frac{1}{2}(1 + \frac{\psi}{\varepsilon} + \frac{1}{\pi}\sin(\pi\psi/\varepsilon)) & \text{if } |\psi| \leq \varepsilon \end{cases} \tag{3.2}$$

In this way the interface is represented as a narrow band with a finite width of $\frac{2\varepsilon}{||\boldsymbol{\nabla}\psi||}$ (Sethian & Smereka [119]) where the physical properties change continuously from one fluid to the other. ε is a small value, proportional to the spatial mesh size. Thus now ψ is a smooth function at the interface, what is useful for the computation of the interface curvature:

$$\kappa = -\boldsymbol{\nabla} \cdot \boldsymbol{n}, \quad \text{with} \quad \boldsymbol{n} = -\frac{\boldsymbol{\nabla}\psi}{||\boldsymbol{\nabla}\psi||}\bigg|_{\psi=0}$$

An advantage of front-capturing methods is that no special procedures are required in order to model topological changes of the interface, such as the reconnections that appear during coalescence or breakup of fluid domains. However, the interface is typically smoothed over several elements, and due to the fact that the schemes used to advect the ψ-function are either diffusive or unstable, it is a major difficulty to keep the interface sharp and non-oscillatory, resulting in an increased interface thickness and loss of precision. These methods differ from the diffuse-interface methods in that the latter use a thermodynamic quantity (e.g. density) to capture the interface. The relaxation (smoothing) of the interface is computed through the Korteweg stresses and therefore, it is thermodynamically consistent. Front-tracking methods explicitly follow the interface avoiding its smoothing, it is kept at a constant thickness of the order of the mesh size, but often fail when there are complex topological changes of the interface. Most of these drawbacks can be overcome with a Lagrangian description of the interface, as in the Particle Finite Element Method.

Interface description in the Particle Finite Element Method

Moving mesh methods naturally track the interface position without necessity of additional techniques. It is often stated that these methods are restricted only to flows with small deformations (e.g. "Lagrangian methods have been used mainly when the deformation of the liquid domain is not too large and when this domain does not suffer from topology changes", Caboussat [13]). A goal of this work is to show that PFEM is able to simulate accurately large deformations in laminar flows of Newtonian viscous multi-fluids.

According to the previous classifications, PFEM is a sharp-interface, moving mesh method where the solution in all fluids is computed simultaneously. One of the features of particle methods is that all the physical properties are attached to the nodes instead of to the elements. The mesh is frequently updated and hence, it is difficult to keep physical properties at the element level. Heterogeneous flows can have a jump in the fluid properties of several orders of magnitude. One must decide where does the internal interface between two different fluids

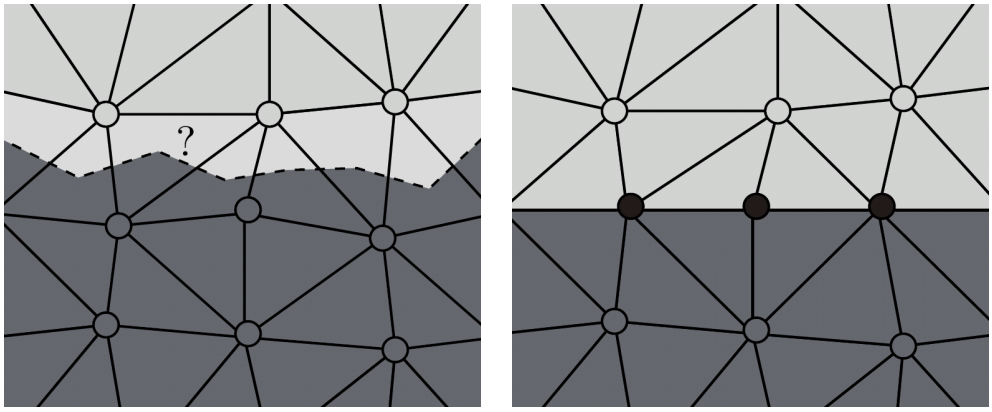

(a) Interface across elements (b) Nodal interface

Figure 3.3: Possible interface representations in PFEM: (a) interface across elements for miscible fluids, (b) nodal interface (with interfacial nodes in black) for immiscible fluids.

occur. The typical solution for a particle method would be to have the interface inside the elements sharing particles with different densities so that, at the element integration point k, density takes the mean value $\rho_k = \frac{1}{nv}\sum_{a=1}^{nv}\rho_a$ (where nv is the number of nodes of the element). We will call this possibility **interface across elements** (Figure 3.3a). Another possibility, which we have developed in this work, is to impose that the interface between different materials is described by element edges. This will be called **nodal interface** (Figure 3.3b). For the nodal interface one must accept that elements sharing particles with two different densities have one or the other particular density value. Now, the density at the element integration point k takes the value

$$\rho_k = \begin{cases} \rho^+ & \text{if } k \in \Omega^+ \\ \rho^- & \text{if } k \in \Omega^- \end{cases} \tag{3.3}$$

Both possibilities have advantages and disadvantages. Interfaces across elements are more stable as they do not change much when remeshing is performed (see Section 3.3) but on the other hand, nodal interfaces are more accurate because they allow to represent exactly the jumps in the physical properties and the discontinuities of the flow variables, as illustrated in Figure 3.4.

We will mainly focus on immiscible multi-fluid flows to exploit the fact that Lagrangian methods are able to track interfaces in a natural and accurate way. The nodal interface will be used, and since in this representation the interface is described by mesh nodes and element edges, it is a well-defined curve and the information regarding its location and curvature is readily available. The interface nodes carry the jump of properties (e.g. density, viscosity), maintaining

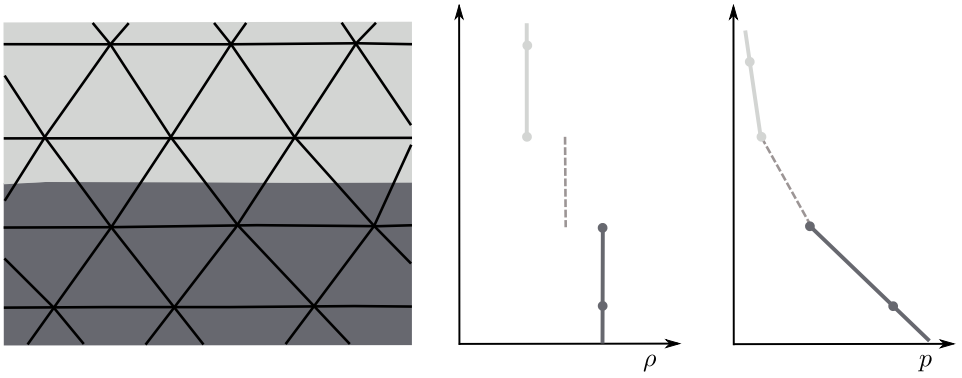

(a) Interface across elements

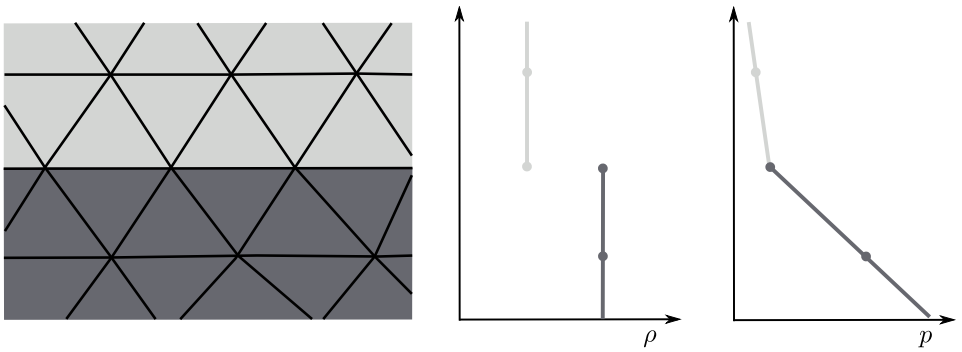

(b) Nodal interface

Figure 3.4: Density and pressure representations for the different interface definitions: in the interface across elements (a), standard linear elements cannot represent accurately the pressure weak discontinuity; while in the nodal interface (b) the representation is exact.

the interface sharp without diffusion along time. Furthermore, it is straightforward to impose the boundary conditions on the interface and to treat any number of fluids. In Section 4.5, we will consider a problem involving miscible fluids, where the properties vary in a smooth way throughout the domain due to its dependence on temperature and composition. In this case, the interface across elements will be used (averaged properties in the elements). The main disadvantage of Lagrangian methods is the need of remeshing when the mesh becomes too distorted due to large deformations.

3.2 Main difficulties in the numerical solution of multi-fluid flows

In addition to the difficulties in the simulation of homogeneous flows, numerical methods for heterogeneous flows face the following challenges:

1. Accurate definition of the interface position.
   The interface separating the fluids needs to be tracked accurately without introducing excessive numerical smoothing.

2. Modeling of jumps in the fluid properties across the interface.
   Large jumps of fluid density and viscosity across the interface need to be properly taken into account in order to satisfy the momentum balance at the vicinity of the interface.

   While typically in fixed mesh methods the interface is considered to have a finite thickness and the fluid properties change smoothly and continuously from the value on the one side of the interface to the value on the other side, PFEM treats the interface in a sharp manner, so that it is clear which property value is valid at each point.

3. Modeling of discontinuities of the flow variables across the interface.
   In fixed mesh methods where the physical properties have been smoothed, functions are continuous across the interface and thus not appropriate for the approximation of discontinuous variables. When the physical properties are modeled sharp, the elements cut by the interface require a special treatment in order to be able to represent the discontinuities (weak and strong) of the flow variables explained in Section 1.3. Gravity dominated flows will require "enrichment" of the pressure approximation, and viscosity dominated flows will require "enrichment" of the velocity approximation.

   When the interface is aligned with the mesh, weak discontinuities need no special attention, as the kinks in the solution are automatically represented. Only the strong discontinuity in the pressure will require special treatment in PFEM, and in a minor extent, the strong discontinuity in the pressure gradient when it appears as a variable in the stabilization.

4. Modeling of the surface tension.
   Since surface tension plays a very important role in the immiscible interface dynamics, this force needs to be accurately evaluated and incorporated into the model.

In PFEM we will specifically need to deal with these aspects:

- Conservation of the interface during the remeshing process.
  The regeneration of the mesh when it becomes too distorted may change the nodes and edges that describe the interface. It is essential to guarantee that the interface is conserved during remeshing.

- Stabilization of pressure at the interfaces where density jumps occur.
  Stabilization procedures are needed in incompressible flows when interpolation spaces for velocity and pressure do not satisfy the inf-sup condition. Many stabilization procedures have been proposed in the literature, such as the Streamline-Upwind/Petrov-Galerkin (Brooks & Hughes [11]), Galerkin Least-Squares (Hughes et al. [61]), Finite Calculus (Oñate [101]), or Orthogonal Sub-Scale (Codina [24]) methods. Those that include the projection of the pressure gradient need to be modified when density changes at the interface to take into account the variation of the hydrostatic pressure gradient.

- Pressure discontinuity at the interfaces where viscosity jumps occur.
  In order to improve the efficiency of the numerical method, pressure is usually approximated with $\mathcal{C}^0$-continuous functions. However, as it has been shown in Section 1.2, pressure is discontinuous at interfaces where viscosity varies:
  $$p^+ - p^- = 2(\mu^+ - \mu^-)\frac{\partial u_n}{\partial n} \tag{3.4}$$
  The use of continuous pressure approximations may introduce errors in the incompressibility condition that in certain cases produce unacceptable results.

- Surface tension at immiscible interfaces.
  The existence of two different fluids in contact with different intermolecular attraction forces introduces the physical phenomena of surface tension. Surface tension is proportional to the curvature of the interface κ and a parameter γ that depends on the materials involved. Surface tension effects are normally added in the numerical simulation as a concentrated force normal to the interface in the momentum equation, $\boldsymbol{f}_{st} = -\gamma\kappa\boldsymbol{n}$, and induce an extra jump in the pressure field:
  $$p^+ - p^- = -\gamma\kappa \tag{3.5}$$
  The accurate computation of the curvature is non-trivial.

In order to simulate immiscible multi-fluid flows with the PFEM, the pressure field will be made discontinuous (double-valued) at the interface to take into account the jump in viscosity and/or surface tension (Idelsohn et al. [69]), and the

pressure gradient field will be also modeled discontinuous to take into account the jump in density (Idelsohn et al. [70]).

3.3 Meshing procedure

Lagrangian methods are characterized by the fact that the mesh follows the flow motion. After a time, nodes that were initially close together may no longer be close, and some nodes that were initially distant begin to approach each other. The mesh needs to be regenerated when it becomes too distorted due to large deformations. For this purpose, we have used the unconstrained Delaunay algorithm developed by Calvo [15].

Given a set of points P in the plane, the Delaunay triangulation constructs a set of triangles whose vertices are the points P such that the circumcircle associated with each triangle contains no other point in P. This is the geometric dual of the Voronoi diagram of P, and each triangle satisfies the empty circumcircle property. The Delaunay triangulation results in a unique mesh for a given set of nodes except in the case when four nodes lie on the same circle (see Figure 3.5). Details of the mesh generation procedure and the shape functions for arbitrary polygons can be found in Idelsohn et al. [72, 66].

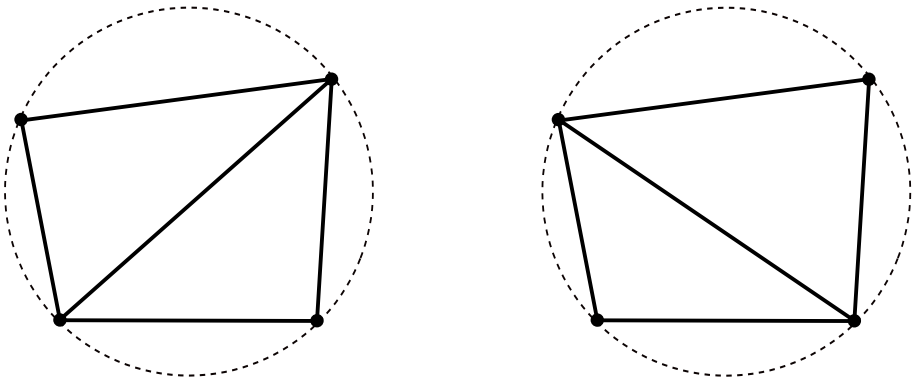

Figure 3.5: Non uniqueness of triangulation when four nodes lie on the same circle: edge swapping.

The mesh is regenerated by allowing each node to have different neighbors as the flow evolves, and by adding and deleting nodes when the size of an element deviates from the prescribed mesh size h. If the distance d_{nodes} between two nodes is $d_{nodes} << h$, one of the nodes is removed (with exception of interface nodes, which are considered to be permanent). If the radius r of an element circumsphere is $r >> h$, a new node is added at the center of the circumsphere. The flow variables in the new node are linearly interpolated from that of the element nodes, and the assigned material properties are the ones of the element.

Unfortunately it is difficult to develop a parallel algorithm to find the Delaunay triangulation, and small changes in the location of the nodes usually produce significant changes in the connectivity of the mesh, as shown in Figure 3.6. Physically meaningful boundaries in the geometry (like interfaces or external boundaries) may not correspond to an edge of a mesh element after edge swapping. These connectivity changes may affect the convergence of the numerical algorithm and the mass conservation. The remedy we have implemented to minimize this effect is to delete those bulk nodes that get too close to the interface, and add nodes on the element edges that are too long. Alternatively, one could use a constrained Delaunay algorithm (Shewchuk [120], Si [122]), which allows to fix certain connectivities. Therefore, by constraining the connectivity of the edges that describe the interface to avoid possible swappings, the interface is conserved exactly after remeshing.

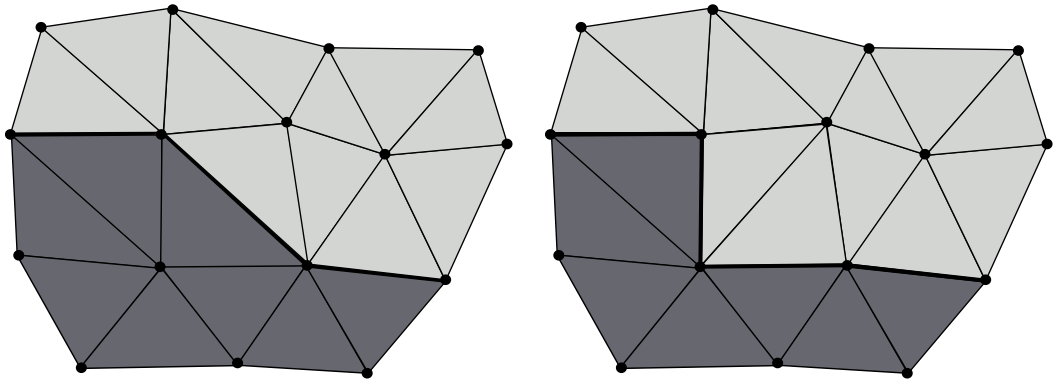

(a) t^n (b) t^{n+1}

Figure 3.6: Connectivity change at the interface from time t^n to t^{n+1}.

Moreover, the mesh should be refined close to the interface to improve the curvature calculation for the surface tension force. We use the medial-axis technique described below to compute the distance to the interface and prescribe an h field depending on this distance. Mesh adaptivity allows us to improve the accuracy (finer interface representation), and the efficiency (refinement only where required) of the method.

3.3.1 Adaptive mesh refinement close to the interfaces

The *medial-axis* transformation (Blum [7]) is a geometric technique allowing a dimensional reduction of any geometric body. In the two-dimensional case, let the body be a compact and connected planar figure. The medial-axis transformation is the set of all pairs {center, radius} of the maximal inscribed circumferences defined everywhere. The locus of centers is a continuous tree-like line with many

bifurcations. This line, along with the associated radius on every point, carries enough data to restore the whole body. The medial-axis line is called so because it is like the "skeleton" of the domain. If the boundary of the body is given in terms of a piecewise linear representation, as a closed polygonal line, the skeleton can be approximated by the set of (inner) vertices of the Voronoi diagram of its boundary vertices. Those are the centers of Delaunay circles, which are not actually tangently inscribed but, for a sufficiently fine discretization, the secant edges are very close to the circumferences. The discrete set of {center, radius} of each Delaunay circle is a useful approximation of the medial-axis transformation.

The medial-axis is used to measure the distance to the boundaries. We make a second fast Delaunay triangulation of the set of centers and the set of boundary nodes. Each center has the radius as associated information, while the boundary nodes have 0 as associated information. This is an auxiliar triangulation used exclusively for calculating the distance of a point to the boundary. For any mesh node inside one of such triangles, its distance is linearly interpolated from the associated data of the triangle nodes. The construction of the medial-axis line and the auxiliar triangulation is illustrated in Figure 3.7.

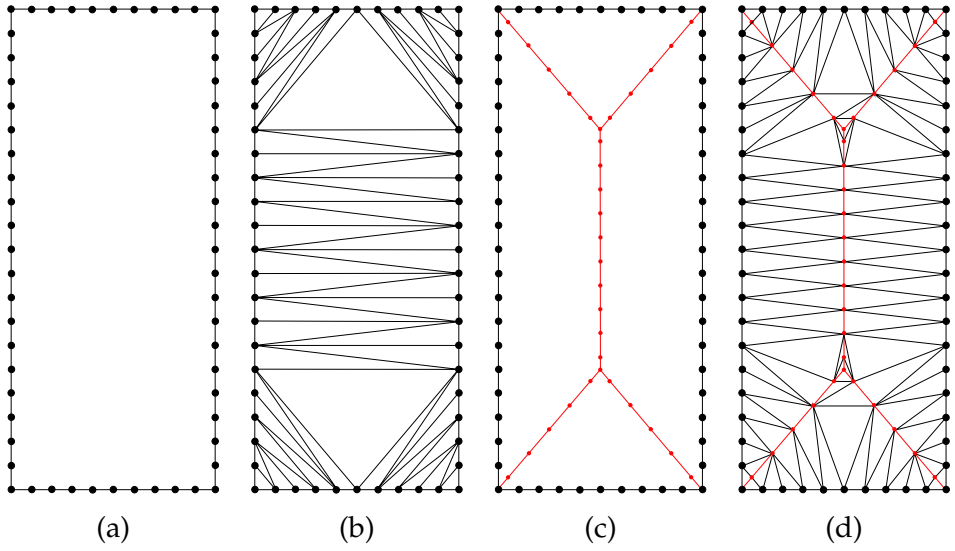

Figure 3.7: Construction of the medial-axis: (a) given external boundary, (b) Delaunay triangulation of the boundary nodes, (c) centers of the Delaunay circles and medial-axis line, (d) auxiliar triangulation for distance interpolation.

In the heterogeneous flow problems, we have internal interfaces in addition to the external boundaries. In this case, interface nodes are considered also 0-points (see Fig. 3.8). This technique allows to prescribe a certain h to the nodes as a function of the distance d to the interfaces and the external boundary. For example, in Figure 3.8c the prescribed h field takes a minimum value h_{min} at the interface, increases linearly with the distance and farther than d_{max} it takes the

constant maximum value h_{max}.

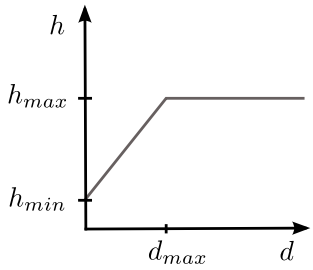

$$h(d) = \begin{cases} h_{max}, & d > d_{max} \\ h_{min} + \frac{h_{max} - h_{min}}{d_{max}}\, d, & d < d_{max} \end{cases} \tag{3.6}$$

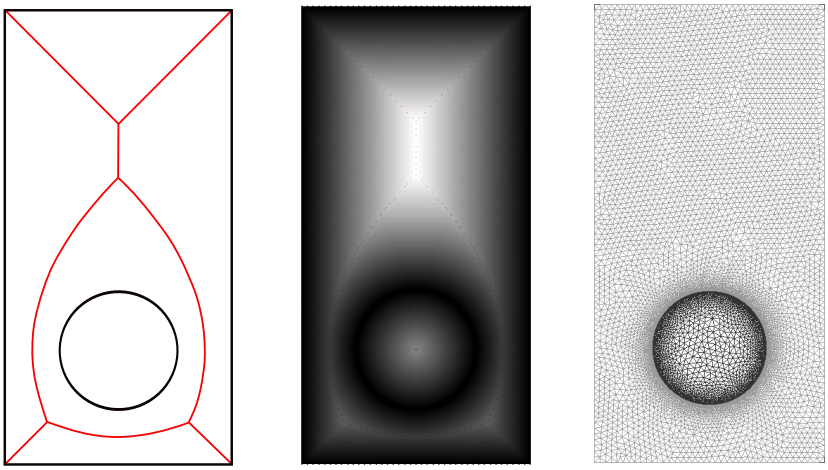

(a) (b) (c)

Figure 3.8: (a) Medial-axis in a domain with internal interface, (b) distance function (black=0, white=maximum distance), (c) mesh refined close to the interface.

3.4 Discretization of the governing equations

As seen in Section 1.2, the incompressible Navier-Stokes equations for multi-fluid flows read

$$\rho \frac{\mathrm{d}\boldsymbol{u}}{\mathrm{d}t} - \boldsymbol{\nabla} \cdot \boldsymbol{\sigma} = \rho \boldsymbol{g}, \quad \boldsymbol{\sigma} = -p\boldsymbol{I} + 2\mu \boldsymbol{D}(\boldsymbol{u}) \quad \text{in } \Omega^+ \cup \Omega^- \tag{3.7a}$$

$$\boldsymbol{\nabla} \cdot \boldsymbol{u} = 0 \quad \text{in } \Omega^+ \cup \Omega^- \tag{3.7b}$$

$$\boldsymbol{u} = \bar{\boldsymbol{u}} \quad \text{on } \Gamma_D, \qquad \boldsymbol{\sigma} \cdot \boldsymbol{n} = \bar{\boldsymbol{\sigma}}_n \quad \text{on } \Gamma_N \tag{3.7c}$$

$$[\![\boldsymbol{u}]\!] = \boldsymbol{0} \quad \text{and} \quad [\![\boldsymbol{\sigma}]\!] \cdot \boldsymbol{n} = \gamma \kappa \boldsymbol{n} \quad \text{on } \Gamma_{int} \tag{3.7d}$$

$$\boldsymbol{u}(\boldsymbol{x}, t = 0) = \boldsymbol{u}_0(\boldsymbol{x}) \tag{3.7e}$$

In the case of constant viscosity in the entire domain, the viscous term $\boldsymbol{\nabla}\cdot 2\mu\boldsymbol{D}(\boldsymbol{u}) = \boldsymbol{\nabla}\cdot\mu(\boldsymbol{\nabla}\boldsymbol{u}+\boldsymbol{\nabla}^T\boldsymbol{u})$ can be simplified to

$$\begin{aligned}\frac{\partial}{\partial x_j}\left(\mu\left(\frac{\partial u_i}{\partial x_j}+\frac{\partial u_j}{\partial x_i}\right)\right) &= \mu\frac{\partial}{\partial x_j}\left(\frac{\partial u_i}{\partial x_j}\right)+\mu\frac{\partial}{\partial x_j}\left(\frac{\partial u_j}{\partial x_i}\right)\\ &= \mu\frac{\partial}{\partial x_j}\left(\frac{\partial u_i}{\partial x_j}\right)+\mu\frac{\partial}{\partial x_i}\left(\frac{\partial u_j}{\partial x_j}\right)=\mu\frac{\partial}{\partial x_j}\left(\frac{\partial u_i}{\partial x_j}\right)\end{aligned} \tag{3.8}$$

and give the well known *Laplace form* of the Navier-Stokes equations

$$\rho\frac{\mathrm{d}\boldsymbol{u}}{\mathrm{d}t} = -\boldsymbol{\nabla}p+\mu\nabla^2\boldsymbol{u}+\rho\boldsymbol{g} \tag{3.9}$$

In this form only the u_i velocity component is present in each *ith* equation, and the equations separate in each velocity component (directional splitting). When using segregation methods such as the fractional step method, this implies that each velocity component may be solved independently from the others, which leads to considerable saving in computing time. For variable viscosity, however, the fully coupled equations (3.7a), the so called *divergence form*, must be used (Limache et al. [85, 86]).

3.4.1 Weak form

In order to obtain the weak (or variational) form of Eqs. (3.7), we first introduce some function spaces. We denote by $L^p(\Omega)$, $1\le p<\infty$, the space of p-integrable functions on $\Omega\subset\boldsymbol{R}^d$,

$$L^p(\Omega) = \{v:\Omega\to\boldsymbol{R}\mid \int_\Omega v^p\,d\Omega<\infty\} \tag{3.10}$$

Here p is the classical notation in functional analysis and should not be confused with the pressure variable. $L^p(\Omega)$ is a Banach space with the associated norm $||v||_{L^p(\Omega)} = \left(\int_\Omega |v(x)|^p\,d\Omega\right)^{1/p}$. For $p=2$, $L^2(\Omega)$ is a Hilbert space with the scalar product $(u,v)_\Omega = \int_\Omega u(x)v(x)\,d\Omega$ and its induced norm $||v||_{L^2(\Omega)} = (v,v)_\Omega^{1/2}$. The Sobolev space $W^{m,p}(\Omega)$, with $m\ge 0$ and $p\ge 1$, is the space of functions in $L^p(\Omega)$ whose weak derivatives up to order m also belong to $L^p(\Omega)$. We use the standard notation $H^m(\Omega)=W^{m,2}(\Omega)$ and indicate by boldface letters the spaces of vector-functions, for instance $\boldsymbol{H}^m(\Omega)=(H^m(\Omega))^d$. In particular,

$$\boldsymbol{H}^1(\Omega) = \{\boldsymbol{v}\in L^2(\Omega)^d\mid \frac{\partial\boldsymbol{v}}{\partial x_i}\in L^2(\Omega)^d\} \tag{3.11}$$

Furthermore, we define

$$\boldsymbol{V} = \{\boldsymbol{v}\in\boldsymbol{H}^1(\Omega)\mid \boldsymbol{v}=\bar{\boldsymbol{u}}\ \text{ on }\Gamma_D\} \tag{3.12}$$

$$\boldsymbol{V}_0 = \{\boldsymbol{v}\in\boldsymbol{H}^1(\Omega)\mid \boldsymbol{v}=\boldsymbol{0}\ \text{ on }\Gamma_D\} \tag{3.13}$$

$$Q\equiv L^2(\Omega)\ \text{ if }\Gamma_N\neq\emptyset,\quad Q=\{q\in L^2(\Omega)\mid \int_\Omega q\,d\Omega=0\}\ \text{ if }\Gamma_N=\emptyset \tag{3.14}$$

The Galerkin variational formulation corresponding to Eqs. (3.7) is obtained by multiplying Eqs. (3.7a) and (3.7b) by test functions and integrating the equation over the computational domain:
Given $\boldsymbol{u}_0 \in \boldsymbol{L}^2(\Omega)^d$ with $\boldsymbol{\nabla}\cdot\boldsymbol{u}_0 = 0$, find $\boldsymbol{u}(t) \in \boldsymbol{V}$ and $p(t) \in Q$ such that for almost every $t \in (0,T)$ and $\forall \boldsymbol{w} \in \boldsymbol{V}_0$, $\forall q \in Q$

$$\int_{\Omega^+\cup\Omega^-}\left(\rho\frac{\mathrm{d}\boldsymbol{u}}{\mathrm{d}t}\cdot\boldsymbol{w} - p\boldsymbol{\nabla}\cdot\boldsymbol{w} + 2\mu\boldsymbol{D}(\boldsymbol{u}):\boldsymbol{\nabla}\boldsymbol{w}\right)d\Omega = \int_{\Omega^+\cup\Omega^-}\rho\boldsymbol{g}\cdot\boldsymbol{w}\,d\Omega + \int_{\partial\Omega^+\cup\partial\Omega^-}\boldsymbol{\sigma}\boldsymbol{n}\cdot\boldsymbol{w}\,d\Gamma \tag{3.15a}$$

$$\int_\Omega q\boldsymbol{\nabla}\cdot\boldsymbol{u}\,d\Omega = 0 \tag{3.15b}$$

The integral over the boundaries $\partial\Omega^+\cup\partial\Omega^-$ in Eq. (3.15a) can be expressed as

$$\begin{aligned}\int_{\partial\Omega^+\cup\partial\Omega^-}\boldsymbol{\sigma}\boldsymbol{n}\cdot\boldsymbol{w}\,d\Gamma &= \int_{\Gamma_N}\boldsymbol{\sigma}\boldsymbol{n}\cdot\boldsymbol{w}\,d\Gamma + \int_{\Gamma_{int}}(\boldsymbol{\sigma}^+-\boldsymbol{\sigma}^-)\boldsymbol{n}\cdot\boldsymbol{w}\,d\Gamma\\ &= \int_{\Gamma_N}\bar{\boldsymbol{\sigma}}_n\cdot\boldsymbol{w}\,d\Gamma + \int_{\Gamma_{int}}\gamma\kappa\boldsymbol{n}\cdot\boldsymbol{w}\,d\Gamma\end{aligned} \tag{3.16}$$

where the integral over Γ_D vanishes due to $\boldsymbol{w} \in \boldsymbol{V}_0$. The interfacial stress jump condition (3.7d) appears to be natural for the weak formulation. Noticing that the integral over $\Omega^+\cup\Omega^-$ can be written over Ω, as $\Omega\setminus(\Omega^+\cup\Omega^-) = \Gamma_{int}$ and Γ_{int} has zero measure, finally we obtain the weak form

$$\begin{aligned}\int_\Omega\left(\rho\frac{\mathrm{d}\boldsymbol{u}}{\mathrm{d}t}\cdot\boldsymbol{w} - p\boldsymbol{\nabla}\cdot\boldsymbol{w} + 2\mu\boldsymbol{D}(\boldsymbol{u}):\boldsymbol{\nabla}\boldsymbol{w}\right)d\Omega &= \int_\Omega\rho\boldsymbol{g}\cdot\boldsymbol{w}\,d\Omega + \int_{\Gamma_N}\bar{\boldsymbol{\sigma}}_n\cdot\boldsymbol{w}\,d\Gamma\\ &\quad + \int_{\Gamma_{int}}\gamma\kappa\boldsymbol{n}\cdot\boldsymbol{w}\,d\Gamma\end{aligned} \tag{3.17a}$$

$$\int_\Omega q\boldsymbol{\nabla}\cdot\boldsymbol{u}\,d\Omega = 0 \tag{3.17b}$$

The Navier-Stokes equations (3.7) include the discontinuous fields $\rho(\boldsymbol{x})$ and $\mu(\boldsymbol{x})$, derivatives of $\mu(\boldsymbol{x})$ and singular surface tension forces. In the weak form (3.17) of the equations, the derivatives on $\mu(\boldsymbol{x})$ are moved over to the test function by applying integration by parts, and the contributions of the surface tension force appear as line integrals along the interfaces, what reduces the singularity of the problem. The weak formulation naturally incorporates the coefficient discontinuities and singular surface tension force into the numerical scheme. These advantages motivate a choice of a method based on a weak formulation of the equations, such as the finite element method, for the treatment of heterogeneous flows.

3.4.2 Lagrangian non-linearity and time integration

We have seen in Section 2.1 that the nonlinearity of the Eulerian convective term is transferred to the node movement, i.e. to the equations for the trajectories, in the Lagrangian description. We have the following coupled system (notice that the final position $\boldsymbol{x}$ is an unknown):

$$\text{Location} \qquad \left.\frac{\partial \boldsymbol{x}}{\partial t}\right|_X = \boldsymbol{u}(\boldsymbol{x}, t) \tag{3.18}$$

$$\text{Momentum} \qquad \rho_0 \left.\frac{\partial \boldsymbol{u}}{\partial t}\right|_X = \boldsymbol{\nabla}_X \cdot (J\boldsymbol{\sigma} \cdot \boldsymbol{F}^{-T}) + \rho_0 \boldsymbol{g} \tag{3.19}$$

$$\text{Continuity} \qquad \boldsymbol{\nabla}_X \cdot (J\boldsymbol{F}^{-1}\boldsymbol{u}) = 0 \tag{3.20}$$

$\boldsymbol{X}$ are the coordinates in the reference configuration Ω_0. When adopting a Lagrangian frame of reference, there are three possible choices for the reference configuration:

(i) $\Omega_0 \equiv \Omega(t = 0)$, i.e. the variables are described in the initial configuration. This is called the *total* formulation.

(ii) $\Omega_0 \equiv \Omega(t = t^n)$, i.e. the variables are described in the current configuration. This is the *updated* formulation.

(iii) $\Omega_0 \equiv \Omega(t = t^{n+1})$, i.e. the variables are described in the last known configuration. This is the *end of step* formulation.

The first option is not well suited for highly dynamic problems with large shape changes, as it is the case in fluid mechanics (Del Pin [35]). The difference between the updated and the end of step formulations lies in the computation of the shape functions. In the end of step formulation, the shape functions are evaluated at the position $\boldsymbol{x}^{n+1}$ and then the deformation gradient matrix $\boldsymbol{F}$ becomes the identity, $\boldsymbol{F} = \boldsymbol{I}$. In the updated formulation, shape functions are evaluated at the reference position $\boldsymbol{x}^n$, and $\boldsymbol{F}$ and its Jacobian need to be calculated.

In this work we have adopted the updated formulation: $\boldsymbol{X} = \boldsymbol{x}^n$. Integrating in time the position and velocity in Eqs. (3.18) and (3.19), we have

$$\frac{\boldsymbol{x}^{n+1} - \boldsymbol{x}^n}{\Delta t} = \boldsymbol{u}(\boldsymbol{x}, t)^{n+\theta_1} \tag{3.21}$$

$$\rho^n \frac{\boldsymbol{u}^{n+1} - \boldsymbol{u}^n}{\Delta t} = \boldsymbol{\nabla}_X \cdot (J\boldsymbol{\sigma} \cdot \boldsymbol{F}^{-T})^{n+\theta_2} + \rho^n \boldsymbol{g} \tag{3.22}$$

$$\boldsymbol{\nabla}_X \cdot (J\boldsymbol{F}^{-1}\boldsymbol{u})^{n+\theta_2} = 0 \tag{3.23}$$

with $\boldsymbol{F} = \dfrac{\partial \boldsymbol{x}^{n+1}}{\partial \boldsymbol{x}^{n}}$ and $\rho^n = \rho(t^n)$. θ_1 and θ_2 are parameters of the trapezoidal rule for the time integration, and $\phi(\boldsymbol{x}, t)^{n+\theta}$ is defined as

$$\phi(\boldsymbol{x}, t)^{n+\theta} := \theta\, \phi(\boldsymbol{x}, t^{n+1}) + (1-\theta)\, \phi(\boldsymbol{x}, t^{n}) = \theta \phi^{n+1} + (1-\theta)\phi^{n} \tag{3.24}$$

The coupling between the velocity field $\boldsymbol{u}$ and the nodes location $\boldsymbol{x}$ causes a strong non-linearity, and therefore an iterative procedure has to be carried out to linearize Eq. (3.21). For this purpose, we have chosen the Picard method, which converges linearly, as the Newton-Raphson implies too many extra storage for a Lagrangian fluid (Aubry [2]). The linearized equation for the trajectories reads

$$\frac{\boldsymbol{x}^{n+1(i+1)} - \boldsymbol{x}^{n}}{\Delta t} = \theta_1\, \boldsymbol{u}^{n+1(i)} + (1-\theta_1)\, \boldsymbol{u}^{n}, \qquad \text{with } \theta_1 \in [0,1] \tag{3.25}$$

At each non-linear iteration, the nodes are moved to the new position $\boldsymbol{x}^{n+1(i+1)}$ until convergence in $\boldsymbol{x}$ or $\boldsymbol{u}$ is achieved, e.g.

$$\frac{||\boldsymbol{u}^{n+1(i+1)} - \boldsymbol{u}^{n+1(i)}||}{||\boldsymbol{u}^{n+1(i+1)}||} < \text{tolerance} \tag{3.26}$$

In the end of step formulation, the variables would be evaluated at the unknown position $\boldsymbol{x}^{n+1}$. This means that shape functions in the last known configuration $\Omega^{n+1(i+1)}$ would have to be recomputed at each iteration. On the other hand, in the chosen updated formulation, the shape functions are calculated once in Ω^n, but then the transformation matrix $\boldsymbol{F}^{n+1(i+1)}$ and its Jacobian have to be computed at each iteration. The steps of the non-linear iterative procedure are sketched in Algorithm 1.

Algorithm 1 Non-linear iterative procedure

1: Generate mesh
2: Initialize $\boldsymbol{F}^{n+1(0)} = \boldsymbol{I}$, $J^{n+1(0)} = 1$ and $\boldsymbol{x}^{n+1(0)} = \boldsymbol{X}^{n}$
3: **while** Not Converged **do**
4: Solve $\boldsymbol{u}^{n+1(i+1)}$ and $p^{n+1(i+1)}$ from Eqs. (3.22) and (3.23)
5: Move nodes to position $\boldsymbol{x}^{n+1(i+1)}$
6: Calculate $\boldsymbol{F}^{n+1(i+1)} = \partial \boldsymbol{x}^{n+1(i+1)} / \partial \boldsymbol{X}^{n}$, $J^{n+1(i+1)} = \det \boldsymbol{F}^{n+1(i+1)}$
7: **end while**
8: Update nodal position $\boldsymbol{X}^{n+1} = \boldsymbol{x}^{n+1(i+1)}$
9: Next time step $t^{n+1} = t^{n} + \Delta t$

$\boldsymbol{u}^{n+1}$ and p^{n+1} correspond to the converged $\boldsymbol{u}^{n+1(i+1)}$ and $p^{n+1(i+1)}$ in the iterative procedure. The mesh is then moved with this last calculated velocity. As mentioned before, the nonlinearity of the problem shifts from the convective term in an Eulerian approach to the search for the final position of the mesh at each time step in a Lagrangian one.

Typical choices for θ_1 and θ_2 are:

- $\theta = 0$: Forward Euler method, explicit, conditionally stable and $\mathcal{O}(\Delta t)$.
- $\theta = 1$: Backward Euler method, implicit, unconditionally stable and $\mathcal{O}(\Delta t)$.
- $\theta = 1/2$: Crank-Nicolson method, implicit, unconditionally stable and $\mathcal{O}(\Delta t^2)$.

Stability analysis in finite differences shows that explicit schemes are conditionally stable, that is, there exists a maximum time step able to ensure the stability. In consequence, when any term in the equations is explicitly treated, the time step size can not be arbitrarily large. In the case of the Navier-Stokes equations, there is a stability condition even if a fully implicit scheme is considered because the equations are non-linear and strongly coupled. If some terms of the momentum equation are treated explicitly in order to uncouple the velocity components, the computational cost is reduced but this introduces a more restrictive stability condition. Furthermore, in Lagrangian methods Δt needs to be small enough to avoid that any element gets inverted due to the mesh movement and preserve $J > 0$. We will see later that the explicit treatment of the surface tension force introduces a very restrictive stability condition.

In this section, $\boldsymbol{x}$ has been decoupled from $\boldsymbol{u}$ through a linearization procedure. The flow is first computed in the "frozen" domain, and then, a new position of the nodes is found using the last computed flow variables. In a monolithic approach the flow variables and the nodes location would have been solved simultaneously. In the next section, $\boldsymbol{u}$ will be also decoupled from p through a fractional step scheme. We will use the end-of-step notation in the following to simplify the presentation.

3.4.3 Pressure segregation

A major difficulty in the numerical simulation of incompressible flows is that the velocity and the pressure are coupled by the incompressibility constraint. The interest in using projection methods to overcome this difficulty in time-dependent viscous incompressible flows started with the works of Chorin [21, 22] and Temam [128]. The main idea of the fractional step method is to replace the singular matrix with some proper submatrices by using a factorization technique. These submatrices are smaller and better conditioned, thereby increasing the efficiency of the numerical scheme.

The Lagrangian approach simplifies the equations by separating the problem into a geometrical part, tracking the motion of the nodes (Eq. (3.18)), and a physical part, calculating how the flow variables change in time at each node (Eqs. (3.19)

and (3.20)) (Oran & Boris [104]). The latter can be further split into two parts: one related to viscosity effects, and the other related to the incompressibility. Consider the following Stokes equations:

$$\rho(\boldsymbol{x})\frac{\partial \boldsymbol{u}}{\partial t} - \boldsymbol{\nabla}\cdot 2\mu(\boldsymbol{x})\boldsymbol{D}(\boldsymbol{u}) + \boldsymbol{\nabla} p = \rho(\boldsymbol{x})\boldsymbol{g} \quad \text{in } \Omega \tag{3.27a}$$

$$\boldsymbol{\nabla}\cdot\boldsymbol{u} = 0 \quad \text{in } \Omega \tag{3.27b}$$

$$\boldsymbol{u} = \bar{\boldsymbol{u}} \quad \text{on } \Gamma_D \tag{3.27c}$$

$$\boldsymbol{\sigma}\cdot\boldsymbol{n} = \bar{\boldsymbol{\sigma}}_n \quad \text{on } \Gamma_N \tag{3.27d}$$

$$[\![\boldsymbol{u}]\!] = 0 \quad \text{and} \quad [\![\boldsymbol{\sigma}]\!]\cdot\boldsymbol{n} = \gamma\kappa\boldsymbol{n} \quad \text{on } \Gamma_{int} \tag{3.27e}$$

$$\boldsymbol{u}(\boldsymbol{x},0) = \boldsymbol{u}^0(\boldsymbol{x}) \quad \text{in } \Omega \tag{3.27f}$$

According to Chorin segregation scheme, and after implicit backward Euler time discretization ($\theta_2 = 1$), we propose the following splitting for equations (3.27) (Smolianski [123]):

1. Find an intermediate velocity $\tilde{\boldsymbol{u}}$ solution of

$$\rho(\boldsymbol{x})\frac{\tilde{\boldsymbol{u}} - \boldsymbol{u}^n}{\Delta t} - \boldsymbol{\nabla}\cdot 2\mu(\boldsymbol{x})\boldsymbol{D}(\tilde{\boldsymbol{u}}) + \beta\boldsymbol{\nabla} p^n = \rho(\boldsymbol{x})\boldsymbol{g} \tag{3.28a}$$

$$\tilde{\boldsymbol{u}} = \bar{\boldsymbol{u}} \quad \text{on } \Gamma_D \tag{3.28b}$$

$$(-\beta p^n\boldsymbol{I} + 2\mu(\boldsymbol{x})\boldsymbol{D}(\tilde{\boldsymbol{u}}))\cdot\boldsymbol{n} = \bar{\boldsymbol{\sigma}}_n \quad \text{on } \Gamma_N \tag{3.28c}$$

$$[\![\tilde{\boldsymbol{u}}]\!] = 0 \quad \text{and} \quad [\![-\beta p^n\boldsymbol{I} + 2\mu(\boldsymbol{x})\boldsymbol{D}(\tilde{\boldsymbol{u}})]\!]\cdot\boldsymbol{n} = \gamma\kappa\boldsymbol{n} \quad \text{on } \Gamma_{int} \tag{3.28d}$$

2. Determine $\boldsymbol{u}^{n+1}$ and p^{n+1} as solution of

$$\frac{\boldsymbol{u}^{n+1} - \tilde{\boldsymbol{u}}}{\Delta t} + \frac{1}{\rho(\boldsymbol{x})}\boldsymbol{\nabla}(p^{n+1} - \beta p^n) = 0 \tag{3.29a}$$

$$\boldsymbol{\nabla}\cdot\boldsymbol{u}^{n+1} = 0 \tag{3.29b}$$

$$\boldsymbol{u}^{n+1}\cdot\boldsymbol{n} = \bar{\boldsymbol{u}}\cdot\boldsymbol{n} \quad \text{on } \Gamma_D \tag{3.29c}$$

$$(p^{n+1} - \beta p^n)\boldsymbol{n} = \boldsymbol{0} \quad \text{on } \Gamma_N \tag{3.29d}$$

$$[\![\boldsymbol{u}^{n+1}]\!]\cdot\boldsymbol{n} = 0 \quad \text{and} \quad [\![p^{n+1} - \beta p^n]\!] = 0 \quad \text{on } \Gamma_{int} \tag{3.29e}$$

This second step represents the L^2-projection of $\tilde{\boldsymbol{u}}$ onto the set of divergence-free functions. It can be reformulated to separate $\boldsymbol{u}^{n+1}$ and p^{n+1} in Eq. (3.29a). Applying the divergence operator on this equation one obtains a Poisson-type equation for the pressure ([49]):

$$\boldsymbol{\nabla}\cdot\frac{1}{\rho(\boldsymbol{x})}\boldsymbol{\nabla}(p^{n+1} - \beta p^n) = \frac{1}{\Delta t}\boldsymbol{\nabla}\cdot\tilde{\boldsymbol{u}} \quad \text{in } \Omega, \tag{3.30a}$$

$$\text{and} \quad \boldsymbol{n}\cdot\boldsymbol{\nabla}(p^{n+1} - \beta p^n) = 0 \quad \text{on } \Gamma_D \tag{3.30b}$$

3. Finally, the $\boldsymbol{u}^{n+1}$ velocity is obtained by

$$\boldsymbol{u}^{n+1} = \tilde{\boldsymbol{u}} - \frac{\Delta t}{\rho(\boldsymbol{x})} \boldsymbol{\nabla}(p^{n+1} - \beta p^n) \tag{3.31}$$

$\beta = 0$ (non incremental scheme) leads to a first order in time splitting error, with some inherent stabilization properties, while $\beta = 1$ (incremental version, introduced by van Kan [138]) leads to a second order splitting but requires extra stabilization.

This splitting ensures mass conservation of the solution, as the final $\boldsymbol{u}^{n+1}$ velocity is divergence-free. But the tangential component of the velocity cannot be controlled on the boundary, and the artificial Neumann boundary condition for the pressure of Eq. (3.30b) induces a numerical boundary layer of width $\mathcal{O}(\sqrt{\nu \Delta t})$, where $\nu = \mu/\rho$ (Gresho [46], Quartapelle [110]). This artificial Neumann boundary condition and the fact that the resulting pressure belongs to $H^1(\Omega)$ instead of its natural $L^2(\Omega)$ are both consequences of the decomposition theorem of Ladyzhenskaya [82].

The interfacial stress jump condition has been consistently split between steps 1 and 2. Although the continuity of the pressure difference $p^{n+1} - \beta p^n$ across the interface expressed in Eq. (3.29e) seems to be in contradiction with the fact that pressure is discontinuous at the interface, the scheme is able to capture this discontinuity without need of enforcing it explicitly (Smolianski [123]). A different splitting of the interface conditions has been proposed in Chen et al. [18], where they extend the projection scheme of Kim & Moin [78] to multi-fluid flows.

The conditions (3.28c) and (3.28d) will be naturally included in the weak form of step 1, while the pressure conditions (3.29d) on Γ_N and (3.29e) on Γ_{int} need to be weakly imposed for being able to solve the pressure Poisson equation (3.30a) of step 2:

$$\int_{\Gamma_N} q\,(p^{n+1} - \beta p^n)\, d\Gamma = 0 \qquad \text{and} \qquad \int_{\Gamma_{int}} q\,[\![p^{n+1} - \beta p^n]\!]\, d\Gamma = 0$$

The details are explained in Section 3.4.6.

3.4.4 Spatial discretization

The weak formulation is solved by means of the finite element method (Hughes [60], Zienkiewicz & Taylor [144]). Let $\boldsymbol{V}_h$ and Q_h be the finite dimensional subspaces approximating $\boldsymbol{V}$ and Q, Eqs. (3.12)-(3.14), and let Ω^e be a finite element partition of the domain Ω.

$$\boldsymbol{V}_h(\Omega) = \{\boldsymbol{v}_h \in \mathcal{C}^0(\Omega)^d \mid \boldsymbol{v}_{h|_{\Omega^e}} \in \mathbb{P}_k(\Omega^e)^d\} \subset \boldsymbol{V} \tag{3.32}$$

$$Q_h(\Omega) = \{p_h \in \mathcal{C}^0(\Omega) \mid p_{h|_{\Omega^e}} \in \mathbb{P}_k(\Omega^e)\} \subset Q \tag{3.33}$$

where $\mathbb{P}_k(\Omega^e)$ is the space of polynomials of degree k on Ω^e. In this work we have chosen the equal order $\mathbb{P}_1/\mathbb{P}_1$ approximations, i.e. piecewise linear continuous interpolations for velocity and pressure, due to its simplicity and efficiency.

In the Galerkin method, the approximate variables are expressed as

$$\boldsymbol{u}(\boldsymbol{x},t) \approx \boldsymbol{u}_h = \sum_{l\in\mathcal{N}} N_l(\boldsymbol{x})\,\boldsymbol{u}_l(t), \qquad p(\boldsymbol{x},t) \approx p_h = \sum_{l\in\mathcal{N}} N_l(\boldsymbol{x})\,p_l(t) \tag{3.34}$$

where $\mathcal{N}$ is the set of mesh nodes and N_l the shape function associated to the node l. The standard Galerkin test functions are $\boldsymbol{w} = \boldsymbol{N}$ and $q = N$.

It must be noted that the shape functions $N(\boldsymbol{x})$ depend on the nodes coordinates. Then, shape functions may change in time following the nodes positions. During a time step, the mesh could be updated and produce a change in the shape functions that should be taken into account. We assume that no remeshing is performed during the non-linear iterations within each time step. This means that the same updated mesh (but deformed) will continue until the end of the time step.

After discretization in time ($\theta_2 = 1$, implicit backward Euler) and space (Galerkin weighted residual method), and assuming Γ_N to be a free surface (i.e. $\bar{\boldsymbol{\sigma}}_n = \boldsymbol{0}$) and $\beta = 1$, the split equations read:

$$1. \qquad \frac{\boldsymbol{M}_\rho}{\Delta t}(\tilde{\boldsymbol{U}} - \boldsymbol{U}^n) + \boldsymbol{K}_\mu\tilde{\boldsymbol{U}} - \boldsymbol{B}\boldsymbol{P}^n = \boldsymbol{F}^n \tag{3.35}$$

$$2. \qquad \Delta t\,\boldsymbol{L}_{(1/\rho)}\boldsymbol{P}^{n+1} = -\boldsymbol{B}^T\tilde{\boldsymbol{U}} + \Delta t\,\boldsymbol{L}_{(1/\rho)}\boldsymbol{P}^n \tag{3.36}$$

$$3. \qquad \frac{\boldsymbol{M}_\rho}{\Delta t}(\boldsymbol{U}^{n+1} - \tilde{\boldsymbol{U}}) - \boldsymbol{B}(\boldsymbol{P}^{n+1} - \boldsymbol{P}^n) = \boldsymbol{0} \tag{3.37}$$

where $\boldsymbol{U}$, $\boldsymbol{P}$ are the vectors of nodal velocities and pressure, $\tilde{\boldsymbol{U}}$ is the intermediate velocity introduced by the fractional step, and Δt the time step. The matrices $\boldsymbol{M}_\rho$ density weighted mass matrix, $\boldsymbol{B}$ gradient matrix, $-\boldsymbol{B}^T$ divergence matrix, $\boldsymbol{K}_\mu$ viscosity weighted stiffness matrix and the external force vector are defined as

$$\boldsymbol{M}_\rho^{ab} = \int_\Omega \boldsymbol{N}^a\rho\boldsymbol{N}^b\,d\Omega \tag{3.38}$$

$$\boldsymbol{K}_\mu^{ab} = \int_\Omega \boldsymbol{\nabla}\boldsymbol{N}^a\mu(\boldsymbol{\nabla}\boldsymbol{N}^b + \boldsymbol{\nabla}^T\boldsymbol{N}^b)\,d\Omega \tag{3.39}$$

$$\boldsymbol{B}^{ab} = \int_\Omega (\boldsymbol{\nabla}\cdot\boldsymbol{N}^a)\,N^b\,d\Omega \tag{3.40}$$

$$\boldsymbol{L}_{(1/\rho)}^{ab} = \int_\Omega \boldsymbol{\nabla}N^a\frac{1}{\rho}\boldsymbol{\nabla}N^b\,d\Omega \tag{3.41}$$

$$\boldsymbol{F}^a = \int_\Omega \boldsymbol{N}^a\rho\boldsymbol{g}\,d\Omega + \int_{\Gamma_{int}} \boldsymbol{N}^a\gamma\kappa\boldsymbol{n}\,d\Gamma \tag{3.42}$$

where the superscripts a, b refer to node indices.

There is another approach to the treatment of step 2 called *discrete projection*. It consists in first discretizing the equations in space and then applying the segregation. In this case, instead of $\boldsymbol{L}_{(1/\rho)}$ in Eq. (3.36) we would get $\boldsymbol{B}^T\boldsymbol{M}_\rho^{-1}\boldsymbol{B}$, which do not coincide in general. The discrete projection approach does not require any artificial boundary condition for the pressure Poisson equation (pressure does not need to satisfy a Neumann condition on Γ_D, Eq. (3.30b), nor a Dirichlet condition on Γ_N, as it must with the standard Laplacian discretization), and seeks pressure in its natural function space L^2. However, it requires the expensive assembly of $\boldsymbol{B}^T\boldsymbol{M}_\rho^{-1}\boldsymbol{B}$ matrix (the bandwith is roughly three times the bandwith of the standard Laplacian in two dimensions, and five times in three dimensions on a structured grid, as it involves the neighbors of the neighbors of each nodes in case of continuous pressure interpolations, Aubry [2]), and does not own any inherent stabilization property. In contrast, the continuous projection requires to invert the standard Laplace matrix, which is a quite explored problem with efficient ways for solution. However, large differences in density ($\rho_1 >> \rho_2$ or $\rho_1 << \rho_2$) may lead to bad conditioned system matrix for the pressure Poisson equation and problems in convergence (Bell & Marcus [4], Unverdi & Tryggvason [136], Tryggvason et al. [133], Bunner & Tryggvason [12], Chen et al. [18], Hua & Lou [58]).

Both the momentum and pressure equations system matrices are symmetric and positive definite. The linear systems are solved using the Conjugate Gradient algorithm and the incomplete LU preconditioner. The degrees of freedom are the (two or three) velocity components and pressure at each node of the finite element mesh.

The accuracy in the treatment of the discontinuous density and viscosity will be determined by how well the numerical method is able to evaluate the integrals where these discontinuities are included. Unless the interface coincides with edges of elements, there is no way for standard finite element shape functions to capture the discontinuity of properties inside an element. This implies that one has either to increase the number of Gauss points (e.g. see discussion about numerical integration of discontinuous and singular functions in Tornberg [132]) or enrich the shape function space, as e.g. in Minev et al. [91], Coppola-Owen & Codina [30] and in the eXtended Finite Element Method (XFEM) (Moës et al. [92], Belytschko et al. [5], Chessa & Belytschko [19, 20], Gross & Reusken. [47]). The nodal interface description for immiscible fluids in PFEM allows to evaluate exactly these integrals.

3.4.5 Pressure stabilization

Finite element solution of the incompressible Navier-Stokes equations with the classical Galerkin method may suffer from numerical instabilities from two sources (Zienkiewicz & Taylor [144]). The first one is due to the convective-

diffusive character of the equations, which may induce unphysical oscillations in convection-dominated flows. The second source is related to the treatment of the incompressibility constrain. When the standard Galerkin method is used, the discrete spaces for the approximation of the velocity and the pressure have to satisfy the inf-sup condition (Brezzi & Fortin [10]), also called the Ladyzhenskaya-Babuska-Brezzi (LBB) condition, in order to get stable solutions.

The convective term is not present in the Lagrangian formulation, therefore no stabilization is required in steps 1 and 3. Nevertheless, the incompressibility condition must still be stabilized for our equal-order approximations to avoid pressure oscillations. Pressure stabilization of the discrete equations can be achieved either by appropriately modifying the formulation or by using first-order projection schemes. Because the inherent stability of the latter decreases with the time step size (Guermond & Quartapelle [48], Codina [25]), and moreover, we have chosen a second order projection scheme for the segregation of velocity and pressure, we are compelled to modify the pressure Poisson equation (3.36) by introducing the term $\boldsymbol{SP}$:

$$(\Delta t \boldsymbol{L}_{(1/\rho)} + \boldsymbol{S})\boldsymbol{P}^{n+1} = -\boldsymbol{B}^T\tilde{\boldsymbol{U}} + \Delta t \boldsymbol{L}_{(1/\rho)}\boldsymbol{P}^n \tag{3.43}$$

The stabilization matrix $\boldsymbol{S}$ must be singular so that the product $\boldsymbol{SP}$ is equal to zero with $\boldsymbol{P} \neq \boldsymbol{0}$. Nevertheless, several stabilization methods presented in the literature are based on non-singular $\boldsymbol{S}$ matrices, therefore introducing compressibility in the solution (Idelsohn et al. [67]).

The reason for the inherent stability of the first order fractional step is that it modifies the discrete continuity equation by adding the term

$$\Delta t(\boldsymbol{L} - \boldsymbol{B}^T\boldsymbol{M}^{-1}\boldsymbol{B})\boldsymbol{P}. \tag{3.44}$$

The positive semi-definite matrix $\boldsymbol{L} - \boldsymbol{B}^T\boldsymbol{M}^{-1}\boldsymbol{B}$ increases the stability of the numerical method (Codina & Blasco [27], Codina et al. [29]). This property can be recovered by defining $\boldsymbol{S} := \tau(\boldsymbol{L} - \boldsymbol{B}^T\boldsymbol{M}^{-1}\boldsymbol{B})$ in Eq. (3.43). Here τ is a pseudo-time stabilization parameter, and the term $\boldsymbol{B}^T\boldsymbol{M}^{-1}\boldsymbol{BP}$ is calculated by taking first the gradient of the pressure, projecting it onto the discrete space of velocities and then taking the divergence of the resulting vector field.

At the continuous level, pressure gradient projection (PGP) methods introduce this projection of the pressure gradient onto the velocity space as a new unknown of the problem called π, and add to the incompressibility equation the difference between the Laplacian of the pressure and the divergence of this new vector field (Codina & Blasco [28], Oñate [101]):

$$\frac{\partial}{\partial x_i}\,\tau\left(\frac{\partial p}{\partial x_i} - \pi_i\right) \quad \text{with } \pi_i \text{ computed as} \quad \int_\Omega w_i \left(\frac{\partial p}{\partial x_i} - \pi_i\right) d\Omega = 0 \tag{3.45}$$

This term can be also deduced from the Finite Calculus (FIC) formulation as follows (Oñate [100, 101, 102]). The incompressibility equation $\varepsilon_V = \boldsymbol{\nabla} \cdot \boldsymbol{u} = 0$ is replaced by the residual FIC form

$$\varepsilon_V - \tau \frac{\partial r_i}{\partial x_i} = 0 \tag{3.46}$$

where r_i is the residual of the momentum conservation equations

$$r_i = \rho \frac{\mathrm{d}u_i}{\mathrm{d}t} - \frac{\partial \sigma_{ij}}{\partial x_j} - \rho g_i \tag{3.47}$$

and τ is the stabilization parameter. The stabilization in Eq. (3.46) is introduced by splitting the residual r_i in two parts

$$r_i = \rho \frac{\mathrm{d}u_i}{\mathrm{d}t} - \frac{\partial}{\partial x_j} 2\mu D_{ij} - \rho g_i + \frac{\partial p}{\partial x_i} = \frac{\partial p}{\partial x_i} - \pi_i \tag{3.48}$$

The π_i functions represent the projection of the pressure gradients in the velocity field and are approximated with the same linear interpolations as for the velocity and the pressure variables. Then the stabilized weak form of the incompressibility equation becomes

$$\int_\Omega q \left(\varepsilon_V - \tau \frac{\partial r_i}{\partial x_i} \right) d\Omega = \int_\Omega q \, \varepsilon_V \, d\Omega - \int_\Omega q \, \frac{\partial}{\partial x_i} \tau \left(\frac{\partial p}{\partial x_i} - \pi_i \right) d\Omega = 0 \tag{3.49}$$

The corresponding $\boldsymbol{S}$ matrix for the multi-fluid discrete system Eqs. (3.35-3.37), i.e. the difference between the continuous and the discrete Laplacian, reads

$$\boldsymbol{S} = \hat{\tau} \, (\boldsymbol{L}_{(1/\rho)} - \boldsymbol{B}^T \boldsymbol{M}_\rho^{-1} \boldsymbol{B}) \tag{3.50}$$

that at the continuous level is equivalent to

$$\frac{\partial}{\partial x_i} \hat{\tau} \left(\frac{1}{\rho} \frac{\partial p}{\partial x_i} - \hat{\pi}_i \right) \quad \text{with } \hat{\pi}_i \text{ computed as} \quad \int_\Omega w_i \left(\frac{\partial p}{\partial x_i} - \rho \hat{\pi}_i \right) d\Omega = 0 \tag{3.51}$$

$\pi_i = \rho \hat{\pi}_i$ is a continuous variable, while $\hat{\pi}_i$ is discontinuous in non-uniform density flows, as corresponds to the weak discontinuity of the pressure at interfaces where a density jump occurs. This improves the accuracy of the PGP stabilization.

The parameter $\hat{\tau}$ is calculated within each element Ω^e as follows

$$\hat{\tau} = \rho \tau = \left(\frac{1}{\Delta t} + \frac{\mu^e}{\rho (h^e)^2} \right)^{-1} \tag{3.52}$$

so that one should write $\boldsymbol{S} = \boldsymbol{L}_{\hat{\tau}/\rho} - \boldsymbol{B}_{\hat{\tau}}^T \boldsymbol{M}_\rho^{-1} \boldsymbol{B}$. Nevertheless, we will keep the notation of Eq. (3.50).

In the product $\boldsymbol{SP}$, the term $\hat{\tau}\boldsymbol{L}_{(1/\rho)}\boldsymbol{P}^{n+1}$ is treated implicitly, while $\hat{\tau}\boldsymbol{B}^T\boldsymbol{M}_\rho^{-1}\boldsymbol{B}\boldsymbol{P}^n$ is treated explicitly. A new vectorial variable $\hat{\boldsymbol{\Pi}}^n := \boldsymbol{M}_\rho^{-1}\boldsymbol{B}\boldsymbol{P}^n$ is defined and its update implies the solution of the following algebraic system

$$\boldsymbol{M}_\rho\,\hat{\boldsymbol{\Pi}}^n = \boldsymbol{B}\boldsymbol{P}^n \tag{3.53}$$

The mass matrix $\boldsymbol{M}_\rho$ can be approximated by its lumped diagonal version, what turns out to be the most efficient choice which does not upset accuracy [28].

The stabilized discrete system reads:

$$1.\qquad \frac{\boldsymbol{M}_\rho}{\Delta t}(\tilde{\boldsymbol{U}}-\boldsymbol{U}^n)+\boldsymbol{K}_\mu\tilde{\boldsymbol{U}}-\boldsymbol{B}\boldsymbol{P}^n=\boldsymbol{F}^n \tag{3.54a}$$

$$2.\qquad \hat{\boldsymbol{\Pi}}^n=\boldsymbol{M}_\rho^{-1}\boldsymbol{B}\boldsymbol{P}^n \tag{3.54b}$$

$$3.\qquad (\Delta t+\hat{\tau})\,\boldsymbol{L}_{(1/\rho)}\boldsymbol{P}^{n+1}=-\boldsymbol{B}^T\tilde{\boldsymbol{U}}+\Delta t\,\boldsymbol{L}_{(1/\rho)}\boldsymbol{P}^n+\hat{\tau}\boldsymbol{B}^T\hat{\boldsymbol{\Pi}}^n \tag{3.54c}$$

$$4.\qquad \frac{\boldsymbol{M}_\rho}{\Delta t}(\boldsymbol{U}^{n+1}-\tilde{\boldsymbol{U}})-\boldsymbol{B}(\boldsymbol{P}^{n+1}-\boldsymbol{P}^n)=\boldsymbol{0} \tag{3.54d}$$

For numerical examples of PFEM with inf-sup stable elements, namely the mini element $\mathbb{P}_1/\mathbb{P}_1^b$, refer to Aubry [2].

3.4.6 Treatment of pressure on free surfaces and internal interfaces

Unfortunately the matrix $\boldsymbol{L}_{(1/\rho)}$ in Eq. (3.54c) is singular if no conditions are applied. Instead of imposing strongly the pressure Dirichlet condition $\bar{p}=0$ on the free surface Γ_N as usual, what would produce mass loss at those elements that have all their nodes on Γ_N, we impose weakly the pressure conditions Eqs. (3.29d) and (3.29e) coming from the segregation:

$$\int_{\Gamma_N} q\,(p^{n+1}-p^n)\,d\Gamma=0 \qquad \text{and} \qquad \int_{\Gamma_{int}} q\,[\![p^{n+1}-p^n]\!]\,d\Gamma=0 \tag{3.55}$$

Both integrals may be discretized in space as

$$\boldsymbol{M}_c(\boldsymbol{P}^{n+1}-\boldsymbol{P}^n) \tag{3.56}$$

with $\boldsymbol{M}_c^{ab}=\int_\Gamma N^a\,N^b\,d\Gamma$ the pressure mass matrix on the contours Γ_N and Γ_{int}, and are incorporated into the pressure Poisson equation in the following way (Nitsche [96], Juntunen & Stenberg [77]):

$$\left[(\Delta t+\hat{\tau})\,\boldsymbol{L}_{(1/\rho)}+\lambda\,\boldsymbol{M}_c\right]\boldsymbol{P}^{n+1}=-\boldsymbol{B}^T\tilde{\boldsymbol{U}}+\left(\Delta t\,\boldsymbol{L}_{(1/\rho)}+\lambda\,\boldsymbol{M}_c\right)\boldsymbol{P}^n+\hat{\tau}\boldsymbol{B}^T\hat{\boldsymbol{\Pi}}^n \tag{3.57}$$

For dimensional consistency, the penalty parameter λ needs to have units of time/length. We have used

$$\lambda=\alpha\,\frac{\Delta t+\hat{\tau}}{h} \tag{3.58}$$

where the scalar factor $\alpha \sim \mathcal{O}(1)$ is a weight of the satisfaction of the Dirichlet boundary conditions in competition with the satisfaction of the differential equation. The higher the value of α, the better the approximation to the boundary condition at the expense of a poorer approximation to the differential equation (Codina & Baiges [26]). λ has to be sufficiently large so that the system matrix becomes invertible. For $\alpha \to 0$, the pressure equation is satisfied but the discrete system may continue singular. $\alpha \to \infty$ is equivalent to apply the pressure condition strongly and the equation may not be satisfied.

The new boundary terms (3.56) eliminate the singularity of the Laplacian matrix $\boldsymbol{L}_{(1/\rho)}$ and avoid the need of imposing essential boundary conditions to solve the pressure equation. These terms can also be interpreted as adding slight compressibility in a thin region close to the free surface and interfaces, as shown in Idelsohn & Oñate [71]. For simplifying the explanation, we will consider only the free surface, but the same argument applies on internal interfaces. The total domain is split into two parts, $\Omega = \Omega_0 \cup \Omega_\kappa$ (see Figure 3.9): a fully incompressible domain Ω_0, with $\varepsilon_V = 0$, and a second domain Ω_κ near the free surface, with a compressibility coefficient such that

$$\varepsilon_V = \frac{1}{\kappa}\frac{d\,p}{d\,\theta} \tag{3.59}$$

with $\kappa = \rho C^2$ the bulk compressibility coefficient, being C a fictitious speed of sound, and θ any time variation. With this assumption, the weak form of the incompressibility equation becomes:

$$\int_{\Omega_0} q\varepsilon_V \, d\Omega + \int_{\Omega_\kappa} q\left(\varepsilon_V - \frac{1}{\kappa}\frac{d\,p}{d\,\theta}\right) d\Omega = 0 \tag{3.60}$$

Supposing that the domain Ω_κ is a thin layer of thickness δ around the free surface, Eq. (3.60) may be written as:

$$\int_{\Omega} q\varepsilon_V \, d\Omega + \delta \int_{\Gamma_N} q\frac{1}{\kappa}\frac{d\,p}{d\,\theta}\, d\Gamma = 0 \tag{3.61}$$

The thickness δ may change within the iterations, decreasing its value until it becomes zero when convergence is achieved. For instance, approximating $Dp/D\theta \approx \Delta p/\Delta\theta$ and starting the first iteration with δ defined as $\delta = C\,\Delta\theta$, the compressible term reads

$$\int_{\Gamma_N} q\frac{1}{\rho C}\Delta p \, d\Gamma, \tag{3.62}$$

what justifies the integral $\lambda \int_{\Gamma_N} q(p^{n+1} - p^n)\, d\Gamma$.

Since we allow for strong discontinuities in the pressure field, it has to be double-valued along the interface. Therefore, pressure degrees of freedom have

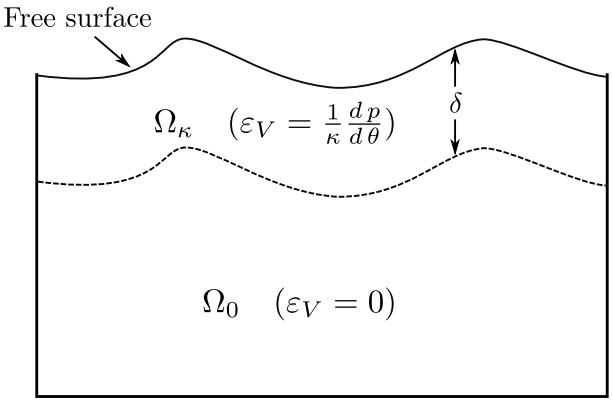

Figure 3.9: Split of the volume into two parts, a compressible and an incompressible one (from Idelsohn & Oñate [71]).

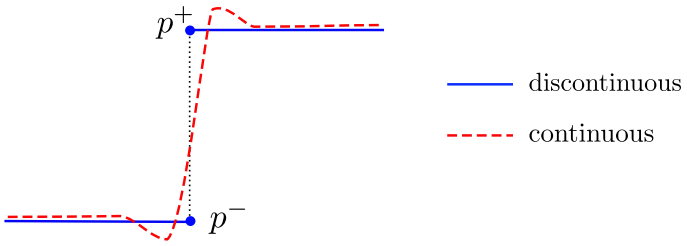

Figure 3.10: Pressure profiles when using continuous and discontinuous representations.

been duplicated (p^+, p^-) in the interface nodes (see Figure 3.10). Each term of the integral on Γ_{int}

$$\int_{\Gamma_{int}} q[\![p^{n+1} - p^n]\!]\, d\Gamma = \int_{\Gamma^+_{int}} q(p^{n+1} - p^n)^+\, d\Gamma + \int_{\Gamma^-_{int}} q(p^{n+1} - p^n)^-\, d\Gamma = 0 \quad (3.63)$$

contributes to the $\boldsymbol{M}_c$ matrix in the corresponding degrees of freedom.

3.4.7 Predictor-corrector scheme

Based on the previous fractional step, Eqs. (3.54), we propose the following predictor-corrector scheme in order to converge to the monolithic problem:

1. $$\frac{\boldsymbol{M}_\rho}{\Delta t}(\boldsymbol{U}^{n+1(i+1)} - \boldsymbol{U}^n) + \boldsymbol{K}_\mu \boldsymbol{U}^{n+1(i+1)} - \boldsymbol{B}\boldsymbol{P}^{n+1(i)} = \boldsymbol{F}^n \quad (3.64a)$$

2. $$\hat{\boldsymbol{\Pi}}^{n+1(i)} = \boldsymbol{M}_\rho^{-1}\boldsymbol{B}\boldsymbol{P}^{n+1(i)} \quad (3.64b)$$

3. $$\left[(\Delta t + \hat{\tau})\,\boldsymbol{L}_{(1/\rho)} + \lambda \boldsymbol{M}_c\right]\boldsymbol{P}^{n+1(i+1)} = -\boldsymbol{B}^T\boldsymbol{U}^{n+1(i+1)} + \\ + \left(\Delta t\,\boldsymbol{L}_{(1/\rho)} + \lambda \boldsymbol{M}_c\right)\boldsymbol{P}^{n+1(i)} + \hat{\tau}\boldsymbol{B}^T\hat{\boldsymbol{\Pi}}^{n+1(i)} \quad (3.64c)$$

and iterate until convergence in pressure is achieved.

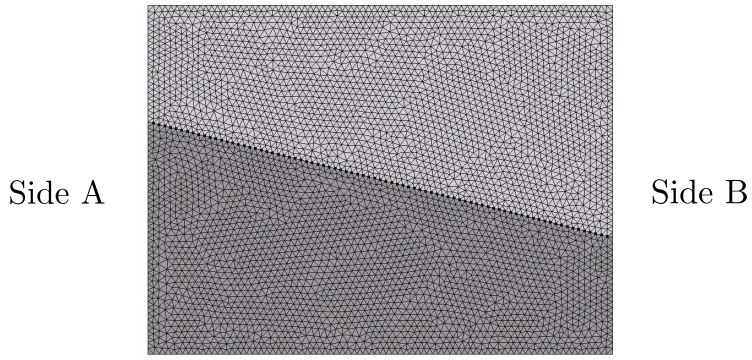

Figure 3.11: Initial mesh (4305 nodes).

The computation in each time step contains two different loops: the predictor-corrector (inner loop) to find $\boldsymbol{U}^{n+1}$ and $\boldsymbol{P}^{n+1}$, and the iterations of the non-linearity (outer loop) to find $\boldsymbol{x}^{n+1}$. The fact of using a predictor-corrector helps to achieve much better precision in each non-linear iteration, so that usually one outer iteration suffices.

In flows with variable viscosity, the term $\boldsymbol{\nabla}^T\boldsymbol{u}$ of the strain rate tensor $\boldsymbol{D} = \frac{1}{2}(\boldsymbol{\nabla}\boldsymbol{u} + \boldsymbol{\nabla}^T\boldsymbol{u})$ is responsible for coupling all the velocity components u_i together, meaning that in step 1 of the predictor-corrector one would have to solve the entire coupled system of equations for the velocity, as opposed to the component by component approach. We have fully decoupled the viscous term into (two or three) separate scalar velocity equations via a semi-implicit scheme that treats the term $\boldsymbol{\nabla}^T\boldsymbol{u}$ explicitly and the decoupled term $\boldsymbol{\nabla}\boldsymbol{u}$ implicitly.

3.5 Numerical results for variable density

The capabilities of the formulation described above will be shown in two examples of fluids with different density. The first is a sloshing problem for which other reference results are available. This example is used to test the stabilization proposed and the ability of the method to deal with large density jumps. In the second example, a three-fluid flow is solved to show that the method can be generalized to an arbitrary number of fluids. Because in these examples the fluids have the same viscosity, we use the Laplace form of the governing equations.

3.5.1 Two-fluid sloshing

This numerical test for two-fluid flows was first proposed by Tezduyar et al. [131] and later deeply investigated in Cruchaga et al. [31]. It consists in a closed rectangular cavity with two immiscible fluids (see Fig. 3.11). The bottom fluid has

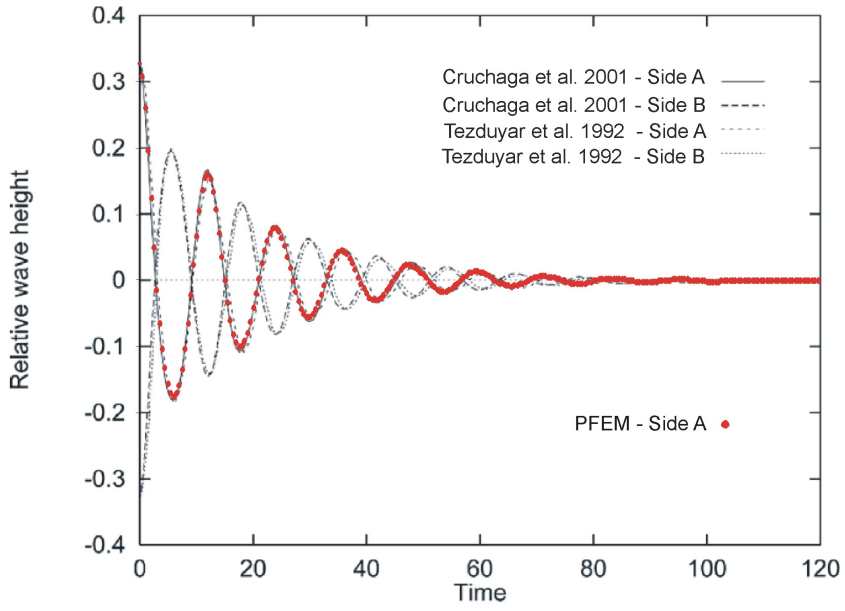

Figure 3.12: PFEM relative wave height at side A (red dots) compared to references.

density $\rho = 2$ kg m^{-3} and the top fluid $\rho = 1$ kg m^{-3}. The dynamic viscosity is constant, $\mu = 10^3$ Pa s in both fluids, and the gravity acceleration is set to $g = -0.294$ m s^{-2} in the vertical direction. Horizontal walls are considered no-slip while vertical walls are free-slip. The interface between both fluids is tilted in the initial configuration.

This is a typical example where the pressure presents a weak discontinuity at the interface between the two materials. We use the nodal interface description to allow the pressure gradient variable to reproduce exactly this discontinuity. Moreover, it is not trivial in Lagrangian methods to model the free-slip condition. We have done it by assigning $\mu = 0$ in the elements adjacent to the free-slip walls.

Figure 3.12 shows the interface relative height at the vertical walls (side A and B) for the previous works [131, 31] compared with our PFEM results, which reproduce well both the interface amplitude and oscillation frequency.

It is remarkable that when the flow reaches the steady state, the interface height is 0.2998, very close to the correct value 0.3. Notice that no mass correction algorithm was implemented. Neither was it necessary to use enhanced element integration nor shape function enrichment as it would be the case in front-capturing methods. The pressure field and the interface discretization are shown in Figure 3.13.

This example allows us to test the stabilization of the incompressibility condition for equal-order formulations as the one presented above. We have seen that standard stabilizations based on pressure gradient projections propose a

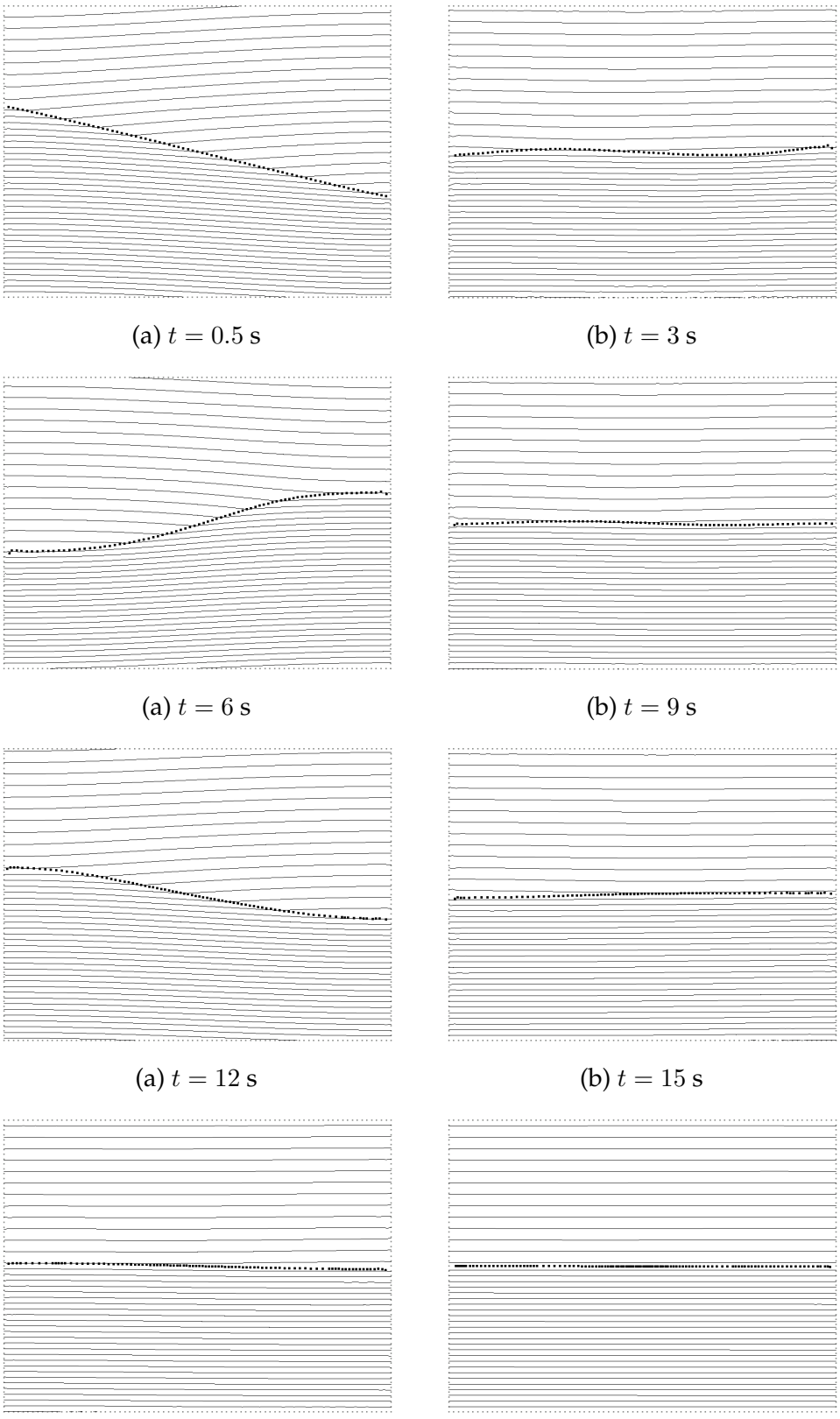

(a) $t = 0.5$ s (b) $t = 3$ s

(a) $t = 6$ s (b) $t = 9$ s

(a) $t = 12$ s (b) $t = 15$ s

(a) $t = 21$ s (b) $t = 120$ s

Figure 3.13: Pressure contour lines for two-fluid sloshing with density ratio 2:1.

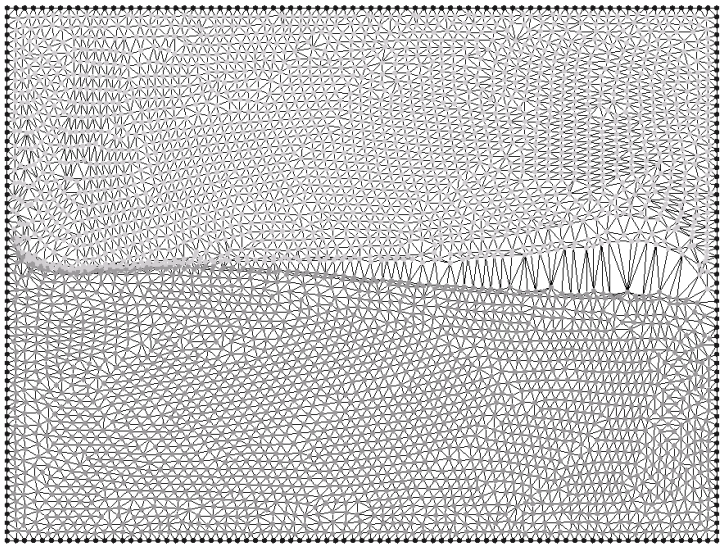

Figure 3.14: Interface tears apart due to the momentum imbalance at the vicinity of the interface.

stabilization term based on the difference between the pressure gradient and the continuous projection of the pressure gradient. Nevertheless, in heterogeneous flows with different densities, the pressure gradient is discontinuous across the interface. The introduction of a continuous variable π produces an error in the incompressibility condition at the interface that can be observed in Figure 3.14. The results shown previously have been obtained using the new stabilization term Eq. (3.51), where the density jump has been taken into account.

The presented formulation allows for arbitrary large jumps in density. For example, in a water-air sloshing problem the density ratio is 1000:1. This kind of problems is usually treated as a single-fluid flow, neglecting the air. Nevertheless, in many situations the influence of air must be taken into account. Results of the interface position and fluid velocity for a water-air sloshing problem are shown in Figure 3.15. Now the gravity has been set to $g = -10$ m s^{-2}. The method has not presented any difficulty even for this large density ratio. However, this example, defined with the same geometry and initial conditions than the previous test, has now a very strong movement of all internal nodes. The interface undergoes large deformations (including the possibility of breaking waves), and thus, remeshing is essential. If during remeshing connectivity changes are allowed, the identification of the interface between the two materials is affected by an error of order h (the average distance between two neighbor nodes) in the volume definition of each material. Therefore, change in nodes connectivity near the interface may cause an important volume variation. In order to check the volume variation due to the remeshing process, the water volume conservation has been measured. Figure

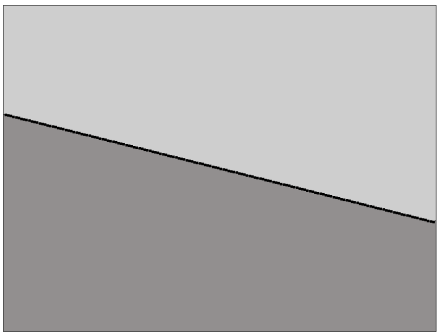

(a) $t = 0$ s

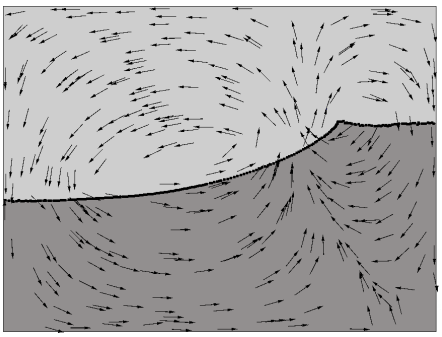

(b) $t = 0.55$ s

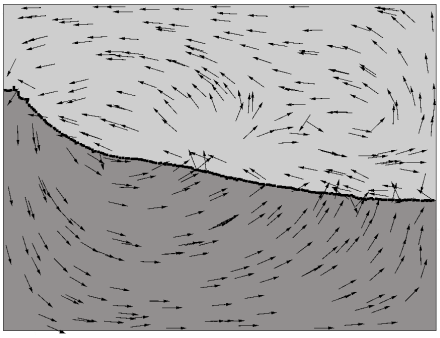

(a) $t = 1.15$ s

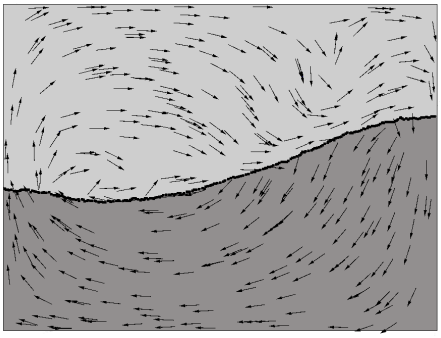

(b) $t = 1.7$ s

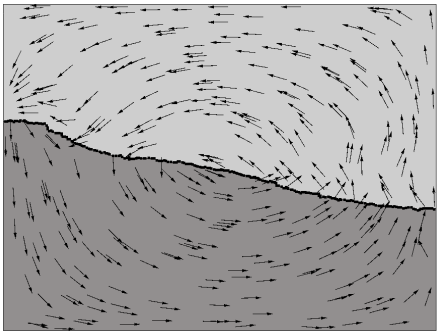

(a) $t = 2.3$ s

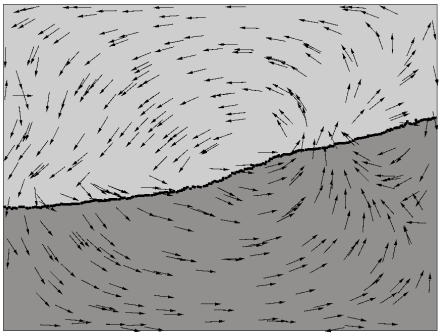

(b) $t = 2.75$ s

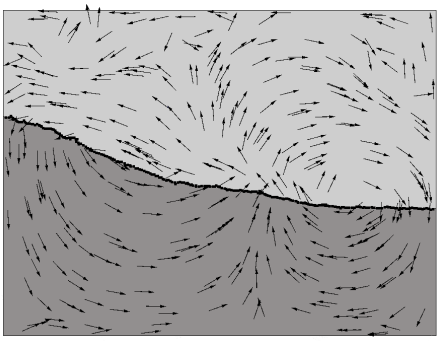

(a) $t = 3.35$ s

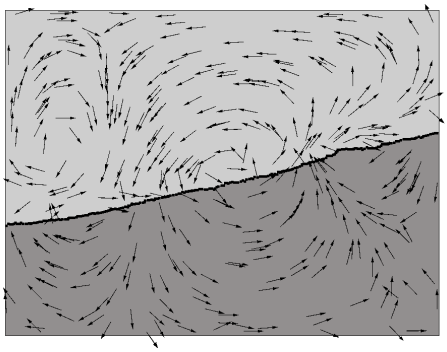

(b) $t = 5$ s

Figure 3.15: Interface position and velocity vectors (fixed length) for two-fluid sloshing 1000:1 during the first three oscillation periods. The bottom fluid is water, top fluid is air.

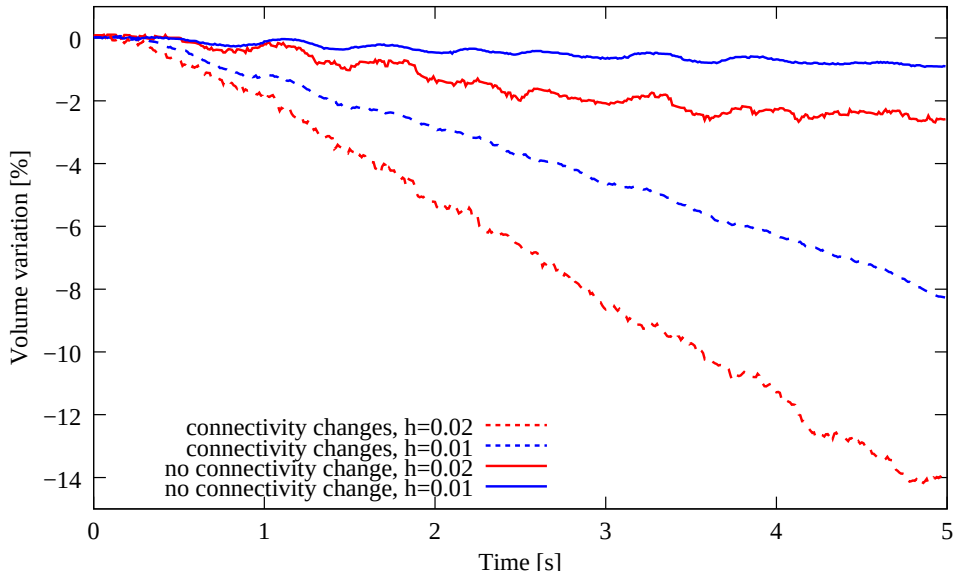

Figure 3.16: Water volume variation due to remeshing with connectivity changes at the interface (dashed lines) compared to no connectivity changes (solid lines) for different mesh sizes ($h = 0.02$ in red, $h = 0.01$ in blue) and same time step.

3.16 shows the water volume for different mesh sizes and fixed time step during a time period of 5 seconds. We can observe that when connectivity changes are limited with the strategy described in Section 3.3, volume conservation improves remarkably.

3.5.2 Heterogeneous flow with several materials

The formulation proposed can be applied with no modification to any arbitrary number of fluids. In this example we simulate the behavior of three fluids with different densities and same viscosity ($\mu = 0.1$ Pa s). The computational domain is a 1×1 m cavity, with free-slip walls and gravity $g = -10$ m s^{-2}.

In the initial configuration (see Fig. 3.17), fluid A is in a stable position, but fluids B and C will move to find the stable horizontal stratification. Figure 3.18 shows the nodes positions at different time steps. During the first time steps fluid C moves from right to left by the bottom part of the domain while fluid B moves from left to right by the upper part. The movement is so sudden that at time $t = 15$ s some particles of fluid C get entrapped inside fluid A on the right hand side. Due to their higher density, they move downwards until they reach fluid C.

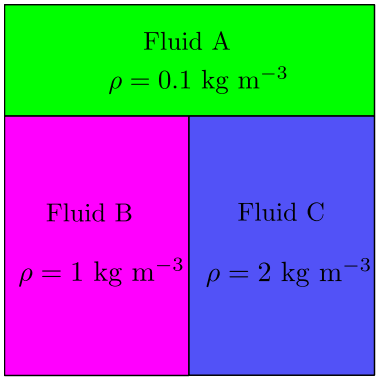

Figure 3.17: Initial configuration and fluid densities.

3.6 Numerical results for variable viscosity

In this section we explore the pressure discontinuity due to the viscosity jump. In the first example, a two-fluid dam break problem, we analyze the pressure profile obtained when the viscosity ratio is increased and the effect in the solution when using the Laplace versus the divergence form of the governing equations. In the second example, we have designed an extrusion problem where the pressure field has an analytic solution and $\frac{\partial u_n}{\partial n} >> 0$. We show the importance of using discontinuous pressure approximations to avoid errors in the incompressibility condition near the interface.

3.6.1 Two-fluid dam break

This example consists in a dam break of two fluids with the same density ($\rho = 1000$ kg m^{-3}) and different viscosities (in Pa s) (see the initial configuration and the viscosity values in Figure 3.19). Gravity acceleration has been set to $g = -10$ m s^{-2}. We use the standard continuous pressure representation instead of the correct discontinuous one since it already allows us to realize the pressure variation across the interface.

In Figure 3.20 we compare the pressure profile along the cut $x = 0.073$ at $t = 0.1$ s for different viscosity jumps. We observe that the pressure variation at the interface is proportional to the viscosity jump, as expected, even when the Laplace form of the Navier-Stokes equations has been used. The pressure variation can also be observed in the pressure field shown in Figure 3.21.

In Figure 3.22 we explore the effect of using the full strain rate tensor in the momentum equations (divergence form) in contrast to the constant viscosity simplification (Laplace form). We observe that the importance of the term $\boldsymbol{\nabla}^T \boldsymbol{u}$ increases with the viscosity ratio, even when it is treated explicitly to avoid the

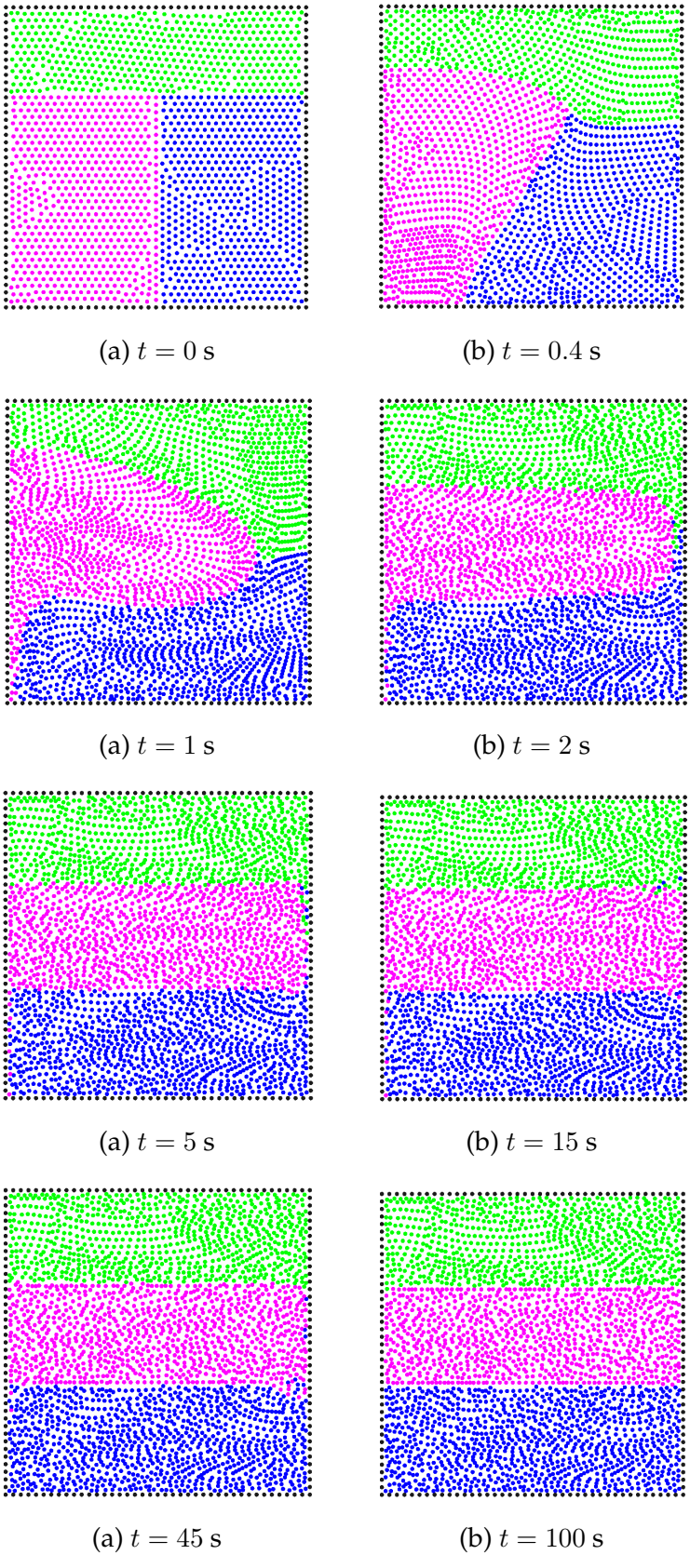

(a) $t = 0$ s (b) $t = 0.4$ s

(a) $t = 1$ s (b) $t = 2$ s

(a) $t = 5$ s (b) $t = 15$ s

(a) $t = 45$ s (b) $t = 100$ s

Figure 3.18: Evolution of the three-fluid flow.

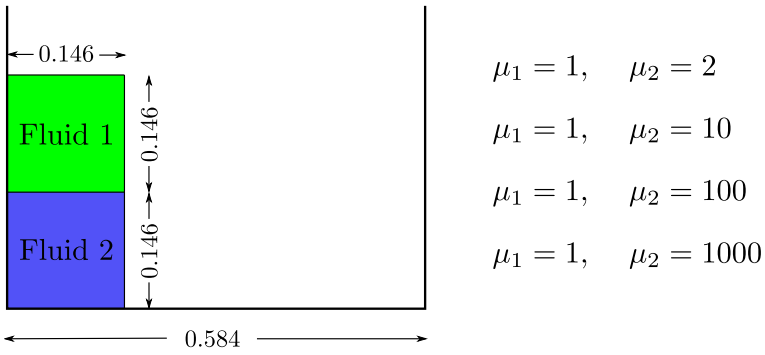

Figure 3.19: Initial configuration and viscosity values (in Pa s).

coupling between all the velocity components.

3.6.2 Extrusion

Pressure discontinuity has been always treated in the literature connected to surface tension effects (see e.g. Unverdi & Tryggvason [136], Scardovelli & Zaleski [117], Smolianski [124], Li & Lubkin [84], Gross & Reusken. [47], Minev et al. [91]) but to our knowledge there is not any previous work focused on the effects of viscosity jumps. For example, the sloshing of a free-surface separating water and air is a common problem with a clearly defined interface. In this problem it is typically assumed that the pressure at the free-surface equals the atmospheric

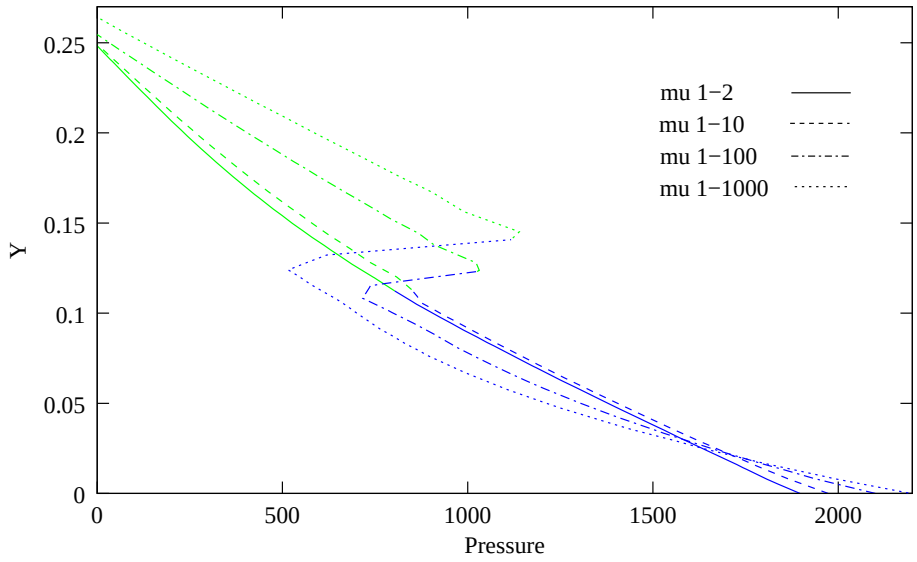

Figure 3.20: Pressure profile comparison for different viscosity ratios along the cut $x = 0.073$ at $t = 0.1$ s.

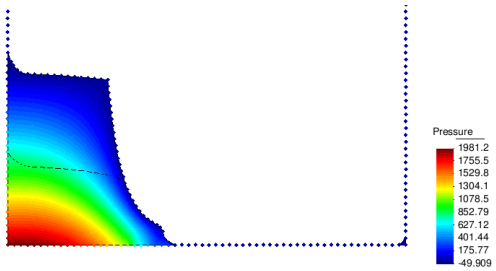

(a) $\mu_1 = 1, \mu_2 = 2$

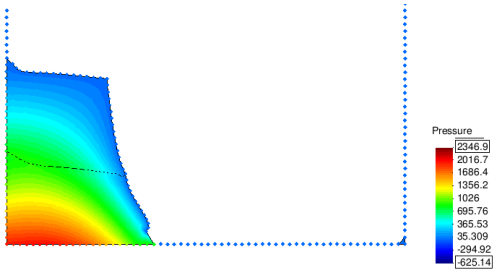

(b) $\mu_1 = 1, \mu_2 = 10$

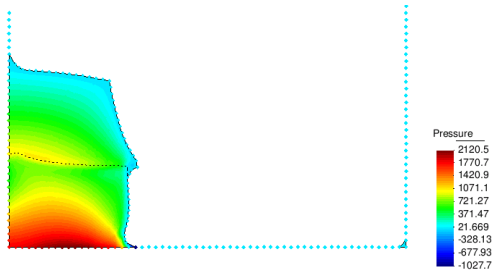

(c) $\mu_1 = 1, \mu_2 = 100$

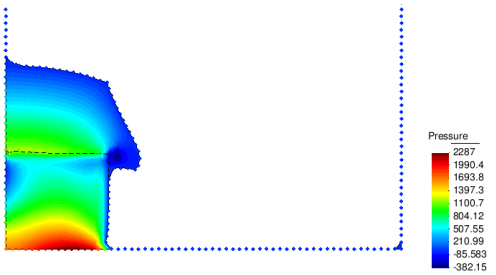

(d) $\mu_1 = 1, \mu_2 = 1000$

Figure 3.21: Pressure field at $t = 0.1$ s.

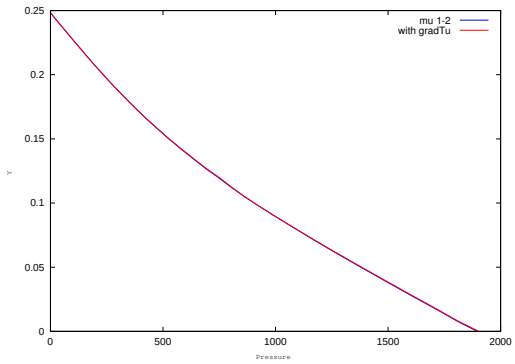

(a) $\mu_1 = 1, \mu_2 = 2$

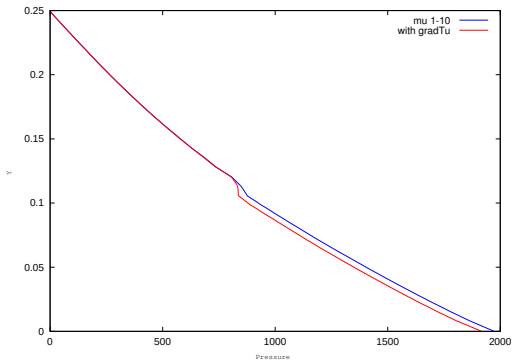

(b) $\mu_1 = 1, \mu_2 = 10$

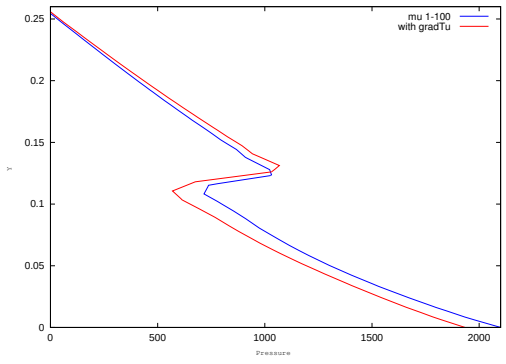

(c) $\mu_1 = 1, \mu_2 = 100$

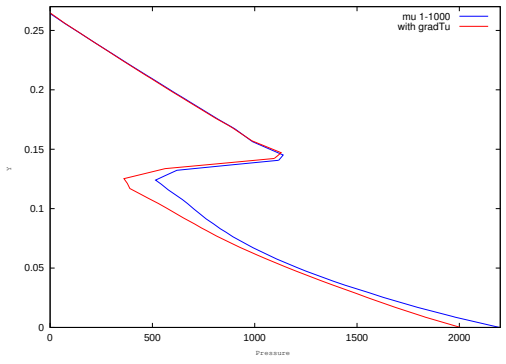

(d) $\mu_1 = 1, \mu_2 = 1000$

Figure 3.22: Pressure profile comparison with and without the term $\boldsymbol{\nabla}^T \boldsymbol{u}$ (along the cut $x = 0.073$ at $t = 0.1$ s).

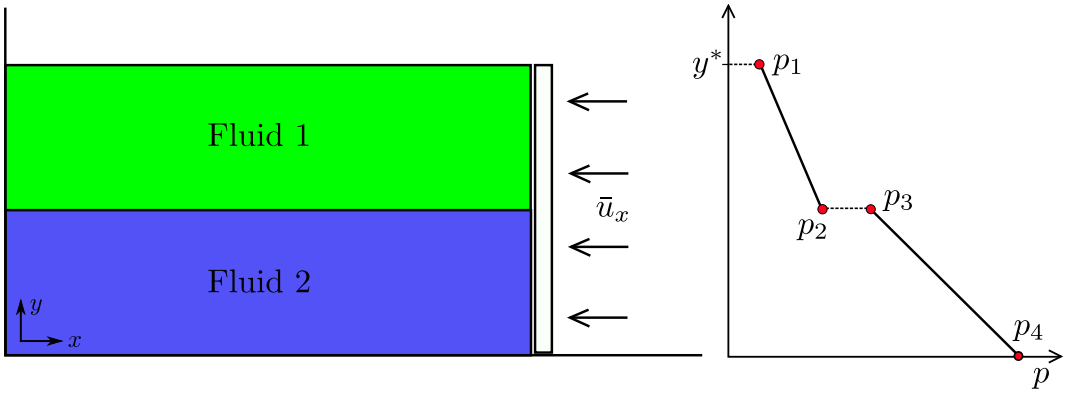

Figure 3.23: Example settings and analytic pressure solution.

pressure (the pressure in the air), what violates the expression $\Delta p = 2(\mu^+ - \mu^-)\dfrac{\partial u_n}{\partial n}$. In this case, the viscosities of air and water are so small, that the pressure jump is also small, regardless of the magnitude of $\dfrac{\partial u_n}{\partial n}$ at the free surface, and therefore the discontinuity is usually unnoticed. Fluid flows with different and high viscosities may be found in several applications, such as in metal extrusion problems, magma flow simulation, or fluid-structure interaction problems where the structure is modeled like a very viscous fluid, but it is not obvious to find an example where $\dfrac{\partial u_n}{\partial n}$ is relevant.

We propose an example for which an analytic solution exist and that may serve as a test to assess the ability of a given numerical method to represent the pressure discontinuity due to viscosity jump at the interface. The example consist in the extrusion against a wall of a rectangular domain composed by two fluids (see Figure 3.23). We will investigate the pressure solution and the volume conservation around the interface when continuous and discontinuous pressure approximations are used.

In this example, due to the choice of the physical parameters, viscous effects dominate over inertial ones, and thus the analytic solution for the "viscous" pressure reads:

$$p_1 = 2\mu_1 \frac{\partial u_n}{\partial n} \tag{3.65a}$$

$$p_2 = p_1 + \rho_1 g \frac{y^*}{2} \tag{3.65b}$$

$$p_3 = p_2 + 2(\mu_2 - \mu_1)\frac{\partial u_n}{\partial n} + \gamma \tag{3.65c}$$

$$p_4 = p_3 + \rho_2 g \frac{y^*}{2} \tag{3.65d}$$

where y^* is the height of the free surface, g the gravity and γ the surface tension coefficient. From volume conservation arguments (Fig. 3.24) we can derive

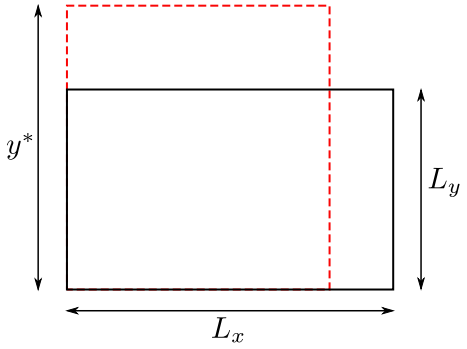

Figure 3.24: Notation for the pressure solution.

expressions for $\frac{\partial u_n}{\partial n}$ and y^*:

$$\frac{\partial u_n}{\partial n} = \frac{\bar{u}_x}{L_x - \bar{u}_x t}, \quad y^* = \frac{L_x L_y}{L_x - \bar{u}_x t} \tag{3.66}$$

The piston speed has been set to $\bar{u}_x = 0.1$ m s^{-1}, the initial domain sizes to $L_x = 0.8$ m and $L_y = 0.4$ m, and the gravity to $g = -10$ m s^{-2}. All walls are considered free-slip. The following numerical tests have been solved to compare the solution using continuous versus discontinuous pressure approximations:

1. jump in the viscosity, with equal density and no surface tension
2. equal density and viscosity, with surface tension
3. jumps in the viscosity and density, including surface tension

In all these cases we compare the pressure fields obtained and the volume variation of the incompressible fluid along a vertical cut. Figure 3.25 illustrates the kind of mesh deformation we have encountered in all the three tests. Figure 3.25a shows the initial mesh at time $t = 0$ and Figures 3.25b and 3.25c the final mesh at $t = 2$ s after extrusion. Figure 3.25b corresponds to the solution with discontinuous pressure, while Figure 3.25c shows the approximation with the continuous pressure field. One can easily distinguish the "not divergence-free" solution (Fig. 3.25c) close to the interface for the continuous pressure approximation. The volume variation we use to quantify $\boldsymbol{\nabla} \cdot \boldsymbol{u}$ in the following moving-mesh examples has been computed as $\varepsilon_V = \frac{Vol^n - Vol^0}{Vol^0}$, where Vol^n is the area associated to a node at time n (see Figure 3.26).

Example extrusion 1: Jump in the viscosity, equal density, no surface tension

In this case the physical parameters used are: $\mu_1 = 1, \mu_2 = 10, \rho_1 = \rho_2 = 1, \gamma = 0$. Figure 3.27 shows the good agreement of the discontinuous pressure solution

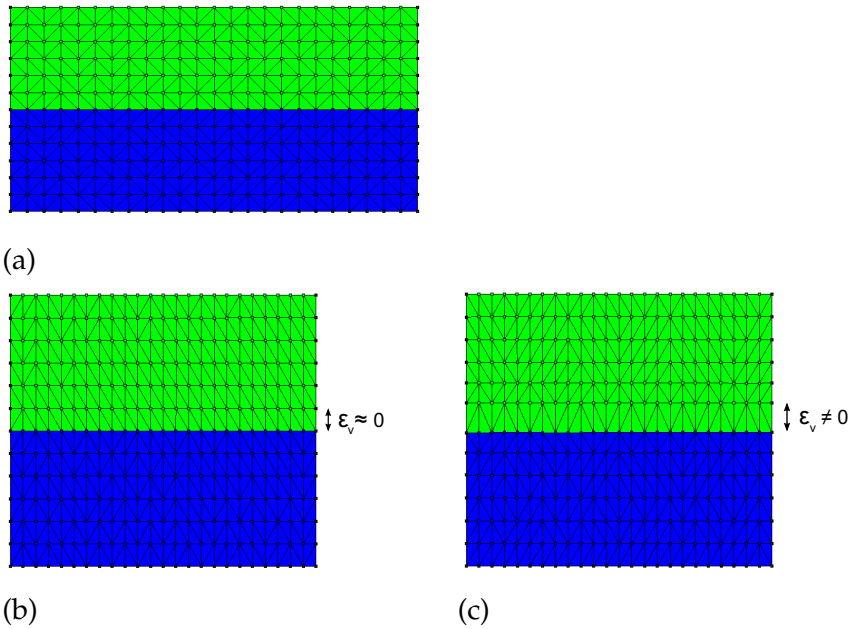

Figure 3.25: Mesh deformation: (a) initial mesh, $t = 0$ s; (b) mesh at $t = 2$ s and discontinuous pressure; (c) mesh at $t = 2$ s and continuous pressure showing a not divergence-free solution around the interface.

against the exact value, while the continuous pressure approximation leads to an excessive diffusive behavior. Figure 3.28 plots the error in the volume conservation, which is remarkable in the continuous approximation.

Example extrusion 2: No jumps in the density and viscosity but with surface tension

In interfaces where the surface tension is present, the following surface force must be computed: $\boldsymbol{f} = -\gamma\kappa\boldsymbol{n}$. In order to avoid the problems of evaluating the curvature and to have an analytic solution to compare the results with, we consider a fictitious tension for planar surfaces (Gross & Reusken. [47]): $\boldsymbol{f} = -\gamma\boldsymbol{n}$. In this

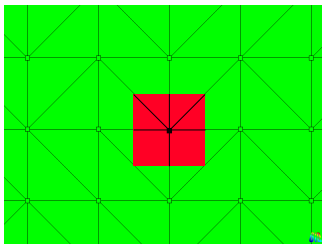

Figure 3.26: Area associated to a node (in red).

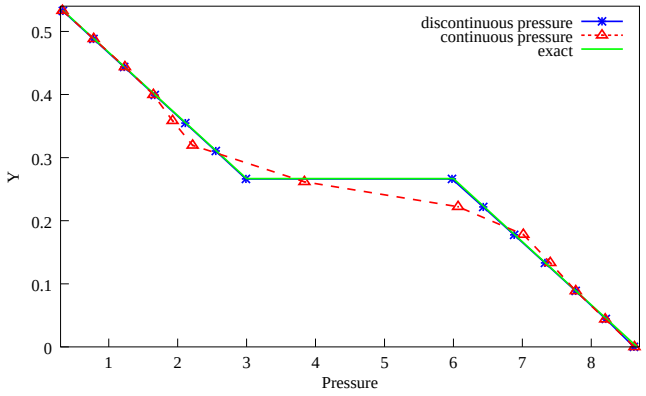

Figure 3.27: $\mu_1 = 1,\ \mu_2 = 10,\ \rho_1 = \rho_2 = 1,\ \gamma = 0$. Pressure cut at $t = 2$ s and $x = 0.3$ m for continuous vs. discontinuous pressure approximations compared with the exact solution.

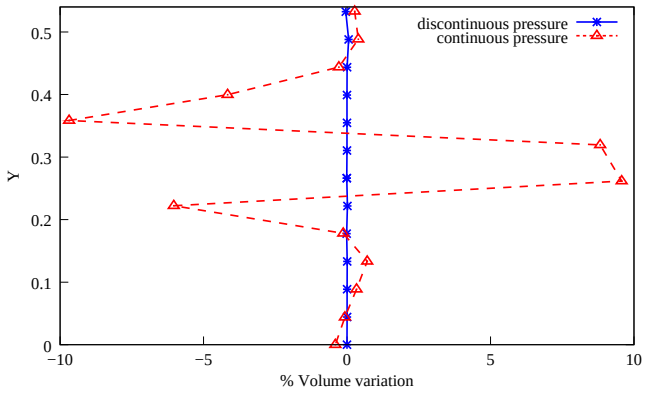

Figure 3.28: $\mu_1 = 1,\ \mu_2 = 10,\ \rho_1 = \rho_2 = 1,\ \gamma = 0$. Volume variation cut at $t = 2$ s and $x = 0.3$ m for continuous vs. discontinuous pressure approximations.

example the normal to the interface is taken as $\boldsymbol{n} = (0, -1)$.

In front-capturing methods, the non-alignment of the interface with the mesh causes severe difficulties in the discretization of this localized surface tension force and spurious velocities appear if pressure is not allowed to be discontinuous inside the elements cut by the interface (Gross & Reusken. [47], Minev et al. [91], Ganesan et al. [43]). Equivalent spurious velocities appear in moving mesh methods when pressure is approximated continuously, as shown in Figure 3.29b.

In order to investigate the influence in the velocity field of the pressure jump due to different viscosities and to the surface tension, we have set the viscosity, the density and the surface tension force to have an equal jump. We know that

$$\Delta p = 2(\mu_2 - \mu_1)\frac{\partial u_n}{\partial n} + \gamma,$$

then for the following parameters: **case (a)** $\mu_1 = 1,\ \mu_2 = 10,\ \rho_1 = \rho_2 = 1,\ \gamma = 0$,

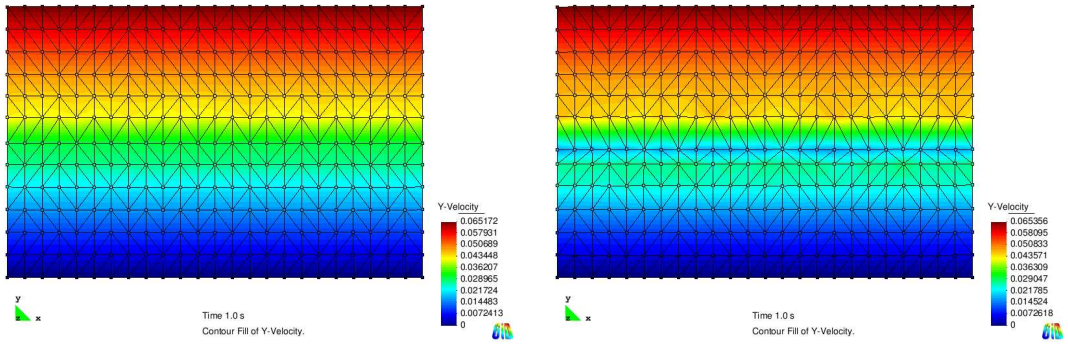

(a) $\mu_1 = 1,\ \mu_2 = 10,\ \rho_1 = \rho_2 = 1,\ \gamma = 0$ (b) $\mu_1 = \mu_2 = 1,\ \rho_1 = \rho_2 = 1,\ \gamma = 3$

Figure 3.29: Vertical velocity field at $t = 1$ s for continuous pressure approximation: (a) case with viscosity jump, (b) case with surface tension.

one obtains $\Delta p = 3$ at $t = 2s$. On the other hand, for **case (b)** $\mu_1 = \mu_2 = 1,\ \rho_1 = \rho_2 = 1,\ \gamma = 3$, one also has $\Delta p = 3, \forall t$.

Figures 3.29a and 3.29b show the velocity results for the continuous pressure approximation. In both cases the pressure profiles are quite similar (see Fig. 3.30), but in the case with surface tension, the non-physical velocities lead to much larger volume variations (Fig. 3.31). All these difficulties are avoided using a discontinuous pressure approximation.

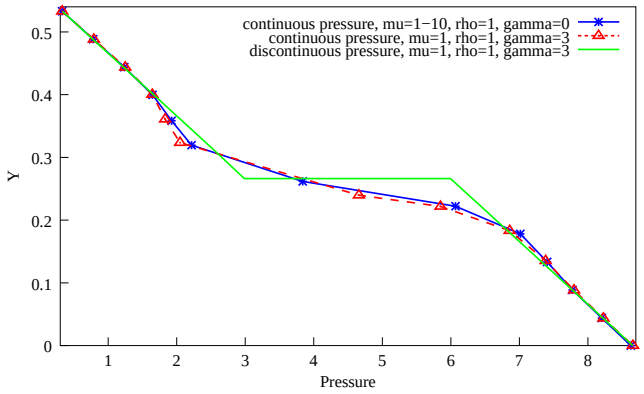

Figure 3.30: Pressure cut comparison at $t = 2$ s and $x = 0.3$ m for continuous pressure approximation and same pressure jump due to surface tension (dashed red line) or viscosity difference (continuous blue line), and discontinuous pressure approximation with surface tension (continuous green line).

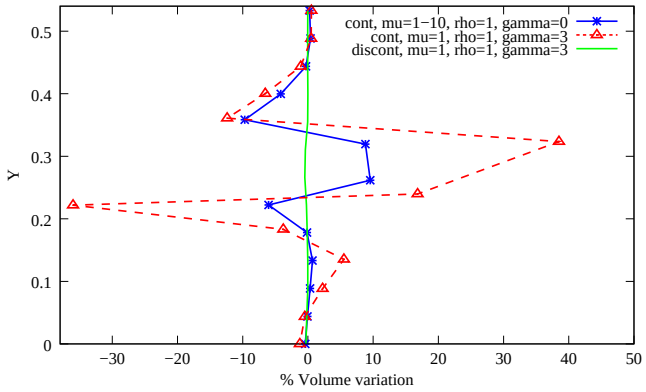

Figure 3.31: Volume variation comparison at $t = 2$ s and $x = 0.3$ m for continuous pressure approximation and same pressure jump due to surface tension (dashed red line) or viscosity difference (continuous blue line), and discontinuous pressure approximation with surface tension (continuous green line).

Example extrusion 3: Jumps in the viscosity and density, including surface tension

A density jump at the interface does not introduce a jump in the pressure field but in the pressure gradient. In this case accurate results can only be achieved with a discontinuous pressure gradient in the stabilization term at the interface as explained in Section 3.4.5.

In the following example, we consider the case where a jump in both the pressure field and also in the pressure gradient is needed to obtain accurate results. We introduce now a jump in the viscosity, in the density and also surface tension: $\mu_1 = 1$, $\mu_2 = 10$, $\rho_1 = 1$, $\rho_2 = 10$, $\gamma = 5$. Figures 3.32 and 3.33 show the pressure profile and the volume variation along $x = 0.3$ m at time $t = 2$ s respectively. The continuous pressure solution shows a volume variation over 15% while in the discontinuous solution the variation is almost zero, as the divergence-free condition requires.

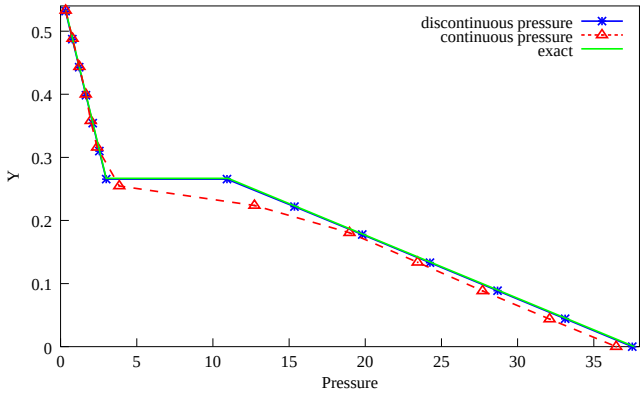

Figure 3.32: $\mu_1 = 1,\ \mu_2 = 10,\ \rho_1 = 1,\ \rho_2 = 10,\ \gamma = 5$. Pressure cut at $t = 2$ s and $x = 0.3$ m for continuous vs. discontinuous pressure approximations compared with the exact solution.

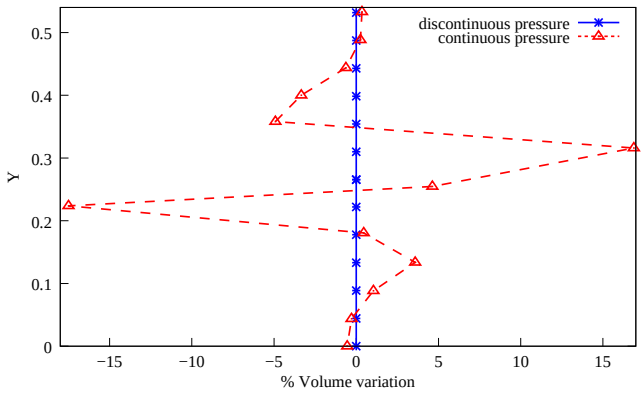

Figure 3.33: $\mu_1 = 1,\ \mu_2 = 10,\ \rho_1 = 1,\ \rho_2 = 10,\ \gamma = 5$. Volume variation at $t = 2$ s and $x = 0.3$ m for continuous vs. discontinuous pressure approximations compared with the exact solution.

3.7 Treatment of surface tension

This section deals about the numerical treatment of the surface tension force. We have seen before that in the weak form of the momentum equation, the following contour integral arises when the term corresponding to the stress tensor is integrated by parts:

$$\int_{\Gamma_{int}} \boldsymbol{w}(\boldsymbol{\sigma}_1 - \boldsymbol{\sigma}_2) \cdot \boldsymbol{n}\, d\Gamma \tag{3.67}$$

In absence of surface tension, the condition $[\![\boldsymbol{\sigma}]\!] \cdot \boldsymbol{n} = 0$ on Γ_{int} is implicitly satisfied if the integral (3.67) is neglected. However, in the case of $\gamma \neq 0$, the contour integral

$$\boldsymbol{f}_{st} = \int_{\Gamma_{int}} \gamma\kappa\boldsymbol{n} \cdot \boldsymbol{w}\, d\Gamma \tag{3.68}$$

remains. Thus the singular capillary force at the interface $\boldsymbol{f}_{st}$ is naturally incorporated in the weak form of the finite element method.

If the surface tension term Eq. (3.68) is discretized explicitly, i.e. the surface tension forces are evaluated on the interface at the previous time step, the stability of the scheme imposes the following restriction on the time step size (Brackbill et al. [9]):

$$\Delta t_{st} < \sqrt{\frac{\langle\rho\rangle\, h^3}{2\pi\gamma}} \tag{3.69}$$

where $\langle\rho\rangle = \frac{1}{2}(\rho_1 + \rho_2)$, h is the mesh size and Δt_{st} the capillary time step. With this restriction the propagation of capillary waves is resolved and their unstable amplification avoided. An alternative stability condition for low Reynolds number flows that also includes the viscosity has been derived by Galusinski & Vigneaux [42]. Unfortunately, Eq. (3.69) can be rather limiting for fine meshes and large surface tension coefficients. An implicit (Bänsch [3]) or semi-implicit (Hysing [63]) treatment of the surface tension would circumvent this constrain.

One of the most difficult tasks in front-capturing techniques is to accurately identify the interface to directly impose the condition $[\![\boldsymbol{\sigma}]\!] \cdot \boldsymbol{n} = \gamma\kappa\boldsymbol{n}$ on Γ_{int} (Daly [32]). This difficulty can be alleviated by interpreting the surface tension as a continuous body force spread across a transition region of thickness ϵ,

$$\boldsymbol{f}_{st} = \int_{\Omega} \gamma\kappa\delta_\Gamma^\epsilon \boldsymbol{n} \cdot \boldsymbol{w}\, d\Omega \tag{3.70}$$

where δ_Γ^ϵ is a regularized Dirac delta function at the interface. The idea was introduced by Peskin [107] in finite differences and later reformulated by Brackbill et al. [9] under the name of Continuum Surface Force (CSF) model. It has been extensively used to model surface tension in Eulerian formulations, in particular in the volume-of-fluid (e.g. Brackbill et al. [9], Richards [114], Lafaurie et al. [83], Wu et al. [140], Scardovelli & Zaleski [117]) and level set methods (e.g. Sussman

et al. [126], Tornberg [132], Hysing [63], Marchandise et al. [88]). This approach has the advantage that the interface does not need to be reconstructed explicitly but, on the other side, the smoothed surface tension may lead to spurious (non-physical) velocities in the neighborhood of the interface due to the fact that it compels pressure continuity at the interface regardless of the appropriate interface conditions.

Most particle-based and meshless methods use the delta function approach as well, e.g. Nomura et al. [98] and Liu et al. [87] in the Moving Particle Semi-implicit (MPS) method, or Morris [94] in the Smoothed Particle Hydrodynamics (SPH) method. Another approach in particle methods is to model the surface tension as an interparticle potential force (Nugent & Posch [99]). Then surface tension arises automatically by introducing repulsion or attraction forces between the neighboring particles of different fluids (Kondo et al. [79], Zhou et al. [143]).

The interface representation by nodes and element edges in PFEM allows for an easy and accurate incorporation of the surface tension, avoiding the need of regularization techniques like the Dirac delta function. Furthermore, the pressure discontinuity across the interface can be optimally approximated.

3.7.1 Curvature calculation

There are several ways to calculate the curvature κ from the information of the interface location. The one we have followed in this work is based on the *osculating circle* of a curve. It is defined as the circle that approaches the curve most tightly among all tangent circles at a given point (see Figure 3.34). The center and radius of the osculating circle at a given point are called center of curvature $\boldsymbol{c}$ and radius of curvature $\boldsymbol{R}$ of the curve at that point, respectively. Thus the quantity $\kappa\boldsymbol{n}$ required for the capillary force Eq. (3.68) can be calculated as:

$$\boldsymbol{n} = \frac{\boldsymbol{R}}{|\boldsymbol{R}|}, \qquad \kappa\boldsymbol{n} = \frac{\boldsymbol{R}}{|\boldsymbol{R}|^2} \tag{3.71}$$

On the unstructured mesh, we build the osculating circle that passes through three adjacent interface nodes as shown in Figure 3.35. If the interface is assumed to be sufficiently regular, the circle circumscribed to $\boldsymbol{x}$, $\boldsymbol{x}_{right}$ and $\boldsymbol{x}_{left}$ converges to the osculating circle of Γ_{int} at point $\boldsymbol{x}$ when $\boldsymbol{x}_{right} \to \boldsymbol{x}$ and $\boldsymbol{x}_{left} \to \boldsymbol{x}$.

Other moving mesh methods compute the radius of curvature from a spline fit to the interface nodes (e.g. Daly & Pracht [33], Fyfe et al. [41]). But whereas an accurate interpolant can be found that goes through a given set of points, it is not always true that other properties of the curve calculated at the points, such as the curvature, are well represented by this interpolant.

To avoid connectivity changes at the interface, long interface edges are refined. If the new node i is inserted at the midpoint between the old end-nodes of the

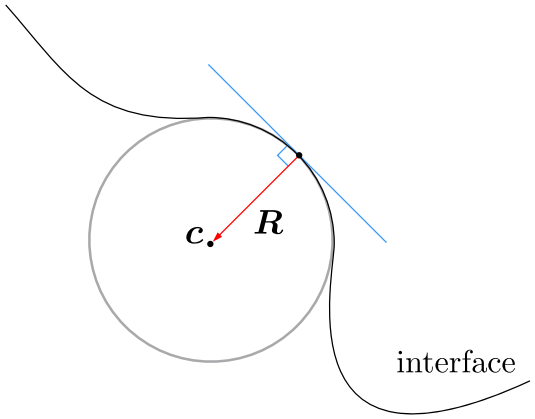

Figure 3.34: Osculating circle of an interface.

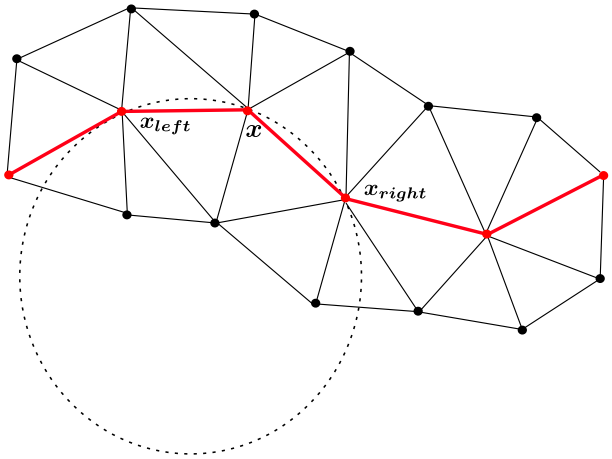

Figure 3.35: Interface curvature computation.

long edge a-c (see notation in Fig. 3.36), the osculating circle at this new node will be degenerated, i.e. curvature is zero because the three points used to calculate the osculating circle lie on the same line. Furthermore, the refinement of the edge a-c increases the curvature at node a (circle in blue color). Both drawbacks are illustrated in Figure 3.36. Thus curvature values will oscillate due to remeshing if the new nodes positions are linearly interpolated. To avoid these difficulties, we take into account the curvature of the interface when inserting nodes, so that the position of the new interface node i' uses the information of the old osculating circle (in black color).

The mesh close to the interface is finer than in the rest of the computational domain, as explained in Section 3.3, for more accurate curvature computation and better interface resolution.

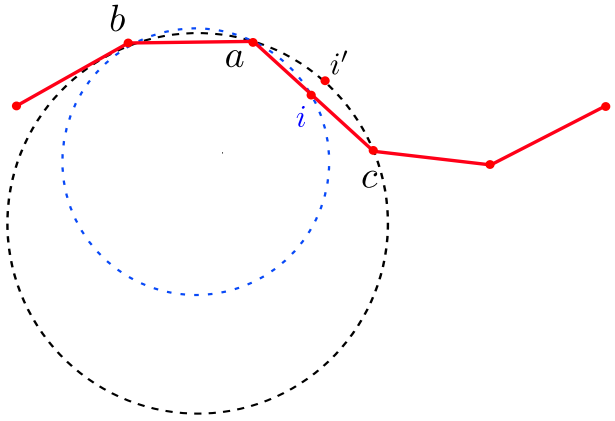

Figure 3.36: Interface curvature after refinement of edge a-c. The curvature is larger at node a and zero at node i. Curvature has been taken into account in the position of i'.

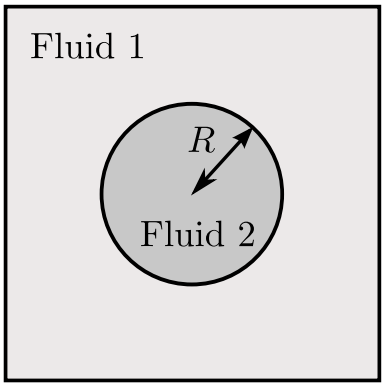

Figure 3.37: Static bubble initial configuration.

3.7.2 Static bubble

We verify our surface tension algorithm with the static bubble test case (e.g. Lafaurie et al. [83], Popinet & Zaleski [108], Tryggvason et al. [133], Smolianski [123], Chen et al. [18], Hysing [64]). It consists in a circular fluid bubble into another viscous fluid at rest (see Figure 3.37), where gravitational or other external forces are neglected. According to the Laplace-Young law, the pressure jump will be $p_2 - p_1 = \gamma\kappa = \gamma/R$, where p_2 is the bubble internal pressure, p_1 the outer pressure and R the bubble radius. Even with non-zero surface tension, the circular shape of the bubble should be preserved and the fluids should remain at rest no matter how long we integrate the equations in time.

We have simulated the equilibrium state of a circular bubble of a radius $R = 0.25$ (constant curvature $\kappa = 1/R = 4$) in a static fluid with $\rho_1 = \rho_2 = 1$, $\mu_1 = \mu_2 = 1$, $g = 0$, and $\gamma = 1$. The simulations have been run 100 time steps with

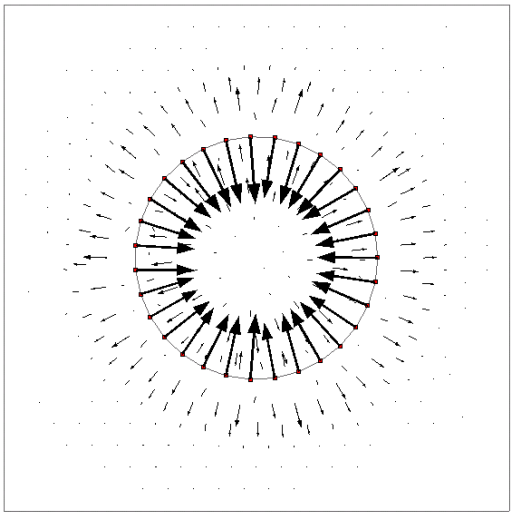

Figure 3.38: Spurious velocities in static bubble for continuous pressure.

h	Continuous	Discontinuous
1/20	4.4×10^{-2}	2.8×10^{-5}
1/40	1.7×10^{-2}	1.3×10^{-5}
1/80	7.2×10^{-3}	8.9×10^{-6}

Table 3.1: Velocity error $||\boldsymbol{u}||_\infty$ at final time for continuous and discontinuous pressure approximations.

Δt fixed to 0.01. The bubble should remain exactly stationary and the velocity of the fluid should be exactly zero. But if the pressure is approximated continuously, the pressure fluctuations near the interface generate spurious velocity currents (see Figure 3.38) that may deform the bubble shape, produce a significant mass loss (Sussman et al. [126]) and spoil the solution. These currents will depend on the grid resolution, the fluids viscosity and the surface tension (Tryggvason et al. [133]). The Reynolds number of the spurious currents is proportional the Laplace number $La = 2R\rho_1\gamma/\mu_1^2$ (Lafaurie et al. [83], Popinet & Zaleski [108]).

Figure 3.39 shows the pressure solution for continuous approximation and different mesh sizes. The exact jump is $\Delta p = \gamma/R = 4$. We observe that the pressure solution fluctuates at the interface, and it improves with finer meshes. In the case of discontinuous pressure approximation shown in Figure 3.40, the solution is already excellent for coarse meshes. The velocity error (measured in the norm $||\boldsymbol{u}||_\infty = \max_i |\boldsymbol{u}_i|$) for both approximations is shown in Table 3.1. The discontinuous pressure produces velocity solutions three orders of magnitude better than the continuous one.

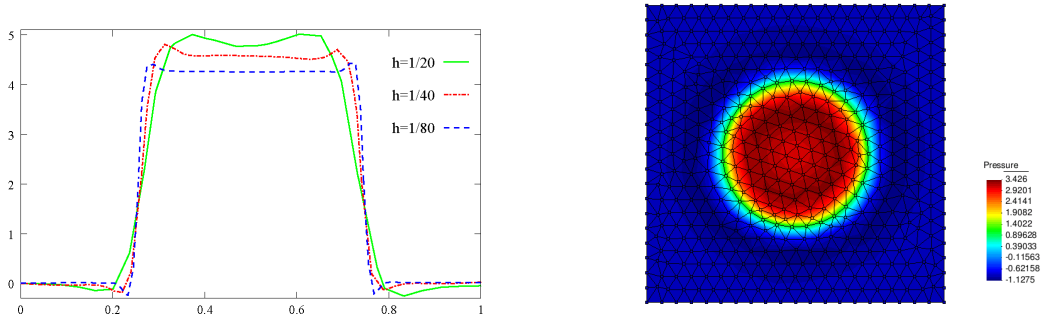

(a) (b)

Figure 3.39: Continuous pressure approximation: (a) profile at final time for different h, and (b) pressure field for $h = 1/20$.

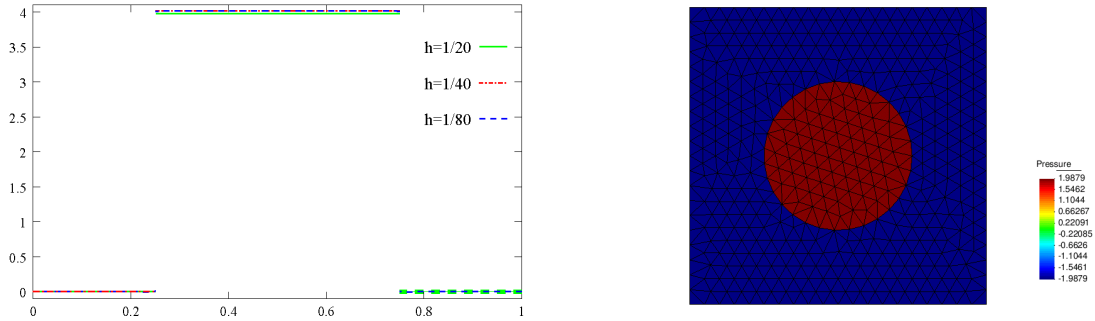

(a) (b)

Figure 3.40: Discontinuous pressure approximation: (a) profile at final time for different h, and (b) pressure field for $h = 1/20$.

Finally, Figure 3.41 shows the influence of the parameter $\lambda = \alpha \frac{\Delta t + \hat{\tau}}{h}$ on the pressure solution at the interface. For the minimum value α_{min} that makes the system Eq. (3.64a) invertible, the pressure profile is flat at the interface, i.e. the jump is represented exactly and incompressibility is satisfied. The larger the value of α, the more strongly the pressure continuity condition at the interface Eq. (3.55) is imposed, so that the flow behaves as slightly compressible in the vicinity of the bubble interface.

The numerical scheme developed in the previous sections will be tested in the problem of a bubble rising in a liquid column.

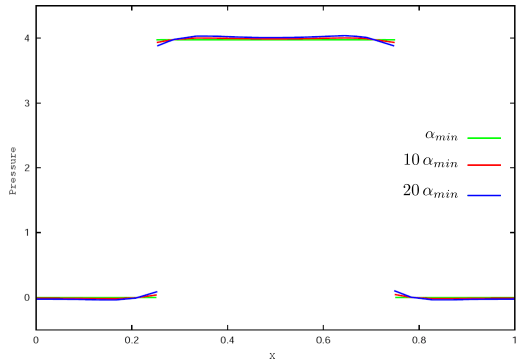

Figure 3.41: Pressure profile for discontinuous approximation and $h = 1/20$. Influence of α value on the pressure jump at the interface: α_{min}, $10\alpha_{min}$, $20\alpha_{min}$.

3.8 Application: Rising Bubble

Bubbles and bubbly flows play a significant role in a wide range of geophysical and industrial processes, such as mixing in chemical reactors, elaboration of alloys, cooling of nuclear reactors, two-phase heat exchangers, aeration processes, and atmosphere-ocean exchanges.

The shape and rise velocity of a bubble are controlled by the physical properties of the fluids and the surrounding flow field. Grace [45] developed a well-known graphical correlation for single gas bubbles rising in an infinite liquid using three dimensionless numbers: the Reynolds number (Re), the Eötvös number (Eo), and the Morton number (Mo).

$$Re = \frac{\rho\, d\, U}{\mu} \tag{3.72}$$

$$Eo = \frac{\rho\, g\, d^2}{\gamma} \tag{3.73}$$

$$Mo = \frac{g\, \mu^4}{\rho\, \gamma^3} \tag{3.74}$$

where ρ and μ are the density and viscosity of the liquid, d is an equivalent diameter of the bubble, U the rising speed of the bubble, g the gravity, and γ the surface tension coefficient. Grace [45] classifies the bubble shapes into three regimes: spherical, ellipsoidal, and spherical cap. Bubbles with low Re or low Eo are spherical. For higher Re, bubbles have an ellipsoidal shape at intermediate Eo and spherical cap shape at high Eo. A more detailed regime diagram was given by Clift et al. [23], which included wobbling bubbles for $Re \sim 10^3$ in the ellipsoidal regime, and the spherical cap regime was subdivided into spherical cap, skirted, and dimpled ellipsoidal cap for high, intermediate, and low Re numbers, respectively. These diagrams were further developed by Bhaga & Weber [6], who also studied the flow field around the bubble, specially the wake that forms in the

rear of the bubble for intermediate and high Re.

Numerous experimental studies have been performed to understand the flow dynamics of a single rising bubble, e.g. by Haberman & Morton [50], Grace [45], Hnat & Buckmaster [57], Clift et al. [23], Bhaga & Weber [6], Maxworthy et al. [89], Raymond & Rosant [113], and Wu & Gharib [141], but the fact that approximate theoretical solutions have only been derived in the limit of very small bubble deformations (Moore [93]), together with the difficulties in experimentally measuring the flow variables of the bubble without any interference while it is rising and deforming, make numerical simulation an important tool to gain insight of the flow.

Previous numerical studies have mostly followed the fixed mesh approach: the pioneering works of Esmaeeli & Tryggvason [37], Esmaeeli & Tryggvason [38], and Bunner & Tryggvason [12] used the front-tracking method (together with finite differences), also de Sousa et al. [34] (finite differences) and Hua & Lou [58] (finite volume method); level set is used by Tornberg [132], Smolianski [123], Hysing [64] (finite elements) and Yu & Fan [142] (finite volumes); Volume-of-Fluid is used in Chen et al. [17] and Van Sint Annaland et al. [139]; Bonometti & Magnaudet [8] use a hybrid approach between VOF and level set (finite volumes); and interface fitting method in Ryskin & Leal [116] and Raymond & Rosant [113]. The Lattice-Boltzmann method is used e.g. in Frank et al. [40] and Kurtoglu & Lin [81]. In these numerical works, results are qualitatively compared with experimental observations of bubble shape under different regimes. Only recently, quantitative tests for two-dimensional rising bubbles have been proposed by Hysing et al. [65]. We have simulated these tests and compared the PFEM results with the reference solutions.

3.8.1 Numerical tests

The problem consists in a bubble rising in a liquid column as illustrated in Figure 3.42. Two tests have been proposed in Hysing et al. [65]: test A considers a bubble in the ellipsoidal regime which undergoes moderate shape deformation, while in the test B the bubble belongs to the skirted regime and experiences much larger deformation. They are remarked in the Clift's diagram of Figure 3.43. Both fluids are Newtonian, incompressible and isothermal, and their physical properties are listed in Table 3.2.

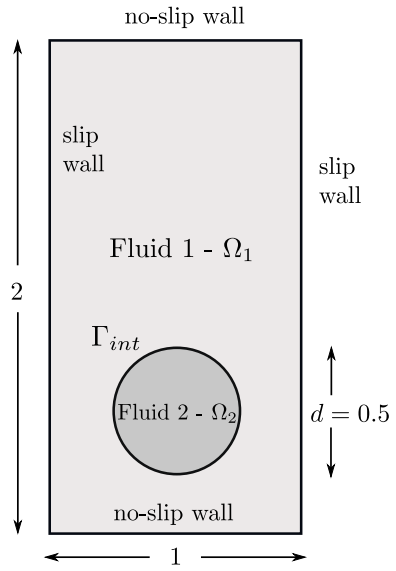

Figure 3.42: Initial configuration.

Table 3.2: Physical parameters.

Test case	ρ_1	ρ_2	μ_1	μ_2	g	γ	Re	Eo	ρ_1/ρ_2	μ_1/μ_2
A	1000	100	10	1	0.98	24.5	35	10	10	10
B	1000	1	10	0.1	0.98	1.96	35	125	1000	100

Subscript 1 refers to the surrounding heavier fluid and subscript 2 to the lighter fluid in the bubble.

The reference solutions presented in [65] have been run with three different numerical approaches: the TP2D of Turek [134] and Hysing [64], the FreeLIFE of Parolini & Burman [106], and the MooNMD of Ganesan et al. [43]. They all use the finite element method, but the two first approaches describe the interface with the level set, while the latter tracks it in an arbitrary Lagrangian-Eulerian way. More specific details about the methods can be found in [65]. The following bubble quantities are used to compare the results:

- shape at the final time $t = 3$ s,
- circularity $\not\in = \dfrac{2\sqrt{\pi \text{Area}}}{\text{Perimeter}}$,
- center of mass $\boldsymbol{X}_c = \displaystyle\int_{\Omega_2} \boldsymbol{x}\, dx / \int_{\Omega_2} 1\, dx$, and
- rise velocity $\boldsymbol{U}_c = \displaystyle\int_{\Omega_2} \boldsymbol{u}\, dx / \int_{\Omega_2} 1\, dx$.

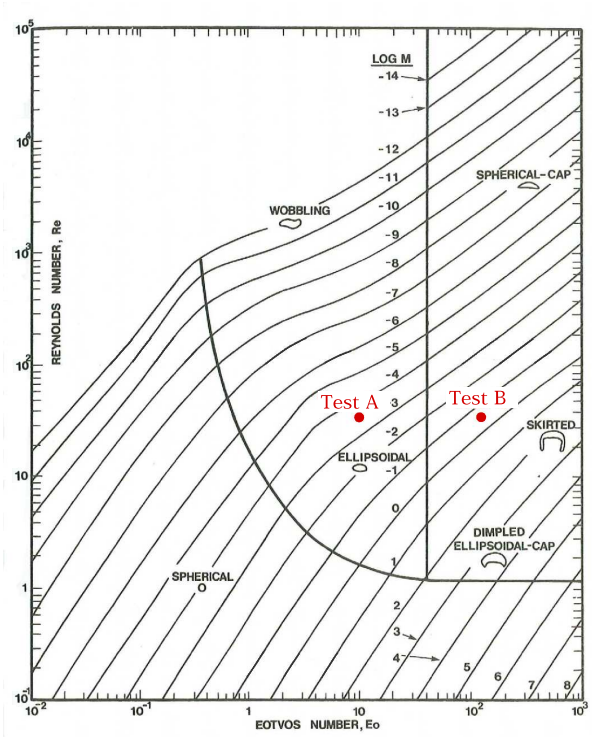

Figure 3.43: Clift et al. [23] shape regime diagram for bubbles in liquids. Test A (elliptic) and test B (skirted ellipsoidal-cap) are marked in red color.

3.8.2 Results

The computations have been performed on unstructured meshes with element size $h = 1/40$ in the bulk of the fluids and wall regions, and the mesh at the interface has been refined to $h = 1/80$, $1/160$, $1/320$ and $1/640$ in order to analyze the convergence in h of the solution. With the "distance function" refinement explained in section 3.3.1, we can use an arbitrarily fine mesh without increasing the total number of nodes to impractical values as would be the case with an uniform mesh (see Figure 3.44).

For test A, Figure 3.45 shows the evolution of the rising bubble. At final time $t = 3$ s we compare the PFEM bubble shapes for the meshes $h = 1/40, 1/80, 1/160$ and $1/320$, and observe that they converge to the shape of the finest mesh (Figure 3.46), which is in good agreement with the TP2D solution reported in [65] (Figure 3.47a). The plots of the bubble circularity (Figure 3.47b) and rise velocity (Figure 3.47d) show that our bubble is slightly oscillating, but the evolution of the center of mass (Figure 3.47c) is again in good agreement. The oscillating behavior of the PFEM results may be explained by the fact that, on the one side, PFEM does not introduce diffusivity at the interface, and on the other side, the geometrical method we use to calculate the curvature (the osculating circle) may not be accurate

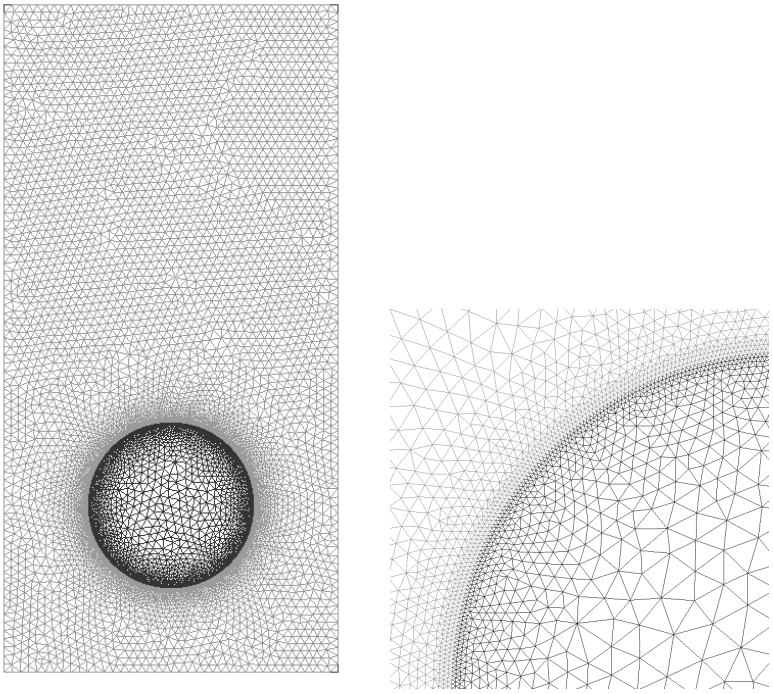

Figure 3.44: Mesh is refined close to the interface with the help of a distance function.

Table 3.3: Volume variation

Test	h	Initial Volume	Final Volume	Variation
A	1/320	0.19635	0.1965	$+7 \times 10^{-4}$
B	1/640	0.19635	0.19633	-1×10^{-4}

enough. Regarding the volume conservation, without any correction technique the bubble volume variation between the initial and final times, $\Delta V = \frac{V_f - V_0}{V_0}$, is of order $\mathcal{O}(10^{-4})$ (Table 3.3).

Same type of results are shown for test B in Figures 3.48, 3.49, and 3.50. Although the bubbles in both test cases rise with similar velocity, the decrease in surface tension causes bubble B to undergo a much larger deformation and to develop thin filaments. In the TP2D and FreeLIFE solutions these filaments break up, in contrast to the moving mesh solutions of PFEM and MooNMD (Figure 3.50a). In the physical reality, breakup occurs due to capillary waves present on the interface, which trigger the three-dimensional Plateau-Rayleigh instability (Section 1.1) when the filament radius is small enough. Thus, capillary waves can cause the skirt filament to fragment during flow, though this response requires very large elongations, typically greater than 20 times the initial bubble radius (Stone [125]).

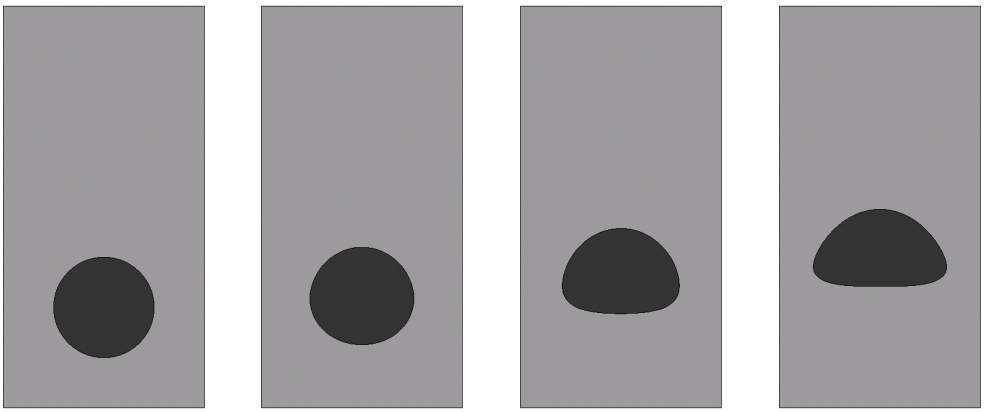

(a) $t = 0$ s (b) $t = 0.5$ s (c) $t = 1.0$ s (d) $t = 1.5$ s

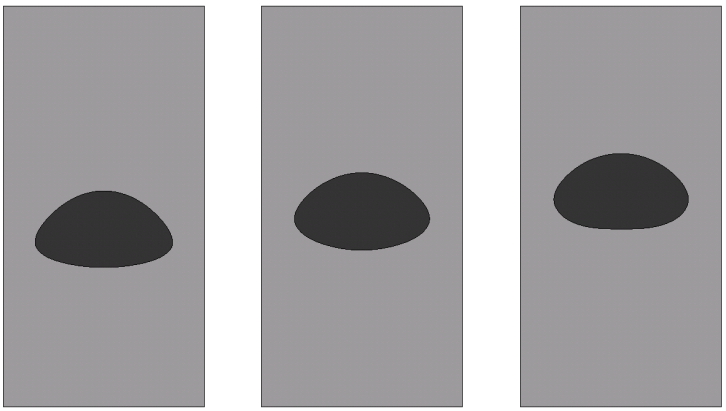

(e) $t = 2.0$ s (f) $t = 2.5$ s (g) $t = 3.0$ s

Figure 3.45: Test A. Bubble evolution for mesh size $h = 1/320$.

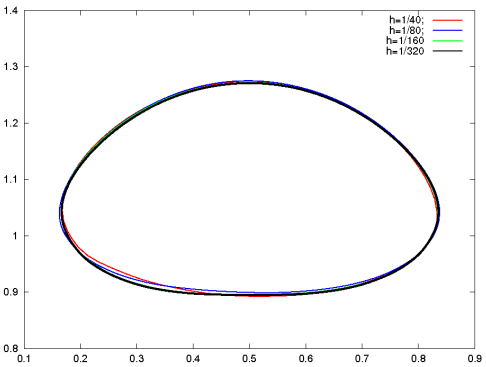

Figure 3.46: Test A. PFEM bubble shape for different mesh sizes at $t = 3$ s.

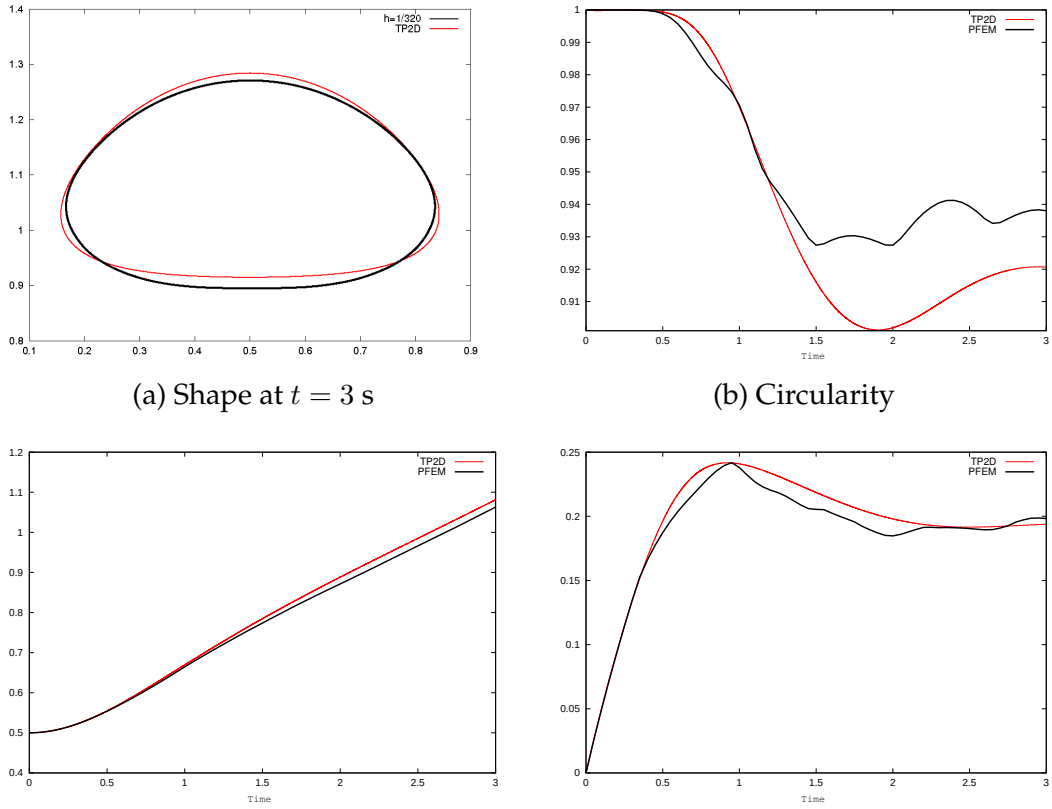

(a) Shape at $t = 3$ s

(b) Circularity

(c) Center of mass

(d) Rise velocity

Figure 3.47: Test A. Comparison of benchmark quantities: PFEM ($h = 1/320$) vs. TP2D results.

Figure 3.51 shows the mesh of the PFEM solution in the skirted region. The filament is not thin enough to break up. The volume variation is excellent again, of order $\mathcal{O}(10^{-4})$.

The fact of using an explicit approach when discretizing in time the surface tension force introduces the stability condition for the time step expressed in Eq. (3.69). If larger time steps are taken, instabilities will develop at the interface. This time step constraint is very restrictive for fine meshes ($\Delta t_{st} \propto h^{3/2}$). In our case, the refined mesh close to the interface imposes rather small global time steps (for test A with mesh $h = 1/320$, $\Delta t_{st} < 3.3 \times 10^{-4}$; and for test B with $h = 1/640$, $\Delta t_{st} < 3.9 \times 10^{-4}$) that undoubtedly affect the computational efficiency.

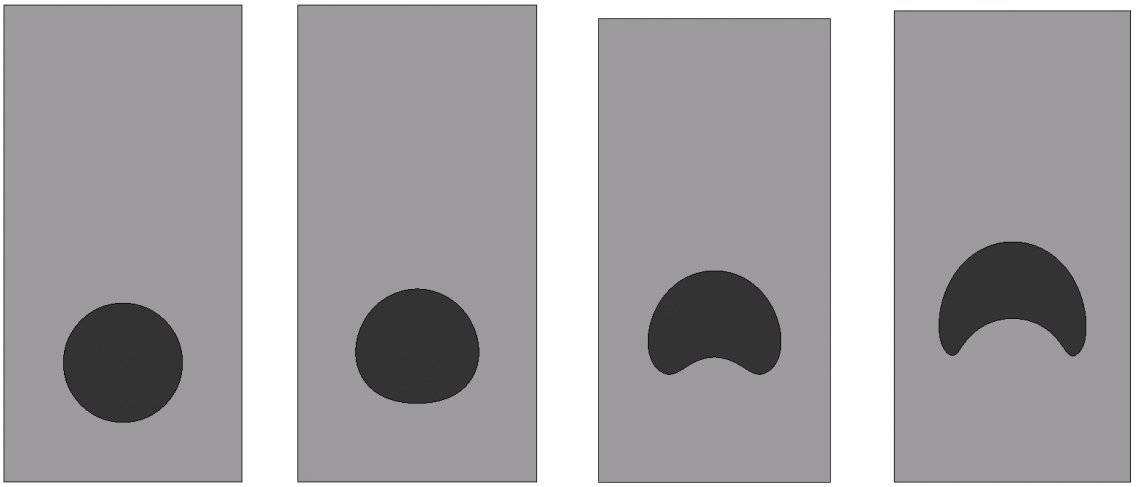

(a) $t = 0$ s (b) $t = 0.5$ s (c) $t = 1.0$ s (d) $t = 1.5$ s

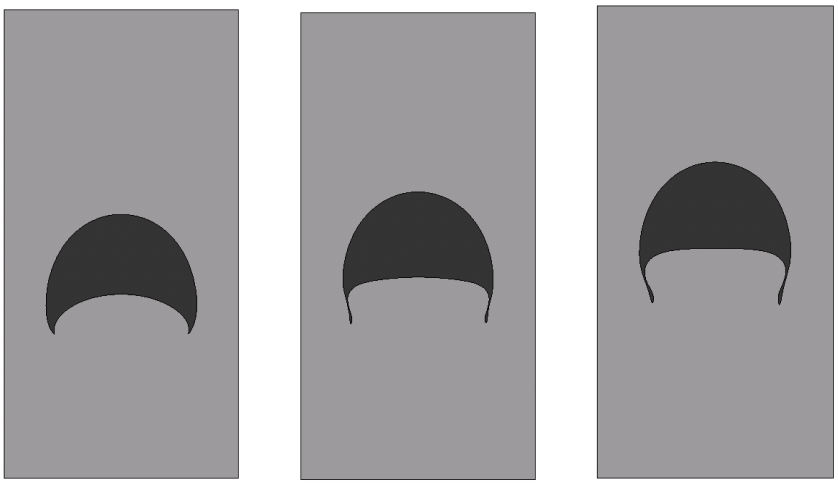

(e) $t = 2.0$ s (f) $t = 2.5$ s (g) $t = 3.0$ s

Figure 3.48: Test B. Bubble evolution for mesh size $h = 1/640$.

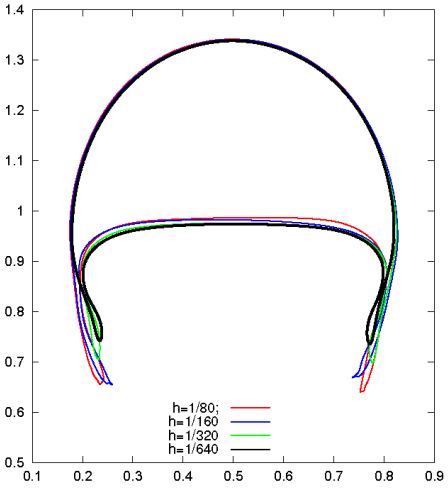

Figure 3.49: Test B. PFEM bubble shape for different mesh sizes at $t = 3$ s.

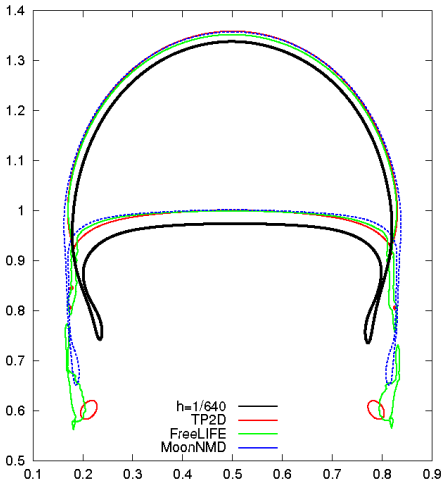

(a) Shape at $t = 3$ s

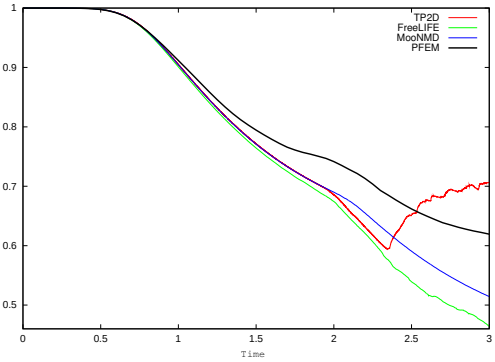

(b) Circularity

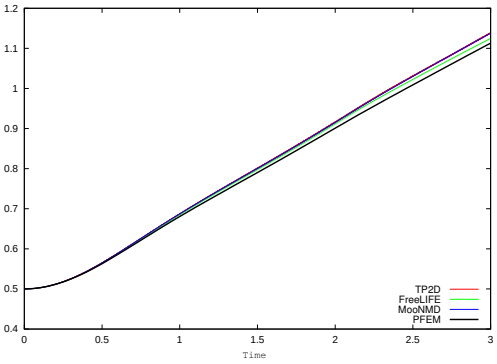

(c) Center of mass

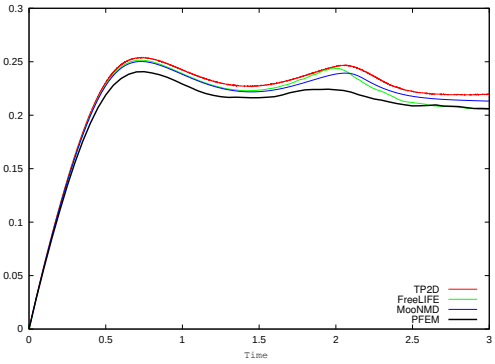

(d) Rise velocity

Figure 3.50: Test B. Benchmark quantities comparison of PFEM (black line) and TP2D (red), FreeLIFE (green) and MooNMD (blue) results.

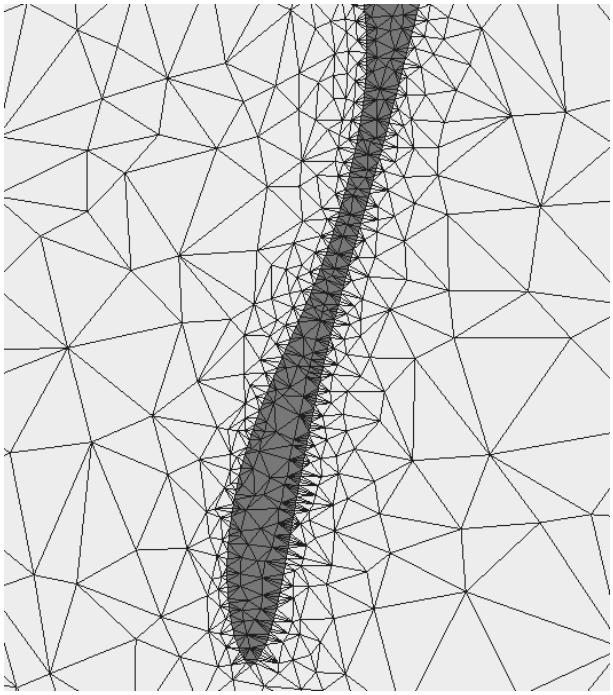

Figure 3.51: Test B. Detail of bubble skirt at $t = 3$ s.

3.8.3 Topology changes of the interface: bubble breakup and coalescence

Topology changes in multi-fluid flows can be divided into two classes (Tryggvason et al. [133]) (see Section 1.1):

- Films that fragment. If a bubble approaches another bubble or a flat surface, the fluid in between must be squeezed out before the bubbles are sufficiently close so that the film becomes unstable to attractive forces and fragment.
- Threads that break. A long and thin cylinder of fluid will generally break by the Plateau-Rayleigh instability in the region where the cylinder becomes sufficiently thin so that surface tension pinches it into two.

In order to test the capabilities of PFEM to handle interfaces with changing topology, and motivated by the disagreement in the solution of test B, we have simulated two examples on a film that fragments, namely the breakup and coalescence of bubbles.

We consider the same fluid properties and configuration of test A. In the case of the breakup, we add a flat interface at $y = 1$ so that the upper region belongs to the same fluid than the bubble (see Figure 3.52a). The bubble rises, approaching the flat interface. The film of heavy fluid that separates the two regions of light fluid becomes thinner and thinner until it fragments and the regions fuse (Figure 3.52). Whereas in the physical reality the fragmentation of the film is caused by attractive forces at the microscopic scale (forces which are usually not included in the continuum description), in our simulations fragmentation is caused by a connectivity change at the interface, as illustrated in Figure 3.53.

One of the main difficulties we face in our Lagrangian approach is the connectivity changes introduced by the remeshing process, which can modify the interface position (as seen in Section 3.3). In general, these connectivity changes alter the equilibrium at the interface, slow down convergence and may affect mass conservation. Thus, in interfacial flows it is essential to avoid them. We are using an unconstrained Delaunay triangulator which does not allow to fix connectivities. Therefore, to ensure that a specific connectivity remains, we refine long interfacial edges and remove nodes too close to the interface. Unfortunately, this strategy would preclude the possibility of breakup, as the interface could elongate endlessly. In the way PFEM defines interfaces, it is possible to have fluid regions spanned by just one element layer. The *breakup criterium* we have implemented in PFEM is to permit connectivity changes in elements where all nodes lie at the interface. In this way, a thin fluid thread can stop elongating and fragment. Breakup is then dependent on the mesh resolution, that is, it happens when the thickness of the film is similar to the mesh resolution of the interface. This is not a drawback

specific of PFEM, breakup is mesh dependent in front-capturing methods as well. For example, in the level set method, two interfaces are described as two different zero contours of the same level set function, and these interfaces will automatically merge once they get close enough, relative to the spatial resolution of the mesh where the level set function is defined (Tornberg [132]). The resolution determines the smallest distance between two zero level sets of the level set function for which they can still be distinguished as separate zero contours. Interfaces can in fact merge faster due to the diffusivity of the schemes used for advection and reinitialization of the level set function.

For the simulation of bubble coalescence, we consider the same rectangular domain $(0,1) \times (0,2)$ as before, with two circular bubbles inside. The center of the first bubble is $(0.5, 1.0)$ and its radius is equal to 0.25, the center of the second bubble is $(0.5, 0.5)$ and the radius 0.2. Since the small bubble is located close to the large one, this lower bubble turns out to be in the wake of the upper bubble and rises faster than that. Figure 3.54 shows the coalescence process. The mechanism is again the rupture of the thin film between the bubbles. This happens not during the impact of the bubbles (around $t = 2.5$ s) but during the separation after impact, as corresponds to the physical reality (Section 1.1).

We can conclude that PFEM solutions for the single rising bubble are in good agreement with those reported in Hysing et al. [65]. For test A, our bubble is slightly oscillating in contrast to the reference solution. A reason for this may be that PFEM does not introduce diffusion at the interface. In any case, more comparisons with other methods are needed. For test B, although PFEM can handle interface breakup without problems (as shown in the bubble breakup and coalescence examples), the skirt filaments remain intact. Breakup happens only when the fluid region is spanned by just one element layer. This allows to model thin films of thickness h, being h the mesh size at the interface. In both tests, we have achieved an excellent mass conservation without any correction.

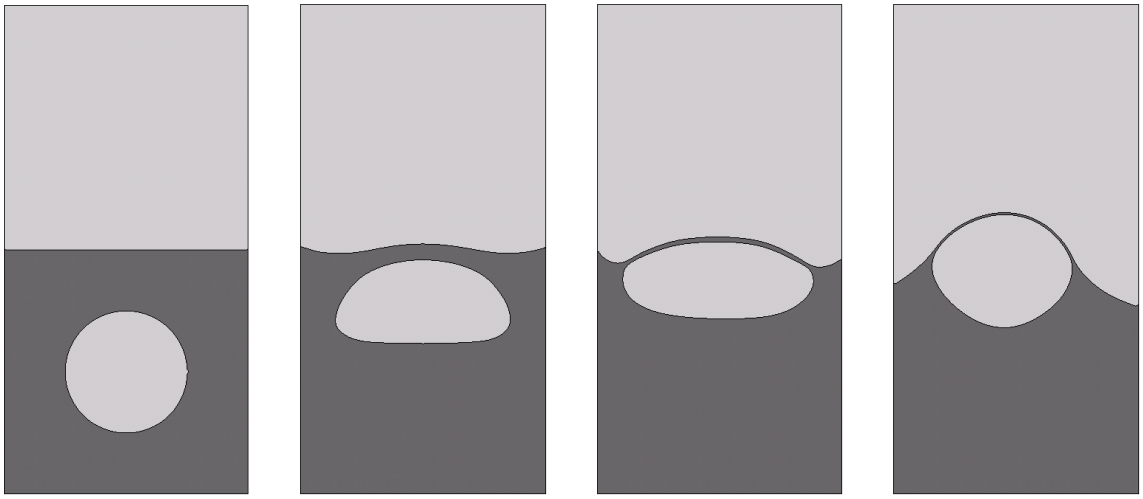

(a) $t = 0$ s (b) $t = 1.5$ s (c) $t = 2.5$ s (d) $t = 3.5$ s

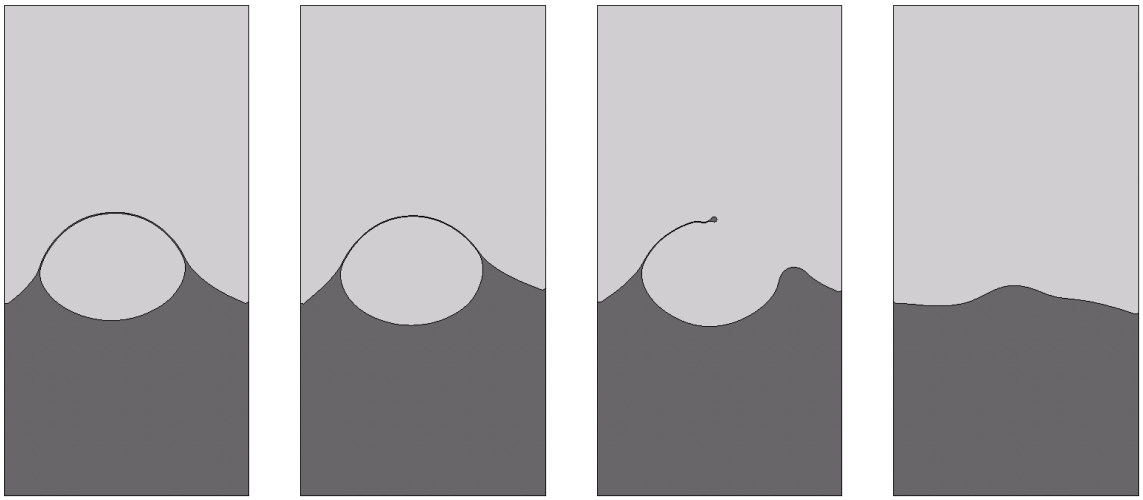

(e) $t = 4.5$ s (f) $t = 5.5$ s (g) $t = 6.0$ s (h) $t = 6.5$ s

Figure 3.52: Bubble breakup.

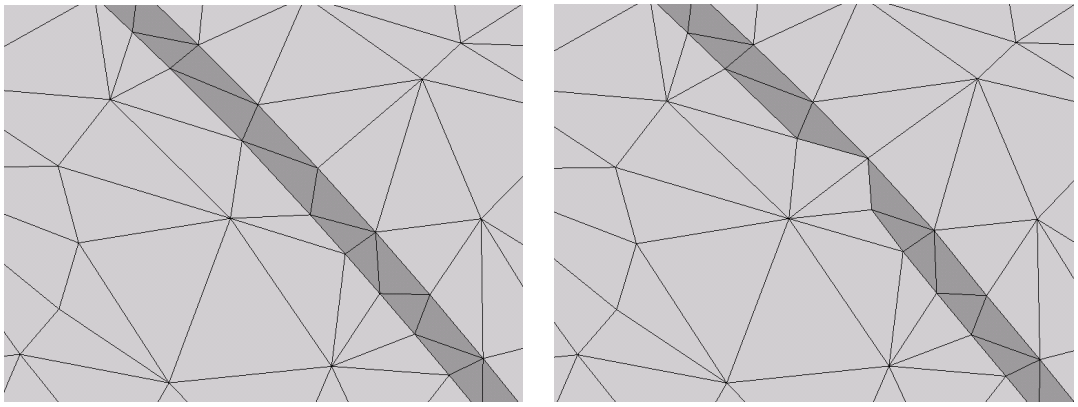

(a) t^n (b) t^{n+1}

Figure 3.53: Connectivity change that produces breakup at fluid films spanned by just one mesh element.

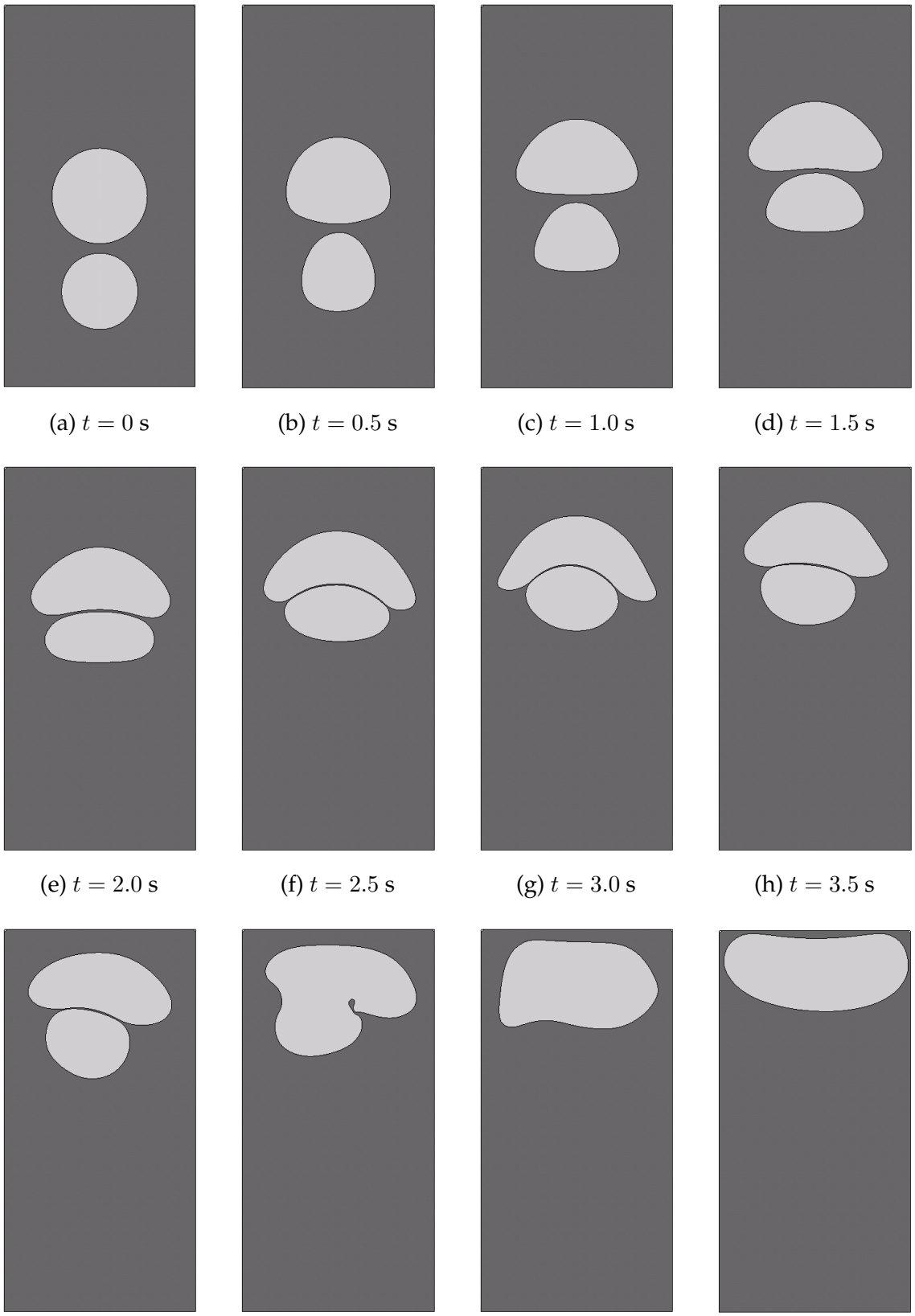

(a) $t = 0$ s (b) $t = 0.5$ s (c) $t = 1.0$ s (d) $t = 1.5$ s

(e) $t = 2.0$ s (f) $t = 2.5$ s (g) $t = 3.0$ s (h) $t = 3.5$ s

(i) $t = 4.0$ s (j) $t = 4.5$ s (k) $t = 5.0$ s (l) $t = 10.0$ s

Figure 3.54: Bubble coalescence.

3.9 Conclusions

In this chapter we have developed a numerical scheme for the simulation of laminar flows of Newtonian, incompressible multi-fluids subject to surface tension using the Particle Finite Element Method.

For immiscible fluids, the interface has been defined to be aligned with the moving mesh, so that it is described by nodes and element edges. In this way, the information about the location of the interface is readily available, and it is straightforward to impose boundary conditions on the interface and to model any number of fluids. The interface nodes carry the jump of the physical properties, maintaining the interface sharp without diffusion along time. The unconstrained Delaunay tesellation used in this work does not allow to fix the connectivities between nodes and therefore, edges describing the interface can swap during remeshing and modify the interface curve. This sudden changes in the interface, although they are localized, alter the equilibrium, slow down the convergence of the fluid solver and affect mass conservation. We have implemented a regeneration of the mesh close to the interface that avoids possible edge swappings and conserves exactly the interface.

The density jump at the interface leads to a weak discontinuity in the pressure variable which requires to work with the variable-density pressure Poisson equation (3.30a) and to model the pressure gradient π discontinuous in the stabilization method. The viscosity jump leads to a strong pressure discontinuity, a weak velocity discontinuity and requires to work with the full strain rate tensor $\boldsymbol{D}$, which couples all velocity components. The inclusion of the surface tension force leads again to a strong pressure discontinuity and requires to compute the interface curvature. In PFEM, weak discontinuities need no special attention, as the kinks in the solution are automatically represented when the interface is aligned with the mesh. The strong discontinuity in the pressure has been modeled by duplicating the pressure degrees of freedom at the interface, and the one in the pressure gradient has been taken into account in the stabilization term Eq. (3.51).

To make the scheme as efficient as possible, we employ a fully segregated solution approach. $\boldsymbol{u}$ has been decoupled from p through a fractional step scheme, and the term $\nabla^T \boldsymbol{u}$ of the strain rate tensor has been treated explicitly to avoid the coupling of the velocity components in the divergence form of the Navier-Stokes equations. A Picard iterative procedure has been used to linearize the trajectories equation and decouple $\boldsymbol{x}$ from $\boldsymbol{u}$. The Neumann boundary and interface conditions are also consistently split in the fractional step. The conditions in the momentum step (prescribed traction and surface tension) are naturally included in the variational form of the equations, whereas the conditions in the pressure step have been weakly imposed and are used to overcome the singularity

of $\boldsymbol{L}_{(1/\rho)}$.

To improve the resolution of the interface and the accuracy of the curvature calculation without compromising the efficiency, we have refined the mesh close to the interface using a distance function based on the medial-axis of the geometry.

Finally, we have run several two-dimensional examples to test the capabilities of the proposed scheme and shown the importance of using a discontinuous pressure field (at least at the interface level). Most of the contents of this chapter have been published in Idelsohn et al. [70, 69] and Mier-Torrecilla et al. [90].

References

[1] Anderson, D., and G. McFadden, 1998. Diffuse-interface methods in fluid mechanics. Annual Reviews of Fluid Mechanics 30, 139–165.

[2] Aubry, R., 2006. Three dimensional Lagrangian fluid flow with thermal coupling. Ph.D. thesis, Universitat Politècnica de Catalunya, Barcelona (Spain).

[3] Bänsch, E., 2001. Finite Element discretization of the Navier-Stokes equations with a free capillary surface. Numerische Mathematik 88, 203–235.

[4] Bell, and Marcus, 1992. A second order projection method for variable-density flows. Journal of Computational Physics 101, 334–348.

[5] Belytschko, T., N. Moës, S. Usui, and C. Parimi, 2001. Arbitrary discontinuities in finite elements. International Journal for Numerical Methods in Engineering 50, 993–1013.

[6] Bhaga, D., and M. Weber, 1981. Bubbles in viscous liquids: shapes, wakes and velocities. Journal of Fluid Mechanics 105, 61–85.

[7] Blum, H., 1967. Models for the Perception of Speech and Visual Form. M.I.T. Press, Ch. A Transformation for Extracting New Descriptors of Shape, pp. 362–379.

[8] Bonometti, T., and J. Magnaudet, 2007. An interface-capturing method for incompressible two-phase flows. Validation and application to bubble dynamics. International Journal of Multiphase Flow 33, 109–133.

[9] Brackbill, J., D. Kothe, and C. Zemach, 1992. A continuum method for modeling surface tension. Journal of Computational Physics 100, 335–354.

[10] Brezzi, F., and M. Fortin, 1991. Mixed and hybrid finite element methods. Springer Verlag.

[11] Brooks, A., and T. J. R. Hughes, 1982. Streamline upwind/Petrov-Galerkin formulations for convection dominated flows with particular emphasis on the incompressible Navier-Stokes equations. Computer Methods in Applied Mechanics and Engineering 32, 199–259.

[12] Bunner, B., and G. Tryggvason, 2002. Dynamics of homogeneous bubbly flows. Part 1. Rise velocity and microstructure of the bubbles. Journal of Fluid Mechanics 466, 17–52.

[13] Caboussat, A., 2005. Numerical simulation of two-phase free surface flows. Archives of Computational Methods in Engineering 12, 165–224.

[14] Cahn, J., and J. Hilliard, 1958. Free energy of a nonuniform system, I. Interfacial energy. Journal of Chemical Physics 28, 258.

[15] Calvo, N., 2005. Generación de mallas tridimensionales por métodos duales. Ph.D. thesis, Universidad Nacional del Litoral, Santa Fe (Argentina).

[16] Chella, R., and J. Viñals, Apr 1996. Mixing of a two-phase fluid by cavity flow. Physical Review E 53 (4), 3832–3840.

[17] Chen, L., S. Garimella, J. Reizes, and E. Leonardi, 1999. The development of a bubble rising in a viscous liquid. Journal of Fluid Mechanics 387, 61–96.

[18] Chen, T., P. Minev, and K. Nandakumar, 2004. A projection scheme for incompressible multiphase flow using adaptive Eulerian grid. International Journal for Numerical Methods in Fluids 45, 1–19.

[19] Chessa, J., and T. Belytschko, 2003. An enriched finite element method and level sets for axisymmetric two-phase flow with surface tension. International Journal for Numerical Methods in Engineering 58, 2041–2064.

[20] Chessa, J., and T. Belytschko, 2003. An extended finite element method for two-phase fluids. ASME Journal of Applied Mechanics 70, 10–17.

[21] Chorin, A., 1967. A numerical method for solving incompressible viscous flow problems. Journal of Computational Physics 2, 12–26.

[22] Chorin, A., 1968. Numerical solution of the Navier-Stokes equations. Mathematics of Computations 22, 745–762.

[23] Clift, R., J. Grace, and M. Weber, 1978. Bubbles, drops and particles. Academic Press.

[24] Codina, R., 2000. Stabilization of incompressibility and convection through orthogonal sub-scales in finite element methods. Computer Methods in Applied Mechanics and Engineering 190, 1579–1599.

[25] Codina, R., 2001. Pressure stability in fractional step finite element methods for incompressible flows. Journal of Computational Physics 170, 112–140.

[26] Codina, R., and J. Baiges, 2009. Approximate imposition of boundary conditions in immersed boundary methods. International Journal for Numerical Methods in Engineering 80, 1379–1405.

[27] Codina, R., and J. Blasco, 1997. A finite element formulation for the Stokes problem allowing equal velocity-pressure interpolation. Computer Methods in Applied Mechanics and Engineering 143, 373–391.

[28] Codina, R., and J. Blasco, 2000. Stabilized finite element method for the transient Navier-Stokes equations based on a pressure gradient projection. Computer Methods in Applied Mechanics and Engineering 182, 277–300.

[29] Codina, R., M. Vazquez, and O. Zienkiewicz, 1998. A general algorithm for compressible and incompressible flows. Part III: the semi-implicit form. International Journal for Numerical Methods in Fluids 27, 13–32.

[30] Coppola-Owen, A., and R. Codina, 2005. Improving Eulerian two-phase flow finite element approximation with discontinuous gradient pressure shape functions. International Journal for Numerical Methods in Fluids 49, 1287–1304.

[31] Cruchaga, M., D. Celentano, and T. Tezduyar, 2001. A moving Lagrangian interface technique for flow computations over fixed meshes. Computer Methods in Applied Mechanics and Engineering 191, 525–543.

[32] Daly, B., 1969. A technique for including surface tension effects in hydrodynamic calculations. Journal of Computational Physics 4, 97–117.

[33] Daly, B., and W. Pracht, 1968. Numerical study of density-current surges. Physics of Fluids 11, 15–30.

[34] de Sousa, F., N. Mangiavacchi, L. Nonato, A. Castelo, M. Tomé, V. Ferreira, J. Cuminato, and S. McKee, 2004. A front-tracking/front-capturing method for the simulation of 3D multi-fluid flows with free surfaces. Journal of Computational Physics 198, 469–499.

[35] Del Pin, F., 2003. The meshless finite element method applied to a lagrangian particle formulation of fluid flows. Ph.D. thesis, Universidad Nacional del Litoral, Santa Fe (Argentina).

[36] Del Pin, F., S. Idelsohn, E. Oñate, and R. Aubry, 2007. The ALE/Lagrangian Particle Finite Element Method: A new approach to computation of free-

surfaces flows and fluid-object interactions. Computers and Fluids 36 (1), 27–38.

[37] Esmaeeli, A., and G. Tryggvason, 1998. Direct numerical simulations of bubbly flows. Part 1. Low Reynolds number arrays. Journal of Fluid Mechanics 377, 313–345.

[38] Esmaeeli, A., and G. Tryggvason, 1999. Direct numerical simulations of bubbly flows. Part 2. Moderate Reynolds number arrays. Journal of Fluid Mechanics 385, 325–358.

[39] Floryan, J., and H. Rasmussen, 1989. Numerical methods for viscous flows with moving boundaries. Applied Mechanics Reviews 42, 323–337.

[40] Frank, X., D. Funfschilling, N. Midoux, and H. Z. Li, 2006. Bubbles in a viscous liquid: Lattice Boltzmann simulation and experimental validation. Journal of Fluid Mechanics 546, 113–122.

[41] Fyfe, D. E., E. S. Oran, and M. J. Fritts, 1988. Surface tension and viscosity with lagrangian hydrodynamics on a triangular mesh. Journal of Computational Physics 76 (2), 349–384.

[42] Galusinski, C., and P. Vigneaux, 2008. On stability condition for bifluid flows with surface tension: application to microfluidics. Journal of Computational Physics 227, 6140–6164.

[43] Ganesan, S., G. Matthies, and L. Tobiska, 2007. On spurious velocities in incompressible flow problem with interfaces. Computer Methods in Applied Mechanics and Engineering 196, 1193–1202.

[44] Glimm, J., O. McBryan, R. Menikoff, and D. Sharp, 1986. Front tracking applied to Rayleigh-Taylor instability. SIAM Journal on Scientific and Statistical Computing 7, 230–251.

[45] Grace, J. R., 1973. Shapes and velocities of bubbles rising in infinite liquids. Transactions of the Institution of Chemical Engineers 51, 116–120.

[46] Gresho, P. M., 1990. On the theory of semi-implicit projection methods for viscous incompressible flow and its implementation via a finite element method that also introduces a nearly consistent mass matrix. Part 1: Theory. International Journal for Numerical Methods in Fluids 11, 587–620.

[47] Gross, S., and A. Reusken., 2007. An extended pressure finite element space for two-phase incompressible flows with surface tension. Journal of Computational Physics 224, 40–58.

[48] Guermond, J.-L., and L. Quartapelle, 1998. On stability and convergence of projection methods based on pressure Poisson equation. International Journal for Numerical Methods in Fluids 26, 1039–1053.

[49] Guermond, J.-L., and L. Quartapelle, 2000. A projection FEM for variable density incompressible flows. Journal of Computational Physics 165, 167–188.

[50] Haberman, W. L., and R. K. Morton, 1954. An experimental study of bubbles moving in liquids. Proceedings of the American Society of Civil Engineers 387, 1–25.

[51] Harlow, F., 1964. The Particle-in-Cell computing method for fluid dynamics. Methods in Computational Physics 3, 313–343.

[52] Harlow, F., and J. Welch, 1965. Numerical calculation of time-dependent viscous incompressible flow of fluid with free surface. Physics of Fluids 8, 2182.

[53] Hayashi, M., K. Hatanaka, and M. Kawahara, 1991. Lagrangian finite element method for free surface Navier-Stokes flow using fractional step methods. International Journal for Numerical Methods in Fluids 13, 805–840.

[54] Hirt, C., A. Amsdem, and J. Cook, 1974. An Arbitrary Lagrangian-Eulerian computing method for all speeds. Journal of Computational Physics 14, 227–253.

[55] Hirt, C., J. Cook, and T. Butler, 1970. A Lagrangian method for calculating the dynamics of an incompressible fluid with free surface. Journal of Computational Physics 5, 103–124.

[56] Hirt, C., and B. Nichols, 1981. Volume of Fluid (VOF) method for the dynamics of free boundaries. Journal of Computational Physics 39, 201–225.

[57] Hnat, J. G., and J. D. Buckmaster, 1976. Spherical cap bubbles and skirt formation. Physics of Fluids 19, 182–194.

[58] Hua, J., and J. Lou, 2007. Numerical simulation of bubble rising in viscous liquid. Journal of Computational Physics 222, 769–795.

[59] Hughes, T., W. Liu, and T. Zimmermann, 1981. Lagrangian-Eulerian finite element element formulation for incompressible viscous flows. Computer Methods in Applied Mechanics and Engineering 29, 239–349.

[60] Hughes, T. J. R., 2000. The finite element method. Dover Publications.

[61] Hughes, T. J. R., L. Franca, and G. Hulbert, 1989. A new finite element formulation for computational fluid dynamics. VIII: The Galerkin/least-squares method for advective-diffusive equations. Computer Methods in Applied Mechanics and Engineering 73, 173–189.

[62] Hyman, J. M., 1984. Numerical methods for tracking interfaces. Physica D: Nonlinear Phenomena 12, 396–407.

[63] Hysing, S., 2006. A new implicit surface tension implementation for interfacial flows. International Journal for Numerical Methods in Fluids 51, 659–672.

[64] Hysing, S., 2007. Numerical Simulation of Immiscible Fluids with FEM Level Set Techniques. Ph.D. thesis, Dortmund university.

[65] Hysing, S., S. Turek, D. Kuzmin, N. Parolini, E. Burman, S. Ganesan, and L. Tobiska, 2009. Quantitative benchmark computations of two-dimensional bubble dynamics. International Journal for Numerical Methods in Fluids 60, 1259–1288.

[66] Idelsohn, S., N. Calvo, and E. Oñate, 2003. Polyhedrization of an arbitrary 3D point set. Computer Methods in Applied Mechanics and Engineering 192, 2649–2667.

[67] Idelsohn, S., F. Del Pin, R. Rossi, and E. Oñate, 2009. Fluid-structure interaction problems with strong added-mass effect. International Journal for Numerical Methods in Engineering 80, 1261–1294.

[68] Idelsohn, S., J. Marti, A. Limache, and E. Oñate, 2008. Unified Lagrangian formulation for elastic solids and incompressible fluids: Application to fluid-structure interaction problems via the PFEM. Computer Methods in Applied Mechanics and Engineering 197, 1762–1776.

[69] Idelsohn, S., M. Mier-Torrecilla, N. Nigro, and E. Oñate, 2009. On the analysis of heterogeneous fluids with jumps in the viscosity using a discontinuous pressure field. Computational Mechanics In press.

[70] Idelsohn, S., M. Mier-Torrecilla, and E. Oñate, 2009. Multi-fluid flows with the Particle Finite Element Method. Computer Methods in Applied Mechanics and Engineering 198, 2750–2767.

[71] Idelsohn, S., and E. Oñate, 2008. The challenge of mass conservation in the solution of free-surface flows with the fractional-step method: Problems and solutions. Communications in Numerical Methods in Engineering.

[72] Idelsohn, S., E. Oñate, N. Calvo, and F. Del Pin, 2003. The meshless finite element method. International Journal for Numerical Methods in Engineering 58 (6), 893–912.

[73] Idelsohn, S., E. Oñate, and F. Del Pin, 2003. A Lagrangian meshless finite element method applied to fluid-structure interaction problems. Computers and Structures 81 (8–11), 655–671.

[74] Idelsohn, S., E. Oñate, and F. Del Pin, 2004. The Particle Finite Element Method: A powerful tool to solve incompressible flows with free-surfaces and breaking waves. International Journal for Numerical Methods in Engineering 61 (7), 964–989.

[75] Idelsohn, S., M. Storti, and E. Oñate, 2001. Lagrangian formulations to solve free surface incompressible inviscid fluid flows. Computer Methods in Applied Mechanics and Engineering 191 (6–7), 583–593.

[76] Ishii, M., 1975. Thermo-fluid dynamic theory of two-phase flow. Eyrolles.

[77] Juntunen, M., and R. Stenberg, 2007. Nitsche's method for general boundary conditions. Tech. rep., Research Reports A530, University of Technology, Institute of Mathematics.

[78] Kim, J., and P. Moin, 1985. Application of a fractional-step method to incompressible Navier-Stokes equations. Journal of Computational Physics 59, 308–323.

[79] Kondo, M., S. Koshizuka, K. Suzuki, and M. Takimoto, 2007. Surface tension model using inter-particle force in particle method. In: 5th Joint ASME/JSME Fluids Engineering Summer Conference. pp. 93–98.

[80] Korteweg, D., 1901. Sur la forme que prennent les equations du mouvements des fluides si l'on tient compte des forces capillaires causees par des variations de densite considerables mais continues et sur la theorie de la capillarite dans l'hypothese d'une variation continue de la densite. Arch. Neerl. Sci. Exactes Nat. Ser. II 6, 1–24.

[81] Kurtoglu, I. O., and C. L. Lin, 2006. Lattice boltzmann study of bubble dynamics. Numerical Heat Transfer B 50, 333–351.

[82] Ladyzhenskaya, O., 1969. The mathematical theory of viscous incompressible flow. Gordon and Breach.

[83] Lafaurie, B., C. Nardone, R. Scardovelli, S. Zaleski, and G. Zanetti, 1994. Modelling merging and fragmentation in multiphase flows with SURFER. Journal of Computational Physics 113, 134–147.

[84] Li, Z., and S. Lubkin, 2001. Numerical analysis of interfacial two-dimensional Stokes flow with discontinuous viscosity and variable surface tension. International Journal for Numerical Methods in Fluids 37, 525–540.

[85] Limache, A., S. Idelsohn, R. Rossi, and E. Oñate, 2007. The violation of objectivity in Laplace formulations of the Navier-Stokes equation. International Journal for Numerical Methods in Fluid 54, 639–664.

[86] Limache, A., P. Sanchez, L. Dalcin, and S. Idelsohn, 2008. Objectivity tests for the Navier-Stokes equations: the revealing of non-physical solutions produced by Laplace formulations. Computer Methods in Applied Mechanics and Engineering 197, 4180–4192.

[87] Liu, J., S. Koshizuka, and Y. Oka, 2005. A hybrid particle-mesh method for viscous, incompressible, multiphase flows. Journal of Computational Physics 202, 65–93.

[88] Marchandise, E., P. Geuzaine, N. Chevaugeon, and J.-F. Remacle, 2007. A stabilized finite element method using a discontinuous level set approach for the computation of bubble dynamics. Journal of Computational Physics 225, 949–974.

[89] Maxworthy, T., C. Gnann, M. Kuerten, and F. Durst, 1996. Experiments on the rise of air bubbles in clean viscous liquids. Journal of Fluid Mechanics 321, 421–441.

[90] Mier-Torrecilla, M., S. Idelsohn, and E. Oñate, 2010. A pressure segregation method for the Lagrangian simulation of interfacial flows. To be submitted to International Journal for Numerical Methods in Fluids.

[91] Minev, P., T. Chen, and K. Nandakumar, 2003. A finite element technique for multifluid incompressible flow using eulerian grids. Journal of Computational Physics 187, 255–273.

[92] Moës, N., J. Dolbow, and T. Belytschko, 1999. A finite element method for crack growth without remeshing. International Journal for Numerical Methods in Engineering 46, 131–150.

[93] Moore, D., 1959. The rise of a gas bubble in viscous liquid. Journal of Fluid Mechanics 6, 113–130.

[94] Morris, J.-P., 2000. Simulating surface tension with smoothed particle hydrodynamics. International Journal for Numerical Methods in Fluids 33, 333–353.

[95] Nadiga, B., and S. Zaleski, 1996. Investigations of a two-phase fluid model. European Journal of Mechanics B 15, 885–896.

[96] Nitsche, J., 1971. Über ein Variationsprinzip zur Lösung von Dirichlet-Problemen bei Verwendung von Teilräumen, die keinen Randbedingungen unterworfen sind. Abh. Math. Univ. Hamburg 36, 9–15.

[97] Noh, W., and P. Woodward, 1976. Lecture Notes in Physics. Vol. 59. Springer Verlag, Ch. SLIC (Simple Line Interface Calculations), p. 330.

[98] Nomura, K., S. Koshizuka, and Y. Oka, 2001. Numerical analysis of droplet breakup behavior using particle method. Journal of Nuclear Science and Technology 38, 1057–1064.

[99] Nugent, S., and H. A. Posch, 2000. Liquid drops and surface tension with smoothed particle applied mechanics. Physical Review E 62, 4968–4975.

[100] Oñate, E., 1998. Derivation of stabilized equations for numerical solution of advective-difusive transport and fluid flow problems. Computer Methods in Applied Mechanics and Engineering 151, 233–265.

[101] Oñate, E., 2000. A stabilized finite element method for incompressible viscous flows using a finite increment calculus formulation. Computer Methods in Applied Mechanics and Engineering 182, 355–370.

[102] Oñate, E., 2004. Possibilities of finite calculus in computational mechanics. International Journal for Numerical Methods in Engineering 60, 255–281.

[103] Oñate, E., S. Idelsohn, F. Del Pin, and R. Aubry, 2004. The Particle Finite Element Method: An Overview. International Journal of Computational Methods 1 (2), 267–307.

[104] Oran, E., and J. Boris, 1987. Numerical simulation of reactive flow. Elsevier.

[105] Osher, S., and J. Sethian, 1988. Fronts propagating with curvature dependant speed: algorithms based on Hamilton-Jacobi formulations. Journal of Computational Physics 79, 12–49.

[106] Parolini, N., and E. Burman, 2005. A finite element level set method for viscous free-surface flows. In: 7th Conference on Applied and Industrial Mathematics in Italy. pp. 416–427.

[107] Peskin, C., 1977. Numerical analysis of blood flow in the heart. Journal of Computational Physics 25, 220–252.

[108] Popinet, S., and S. Zaleski, 1999. A front tracking algorithm for accurate representation of surface tension. International Journal for Numerical Methods in Fluids 30, 775–793.

[109] Puckett, E., A. Almgren, J. Bell, D. Marcus, and W. Rider, 1997. A high-order projection method for tracking fluid interfaces in variable density incompressible flows. Journal of Computational Physics 130, 269–282.

[110] Quartapelle, L., 1993. Numerical solution of the incompressible Navier-Stokes equations. Birkhäuser.

[111] Ramaswamy, B., and M. Kawahara, 1986. Arbitrary Lagrangian-Eulerian finite element method for the analysis of free surface fluid flows. Computational Mechanics 1, 103–108.

[112] Ramaswamy, B., and M. Kawahara, 1987. Lagrangian finite element analysis applied to viscous free surface fluid flow. International Journal for Numerical Methods in Fluids 7, 953–984.

[113] Raymond, F., and J. Rosant, 2000. A numerical and experimental study of the terminal velocity and shape of bubbles in viscous liquids. Chemical Engineering Science 55, 943–955.

[114] Richards, J., 1994. Fluid mechanics of liquid-liquid systems. Ph.D. thesis, University of Delaware.

[115] Rudman, M., 1997. Volume tracking methods for interfacial flow calculations. International Journal for Numerical Methods in Fluids 24, 671–691.

[116] Ryskin, G., and L. G. Leal, 1984. Numerical solution of free-boundary problems in fluid mechanics. Part 2. Buoyancy-driven motion of a gas bubble through a quiescent liquid. Journal of Fluid Mechanics 148, 19–35.

[117] Scardovelli, R., and S. Zaleski, 1999. Direct Numerical Simulation of free-surface and interfacial flow. Annual Reviews of Fluid Mechanics 31, 567–603.

[118] Sethian, J., 1996. Level Set Methods. Cambridge University Press.

[119] Sethian, J., and P. Smereka, 2003. Level set methods for fluid interfaces. Annual Reviews of Fluid Mechanics 35, 341–372.

[120] Shewchuk, J., 2003. Triangle: A Two-Dimensional Quality Mesh Generator and Delaunay Triangulator.
URL `http://www-2.cs.cmu.edu/~quake/triangle.html`

[121] Shyy, W., 1996. Computational Fluid Dynamics with moving boundaries. Taylor&Francis.

[122] Si, H., 2002. TetGen: Tetrahedral Mesh Generator and 3D Delaunay Triangulator.
URL http://tetgen.berlios.de

[123] Smolianski, A., 2001. Numerical modeling of two fluid interfacial flows. Ph.D. thesis, University of Jyväskylä, Finnland.

[124] Smolianski, A., 2005. Finite-Element/Level-Set/Operator-Splitting (FELSOS) approach for computing two-fluid unsteady flows with free moving interfaces. International Journal for Numerical Methods in Fluids 48, 231–269.

[125] Stone, H., 1994. Dynamics of drop deformation and breakup in viscous fluids. Annual Reviews of Fluid Mechanics 26, 65–102.

[126] Sussman, M., P. Smereka, and S. Osher, 1994. A level set approach for computing solutions to incompressible two-phase flows. Journal of Computational Physics 114, 146–159.

[127] Szabo, P., and O. Hassager, 1995. Simulation of free surfaces in 3-D with the arbitrary Lagrange-Euler method. International Journal for Numerical Methods in Engineering 38, 717–734.

[128] Temam, R., 1969. Sur l'approximation de la solution des equations de Navier-Stokes par la mithode des pas fractionaires (I). Arch. Rat. Mech. Anal. 32, 135–153.

[129] Tezduyar, T., 2001. Finite element methods for flow problems with moving boundaries and interfaces. Archives of Computational Methods in Engineering 8, 83–130.

[130] Tezduyar, T., M. Behr, and J. Liou, 1992. A new strategy for finite element computations involving moving boundaries and interfaces. The deforming-spatial-domain/space-time procedure: I. The concept and preliminary numerical tests. Computer Methods in Applied Mechanics and Engineering 94, 339–351.

[131] Tezduyar, T., M. Behr, S. Mittal, and J. Liou, 1992. A new strategy for finite element computations involving moving boundaries and interfaces. The deforming-spatial-domain/space-time procedure: II. Computation of free-surface flows, two-liquid flows and flows with drifting cylinders. Computer Methods in Applied Mechanics and Engineering 94, 353–371.

[132] Tornberg, A.-K., 2000. Interface tracking methods with application to multiphase flows. Ph.D. thesis, Royal Institute of Technology, Stockholm.

[133] Tryggvason, G., B. Bunner, A. Esmaeeli, D. Juric, N. Al-Rawahi, W. Tauber, J. Han, S. Nas, and Y.-J. Jan, 2001. A front-tracking method for the computations of multiphase flow. Journal of Computational Physics 169, 708–759.

[134] Turek, S., 1998. Efficient Solvers for Incompressible Flow Problems. Springer.

[135] Unverdi, S., and G. Tryggvason, 1992. Computations of multi-fluid flows. Physica D: Nonlinear Phenomena 60, 70–83.

[136] Unverdi, S., and G. Tryggvason, 1992. A front-tracking method for viscous, incompressible, multi-fluid flows. Journal of Computational Physics 100, 25–37.

[137] van der Waals, J., 1893. The thermodynamic theory of capillarity under the hypothesis of a continuous density variation. Journal of Statistical Physics 20, 197–244.

[138] van Kan, J., 1986. A second-order accurate pressure correction scheme for viscous incompressible flow. SIAM Journal on Scientific and Statistical Computing 7, 870–891.

[139] Van Sint Annaland, M., N. G. Deen, and J. A. M. Kuipers, 2005. Numerical simulation of gas bubbles behavior using a three-dimensional volume of fluid method. Chemical Engineering Science 60, 2999–3011.

[140] Wu, J., S.-T. Yu, and B.-N. Jiang, 1998. Simulation of two-fluid flows by the Least-Squares finite element method using a continuum surface tension model. International Journal for Numerical Methods in Engineering 42, 583–600.

[141] Wu, M., and M. Gharib, 2002. Experimental studies on the shape and path of small air bubbles rising in clean water. Physics of Fluids 14, 49–52.

[142] Yu, Z., and L.-S. Fan, 2008. Direct simulation of the buoyant rise of bubbles in infinite liquid using level set method. Canadian Journal of Chemical Engineering 86, 267–275.

[143] Zhou, G., W. Ge, and J. Li, 2008. A revised surface tension model for macro-scale particle methods. Powder Technology 183, 21–26.

[144] Zienkiewicz, O., and R. Taylor, 2005. The Finite Element Method, 6th Edition. Vol. 3, Fluid Mechanics. Butterworth-Heinemann.

Chapter 4

Geological applications

Geological processes like tectonic plate subduction, mantle convection or magma chamber dynamics involve a large variety of materials and phases (Hamblin [42]). Most of these processes are not directly observable, and although they can be experimentally investigated using analogue systems, it is in general not possible to quantitatively extrapolate the results to the natural reality. Therefore, the numerical modeling of heterogeneous flows is necessary for understanding these processes and their flow dynamics, which is mainly driven by gravitational instabilities caused by gradients in the physical properties due to composition, temperature or pressure.

In this chapter we have applied the Particle Finite Element Method to geological problems, and compared our numerical results with field observations and experimental data. We have simulated two magmatic processes that occur in the Earth's interior with the goal of quantifying the extent of mixing, and finally, we have solved a common geological flow, the negatively buoyant jet, which is closely related to magma chambers.

The first example is a simplified overturn problem (a dense layer over a lighter one) where temperature and composition of the fluids are assumed constant. The flow is driven by Rayleigh-Taylor instabilities and the evolution of the interface is analyzed. This example is followed by the problem of thermo-chemical mixing inside a magma chamber. Here the full variation of the physical properties as a function of temperature and composition is taken into account. Thermal effects are modeled with the Boussinesq approximation, although other more general approaches are also mentioned and briefly explained. In this second example we consider realistic magma chamber sizes and fluid properties from the San Pedro volcano (Chilean Andes), and study the influence of the initial configuration on the mixing achieved. The numerical results are compared with field data and allow to gain some insight on the temporal evolution of mixing. We finish the chapter with the negatively buoyant jet example. It consists in an upward injection of a

heavy fluid into a lighter one, and occurs e.g. in replenishing magma chambers or underwater eruptions. The numerical results are compared with experiments performed specifically to verify the computations.

4.1 Internal magmatic processes

Magma is produced by melting of rocks in the Earth's mantle or crust. It typically consists of three phases: 1. viscous melt (liquid); 2. a variable proportion of crystals (solid); and 3. volatiles (gas). The melt is composed mainly by SiO_2, Al_2O_3, MgO, CaO, Na_2O and K_2O. Volatiles (H_2O, CO_2, SO_2, F_2, S_2, etc) can be dissolved in the melt or exsolved in form of bubbles if the pressure is low enough.

There are several mechanisms that lead to magma formation. One of them is convection in the mantle and plume generation. The rising mantle plume partially melts due to the pressure reduction, and the resulting low-density fluid constitutes a buoyant diapir rising through the surrounding mantle rocks (Marsh [64]) (see Fig. 4.1). Diapirs cease to rise when they reach a region where the rock density is similar to that of the diapir, or when the increasing viscosity of the surrounding rocks stall its ascent. In this latter case, the melt within the diapir may create large fractures called dikes through which melt moves much more efficiently (Rubin [90]). When magma cannot find a path upwards, what commonly happens at the base of the crust, it starts to accumulate, forming magma reservoirs. Once there, it may cool by loosing heat through the walls of the reservoir. The components with a higher melting point will crystallize and form a denser conglomerate that sinks. During this chemical evolution the melt becomes richer in silica SiO_2 (Sparks et al. [95]).

Thus, magma chambers are reservoirs of molten rock lying under the Earth's surface. As more batches of magma arrive, the pressure grows inside the chamber. Pressure can gradually fracture the rock around it (called host rock) and create outlets. When magma finds a way to the surface, the result will be a volcanic eruption. Pressure is also greatly influenced by the convection dynamics inside the chamber due to thermal and compositional gradients. Convection will affect the cooling rate, volatile exsolution and the extent of magma mixing. All these influences on the evolving magma composition lead to variations in rheology that may determine the characteristics of the eruption (Marti & Folch [66]). In this work we have not considered volatile exsolution, which would lead to gas bubbles formation and a slightly compressibility of the magma. Fluids are always treated as incompressible and therefore we have not taken into account pressure variation in the physical properties. Neither we have consider surface tension between magmas, as there is not any data available for the γ coefficient (Philpotts [83], Roedder [89], Veksler et al. [109], Valentini & Moore [108]). An overview of

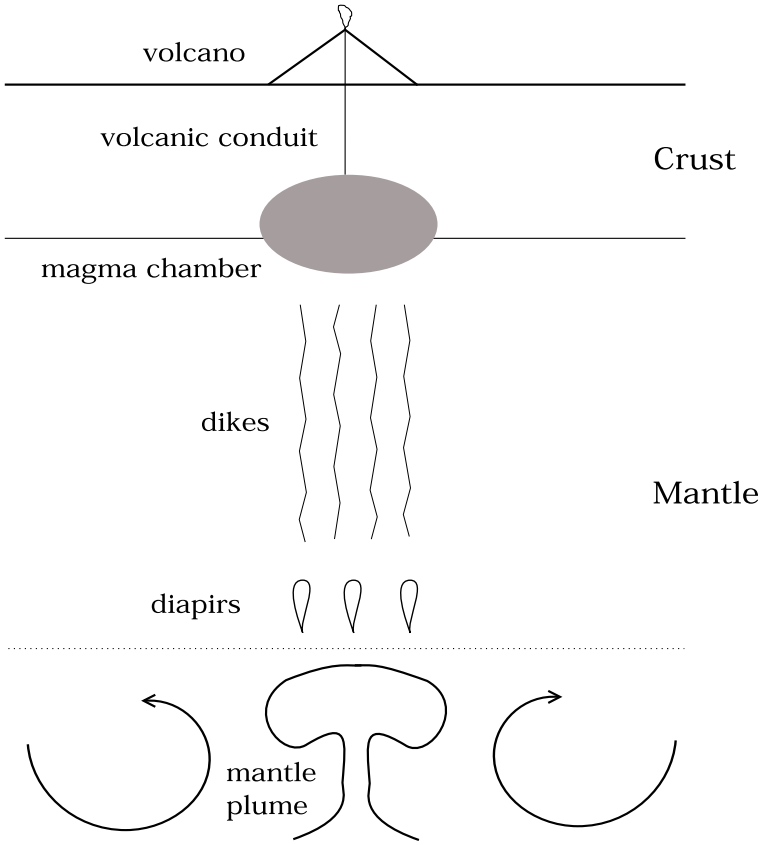

Figure 4.1: Stages from magma genesis to eruption: 1. Magma generation by partial melting of rock in the mantle, 2. Ascent in form of diapirs and dikes, 3. Storage in a reservoir, 4. Possible eruption (Marsh [64], Parfitt & Wilson [79])

further volcanic processes can be found in Houghton et al. [44] and Dobran [30].

Depending on the content in silica there are different types of magmas with different physical properties. Those with large amount of SiO_2 are called *silicic* magmas and are more viscous and lighter than those with smaller amount of SiO_2, called *mafic* magmas (see Figure 4.2). Because the chemical evolution increases the SiO_2 content, mafic magmas (typically at a temperature of 1000-1200 $°C$) transform into silicic ones (800-900 $°C$) over time.

The physical properties and flow styles of silicate melts control a large range of magmatic processes: from melt segregation and transport, through storage and differentiation in crustal magma reservoirs, to the emplacement of pyroclastic flows on the Earth's surface. To understand these processes it requires observations and measurements of the natural objects, but also a good knowledge of the high temperature and pressure physical properties silicate melts, and robust theoretical models. A major advance in the understanding of the fluid dynamics in magma reservoirs was gained in the 90's by a series of experiments using low temperature

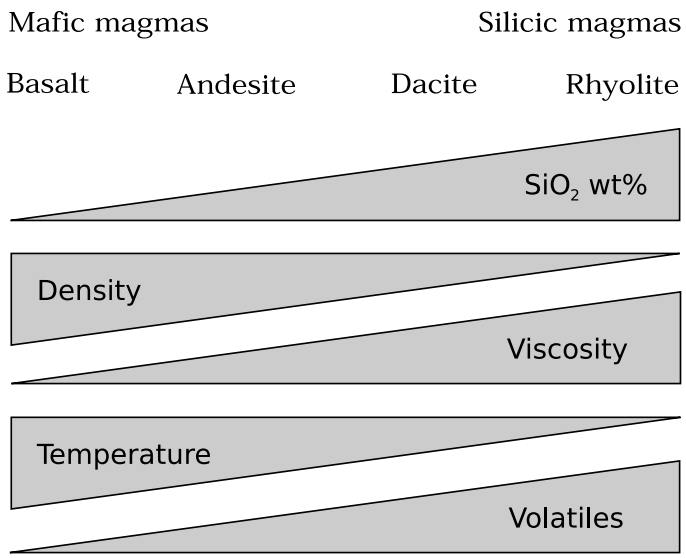

Figure 4.2: Magmas classification by SiO_2 content (in weight percent, wt%). Influence of the composition on the physical properties of magmas.

analogue materials (e.g. Sparks et al. [95], Turner & Campbell [104]). These experiments illustrated the likely fluid dynamic scenarios and identified the role of the different variables. They were combined in some cases with theoretical analysis and used to predict the results of various magma mixing and differentiation possibilities (e.g. [104]).

Numerical modeling of the fluid dynamics of magmatic processes remains challenging nowadays (e.g. Valentine et al. [107]). Many processes involve large ranges of time (e.g. seconds to thousands of years) and space (e.g. micrometers to kilometers), the physical properties depend non-linearly on temperature and composition, and the set of governing equations are coupled, and also non-linear. In addition, magmas are commonly multiphase mixtures of melt, crystals, and bubbles. Due to this complexity most studies have used a set of dimensionless numbers or parameterized equations to characterize flow styles and obtain conclusions of general validity (e.g. Bergantz [11], Jaupart & Tait [46]).

4.2 Characterization of mixing

In most cases, geological flows lead to some kind of mixing between different fluids. The term *mixing* is generally applied to processes which tend to reduce the heterogeneities or gradients in composition, temperature or any other physical property (Uhl & Gray [106], Nagata [72]). Ottino [75] defines mixing as the efficient stretching and folding of material lines and surfaces. Its result is the reduction of length scales (thinning of material volumes and dispersion throughout the space,

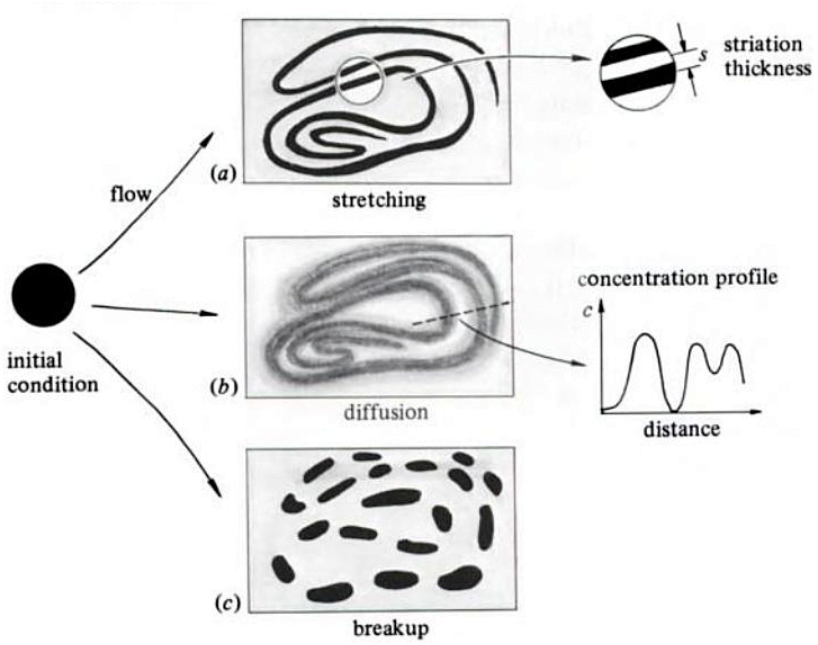

Figure 4.3: Basic processes occurring during mixing of fluids (from Ottino [75]): (a) two fluids with negligible interfacial tension and negligible diffusion; the material region stretches and folds by the action of the flow; (b) a fluid diffusing in another fluid; boundaries become diffuse and the extent of mixing is given by level curves of concentration; (c) the fluid breaks due to interfacial tension forces producing smaller fragments which might stretch and break producing smaller fragments. In (a) and (b) the interface is passive, in (c) it is active.

possibly involving breakup), and in the case of miscible fluids, uniformity of concentration.

The basic processes occurring during mixing of fluids (stretching, diffusion and breakup) are illustrated in Fig. 4.3. Any material region stretches and folds by the action of the flow (Fig. 4.3a). If chemical diffusion is not negligible, the sharp interface between the two fluids becomes progressively diffuse and the extent of mixing of the two fluids has to be characterized not only by the interface stretching but by the spreading of the concentration profile as well (Fig. 4.3b). In the case of fluids with similar properties and no interfacial tension, the interface is called *passive* (Aref & Tryggvason [2]). If the fluids are immiscible, at some point in the mixing process the striations do not remain connected and break into smaller fragments (see Fig. 4.3c). At these length scales, surface tension effects become dominant and the interface, instead of being passively convected, modifies the surrounding flow, making the analysis more complicated. The interface is then called *active*.

The type of flow is determinant for the efficiency of mixing. Turbulence is

Figure 4.4: Magma mingling in a plutonic rock. Picture taken at the Costa Brava.

the most efficient mixing mechanism, as the presence in the flow of numerous vortices of a wide range of sizes will rapidly result in the reduction of the existing heterogeneities. If the viscosity is so high that turbulence is not possible, mixing can also be achieved under laminar flow conditions (Byrde [18]). In the absence of turbulence and chemical diffusion, laminar mixing consists of stretching and folding of a fluid material. Stretching results from high shear regions in the flow. The combined action of two shear flows with different stretching directions generally results in the folding of the fluid material. All different stretching directions associated with each vortex cause a continuous reorientation of the flow, and this produces exponential area growth of the interface (Ottino [75]).

In the context of magmatic systems, the mixing processes are termed *blending* and *mingling*:

- Blending (diffusion) involves the chemical mixing of two or more different magmas, forming a homogeneous mixture of an intermediate composition.
- Mingling (stretching and folding) involves the mechanical mixing of different magmas, and produces a heterogeneous mixture containing discrete portions of the end-members (Figure 4.4).

The small chemical diffusivities of magma components (of order $\mathcal{O}(10^{-6})$ $m^2\ s^{-1}$ or smaller) prevent diffusion-related mixing from being a significant process until the sizes of heterogeneities have been reduced to a diffusive scale (typically of order 1 m) through the action of convective deformation (Oldenburg et al. [73]). Therefore, mixing occurs when convection leads to large-volume entrainment of one fluid into the other, exchange of momentum and large-scale circulation (Jellinek et al. [47]), as illustrated in Figure 4.5. In the case of replenishing magma chambers, Campbell & Turner [19] concluded that mixing only happens if the jet of injected fluid has sufficient momentum to penetrate and engulf the resident magma.

During mixing, magmas record in their crystals the mixing phenomenon

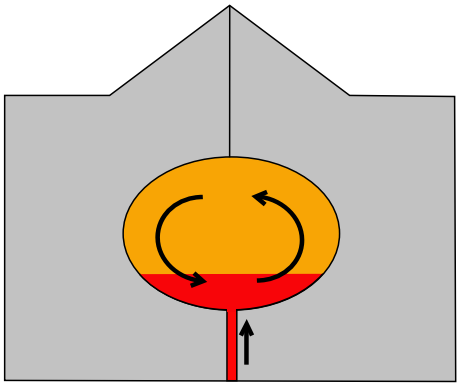

Figure 4.5: Magma mixing during storage in the chamber.

as well as the original environment previous to mixing. It is then possible to reconstruct the conditions of temperature, pressure, composition and volatile content of melts in the reservoir before eruption (Anderson [1]).

4.3 Thermal models

Most geological processes involve thermal gradients and variations of the physical properties due to temperature. The pioneering studies in convection of fluids (Bénard [10], Boussinesq [15], Rayleigh [87]) came to the conclusion that the thermodynamic properties of incompressible fluids can be assumed constant except when considering the body force $\rho \boldsymbol{g}$ in the momentum equation (Turner [103], Tritton [101], Dobran [30]). This assumption, together with a linear variation of the density as a function of temperature T in the body force,

$$\rho = \rho_0[1 - \alpha(T - T_0)], \tag{4.1}$$

is called the *Boussinesq approximation*:

$$\boldsymbol{\nabla} \cdot \boldsymbol{u} = 0 \tag{4.2a}$$

$$\rho_0 \frac{\mathrm{d}\boldsymbol{u}}{\mathrm{d}t} = -\boldsymbol{\nabla} p + \boldsymbol{\nabla} \cdot \mu(\boldsymbol{\nabla}\boldsymbol{u} + \boldsymbol{\nabla}^T \boldsymbol{u}) + \rho_0[1 - \alpha(T - T_0)]\boldsymbol{g} \tag{4.2b}$$

$$\rho_0 C_p \frac{\mathrm{d}T}{\mathrm{d}t} = \boldsymbol{\nabla} \cdot (k \boldsymbol{\nabla} T) \tag{4.2c}$$

with k the thermal diffusion coefficient, C_p the specific heat at constant pressure, α the thermal expansion coefficient, T_0 a reference temperature, and $\rho_0 = \rho(T_0)$.

This approximation is only valid for small density changes relative to the reference density. Gray & Giorgini [40] state that allowed temperature difference must satisfy $\alpha \, \Delta T < 0.1$. For example in the case of air, $\Delta T < 28.6\ ^\circ\mathrm{C}$. The Boussinesq approximation should then be applied with caution. In practice, the

condition that all fluid properties are constant except in the gravity term is relaxed for properties other than density, allowing e.g. variable viscosity, thermal and chemical diffusivities. Although we have used the Boussinesq approximation in Section 4.5, it is also worth to mention other more general models that could be implemented in the future.

The natural way to take into account the expansion and compression in the fluid due to temperature changes is through the *compressible Navier-Stokes equations (cNS)*. They are usually written in conservative form (Oran & Boris [74]):

$$\frac{\partial \rho}{\partial t} = -\boldsymbol{\nabla} \cdot (\rho \boldsymbol{u}) \tag{4.3a}$$

$$\frac{\partial \rho \boldsymbol{u}}{\partial t} = -\boldsymbol{\nabla} \cdot (\rho \boldsymbol{u}\boldsymbol{u}) + \boldsymbol{\nabla} \cdot \boldsymbol{\sigma} + \rho \boldsymbol{g} \tag{4.3b}$$

$$\frac{\partial E}{\partial t} = -\boldsymbol{\nabla} \cdot (E \boldsymbol{u}) + \boldsymbol{\nabla} \cdot (\boldsymbol{\sigma} \boldsymbol{u}) - \boldsymbol{\nabla} \cdot \boldsymbol{q} + Q \tag{4.3c}$$

where $\boldsymbol{\sigma} = -p\boldsymbol{I} + \mu \left(\boldsymbol{\nabla}\boldsymbol{u} + \boldsymbol{\nabla}^T \boldsymbol{u} - \frac{2}{3}(\boldsymbol{\nabla} \cdot \boldsymbol{u})\boldsymbol{I} \right)$ is the stress tensor, $E = \rho e + \frac{1}{2}\rho \boldsymbol{u}^2$ the total energy (sum of internal energy e and kinetic energy) and $\boldsymbol{q} = -k\boldsymbol{\nabla}T$ the heat flux. This system has five equations for six unknowns, and therefore requires an equation of state $\rho = \rho(p, T)$ to be closed.

In Lagrangian formulation, the cNS equations (4.3) read:

$$\frac{\mathrm{d}\rho}{\mathrm{d}t} = -\rho \boldsymbol{\nabla} \cdot \boldsymbol{u} \tag{4.4a}$$

$$\rho \frac{\mathrm{d}\boldsymbol{u}}{\mathrm{d}t} = \boldsymbol{\nabla} \cdot \boldsymbol{\sigma} + \rho \boldsymbol{g} \tag{4.4b}$$

$$\rho \frac{\mathrm{d}}{\mathrm{d}t}(e + \frac{1}{2}\boldsymbol{u}^2) = \boldsymbol{\nabla} \cdot (\boldsymbol{\sigma} \boldsymbol{u}) - \boldsymbol{\nabla} \cdot \boldsymbol{q} + Q \tag{4.4c}$$

The energy equation can be rewritten in terms of temperature in two different ways using the perfect gas assumption ($e = C_v T$ and enthalpy $h = e + p/\rho = C_p T$):

$$\rho C_v \frac{\mathrm{d}T}{\mathrm{d}t} = -p \boldsymbol{\nabla} \cdot \boldsymbol{u} + \boldsymbol{\nabla} \cdot (k \boldsymbol{\nabla} T) + Q \tag{4.5a}$$

$$\rho C_p \frac{\mathrm{d}T}{\mathrm{d}t} = \frac{\mathrm{d}p}{\mathrm{d}t} + \boldsymbol{\nabla} \cdot (k \boldsymbol{\nabla} T) + Q \tag{4.5b}$$

The conservative cNS equations (4.3) are usually solved completely explicit. The allowable time step is limited by the Courant-Friedrichs-Lewy (CFL) condition, which states that a sound wave cannot travel more than one element length in one time increment: $\Delta t < \dfrac{h}{u}$, where u is the highest velocity modulus, $u = \max\{|\boldsymbol{u}_{flow}|, c_{sound}\}$.

In low Mach number flows (usual case in geophysics), $Ma = \frac{\boldsymbol{u}_{flow}}{c_{sound}} << 1$ leads to $c_{sound} >> \boldsymbol{u}_{flow}$, what reduces the time step to impractical values. Two possibilities to overcome this restriction are:

- the zero Mach number model, that removes all acoustic effects from the cNS equations (Rehm & Baum [88], Paolucci [78], Paillere et al. [77]),
- the Barely Implicit Correction (BIC) algorithm, that treats implicitly those terms of equations that contain the acoustic waves (Patnaik et al. [80]).

Zero Mach number model

The zero Mach number model filters the acoustic modes contained in the cNS equations through an asymptotic analysis. The limit $Ma \rightarrow 0$ gives rise to a splitting of the pressure into a constant-in-space thermodynamic pressure $P(t)$ and a mechanical pressure $p'(x,t)$ (Principe [84]):

$$p = P(t) + p'(x,t) \tag{4.6}$$

The mechanical pressure is the one that appears in the momentum equation. The flow behaves as incompressible, in the sense that the mechanical pressure is determined by the mass conservation equation and not by the state equation, but however, large variations of density due to temperature variations are allowed.

The zero Mach number model in Lagrangian formulation reads

$$\frac{\mathrm{d}\rho}{\mathrm{d}t} = -\rho \boldsymbol{\nabla} \cdot \boldsymbol{u} \tag{4.7a}$$

$$\rho \frac{\mathrm{d}\boldsymbol{u}}{\mathrm{d}t} = -\boldsymbol{\nabla} p' + \boldsymbol{\nabla} \cdot \boldsymbol{\tau} + \rho \boldsymbol{g} \tag{4.7b}$$

$$\rho C_p \frac{\mathrm{d}T}{\mathrm{d}t} = \frac{\mathrm{d}P}{\mathrm{d}t} + \boldsymbol{\nabla} \cdot (k \boldsymbol{\nabla} T) + Q \tag{4.7c}$$

Pressure $P(t)$ depends on the boundary conditions of the problem. If the domain is open, $P(t)$ is determined by the external (atmospheric) pressure, while in a closed domain, $P(t)$ is determined by a global energy balance:

$$\frac{\mathrm{d}P}{\mathrm{d}t} = -\beta \; P \; \boldsymbol{\nabla} \cdot \boldsymbol{u} + (\beta - 1) \; \boldsymbol{\nabla} \cdot (k \boldsymbol{\nabla} T) + Q \tag{4.8}$$

where $\beta = C_p / C_v$. This equation can be interpreted as the constant-in-space thermodynamic pressure changes in time due to addition or substraction of mass $P \, \boldsymbol{\nabla} \cdot \boldsymbol{u}$, or to heat addition or substraction either by the boundary $\boldsymbol{\nabla} \cdot (k \boldsymbol{\nabla} T)$, or by volumetric sources Q (Principe [84]).

Benchmark problems for low Mach number solvers can be found in Le-Quere et al. [54] and Paillere et al. [76].

Barely Implicit Correction (BIC) algorithm

Another way to avoid the sound-speed limit on the time step is to make the calculation fully implicit (Harlow [43]). Patnaik et al. [80] developed an algorithm where only those terms which force the time step constraint are treated implicitly, namely the pressure in Eq. (4.3b) and the velocity in Eq. (4.3c), resulting in an elliptic equation for pressure.

These non-Boussinesq models can be adapted to other fluids different from perfect gas using the appropriate equation of state.

In PFEM it is straight forward to update the density of each particle according to its temperature and possibly apply this new density also to the inertia term in the momentum equation (Idelsohn et al. [45]). One has then to take into account the dilatation in the mass conservation:

$$\frac{\mathrm{d}\rho}{\mathrm{d}t} + \rho\frac{\partial u_i}{\partial x_i} = \frac{\mathrm{d}}{\mathrm{d}t}\rho_0[1-\alpha(T-T_0)] + \rho\frac{\partial u_i}{\partial x_i} = -\rho_0\alpha\frac{\mathrm{d}T}{\mathrm{d}t} + \rho\frac{\partial u_i}{\partial x_i} = 0 \qquad (4.9)$$

which implies

$$\rho\frac{\partial u_i}{\partial x_i} = \varepsilon_T := \frac{\rho_0}{\rho}\alpha\frac{\mathrm{d}T}{\mathrm{d}t} \qquad (4.10)$$

In this case, the fluid remains incompressible due to the pressure forces but becomes compressible for temperature dilatation. The temperature volumetric variation ε_T is explicitly introduced as an initial volume variation at the beginning of each time step. It must be noted that the case of an incompressible flow inside a closed recipient may not be computed with this approach.

4.3.1 Natural convection in a square cavity

We have simulated the classical example of natural convection in a square cavity (DeVahl Davis & Jones [29]) to test the numerical solution when using the Boussinesq approximation.

This example deals with one fluid only, but now density changes as a function of temperature: $\rho = \rho_0[1-\alpha(T-T_0)]$. The problem domain is a square cavity with vertical walls at T = 20.5 and 19.5 °C, and adiabatic horizontal walls. Fluid properties are the following: $\rho = 1$ kg m^{-3}, $\mu = 10^3$ Pa s, $g = -10$ m s^{-2}, $\alpha = 0.1$ °C^{-1}, $\kappa = 10^3$ m^2 s^{-1}, $\Delta T = 1$ °C, $L = 1$ m. This gives a Rayleigh number (ratio between the destabilizing effect of buoyancy and stabilizing effects of diffusion and dissipation) of $Ra = \dfrac{\rho g\alpha\Delta T L^3}{\mu\kappa} = 10^6$. All walls are considered no-slip.

This is a standard problem used for verification of thermal codes. However, we must note that for the Lagrangian formulation it is a difficult test because although the temperature distribution achieves very quickly a stationary state, the position of the particles is never stationary.

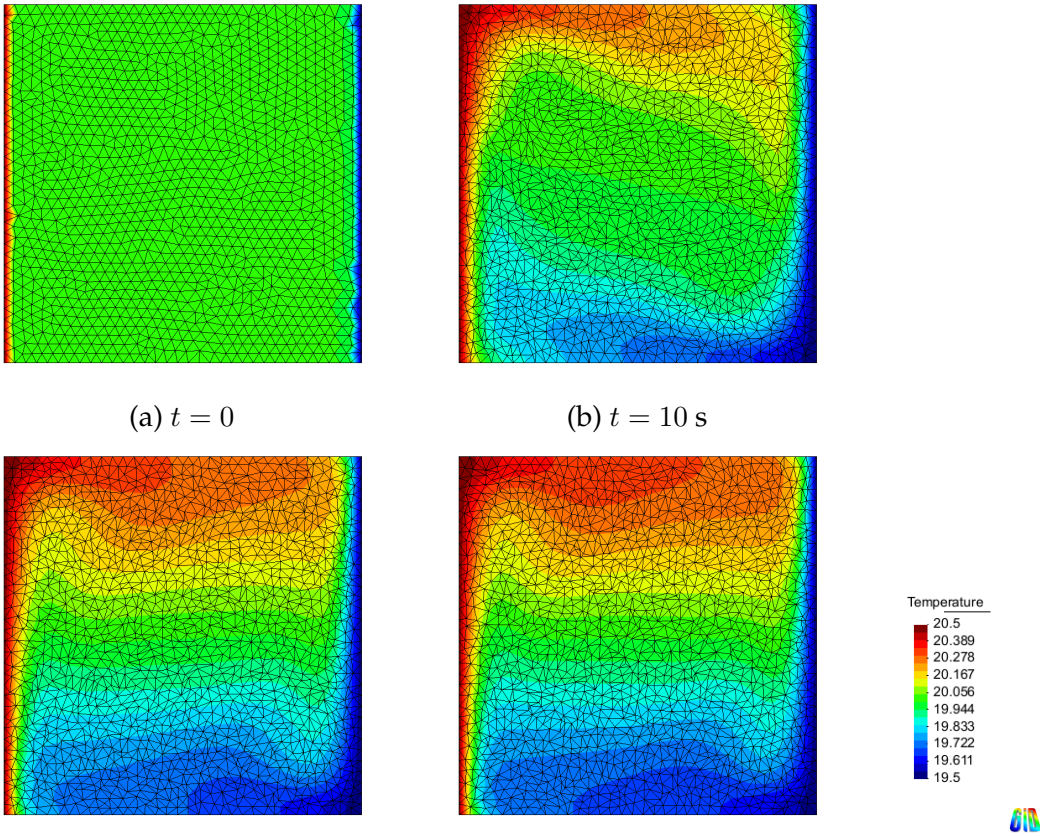

(a) $t = 0$ (b) $t = 10$ s

(c) $t = 30$ s (d) $t = 50$ s

Figure 4.6: Temperature field and mesh at different time steps for $Ra = 10^6$

A benchmark solution can be found in DeVahl Davis [28]. Figure 4.6 shows the temperature field evolution to the steady state during the first 50 seconds. The good agreement between the reference [28] and PFEM's solution is shown in Figure 4.7.

4.4 Magmatic Overturn

A first approach to gravitational instabilities in magma chambers is to have a layer of denser fluid above a lighter one. This could be the result, for example, of an intrusion of mafic magma in a reservoir filled with silicic magma in the case that the intrusion had enough momentum to penetrate and create a layer at the top, or the result of a density decrease in the inflow magma due to gas exsolution. When heavy fluid lies above lighter, the equilibrium in unstable and a small perturbation of the interface from the horizontal will grow with time, producing the phenomenon known as *Rayleigh-Taylor instability*, and lead to convective motions (Turner [103]).

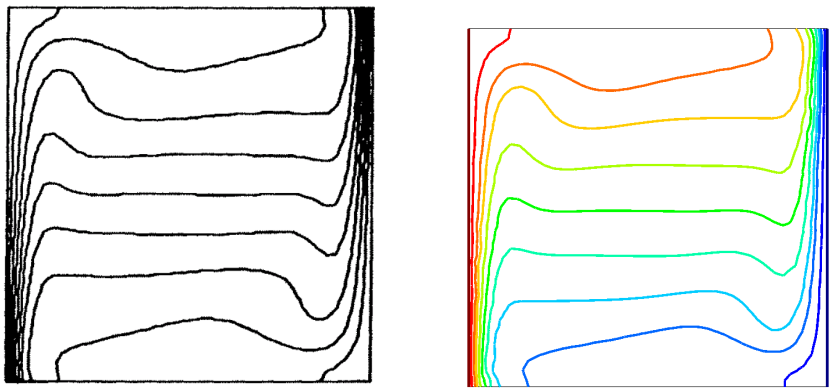

(a) (b)

Figure 4.7: Contour lines of temperature at steady state for $Ra = 10^6$. (a) De Vahl's benchmark solution [28]; (b) PFEM solution.

The Rayleigh-Taylor instability [86, 99] occurs when a light fluid is accelerated into a heavy fluid, i.e. when the density gradient is opposite to the pressure gradient, and it is a fundamental fluid mixing mechanism. The growth rate of the instability and the rate of mixing of the fluids depend on the Atwood number $A = \frac{\rho_{heavy}-\rho_{light}}{\rho_{heavy}+\rho_{light}}$, and the effective viscosity of the two fluids (Chandrasekhar [22]). Understanding the rate of mixing caused by Rayleigh-Taylor instabilities is important to a wide variety of applications.

This instability is a prototype problem for computational studies of multi-fluid flows. The early calculations by Daly [27] using the Marker-And-Cell method have been followed by a number of numerical works, e.g. Baker et al. [8], Sharp [92], Tryggvason [102], Aref & Tryggvason [3], Bell & Marcus [9], Puckett et al. [85], Guermond & Quartapelle [41] and Smolianski [93]).

4.4.1 Numerical example

We have simulated the isothermal gas-driven magmatic overturn proposed in Ruprecht et al. [91]. It consists of a rectangular 200×100 m domain where the initial conditions are a 60 m thick dense magma (fluid 1) overlying a 40 m thick lighter magma (fluid 2) (see Figure 4.8). The physical properties are $\rho_1 = 2400$ kg m^{-3}, $\mu_1 = 10^4$ Pa s, $\rho_2 = 2220$ kg m^{-3}, and $\mu_2 = 1.032 \times 10^4$ Pa s. Surface tension and miscibility are neglected. Vertical walls are considered free-slip, while the horizontal are noslip. Thermal effects are not taken into account because the time scale of convection is much faster than that of heat transfer. The mesh size has been chosen to $h = 1$ m.

For this example we model the interface aligned with the mesh (nodal

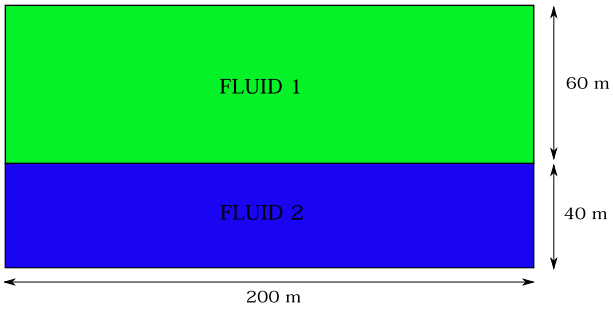

Figure 4.8: Initial configuration in magmatic overturn.

interface) and use the techniques described in the previous chapter for problems with different densities. Due to the similar viscosities of fluid 1 and 2, we consider the problem isoviscous and therefore, the continuous pressure approximation is used.

Figure 4.9 shows the evolution in time of the immiscible fluids. Small perturbations have been introduced at the initial interface to control the locations of the Rayleigh-Taylor instabilities, instead of being triggered by numerical errors.

In Ruprecht et al. [91], they model the multiphase character of magmas by including spherical bubbles and crystals. Their interface is determined by the bubble volume fraction which diffuses in time, whereas with a Lagrangian tracking of the interface nodes, immiscible interfaces remain sharp, as can be observed in Figure 4.9.

4.4.2 Quantification of mixing

In this example we are interested in quantifying the mechanical mixing (mingling) produced during the overturn. Several methods have been developed for the assessment of the stirring/mixing efficiency in industrial mixers and micro fluidic devices (Byrde [18], Kim & Beskok [50]) such as particle dispersion, the box counting method or, based in the theory of chaotic flows (Ottino [75]), the Poincare sections to identify chaotic motion regions and the Liapunov exponents to quantify chaotic strength. To measure the extent mixing in the specific context of overturn processes some authors have used the change in potential energy of the system (Jellinek et al. [47], Ruprecht et al. [91]) or the stretching of the interface (Chella & Viñals [23]). We follow here this latter approach and use the mixing metric based on the growth of the interface area (length in two-dimensional models).

Flow patterns generated by Rayleigh-Taylor instabilities fall in two classes (Burgisser & Bergantz [16], Wiggins & Ottino [111]): elliptic flow, where streamlines wrap around a stagnation point; and hyperbolic flow, where streamlines diverge at the stagnation point. The interface stretches with time either by being linearly

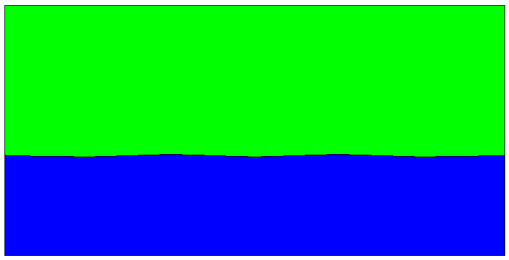

(a) $t = 0$

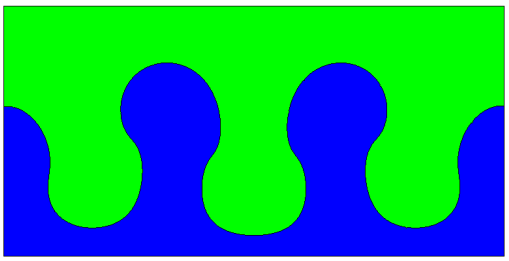

(b) $t = 50$ s

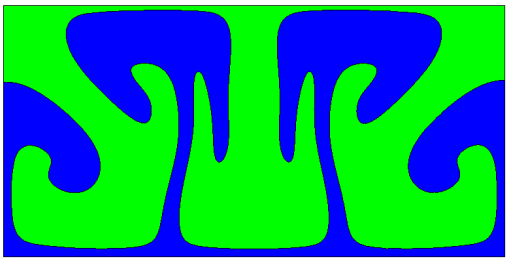

(a) $t = 70$ s

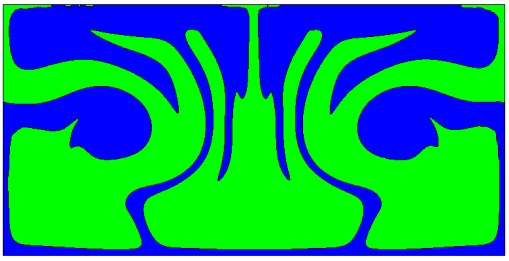

(b) $t = 90$ s

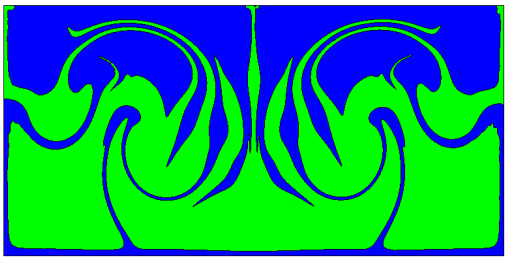

(a) $t = 120$ s

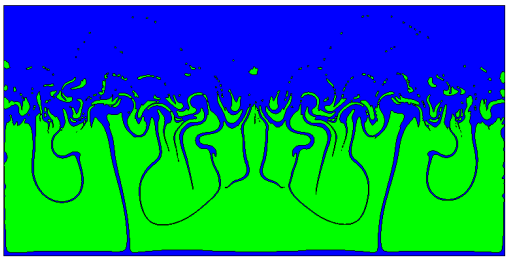

(b) $t = 300$ s

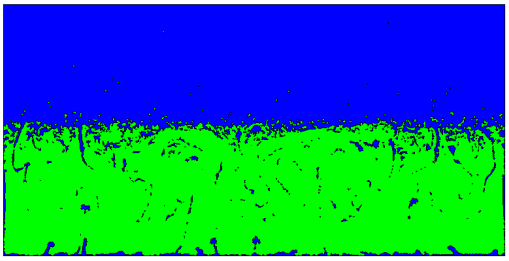

(a) $t = 800$ s

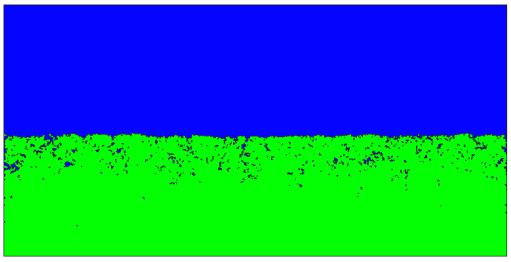

(b) $t = 3500$ s

Figure 4.9: Magmatic overturn. Materials field in time.

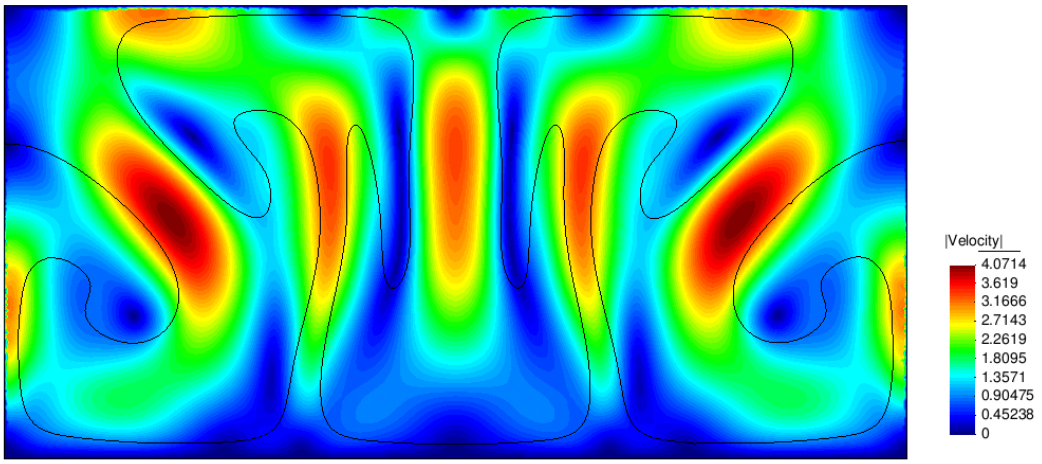

Figure 4.10: Magmatic overturn. Velocity field at time $t = 70$ s.

twirled around elliptic points, or by being exponentially folded by hyperbolic points (see Figures 4.10 and 4.11). Ultimately, mixing is about the formation of hyperbolic and elliptic points by the vorticity, and the advection of these kinematic elements through the domain.

We have measured the interface stretching during the magmatic overturn, and the exponential growth of the interface length during the instability development ($t \sim$ 0-100 s) is shown in Figure 4.12.

4.4.3 Conclusions

In this first magmatic example we have shown that PFEM is able to solve complex flows like the complete overturn produced by gravitational instability, and to preserve the interface sharp despite the large deformations. Furthermore, we have used the interface length to quantify the mechanical mixing produced by the overturn, and shown its exponential growth during the development of the Rayleigh-Taylor instability.

4.5 Mixing of magmatic liquids

Many magmatic and volcanic processes are controlled by the physical properties and flow styles of high-temperature silicate melts in the chamber. These processes can be experimentally investigated using analogue systems and scaling methods, but it is generally not possible to quantitatively extrapolate the results to the natural system. An alternative means of studying fluid dynamics in magmatic systems is via numerical models, in our case with the Particle Finite Element Method. We

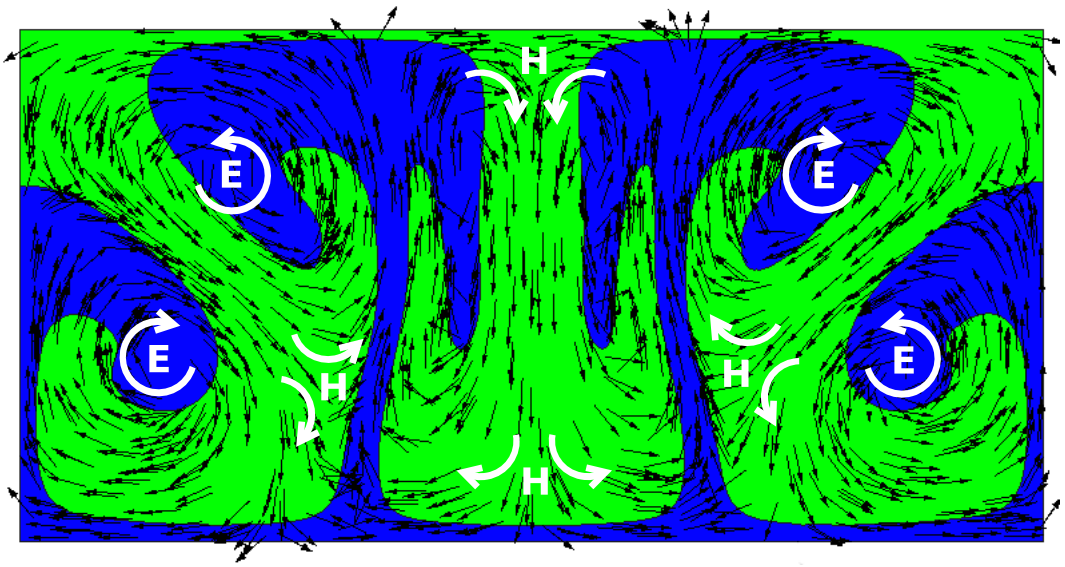

Figure 4.11: Magmatic overturn. Velocity vector field at time $t = 70$ s (uniform vector size). Elliptic E and hyperbolic H points are remarked.

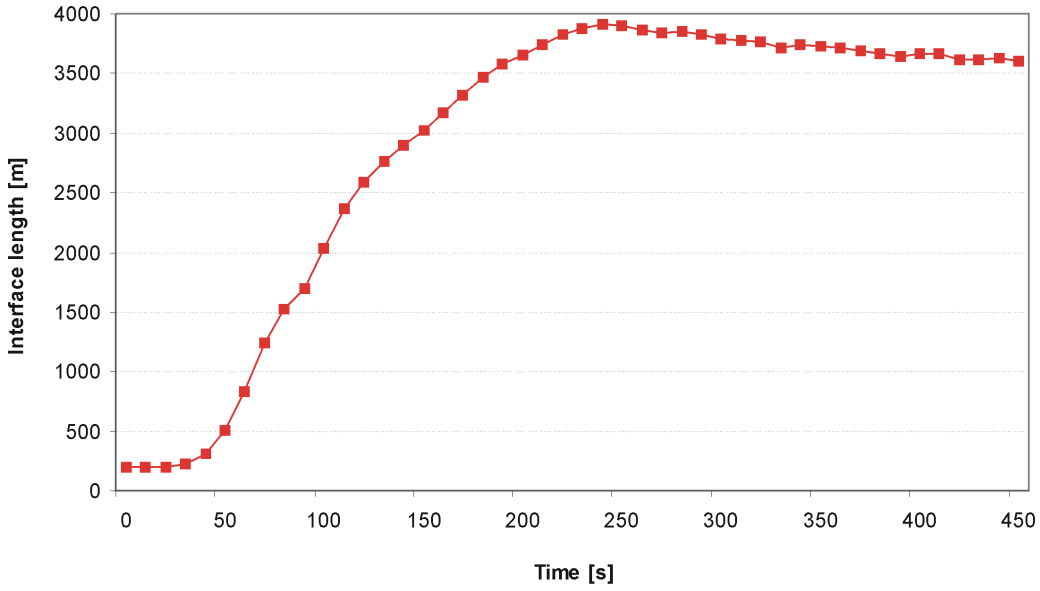

Figure 4.12: Magmatic overturn. Measured interface length up to time $t = 450$ s.

have performed a series of two-dimensional simulations of a classical 'case study' of fluid dynamics and mixing in magmatic systems: intrusion of a basaltic melt in a silica-rich melt reservoir. The numerical results are compared with natural data from the eruption of San Pedro volcano (Chilean Andes). This second geological example incorporates the heat and mass transfer equations to simulate the thermo-chemical mixing inside a magma chamber and has been done in collaboration with Dr. F. Costa from the Institute of Earth Sciences Jaume Almera, CSIC.

The amount of work and insights gained from analogue experiments contrast with the few numerical models that have been done aimed at reproducing fluid dynamics of magma reservoirs (e.g. Marsh [65], Oldenburg et al. [73], Bagdassarov & Fradkov [5], Thomas et al. [100]). This may partially reflect the limited data on the physical properties and theoretical models of silicate melts available at that time (e.g. Murase & McBirney [70], McBirney & Murase [67]). Major improvements have occurred in the last twenty years with the experimental determination and development of theoretical models of physical properties of silicate melts (heat capacity, viscosity, density, and diffusion; e.g. Lange & Carmichael [53], Chakraborty [21], Ghiorso & Sack [38], Mysen & Richet [71], Giordano et al. [39]). These new data and models set a robust basis for performing fluid dynamic numerical simulations of magmatic processes involving multicomponent fluids.

Magma mixing is one of the most common processes proposed to explain the variety of igneous rocks and the composition of the continental and oceanic crust. It has also been proposed to be a main trigger mechanism of eruptions (e.g. Sparks et al. [96]) and has been documented in many geochemical and petrological studies of igneous rocks (e.g. Anderson [1], Dungan & Rhodes [32], Bacon [4], Wiebe [110]). Previous numerical studies of magma mixing have concentrated on the role of volatiles as driving force for convection in a isochemical and isothermal magmatic system (e.g. Bagdassarov & Fradkov [5], Thomas et al. [100], Longo et al. [63], Ruprecht et al. [91]), with limited studies devoted to mixing of contrasting compositions (e.g. Oldenburg et al. [73], Sparks & Marshall [97], Snyder [94]). We use the Particle Finite Element Method to investigate mixing of mafic and silicic magmas with different temperatures, and in particular, the role of the initial conditions (passive or forceful intrusion of the mafic magma in the silicic reservoir). The numerical simulations have been designed to reproduce the magma mixing processes recorded in a zoned eruption of San Pedro volcano, the details of which are introduced in the next section.

4.5.1 San Pedro volcano

The San Pedro volcano in the Chilean Andes (Fig. 4.13) has been chosen as case study. Costa & Singer [25] showed that the eruption produced a chemically,

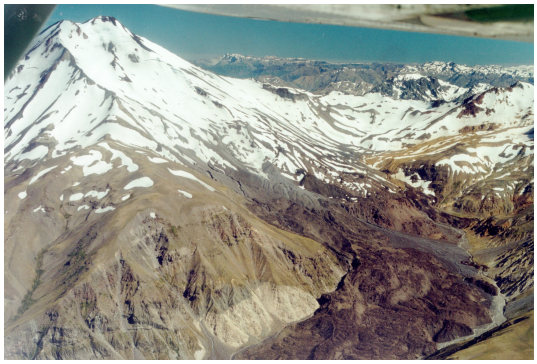

Figure 4.13: San Pedro volcano (from Costa & Singer [25]).

mineralogically, and thermally zoned sequence of silicic lavas (about 0.8 km^3). This was followed by basaltic andesites (about 0.2 km^3, 1100 °C) which rebuilt the summit cone of the volcano. The products of the zoned eruption comprise three different flows: a silica-rich dacite (about 0.2 km^3, 850 $\pm$ 20 °C), a less silicic dacite (0.5 km^3, 920 $\pm$ 40 °C), and andesite (about 0.1 km^3, 930 $\pm$ 40 °C). The SiO_2 content and proportions of each flow have been represented in Figure 4.14. Based on petrological and geochemical data, Costa & Singer [25] proposed that the compositional zoning of the erupted products was due to incomplete mixing between about 60 wt% of the most silica-rich dacite and about 40 wt% of the basaltic andesite. From this we have obtained that about 0.5 km^3 of dacite and 0.5 km^3 basaltic andesite are the proportions of the two end-members prior to mixing.

The specific goal of the simulation in the context of San Pedro volcano was to reproduce the volumes (reduced to proportions of areas in the two-dimensional simulations) of the different erupted materials using the composition, proportions and temperatures of the end-members deduced from field work, petrological, and geochemical data. In addition, because there are time constraints on the time since arrival of the mafic magma and the eruption, the model was also originally thought to match the temporal scale. This aspect was not possible to achieve because the simulations became computationally very intensive and long CPU times were required (see Section 4.5.5).

4.5.2 Quantification of mixing and comparison with natural rocks

The type of approach that we are taking requires to characterize and quantify the extent of mixing in the numerical calculations but also in the natural rocks. As explained in Section 4.4, several metrics have been previously developed for the quantification of mixing intensity. In this example we have adopted the approach of Perugini et al. [81], which uses image analysis to obtain compositional histograms. We have converted our composition results to 256 levels gray-scale with GiD

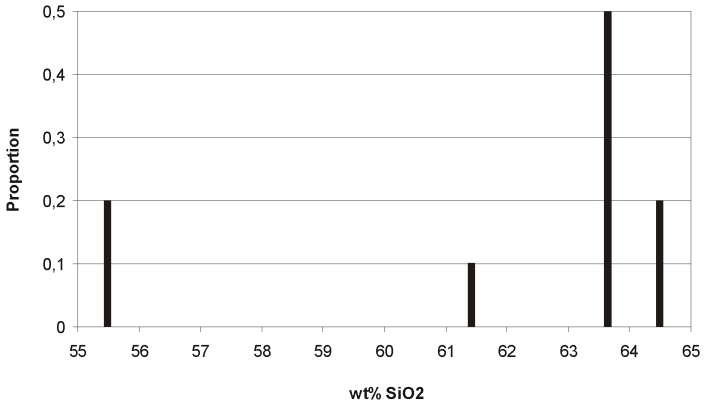

Figure 4.14: Histogram of SiO_2 content of lavas from the San Pedro eruption. The proportions also correspond to erupted volume in km^3.

postprocessing tool and analyzed with ImageJ software to obtain an histogram in text format. The 256 bins are then gathered in 32 bins to construct histograms of area vs. composition and these are compared to the volumes or relative proportions (directly transformed into areas) of erupted material of different compositions.

4.5.3 Model equations and parameters

We use a formulation for incompressible Newtonian fluids with variable density and viscosity. No solid particles or gas phase are considered. The system is modeled by the following set of governing equations:

$$\text{Continuity:} \qquad \boldsymbol{\nabla} \cdot \boldsymbol{u} = 0 \tag{4.11a}$$

$$\text{Momentum:} \qquad \rho \frac{\mathrm{d}\boldsymbol{u}}{\mathrm{d}t} = -\boldsymbol{\nabla} p + \boldsymbol{\nabla} \cdot \mu(\boldsymbol{\nabla}\boldsymbol{u} + \boldsymbol{\nabla}^T \boldsymbol{u}) + \rho \boldsymbol{g} \tag{4.11b}$$

$$\text{Heat:} \qquad \frac{\mathrm{d}T}{\mathrm{d}t} = \kappa \nabla^2 T \tag{4.11c}$$

$$\text{Composition:} \qquad \frac{\mathrm{d}c}{\mathrm{d}t} = \boldsymbol{\nabla} \cdot (D \boldsymbol{\nabla} c) \tag{4.11d}$$

where
$\dfrac{\mathrm{d}}{\mathrm{d}t} = \dfrac{\partial}{\partial t} + \boldsymbol{u} \cdot \boldsymbol{\nabla}$ is the material derivative, and other symbols are explained in Table 4.1.

Thermal diffusivity κ is considered constant in time and space, while density ρ, dynamic viscosity μ and chemical diffusion D change with temperature and composition (see below for details). The effect of pressure variation in physical properties has not been taken into account since it is negligible for the pressure

Description	Symbol	Value	Units
Velocity	$\boldsymbol{u}$		m s^{-1}
Pressure	p		Pa
Temperature	T	600 - 1150	°C
Composition	c	55.5 - 64.5	
Density	ρ	2560 - 2700	kg m^{-3}
Dynamic viscosity	μ	12.8 - 1.3×10^7	Pa s
Thermal diffusivity	κ	10^{-6}	m^2 s^{-1}
Chemical diffusion	D	2.2×10^{-13} - 1.35×10^{-7}	m^2 s^{-1}
Gravity force	$\boldsymbol{g}$	9.81	m s^{-2}
Thermal expansion	α	4.5×10^{-5} - 5.5×10^{-5}	$°C^{-1}$

Table 4.1: Symbols, units, and ranges of values of the physical properties we have used in the models.

range and processes we are simulating. Thermal variations of density are sufficiently small so that the flow can be considered incompressible, Eq. (4.11a), and thermal buoyancy is modeled by the Boussinesq approximation (Gray & Giorgini [40]). We have neglected the surface tension, the heats of mixing and crystallization, and do not have a multiphase treatment (e.g. Dufek & Bergantz [31], Ruprecht et al. [91]).

4.5.4 Physical properties of silicate melts

The complexity of the numerical simulations is increased by the non-linear formulations that describe how viscosity, density, and chemical diffusivity change with composition and temperature. The composition of the end-member magmas is shown in Table 4.2.

	SiO_2	TiO_2	Al_2O_3	FeO	MnO	MgO	CaO	Na_2O	K_2O	P_2O_5	H_2O
Dacite	64.5	0.51	16.26	3.74	0.08	1.78	4.08	4.54	2.70	0.16	5.0
Bas. andesite	55.5	1.02	18.03	7.47	0.13	4.60	7.63	3.64	1.36	0.25	1.0

Table 4.2: End-members composition (in wt%)

Viscosity For the viscosity we have used the calibration of Giordano et al. [39]

$$\log \mu = A + \frac{B}{T - C} \tag{4.12}$$

where T is temperature in Kelvin degrees K and the values of A, B and C are listed in Table 4.3. The viscosity values of the end-members for different temperatures are

plotted in Figure 4.15.

	Basaltic andesite	Dacite
A	-4.55	-4.55
B	6042.88	8106.06
C	355.05	162.34

Table 4.3: Parameters for viscosity (Giordano et al. [39])

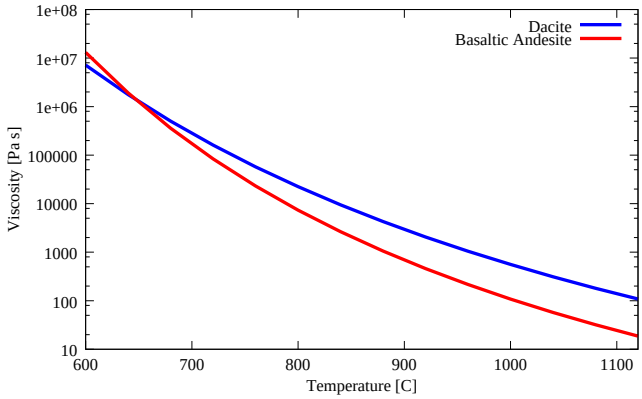

Figure 4.15: End-members viscosity (semi-log scale).

Density For the density we have used the equations of state of Lange & Carmichael [53] and Lange [52]:

$$\rho = \frac{\sum_i f_{m,i} P_{m,i}}{V_{liq}}, \quad V_{liq} = \sum_i f_{m,i}(V_{ref,i} + \frac{\partial V_i}{\partial t}(T - T_{ref})) \tag{4.13}$$

where ρ is the density; $f_{m,i}$ the molar fraction of species i; $P_{m,i}$ the molecular weight of species i; V_{liq} the liquid volume; and $V_{ref,i}$ the reference volume of species i (at T_{ref}). The values of these properties for each species are collected in Table 4.4, and the computed density is shown in Figure 4.16.

Thermal diffusivity There are only few data on the dependency of thermal diffusivity on temperature and composition (e.g. Murase & McBirney [70], Buttner et al. [17]), so we have decided to use a single value of 10^{-6} m^2 s^{-1} as has been done in other works (e.g. Jellinek et al. [48], Valentine et al. [107]).

Chemical diffusivity For chemical diffusion we have simplified the multi-component treatment by considering silica, Si, as a good proxy for chemical

	Basaltic andesite	Dacite			
Oxide	f_m	f_m	V_{ref}	$\frac{\partial V_i}{\partial t}$	P_m
SiO_2	0.5098	0.6044	26.9	0	60.08
TiO_2	0.007	0.0035	23.16	7.24	79.88
Al_2O_3	0.0976	0.0880	37.11	2.60	101.96
Fe_2O_3	0	0	42.13	9.09	159.69
FeO	0.0574	0.0287	13.65	2.92	71.85
MnO	0.001	0.0006	0	0	70.94
MgO	0.063	0.0244	11.45	2.62	40.3
CaO	0.0751	0.0402	16.57	2.92	56.08
Na_2O	0.0324	0.0404	28.78	7.41	61.98
K_2O	0.008	0.0158	45.84	11.91	94.2
P_2O_5	0.001	0.0006	0	0	141.94
H_2O	0.0307	0.1533	0	0	18
$T_{ref} = 1400\,^\circ C$					

Table 4.4: Data used for computing the density, after the model of Lange [52] and Lange & Carmichael [53].

diffusivity and used the formulation of Lesher [55]. D_{Si} depends on temperature T and composition X_{Si} (wt.% Si) in the following manner:

$$\ln D_{Si} = 6.7 - (31195/T) + 12.28(0.52 - X_{Si}) \tag{4.14}$$

The chemical diffusivity values of the end-members for different temperatures are plotted in Figure 4.17.

The silica content of the end-members was normalized to vary between 0 and 1, and the different physical properties Y (density, viscosity and chemical diffusivity) are interpolated linearly to intermediate compositions

$$Y(T, c) = c \cdot Y_1(T) + (1 - c) \cdot Y_0(T), \quad Y = \rho, \mu, D \tag{4.15}$$

This approximation introduces errors smaller than 0.5% in all the interpolated variables, as shown in Table 4.5. It compares the exact thermodynamic and the linearly interpolated values (Eq. (4.15)) for density, viscosity and chemical diffusion.

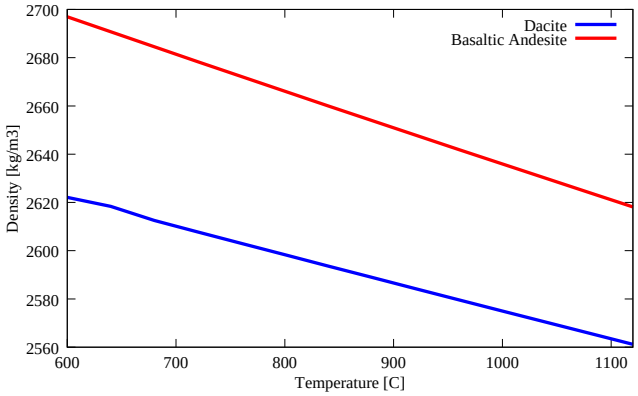

Figure 4.16: End-members density.

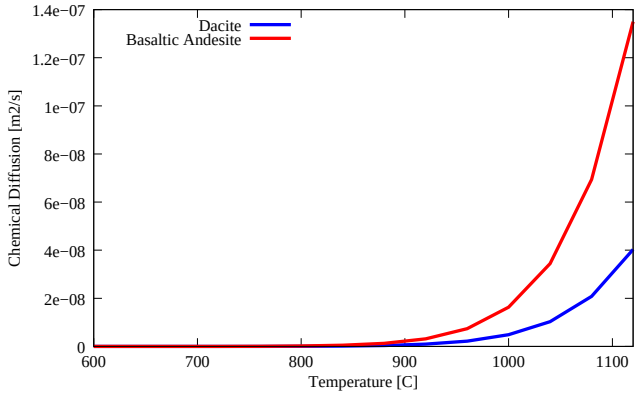

Figure 4.17: End-members chemical diffusivity, calculated after Lesher [55].

4.5.5 Numerical settings, initial and boundary conditions

Boundary and initial conditions from geological constrains

For all simulations except for the diffusion-only case we have used a circular reservoir with a radius of 680 m which corresponds in three-dimensions to a sphere of about 1 km^3, the volume of the San Pedro eruption. The two initial fluids are basaltic andesite at 1150 °C and dacite at 850 °C (Table 4.6), each with the same proportion (50%, as explained in Section 4.5.1). Chamber wall is considered adiabatic and initially at 600 °C.

One of the key aspects that we are interested in testing is the influence of the initial configuration of the mafic and silicic liquids. In other words, the difference between a situation where basalts may pond at the base of the silicic melt versus forceful intrusion of basalt that may reach the intermediate zones of the reservoir. Modeling forceful intrusion in the reservoir is, however, very complex. We have performed a series of exploratory simulations (Fig. 4.18) and it quickly became apparent that to be able to inject new magma in the reservoir it is necessary to

Density

$T[^\circ C]$	Exact	Interpolated	Error %
600	2658	2660	0.05
720	2641	2643	0.06
960	2609	2611	0.08
1120	2587	2590	0.09

Viscosity

$T[^\circ C]$	Exact	Interpolated	Error %
600	7855805	9521177	0.17
720	112094	130037	0.14
960	511	714	0.28
1120	49	73	0.32

Chemical diffusion

$T[^\circ C]$	Exact	Interpolated	Error %
600	7.1×10^{-14}	1.4×10^{-13}	0.5
720	5.3×10^{-12}	1.1×10^{-11}	0.5
960	2.4×10^{-9}	4.8×10^{-9}	0.49
1120	4.4×10^{-8}	8.7×10^{-8}	0.49

Table 4.5: Exact thermodynamic values compared to the interpolated by Eq. (4.15) for the case $c = 0.5$.

couple the fluid dynamics of the magmas with a rheological model of the host rock and take into account the compressibility of the magma. This is beyond the scope of this work and to circumvent the problem we have used a simpler approach where the reservoir contains a layer of mafic liquid within the silicic liquid already at the beginning of the simulation. We think that this situation reflects the case where a new pulse enters with enough momentum to rise into the host silicic magma and spreads laterally before it falls back when negative buoyancy forces overcome the initial momentum of the pulse. Whether a denser but less viscous liquid can intrude a lighter and more viscous liquid depends mainly of the viscosity ratio of the two liquids (Campbell & Turner [19]).

Dynamic similarity analysis

One of the difficulties to model fluid dynamics is the large stretching and folding that occurs during convection. Such deformations require precise calculations of the positions at each time step (adaptive mesh, small time steps), and are thus

	T_0 [°C]	ρ_0 [$kg\,m^{-3}$]	μ_0 [$Pa\,s$]	D [$m^2\,s^{-1}$]	wt% SiO_2
Dacite	850	2593	7727	1.85×10^{-10}	64.5
Basaltic andesite	1150	2614	12.8	2.16×10^{-7}	55.5

Table 4.6: End-members initial physical properties.

computationally very demanding. In addition, the low thermal and chemical diffusivities require long simulation times for homogenization to be noticeable. These two requirements (small time steps for convection, long simulation times for diffusion) have appeared to be incompatible in our simulations. To overcome this limitation we have extrapolated the coefficients of thermal and chemical diffusivities: $\kappa = \kappa_{real} \times 10^n$, $D = D_{real} \times 10^n$ (with n between 7 and 9). We have done a dynamic similarity analysis using dimensionless numbers to address whether the numerical simulations with the extrapolations still capture the main dynamics of the system. This is the same approach as done in analogue experiments (e.g. Sparks et al. [95]).

Heat and mass transfer flows are characterized by three dimensionless numbers:

(i) the Prandtl number Pr, that describes the ratio of momentum diffusivity to thermal diffusivity,

$$Pr = \frac{\mu}{\rho\kappa}$$

(ii) the Rayleigh number Ra, that describes the strength of convection in buoyancy driven flows,

$$Ra = \frac{\rho\, g\, \alpha\, \Delta T\, H^3}{\mu\kappa}$$

(iii) the Schmidt number Sc, ratio of momentum to compositional diffusivities,

$$Sc = \frac{\mu}{\kappa D}$$

ΔT is the temperature difference across the interface ($\Delta T = 300\,°C$ in our case), H is the characteristic length of the flow, for which we have taken the chamber radius, and $\alpha = 1/\rho\, d\rho/dT$ is the thermal expansion coefficient. The Prandtl and Schmidt numbers can be combined in the Lewis number, $Le = Sc/Pr = \kappa/D$, ratio of thermal diffusivity to chemical diffusivity.

Table 4.7 shows the values of these dimensionless numbers at the initial time. Note that the Pr, Ra and Sc numbers are all very large ($> 10^3$). Because $Le > 1$, temperature gradients will decay faster than compositional gradients. Flows with large Rayleigh and Lewis numbers result in thin, vigorous plumes and highly distorted interfaces (Valentine et al. [107]). With the extrapolations noted above

the Lewis number remains unchanged but the Rayleigh number of the flow is decreased by n orders of magnitude. Despite this, in the simulations the Rayleigh number will be still high enough ($Ra > 10^6$) to produce turbulent dynamics (Sparks et al. [95]) and therefore we believe that this has little effect in the overall mixing, although the time scale of the results can not be compared to real time magmatic processes.

	Pr	Ra	Sc	Le
Dacite	3×10^6	1.4×10^{13}	1.6×10^{10}	5.4×10^3
Basaltic andesite	4.9×10^3	10^{16}	2.3×10^4	4.7

Table 4.7: End-members initial dimensionless numbers that characterize flow dynamics.

Numerical settings

In this example, we have used the interface across elements representation (Fig. 3.3a), which is better suited for the miscible fluids with smoothly varying properties that we are studying here.

The mesh size h is 6 m in the bulk of the fluids and 4 m around the interface. Time step Δt needed to be of order $\sim$ 0.1 s to compute accurately convection and avoid excessive fluid fragmentation due to changes in connectivity during remeshing. This limits the total time that we can model to few thousand seconds. The extrapolation of κ and D increases the diffusive length scale so that diffusion processes can be resolved with our mesh.

Mesh distortion requires to introduce and delete nodes during remeshing at each time step. If the variables are interpolated linearly to the new nodes, this introduces an artificial diffusion of order $\mathcal{O}(h^2/\Delta t)$, much larger than the real one. We found that if variables are interpolated randomly instead of linearly this almost completely avoids artificial diffusion (Fig. 4.18). The mesh contains initially 35000 nodes and 68000 elements. As time progresses, convection increases the interface length and the mesh becomes larger (around 90000 nodes, 180000 elements).

4.5.6 Results

With the initial volumes, temperatures, and physical properties of the two end-members we have produced a series of two-dimensional simulations of increasing complexity. We start by testing the case of diffusion between the two melts without convection, and follow by the case of mafic melt ponding at the base of the silicic reservoir. Two additional simulations incorporate the possibility of one and two

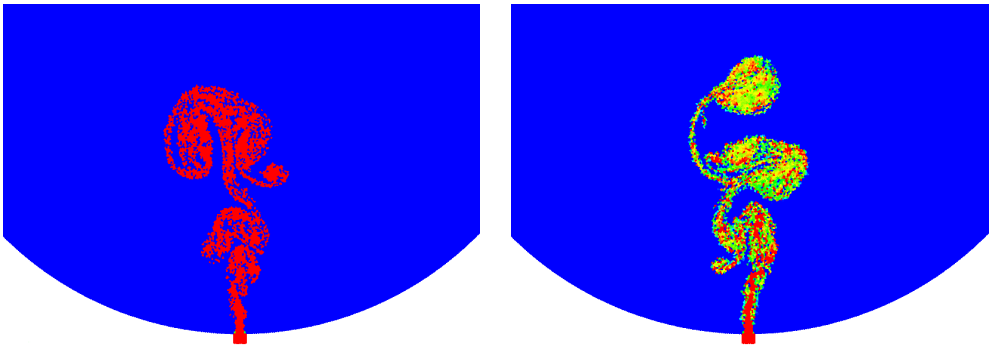

(a) Random interpolation (b) Linear interpolation

Figure 4.18: Results of a numerical simulation of a jet of mafic melt (red) intruding in a silica-rich melt reservoir (blue). Notice the artificial numerical diffusion (range of colors) in (b), but absent in (a) where both liquids are still unmixed.

forceful intrusions in the silicic reservoir following the approach described in Section 4.5.5.

Gravitationally stable, diffusion only

For this case we have used a two-dimensional closed system of 20 m in length consisting of equal proportions of basaltic andesite and dacite (Figs. 4.19 to 4.21). We highlight the following observations from the results: (i) in about 10000 years chemical diffusion has affected only about 10 m (Fig. 4.21). This shows the inefficiency of volume diffusion alone to produce mixing of large melt bodies. It also shows that with the mesh size we are using of about 6 m (necessary to also be able to model the entire size of the reservoir) it was required to use much large values for the chemical diffusivity in the following convection models if the combined effects of the two transport mechanisms are to be investigated. (ii) the histograms of concentration are U-shaped during most of the evolution and only become I-shaped close to equilibrium (Fig. 4.21). None of the concentration distributions match those of the natural samples, which implies that diffusion-only can not result in the natural data, as was anticipated by the small chemical diffusivities of the melts. However, this shows that histograms are valid means to compare the natural data with the numerical simulations and extract information about processes.

Gravitationally stable with convection

In this case we start from a stable density configuration, with the mafic, denser and less viscous magma in the bottom layer, and the silicic, lighter and more viscous

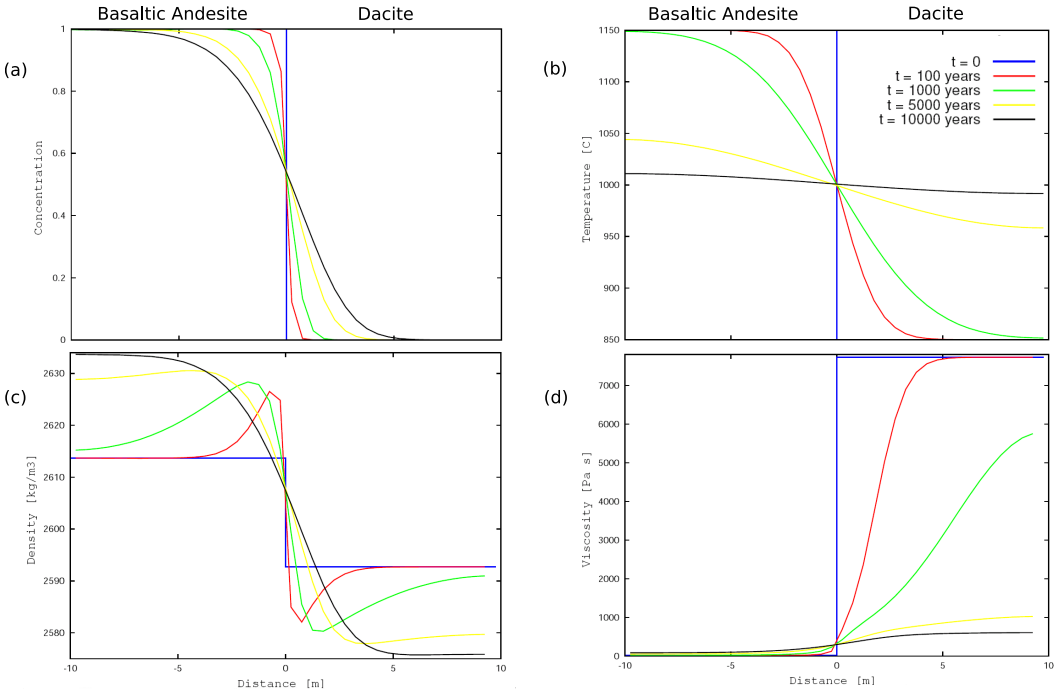

Figure 4.19: (a) Composition, (b) temperature, (c) density and (d) viscosity profiles next to the interface, at $t = 0$, 100, 1000, 5000 and 10000 years for diffusion only case. Note that the asymmetry of the chemical diffusion profiles is due to the concentration dependent diffusion coefficient.

magma on the top (Figs. 4.22 to 4.24). For this simulation we increased κ and D by nine orders of magnitude to have any significant dynamics in the computer times that we can access. Heating of the silicic liquid by the mafic one near the interface leads to unstable conditions and triggers convection (see density profile in Fig. 4.19c). Small plumes develop, and the length scale of this convection is only few meters (Fig. 4.22).

The compositional histogram of this configuration is also U-shaped, although we have not been able to run the simulations for a very long time and thus we are still far from equilibrium (Fig. 4.23). It seems difficult to us that a histogram consisting of several distinct compositional peaks as the natural data would be produced from the evolution of such a situation. We thus conclude that passive intrusion of mafic melt at the base of the reservoir cannot lead to the histogram of the natural data.

Gravitationally unstable and forceful intrusions

We have simulated two cases that represent the forceful intrusion of mafic melt in the silicic reservoir: either with one (Figs. 4.25 to 4.27) or two mafic layers

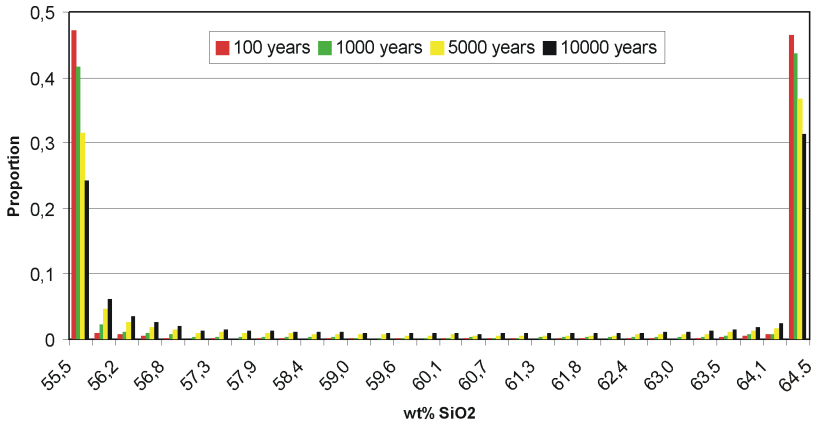

Figure 4.20: Diffusion only histograms. Note that the asymmetry of the histograms is due to the concentration dependence of the diffusion coefficients.

(Figs. 4.28 to 4.30) present at an intermediate level of the reservoir. In both cases diffusivity coefficients have been increased by seven orders of magnitude to obtain enough mixing in the simulation time scale. The proportions of the mafic to the silicic melt were the same (50%), and also the same as the previous gravitationally stable case. This configuration leads to unstable density profiles from the beginning and several Rayleigh-Taylor instabilities develop along the interface and force convection (Figs. 4.25 and 4.28).

The compositional histograms of one intrusion show that in addition to the two peaks of the end-members, another peak appears close to the dacite (Fig. 4.27). This occurs because the system effectively behaves as a smaller domain than the bulk, with a local composition of some dacite plus the intermediate mafic layer. We think that such compositional peak is transient but probably a characteristic feature of the simulation. With increasing time the whole system should evolve towards the equilibrium mean composition, with a single intermediate peak as we have obtained in the diffusion-only simulation (Fig. 4.21). The interesting observation is that this new peak overlaps with one of the natural compositions (Fig. 4.27). This shows the capacity of the simulation to reproduce natural data applying the geological constraints also supports the idea of forced magma injection. However, this simulation does not produce the andesite peak, which is also present in the natural rocks (Fig. 4.27).

The simulation with two initial intrusions (Figs. 4.28 and 4.29) was performed in part to account for the fact that more than one mafic intrusion is recorded in the natural rocks (e.g. Costa & Singer [25]), but also to see if we could produce the andesite composition seen in the natural histogram (Fig. 4.14). The results show that the compositional histogram from the simulations contains four different

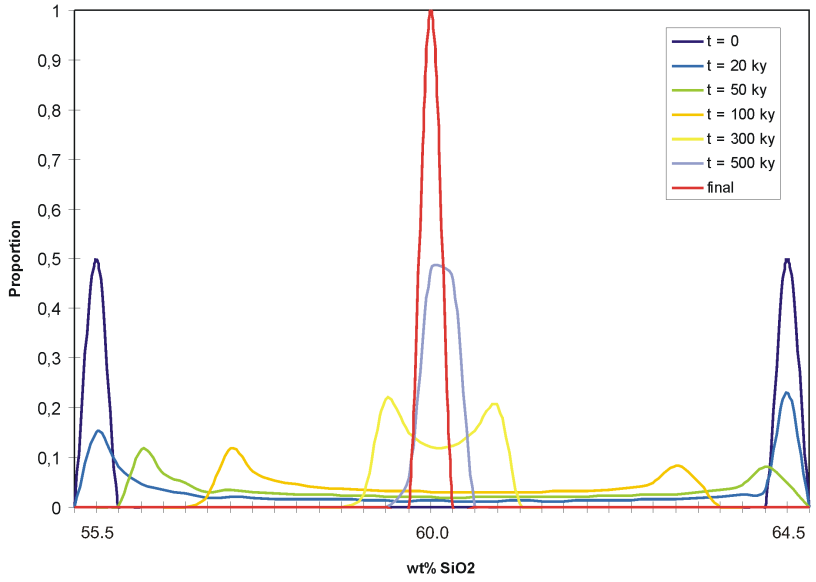

Figure 4.21: Composition evolution until total homogenization in the diffusion only case. Note that the natural compositional histogram is not reproduced (Fig. 4.14).

peaks (Fig. 4.30). Two are those of the end-members, and the two additional ones are slightly more silica-rich and silica-poor, than the mafic and dacitic end-members, respectively. The presence of these two additional peaks can be reasoned in a similar manner as for the one intrusion case. Close to the initial conditions the system behaves as domains that are smaller than the whole and thus with different local compositions that lead to the observed peaks. Again we think that this is a transient behavior and with increasing time the mean bulk composition should be reached. The two additional peaks are however unlike those seen in the natural data (Fig. 4.30). One is close to the mafic end-member, and it is absent in natural data, and the other is slightly shifted to higher SiO_2 content than the natural data. Note also that this situation is not capable of producing the peak of andesitic composition seen in the natural histogram. From these simulations we conclude that the case with a single intrusion better reproduces the natural data, but other factors that were not incorporated in the model have also played a role and they are discussed below.

4.5.7 Conclusions

The numerical results show that the initial conditions and type of melt interactions (e.g. passive versus forceful intrusion) are a major control in the resulting volume and compositional distribution, and are consistent with the results obtained from

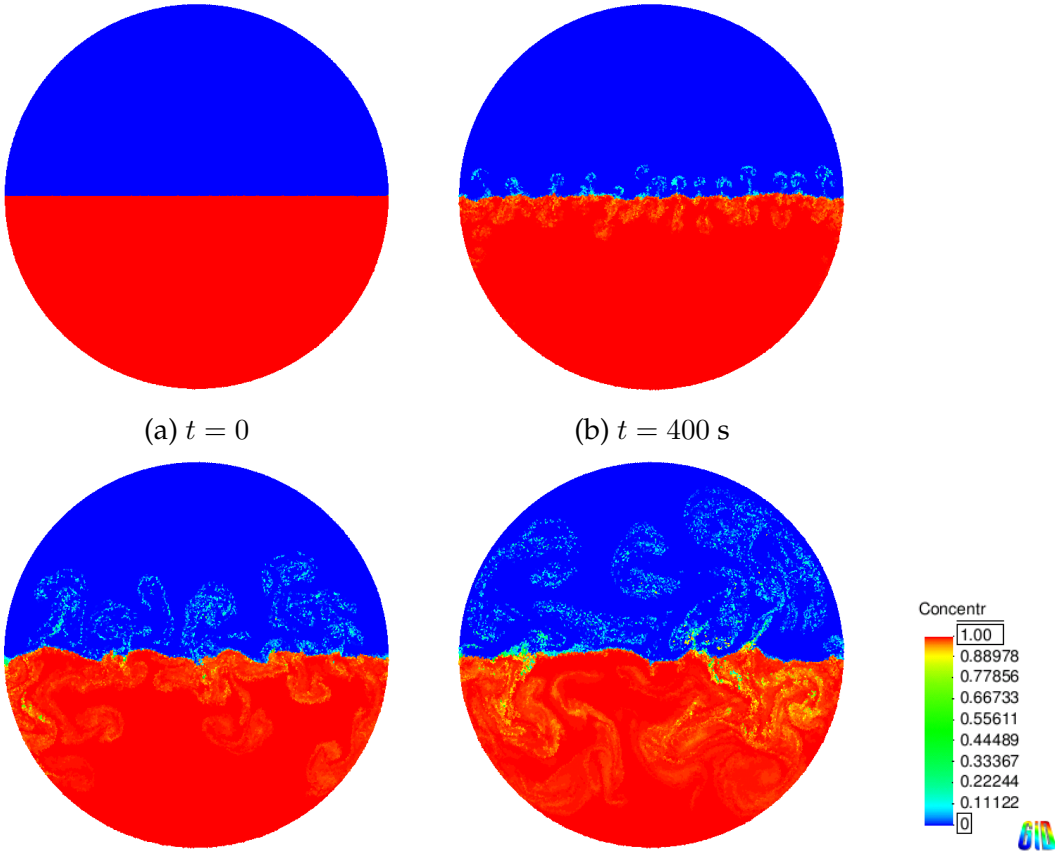

(a) $t = 0$ (b) $t = 400$ s

(c) $t = 800$ s (d) $t = 1200$ s

Figure 4.22: Gravitationally stable case ($\kappa = \kappa_{real} \times 10^9$, $D = D_{real} \times 10^9$). Composition (red = basaltic andesite, blue = dacite).

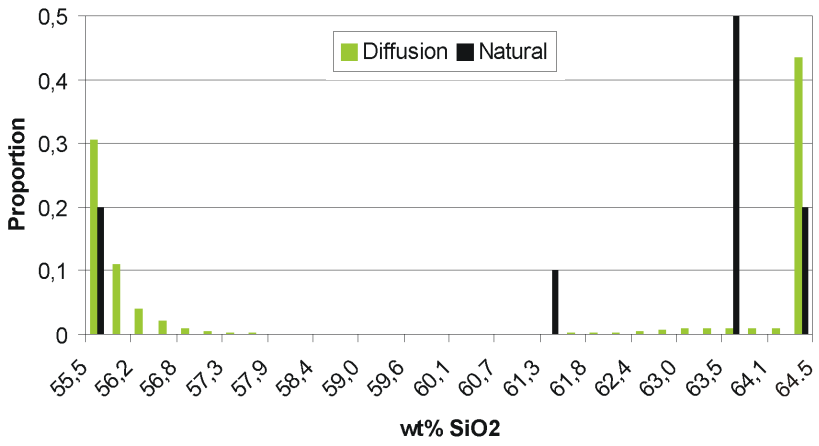

Figure 4.23: Gravitationally stable case. Compositional histogram at $t = 1200$ s compared to the natural one.

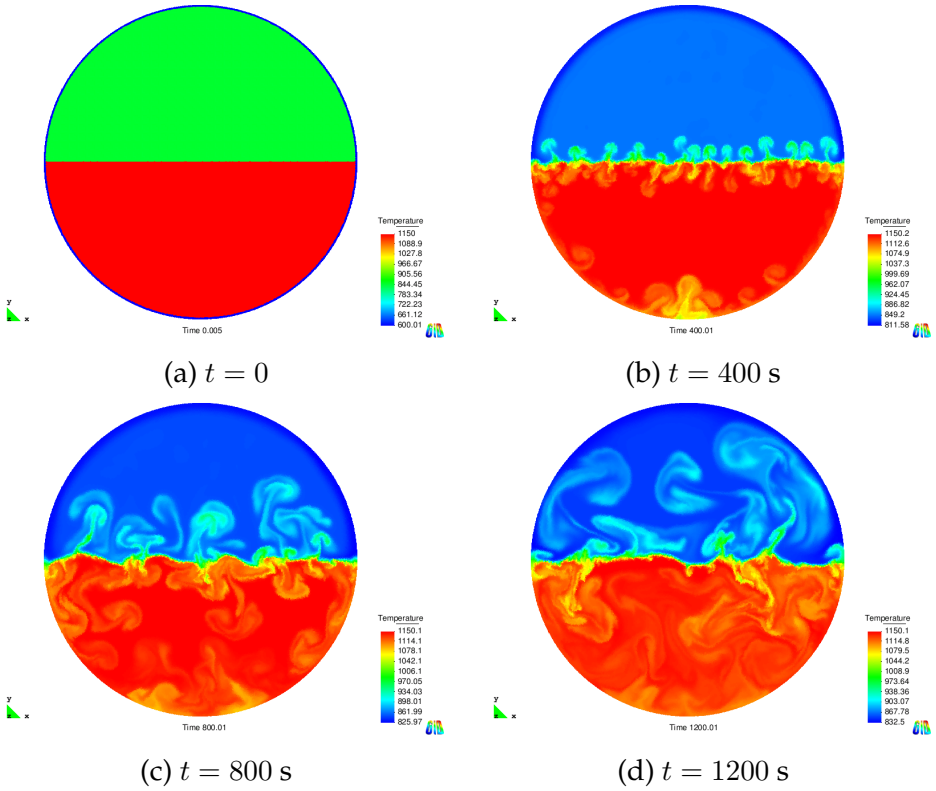

(a) $t = 0$ (b) $t = 400$ s

(c) $t = 800$ s (d) $t = 1200$ s

Figure 4.24: Gravitationally stable case. Temperature field (note that the ranges of the legends change in each subfigure to make plumes more visible).

geological, geochemical, and petrological data on the San Pedro eruption. The natural compositional histograms (Fig. 4.31a) cannot be achieved by mixing with diffusion only, as could be anticipated by the small diffusion rates on silicate melts to allow for volumetrically significant magma hybridization. A scenario where the mafic magma passively intruded at the base of the silicic reservoir with a simple flat interface does not lead to the natural compositional distribution either (Fig. 4.31b). Some form of forced convection by forceful intrusion is necessary. The scenario of forceful intrusion of mafic melt at the intermediate parts of the silicic reservoir leads to compositions in the silica-rich part of histogram that overlap with those of the natural rocks (Fig. 4.31c). The exception is the mode in the andesite that is not found in the numerical calculations. This composition is not seen either in the simulation with two ”instantaneous intrusions” (Fig. 4.31d) and thus other processes or situations not included in the model have played a role.

The Particle Finite Element Method is a good approach for simulating mixing of multicomponent fluids with non-linear dependencies of physical properties (viscosity, density, diffusivity) on composition and temperature. However, we were not able to achieve a steady state and we had to increase both the thermal

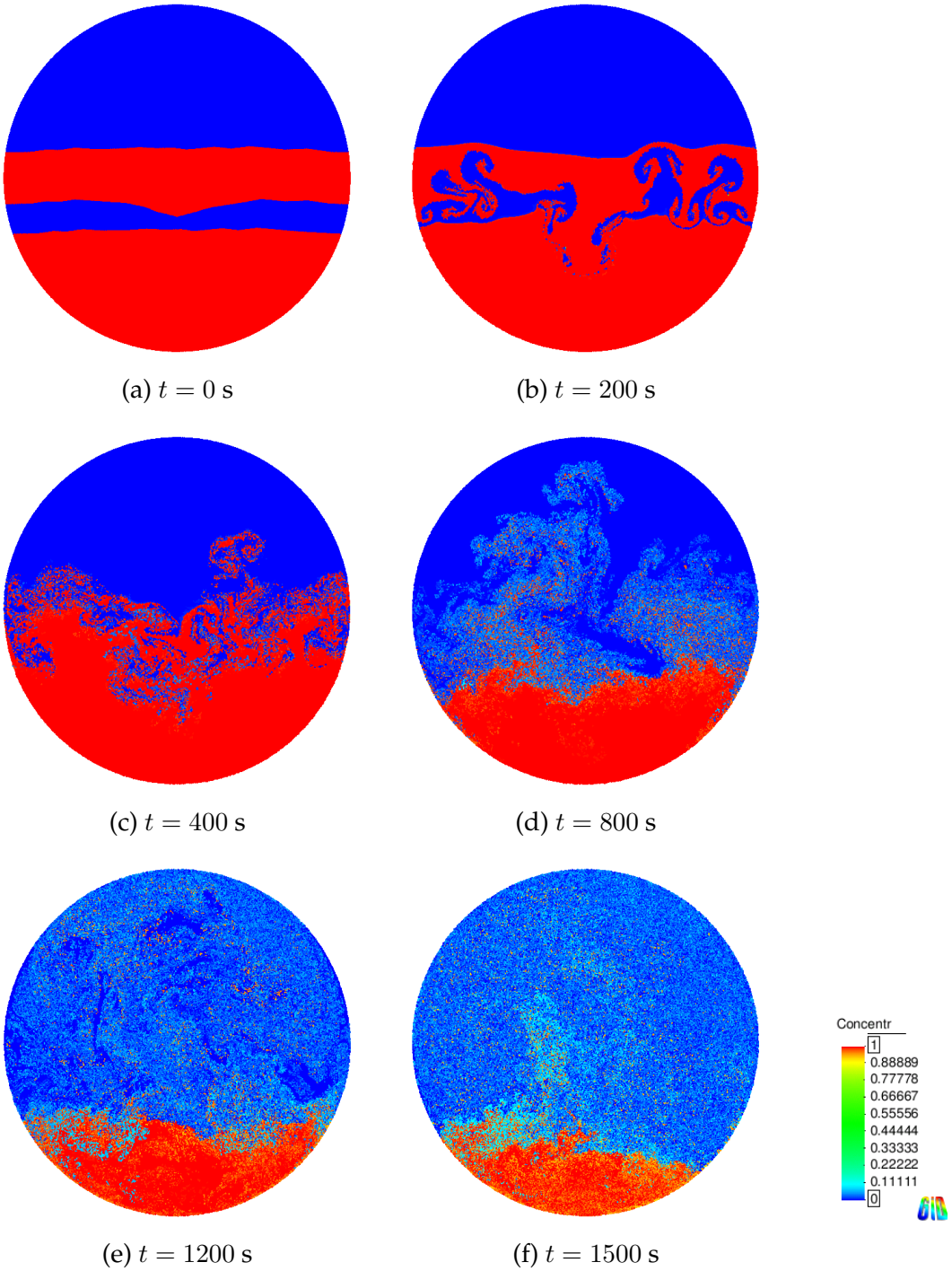

(a) $t = 0$ s (b) $t = 200$ s

(c) $t = 400$ s (d) $t = 800$ s

(e) $t = 1200$ s (f) $t = 1500$ s

Figure 4.25: Composition field in one-intrusion case at different times (red = basaltic andesite, blue = dacite).

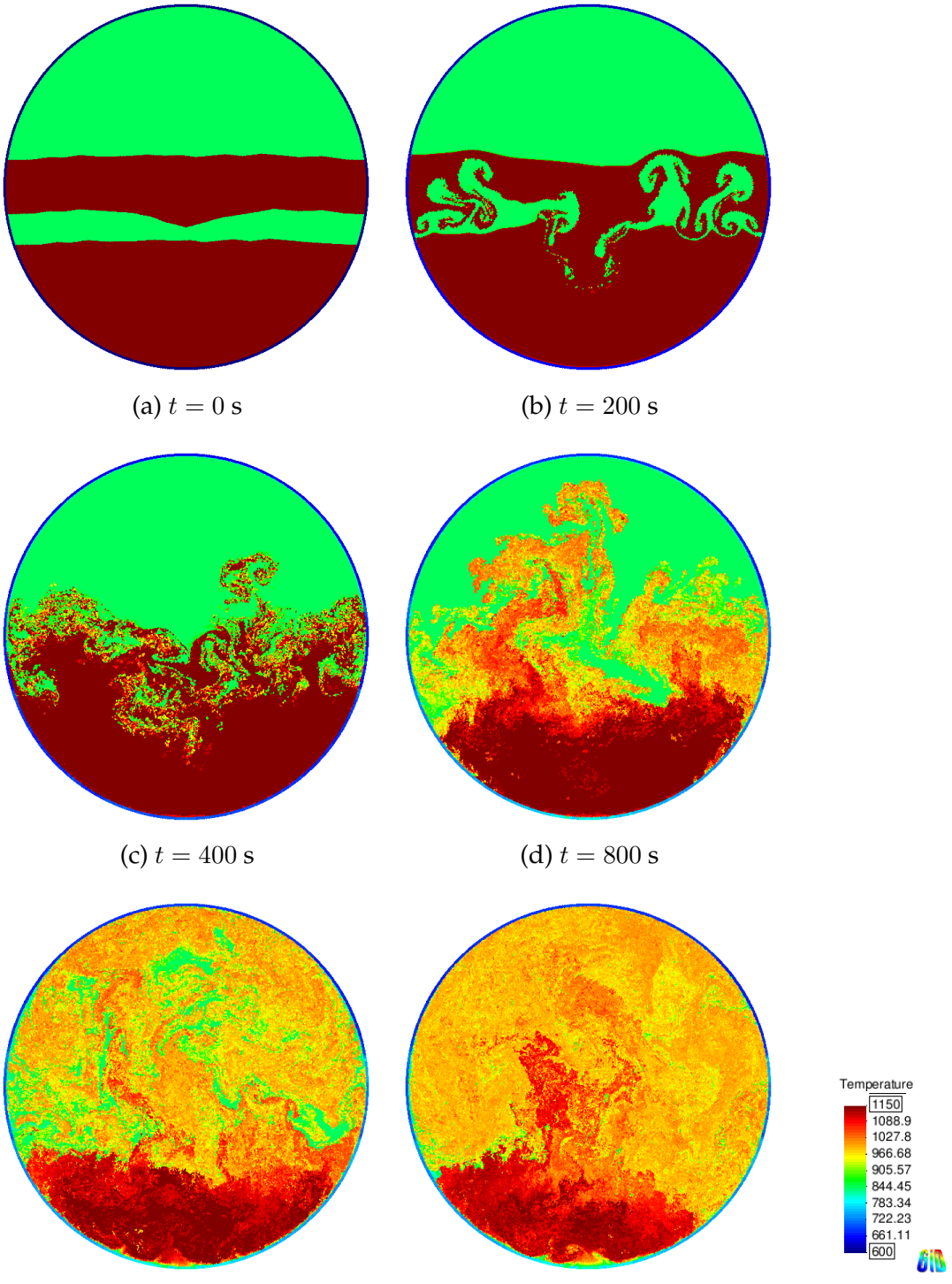

(a) $t = 0$ s (b) $t = 200$ s

(c) $t = 400$ s (d) $t = 800$ s

(e) $t = 1200$ s (f) $t = 1500$ s

Figure 4.26: Temperature field [$^{\circ}C$] in one-intrusion case at different times.

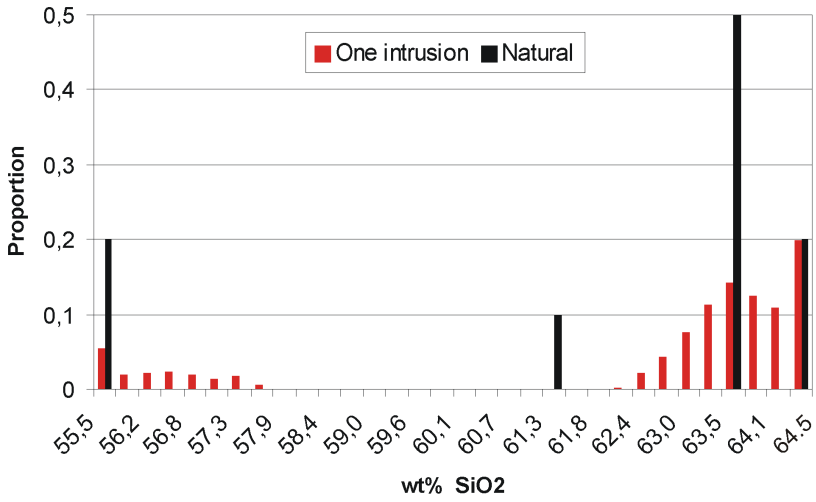

Figure 4.27: Comparison of one-intrusion composition histogram at $t = 1500$ s with the natural one.

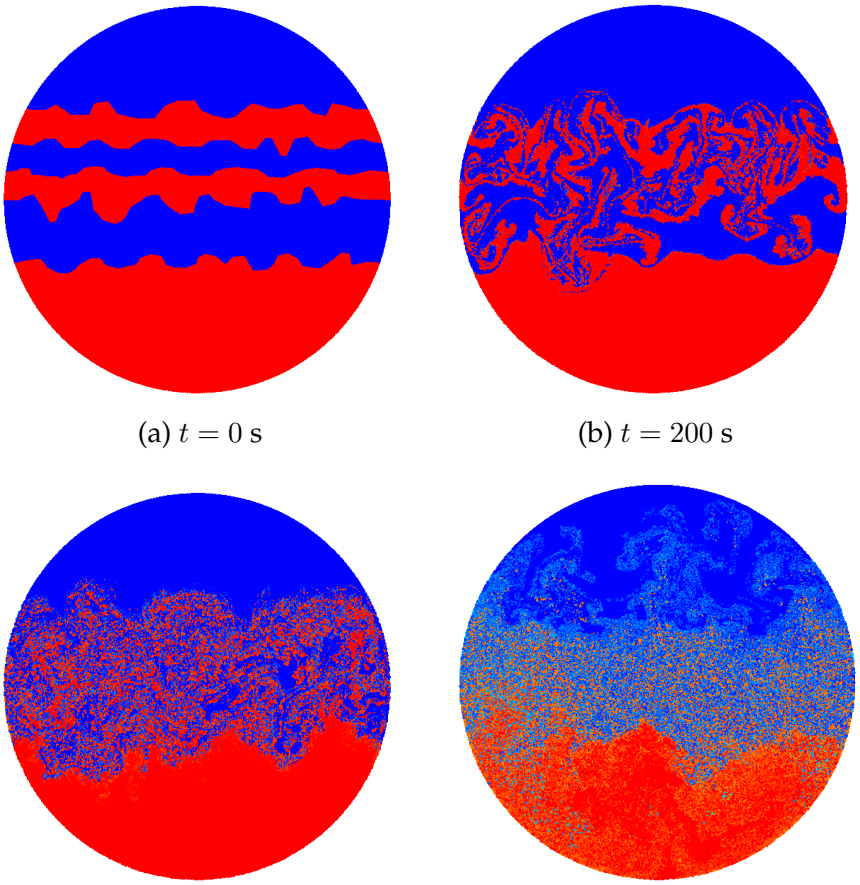

(a) $t = 0$ s (b) $t = 200$ s

(c) $t = 400$ s (d) $t = 1000$ s

Figure 4.28: Composition field in two-intrusion case (red = basaltic andesite, blue = dacite).

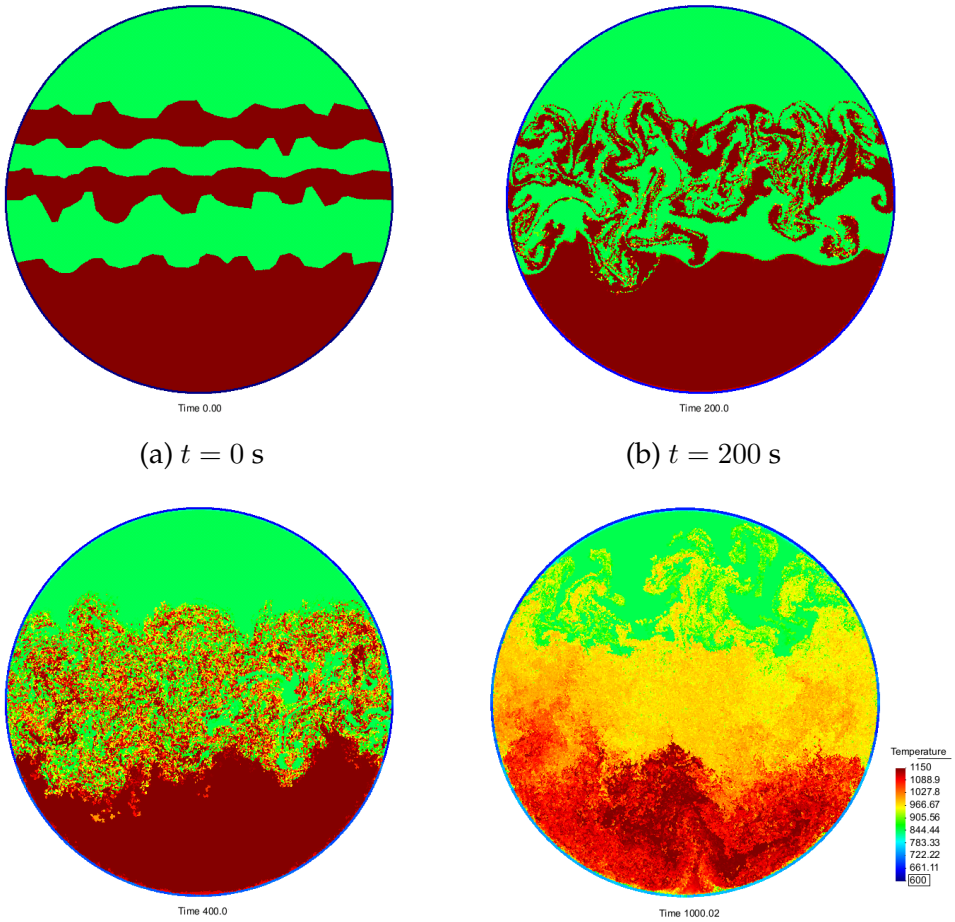

(a) $t = 0$ s (b) $t = 200$ s

(c) $t = 400$ s (d) $t = 1000$ s

Figure 4.29: Temperature field in two-intrusion case.

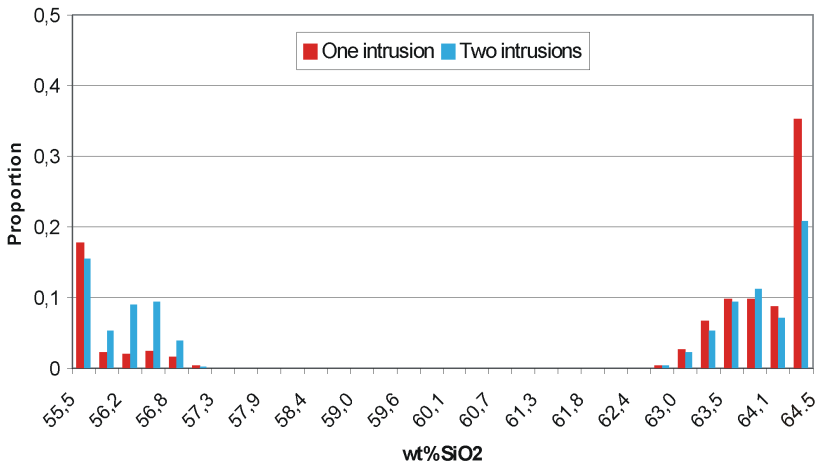

Figure 4.30: Comparison of two-intrusion composition histogram (blue) to one-intrusion (red) at $t = 1000$ s.

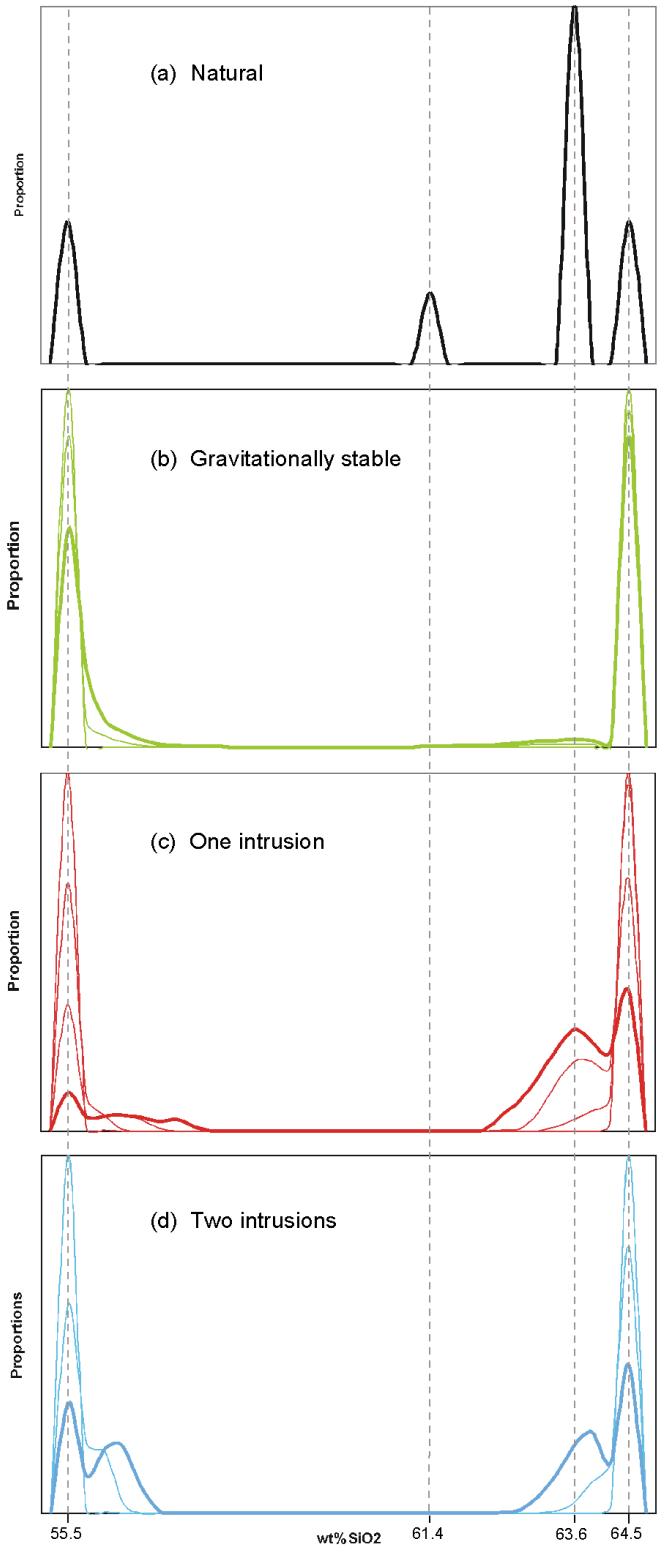

Figure 4.31: Summary of compositional histograms (time evolution) produced by the simulations and compared to the San Pedro volcano erupted rocks. In bold are the results of longest simulation.

and chemical diffusivity coefficients by several orders of magnitude to obtain meaningful results in a reasonable computing time. Additional progress in numerical methods is in general required to cope with the large ranges of space (μm to km) and time (hours to thousands of years), as well as with the open system behavior of magma reservoirs (repetitive intrusion and eruption).

4.6 Negatively buoyant jets: experimental and numerical study

We have seen that in the case of replenishing magma chambers, mixing only happens if the jet of injected fluid has sufficient momentum to penetrate and engulf the resident magma. We are now interested in understanding the evolution of the replenishment by a denser input of magma and will focus on the behavior of these forceful intrusions. For this purpose we have chosen a controlled example with simpler fluids (oil and water) and compared our numerical results with the experiments performed at the Earth Sciences Laboratory of the University of Bristol (Geyer et al. [37]). This work has been done in collaboration with Dr. A. Geyer.

In this section the flow produced by the injection of a dense fluid into a lighter one is investigated. When a dense fluid is injected vertically upward into a lighter fluid, its momentum is continually being decreased by the gravity force until the vertical velocity vanishes at some distance from the source. The jet reaches its maximum penetration length, reverses its direction and flows back in an annular region around the upflow (Fig. 4.32). Such jets are called *negatively buoyant jets* or *fountains*, and the density difference may be due to a variation in either chemical composition or temperature.

Fluid dynamic behavior of negatively buoyant jets may be applied to several geological situations, e.g. the mentioned replenishment of magma chambers in the Earth's crust (Campbell & Turner [19], Turner & Campbell [104], Campbell & Turner [20], Baines et al. [7, 6]) or underwater volcanic eruptions (Friedman et al. [35]). In the latter case, the mixing and mingling process between the injected (hot magma) and the ambient fluid (marine water) may be important, since the amount of phase mingling between fluids determines whether the eruption is an explosive or passive event (Kokelaar [51], Wohletz [113]).

During the last fifty years, the behavior of negatively buoyant jets or fountains has been widely explored theoretically, experimentally and numerically (Morton [69], Turner [105], List [62], Mizushina et al. [68], Baines et al. [7], Bloomfield & Kerr [12], Clanet [24], Bloomfield & Kerr [13, 14], Lin & Armfield [58, 59], Philippe et al. [82], Kaye & Hunt [49], Friedman et al. [36], Williamson et al. [112], Lin &

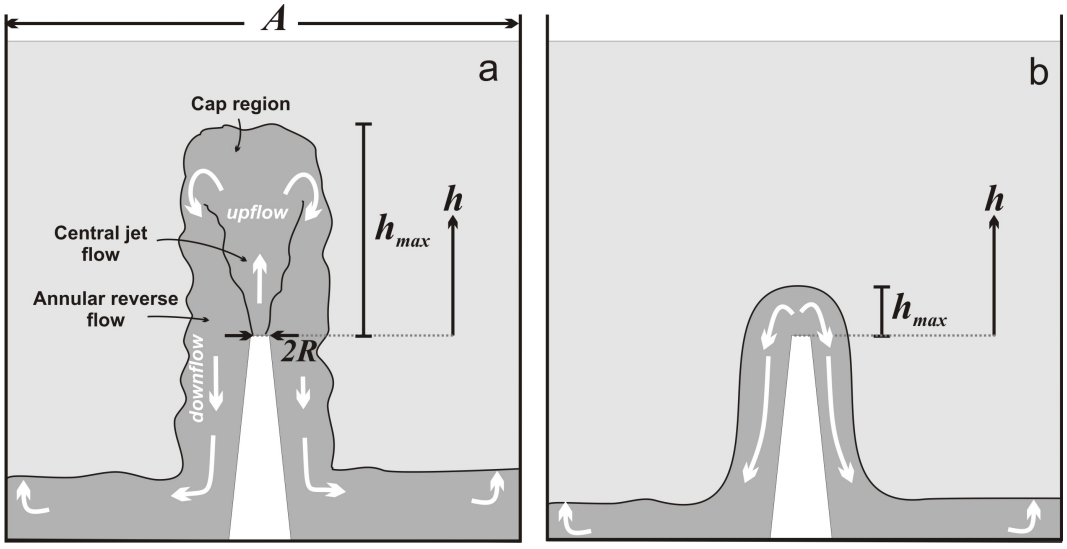

Figure 4.32: Sketch of a strong (a) and a weak (b) fountain. Description of the different parameters is found in Table 4.8 and text.

Armfield [61]). Since the pioneering work of Morton [69], significant progress has been made in understanding the dynamics of negatively buoyant jets, arriving to a general description of their flow behavior, summarized briefly as follows. The jet penetrates initially to a maximum height h_{max} in the tank, which depends on the initial upward momentum and the opposing downward negative buoyancy force. Then the jet collapses decreasing its penetration height and reaching a steady state where the penetration depth remains constant. This stationary depth is slightly smaller than h_{max}. In negatively buoyant jets, three flow regimes can be distinguished (Fig. 4.32a) (Cresswell & Szczepura [26]): the central jet flow, the annular reverse flow, and the "cap" region where the large scale reversal of fluid takes place. For strong fountains (where the discharge momentum is relatively larger than negative buoyancy of the flow) the fountain top, plunging plume and intrusion flow are distinct features (Fig. 4.32a), whereas for weak fountains (discharge momentum equal or less than negative buoyancy) the fluid exiting the fountain remains attached to the nozzle due to capillary and gravity forces, i.e. the upward and downward flows cannot be visually distinguished. Instead, the streamlines curve and spread from the source and fountain top (Fig. 4.32b).

The most common dimensionless numbers applied to the study of negatively buoyant jets are summarized in Table 4.8. The Reynolds number (Re) as defined here characterizes the ratio between inertia and viscous effects in the flow at the nozzle. The Froude number (Fr) compares kinetic energy to gravitational energy, which can be also expressed by the Richardson number Ri, being $Fr = Ri^{-1/2}$.

Furthermore, interfacial tension effects and characteristic frequency for the flow structure are non-dimensionalized in the Weber (We) and Strouhal (Str) numbers, respectively. Phase mingling onset conditions and characteristic diameters are non-dimensionalized in the Bond number (Bo).

4.6.1 Numerical results

Numerical simulation of negatively buoyant jets is challenging as it may involve fluids with considerably different density and viscosity, and complex interfacial phenomena such as surface tension and changes in topology (e.g. jet breakup in drops, or coalescence of drops). Previous numerical studies (Table 4.9) have performed direct numerical simulation of thermal axisymmetric and plane fountains up to $Fr = 10$ using the finite volume method. In these models, the density gradient between both fluids is due to a difference in temperature, therefore the density jump between fluids is smoothed due to thermal diffusion, and viscosity is considered equal in both fluids. None of these studies considers the role of interfacial tension.

We have numerically investigated the dynamics of negatively buoyant jets in a homogenous immiscible ambient fluid. For this purpose, we have used the Particle Finite Element Method (PFEM) to solve the isothermal, incompressible Navier-Stokes equations. The presented two-dimensional models include interfacial tension and the sharp jumps in the physical properties (density and viscosity) of the fluids. Pressure approximation is discontinuous at the interface to resolve accurately the pressure jump caused by surface tension and viscosity difference. In the first attempts of modeling this problem with continuous pressure, incompressibility could not be satisfied at the interfaces, and water drops lost mass and even disappear.

The simulated process corresponds to the continuous injection of colored water into a cylindrical container filled with rapeseed oil, through a conical nozzle located at the base of the oil container. The physical properties of both fluids are listed in Table 4.8 and the computational domain consists of a container of width A, non-slip side and bottom walls, and open top. In this problem, the injection of the dense fluid (water) has been implemented as a solid piston that pushes the fluid into the container filled with the lighter ambient fluid (oil). This yields uniform source velocity profiles. The element size of the unstructured triangular mesh is $\Delta x = 0.002$ m (50 elements along the tank width) and has been refined to $\Delta x/4$ at the interface to calculate the curvature more accurately (see Figure 4.33). Note that in this section Δx denotes the mesh size and h, the jet height.

In the different numerical runs, we have varied the injection velocity and the nozzle radius to reproduce a wide range of Reynolds and Froude numbers. In

A	Container diameter	0.1	m
d	Nozzle diameter (in numerical models)	2.62-3.5 $\times 10^{-3}$	m
R	Nozzle radius	$d/2$	m
g	Gravity	9.81	m s^{-2}
g'	Reduced gravity	$g' = g\frac{\rho_j - \rho_a}{\rho_j}$	m s^{-2}
h_{max}	Maximum penetration depth		m
$\boldsymbol{n}$	Normal direction		-
Q	Volumetric flow rate		m^3 s^{-1}
u_j	Vertical jet velocity		m s^{-1}
$\bar{u}$	Average vertical velocity		m s^{-1}
u^*	Characteristic jet velocity		m s^{-1}
ρ_a	Density of ambient fluid (oil)	900	kg m^{-3}
ρ_j	Density of jet fluid (water)	1000	kg m^{-3}
γ	Interfacial tension coefficient (water-oil)	0.02	N m^{-1}
μ_a	Dynamic viscosity of ambient fluid (oil)	200×10^{-3}	Pa s
μ_j	Dynamic viscosity of jet fluid (water)	10^{-3}	Pa s
f	Characteristic frequency of flow structure		s^{-1}

Bo	Bond number : Gravity vs. Surface tension	Bo=$\frac{R^2 g(\rho_j - \rho_a)}{\gamma}$
Fr	Froude Number: Inertia vs. Buoyancy	$Fr = \frac{u_j}{\sqrt{Rg'}} = Ri^{-1/2}$
H_{max}	Dimensionless h_{max}	$H_{max} = \frac{h_{max}}{R}$
Re	Reynolds number: Inertia vs. Viscosity	$Re = \frac{\rho_j u_j R}{\mu_j}$
Ri	Richardson number: Buoyancy vs. Inertia	$Ri = \frac{Rg'}{u_j^2} = Fr^{-2}$
Str	Strouhal number: Oscillations frequency	$Str = \frac{fR}{u_j}$
We	Weber number: Inertia vs. Surface tension	$We = \frac{\rho_a u_j^2 R}{\gamma}$

Table 4.8: List of variables, parameter values and their SI units, and dimensionless groups.

Reference	Jet flow	Range of Fr	Range of Re
Lin & Armfield [58]	laminar/very weak	$0.0025 < Fr < 0.2$	$5 < Re < 800$
Lin & Armfield [57]	laminar/weak	$0.2 < Fr < 1.0$	$Re = 200$
Lin & Armfield [56, 59]	laminar/weak	$0.2 < Fr < 1.0$	$5 < Re < 200$
Lin & Armfield [60]	laminar/weak	$Fr = 1$	$5 < Re < 800$
Lin & Armfield [61]	laminar/weak-forced	$1 < Fr < 8$	$200 < Re < 800$
Srinarayana et al. [98]	laminar/weak-forced	$0.25 < Fr < 10.0$	$Re = 100$
Williamson et al. [112]	turbulent/weak-forced	$Fr = 0.45, 2.2$	$Re = 3350$

Table 4.9: Summary of previous numerical models for negatively buoyant jets.

contrast to previous published results (Table 4.9), numerical simulations presented here cover a larger Froude number interval, $0.1 < Fr < 30$, being able to reproduce both weak and strong fountains in a laminar regime ($8 < Re < 1350$). The numerical results allow us to describe three different fountain behaviors (Type I, II and III), as well as to analyze quantitatively the whole injection process, and they are compared to the results of a parallel experimental study by Geyer et al. [37].

We have performed a total of 12 two-dimensional numerical simulations which are compared to more than 70 experimental results. Figure 4.34 shows the values of Fr and Re for both the numerical and the experimental models, and includes also the ranges covered by the previous numerical works. The PFEM simulations A-L, together with the corresponding values for the dimensionless maximum height H_{max}, Fr and Re are listed in Table 4.10.

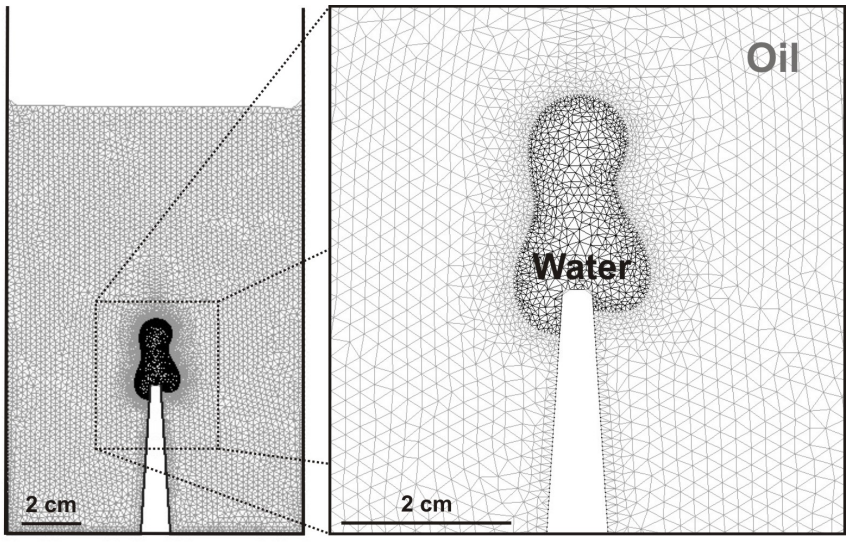

Figure 4.33: Detail of the unstructured mesh refined close to the interface.

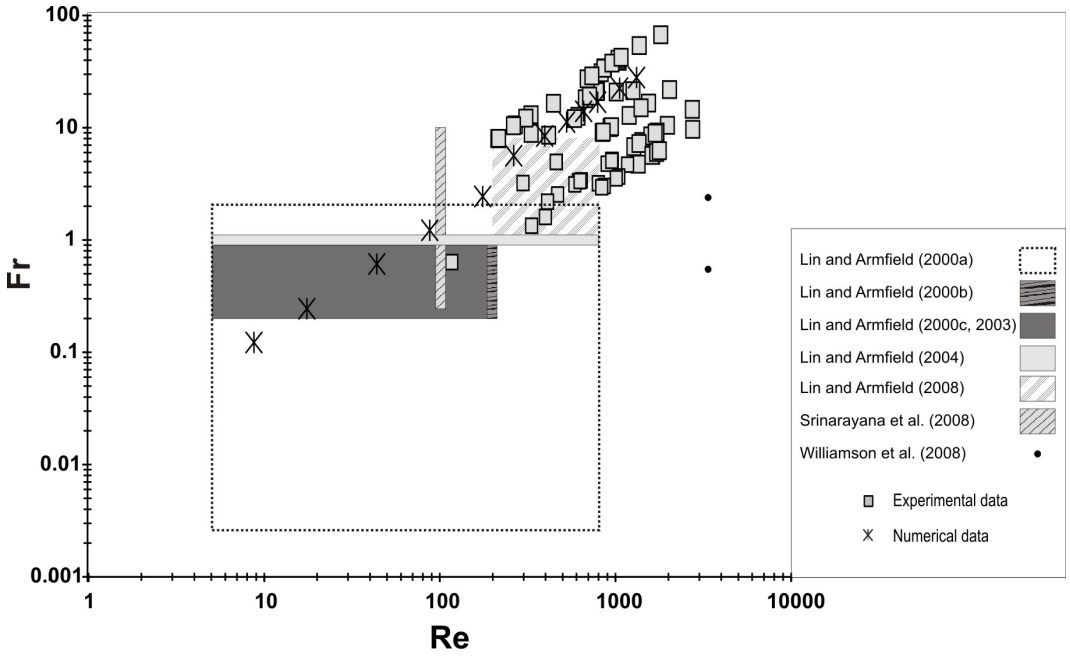

Figure 4.34: Fr-Re graph showing the parameter ranges investigated by previous numerical studies. The (Fr, Re) pair values for both the numerical and the experimental studies presented here are shown as symbols.

Simulation	R (m)	$\boldsymbol{u}$ (m/s)	H_{max}	Fr	Re
A	1.75×10^{-3}	0.005	2.25	0.12	8.75
B	1.75×10^{-3}	0.01	3.24	0.24	17.50
C	1.75×10^{-3}	0.025	2.74	0.60	43.75
D	1.75×10^{-3}	0.05	3.7	1.21	87.50
E	1.75×10^{-3}	0.1	6.04	2.41	175.00
F	1.31×10^{-3}	0.2	18.58	5.57	262.50
G	1.31×10^{-3}	0.3	23.9	8.36	393.75
H	1.31×10^{-3}	0.4	43.28	11.15	525.00
I	1.31×10^{-3}	0.5	66.82	13.93	656.25
J	1.31×10^{-3}	0.6	76.58	16.72	787.50
K	1.31×10^{-3}	0.8	–	22.29	1050.0
L	1.31×10^{-3}	1.0	–	27.87	1312.50

Table 4.10: List of the performed simulations.

Figures 4.35 and 4.36 illustrate the results obtained for increasing Fr values. For low Fr and Re numbers (simulation C) (Fig. 4.35a), we observe a weak fountain with almost indistinguishable upward and downward flow. The fluid exiting the nozzle remains attached to the nozzle due to capillary and gravity forces. However, as the jet velocity is increased, i.e. increasing Fr and Re (simulation F) (Fig. 4.35b), the jet penetrates upward into the ambient liquid reaching h_{max} shortly after the start. Due to the fact that the simulations are two-dimensional, some oil regions get enclosed by water. These oil bubbles are lighter and therefore, they move upward until they merge the bulk oil. In Figure 4.36 we have included results for two simulations with high inlet velocity. In case of simulation I ($u_j = 0.5$ m s^{-1}) (Fig. 4.36a), a cap forms when the jet reaches h_{max}, spreading radially as it is supplied with negatively buoyant jet fluid. In this simulation, we observe that the fountain flow emanating from the nozzle may be divided into a "smooth" part and a "wavy" one (Fig. 4.36a). The instability of the flow that leads to this transformation is due to the Kelvin-Helmholtz instability that occurs at the shear layer between the jet and the ambient fluid. Interfacial tension and viscosity delay the appearance of this instability. As the injection velocity is further increased (simulation L, $u_j = 1.0$ m s^{-1}) (Fig. 4.36b), the injected fluid breaks into droplets. In both simulations of Figure 4.36 it can be seen that some of the drops remain attached to the central cap region. This phenomenon is not a numerical artifact, it is also observable in the experimental results (see Figure 4.39).

The time evolution of the fountain height h for simulations A-G is presented in Figure 4.37. For the simulations with lower Fr numbers (simulations A-E), it can be seen that after reaching h_{max}, the jet height decreases and remains stably at a lower height. Oscillations are mainly due to capillary waves that propagate along the oil-water interface. As the injection velocity is increased (simulations F-G), this behavior changes and, after reaching h_{max}, the flow does not stabilize. Furthermore, in simulation F the flow oscillates in both a high frequency and a low frequency mode. In the case of simulations H to L, it is not possible to precisely define h due to the breakup of the jet into drops.

Figure 4.38 shows the vertical velocity field for simulations F, I and L. Upflow and downflow can be clearly identified in simulation F. The velocity profile also shows that the vertical velocity is nearly constant outside the jet. In strong fountains (simulations I and L), the ambient fluid is transported upward by the shear against the jet, and it can be observed that the flow accelerates in the narrower regions of the jet. The velocity profile is almost uniform close to the source due to the fact that the injection has been implemented as a piston.

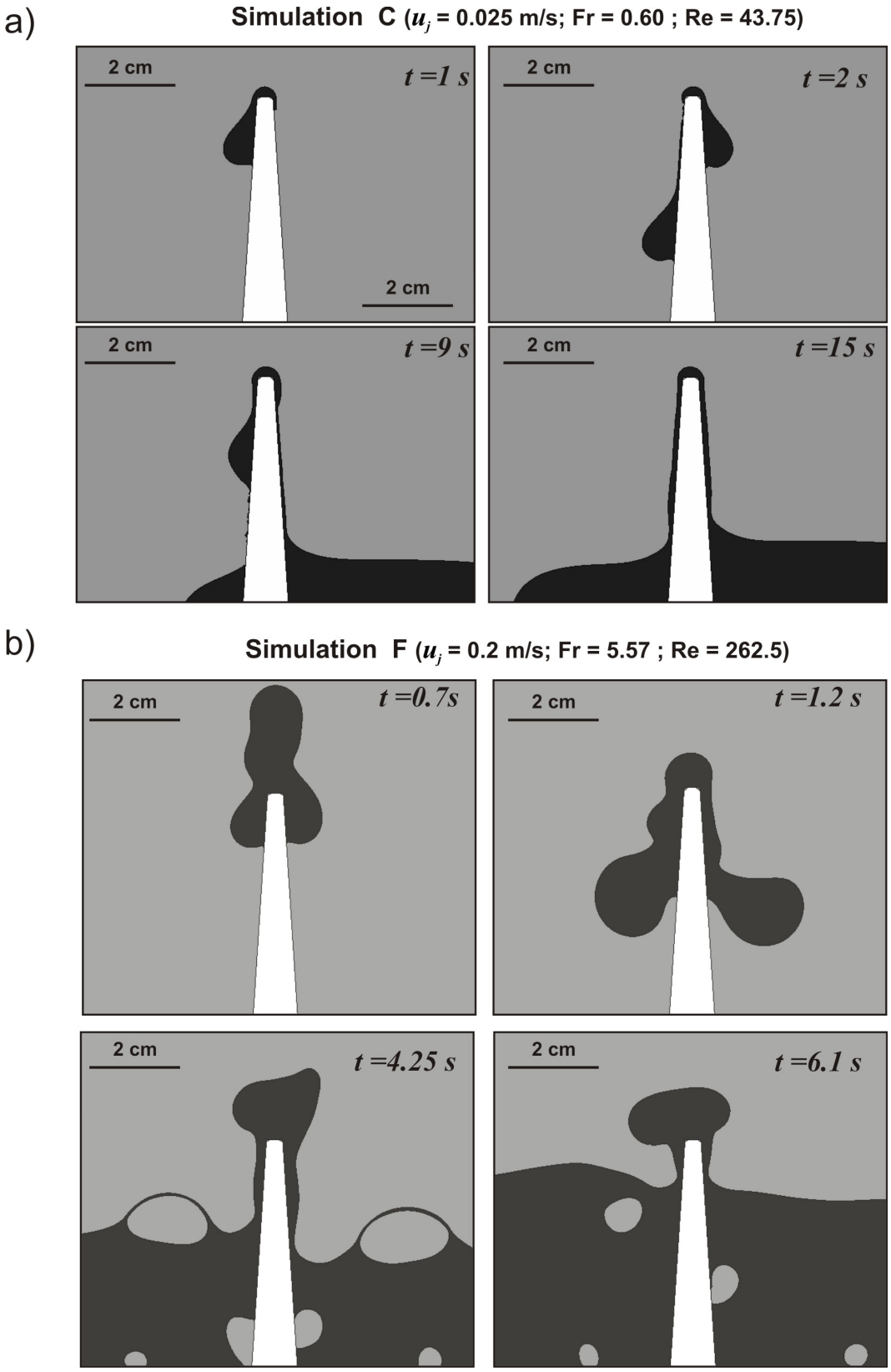

Figure 4.35: Flow evolution for simulations C and F (very weak and weak fountain, respectively).

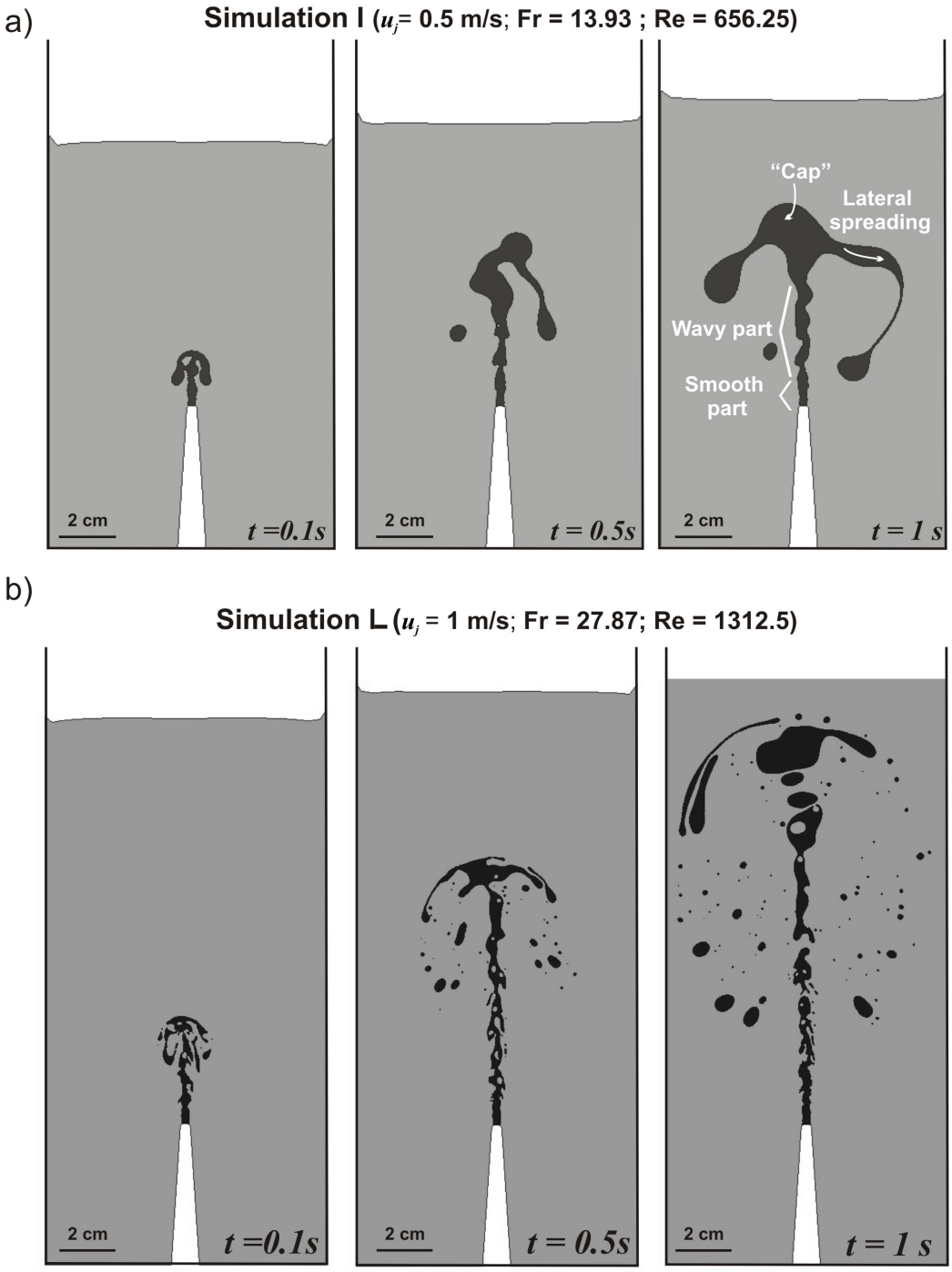

Figure 4.36: Flow evolution for simulations I and L (both strong fountains).

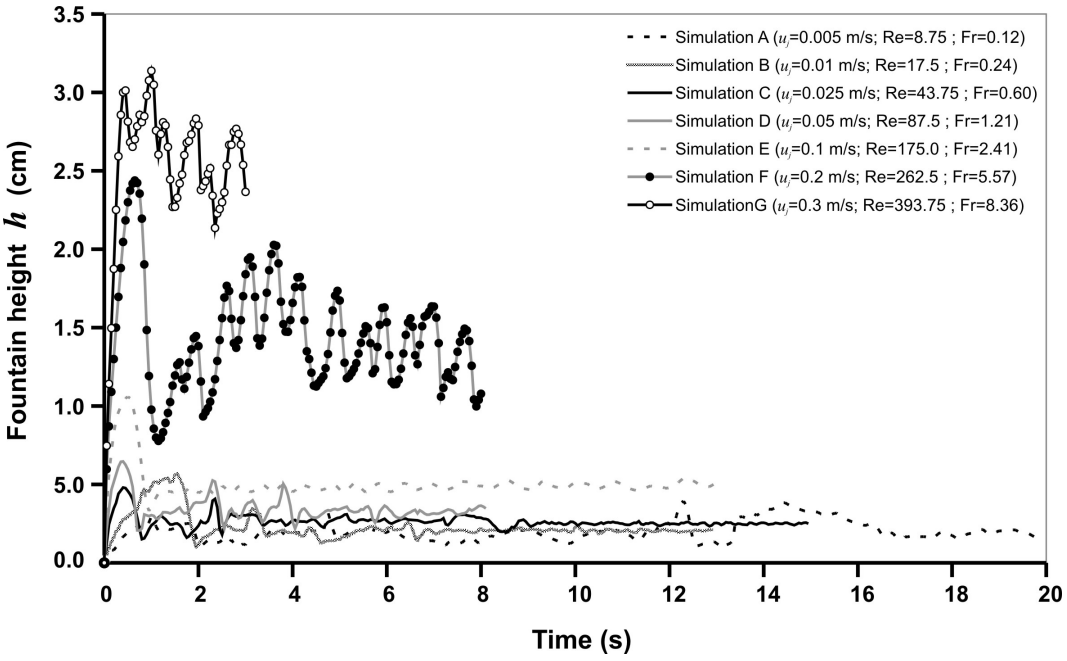

Figure 4.37: Jet height versus time for various numerical simulations.

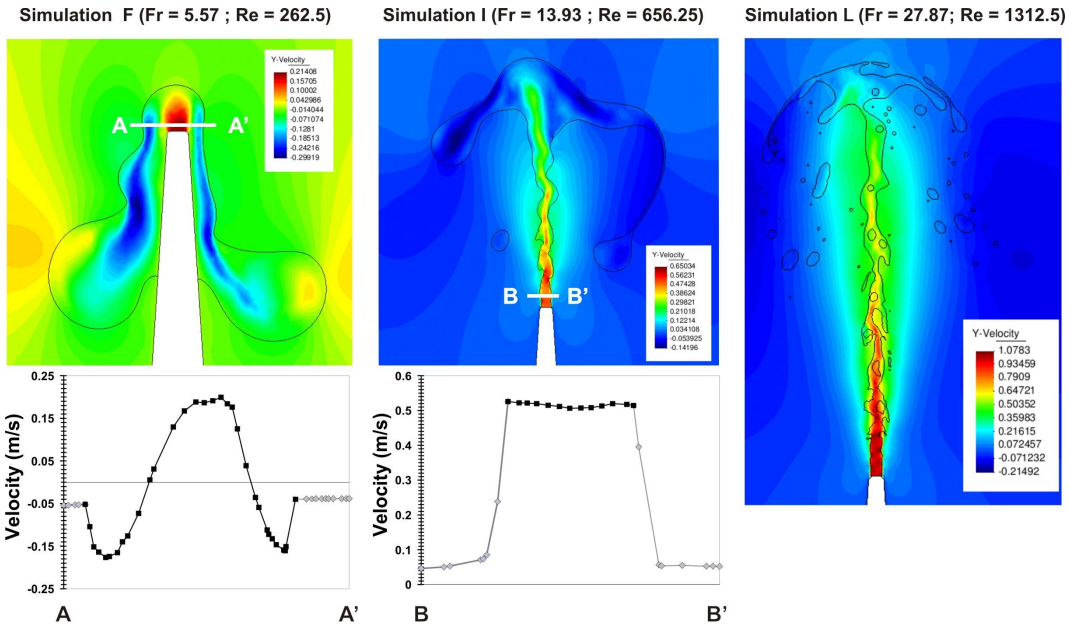

Figure 4.38: Vertical velocity field for simulation F (at time $t = 1.2$ s), I ($t = 1.0$ s) and L ($t = 0.5$ s), and profile along the cross sections AA′ and BB′ (2 mm above the nozzle).

4.6.2 Comparison between numerical and experimental data

In order to validate the PFEM simulations, the numerical results obtained have been compared to a series of laboratory experiments (Geyer et al. [37]). Our experimental results show that, for a given fountain geometry, the fountain exhibits distinct flow regimes as the inlet volumetric flow rate is increased, as previously observed in other experimental studies ([34, 35, 36]). But whereas Friedman et al. [35, 36] propose a classification in "stable" and "unstable" jets, our experiments identify three distinct flow regimes (Fig. 4.39): Type I, II and III. Flow regime I is observed at low source volumetric flowrates and is characterized by an approximately constant fountain height. As the source volumetric flowrate is increased, corresponding to increasing inlet velocity and thus fountain momentum, the fountain height is not constant, but is characterized by continuously varying with time t between a maximum h_{max} and a minimum height h_{min}; this is type II behavior. As the source volumetric flux and velocity is further increased, Type III behavior is observed. The jet initially penetrates upward into the ambient fluid and when it reaches h_{max}, a cap forms at the top of the jet. The size of this cap increases due to the continuous fluid supply from the fountain, but its vertical position remains constant at h_{max}. Once the cap exceeds a critical size, it breaks up and water droplets fall back to the base of the tank. In this regime, the fountain is also characterized by a smooth and a wavy part, as observed in the numerical simulations (Fig. 4.36). These three flow regimes are controlled by the Fr and Re values of the fountains. In Figure 4.40 we have plotted again the (Fr, Re) pairs for the different experimental and numerical results, and identified in each case the type of flow observed. According to this figure, simulations from A to E behave as Type I (see Fig. 4.35a); simulation F to J as Type II (see Fig. 4.35b) and simulation I onwards as Type III (see Fig. 4.36).

The correspondence between the numerical and experimental results is not limited to qualitative observations. In Figure 4.41 we have plotted the dimensionless height H_{max} against Fr in order to compare the results in a quantitative way. For Fr less than about 2, H_{max} is approximately constant with a value of about 3, but for greater Fr, H_{max} increases systematically with Fr. A plausible explanation for the constant H_{max} when $Fr < 2$ is that in our experiments, for a fixed nozzle radius, the Fr value is decreased by diminishing the jet velocity, what decreases the Weber number as well, so that capillary effects become dominant. The surface tension will cause the injected fluid to accumulate at the nozzle tip in a drop until its mass overcomes the surface tension force. Also important is the fact that, for $Fr \lesssim 4$, only Type I behavior is observed, whereas for greater Fr both Type II and Type III behaviors are observed. Comparing this result with the classification proposed by Friedman and co-workers (Friedman &

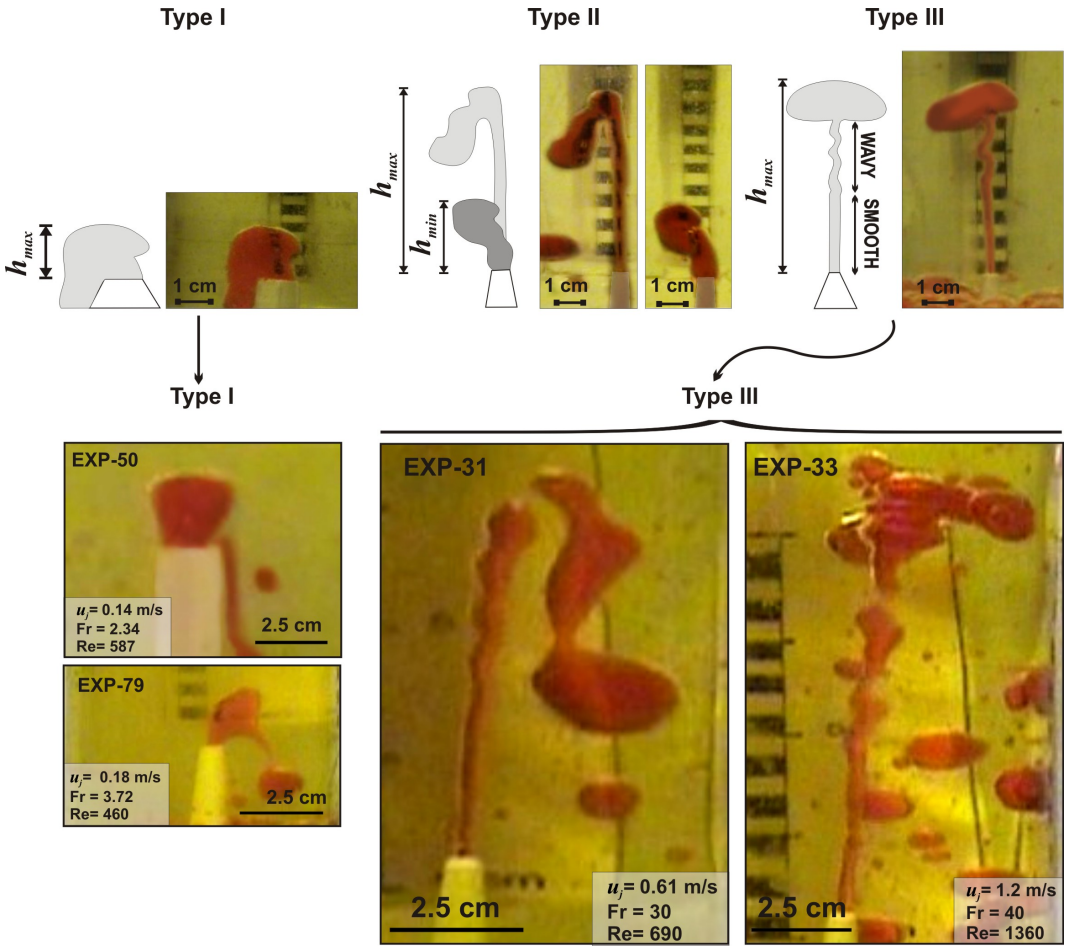

Figure 4.39: Sketches and images of the three different flow types observed in the experiments, and images of four different Type I and III experiments at a range of Fr and Re numbers.

Katz [34], Friedman [33], Friedman et al. [35, 36]) (i.e. unstable or stable), we can relate our Type I flow with their "stable" regime and Type II with their "unstable" one. However, no direct correlation can be made with Type III flow. Although some fluctuations of the column are observed in Type III flows, they are not related to a collapse of the fountain as is the case of the jets in Type II regime but to the growth and breakup of the cap region. Numerical and experimental results are in good agreement.

4.6.3 Conclusions

We have numerically investigated the dynamics of negatively buoyant jets in an immiscible fluid using the Particle Finite Element Method (PFEM). The realistic properties of the fluids used in the experiments have been taken into account, and

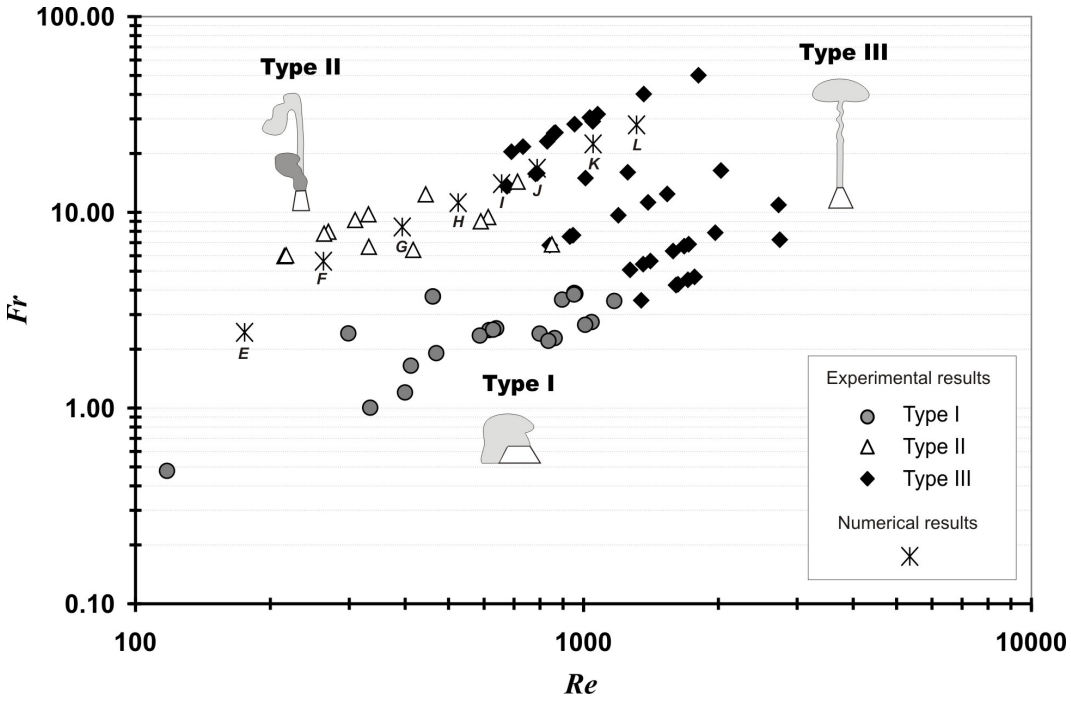

Figure 4.40: Fr vs. Re plot for the experimental and numerical results presented. Experimental results are classified according to the flow type: Type I, II and III.

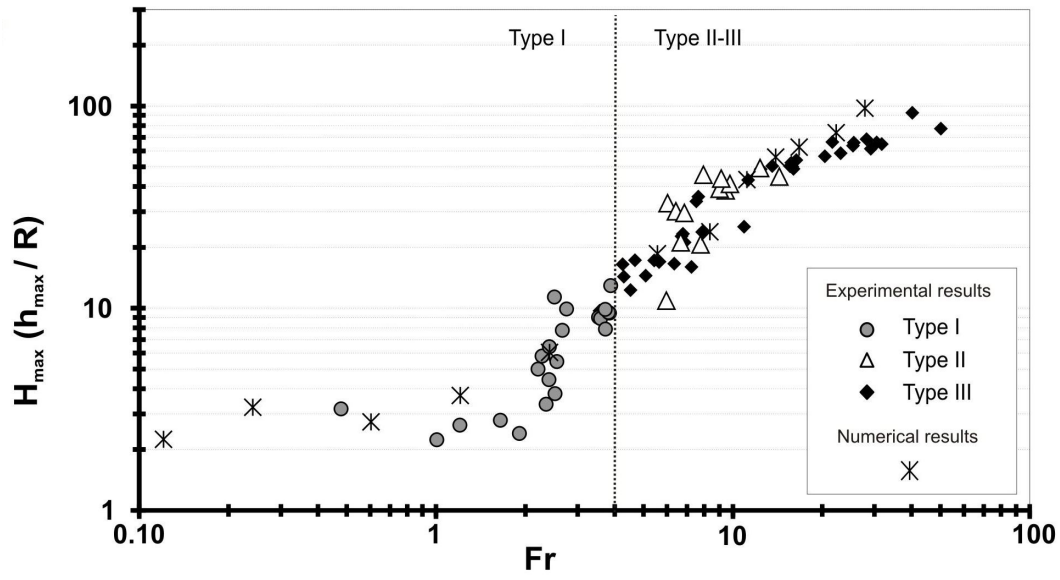

Figure 4.41: H_{max} vs. Fr plot for the experimental and numerical results presented.

the non-negligible interfacial tension, together with the large jumps in density and viscosity at the interface, and the frequent topology changes of the interface, make this problem challenging.

The simulated process corresponds to the injection of dyed water into a cylindrical container filled with oil through a conical nozzle located at the base of the container. In the different numerical runs, we have varied the injection velocity and the nozzle radius to reproduce a wide range of Froude ($0.1 < Fr < 30$) and Reynolds ($8 < Re < 1350$) numbers. The validation of the numerical results with experimental data has proven the accuracy of the PFEM and its potential for solving this kind of problems.

Whereas previous published works propose a classification in stable and unstable flows, our experimental results allow us to identify three distinct flow regimes:

- Type I is characterized to be very stable. The height of the fountain is approximately constant although we should not discard a slightly fluctuation of the column height but not detectable due to experimental accuracy.

- Type II behavior is described as a pulsating fountain which height oscillates with time t from a maximum h_{max} to a minimum height h_{min}. Additionally, it is possible to observe in the results that h_{max} decreases with t.

- Type III behavior is observable for higher injection velocities. The jet initially penetrates upward into the ambient fluid and, when it reaches h_{max}, a cap forms at the top of the jet. The fountain is characterized by a smooth and a wavy part.

Numerical results are in good agreement with the experiments, and are able to reproduce the main flow features, such as the three regimes types (I, II and III), the smooth and wavy parts of the jet, drops formation, penetration height transient behavior, and dimensionless maximum height. These simulations are a first step towards understanding the fluid dynamics of several geological situations (e.g. subaqueous lava fountains or the replenishment of magma chambers by a dense input of magma).

References

[1] Anderson, A., 1976. Magma mixing: petrological process and volcanological tool. Journal of Volcanology and Geothermal Research 1, 3–33.

[2] Aref, H., and G. Tryggvason, 1984. Vortex dynamics of passive and active interfaces. Physica D: Nonlinear Phenomena 12, 59–70.

[3] Aref, H., and G. Tryggvason, 1989. Model of Rayleigh-Taylor instability. Physical Review Letters 62.

[4] Bacon, C., 1986. Magmatic inclusions in silicic and intermediate volcanic rocks. Journal of Geophysical Research 91, 6091–6112.

[5] Bagdassarov, N., and A. Fradkov, 1993. Evolution of double diffusion convection in a felsic magma chamber. Journal of Volcanology and Geothermal Research 54, 291–308.

[6] Baines, W. D., A. Corriveau, and T. J. Reedman, 1993. Turbulent fountains in a closed chamber. Journal of Fluid Mechanics 255, 621–646.

[7] Baines, W. D., J. S. Turner, and I. H. Campbell, 1990. Turbulent fountains in an open chamber. Journal of Fluid Mechanics 212, 557–592.

[8] Baker, G., D. Meiron, and S. Orszag, 1980. Vortex simulations of the Rayleigh-Taylor instability. Physics of Fluids 23(8), 1485–1490.

[9] Bell, and Marcus, 1992. A second order projection method for variable-density flows. Journal of Computational Physics 101, 334–348.

[10] Bénard, H., 1901. Les tourbillons cellulaires dans une nappe liquide transportant de la chaleur par convection en regime permanent. Annales des Chimie et des Physique XXIII, 62–144.

[11] Bergantz, G., 1995. Changing techniques and paradigms for the evaluation of magmatic processes. Journal of Geophysical Research 100, 17603–17613.

[12] Bloomfield, L., and R. Kerr, 1998. Turbulent fountains in a stratified fluid. Journal of Fluid Mechanics 358, 335–356.

[13] Bloomfield, L., and R. Kerr, 1999. Turbulent fountains in a confined stratified environment. Journal of Fluid Mechanics 389, 27–54.

[14] Bloomfield, L., and R. Kerr, 2000. A theoretical model of a turbulent fountain. Journal of Fluid Mechanics 424, 197–216.

[15] Boussinesq, J., 1903. Theorie analytique de la chaleur mise en harmonie avec la thermodynamique et avec la theori mecanique de la lumiere. In: Cours de physique mathématique de la Faculté des sciences. Gauthier-Villars, pp. 1–32.

[16] Burgisser, A., and G. Bergantz, 2004. Unfolding magma mixing. In: American Geophysical Union Spring Meeting 2004.

[17] Buttner, R., B. Zimanowski, J. Blumm, and L. Hagemann, 1998. Thermal conductivity of a volcanic rock material olivine-melilitite in the temperature range between 288 and 1470 k. Journal of Volcanology and Geothermal Research 80, 293–302.

[18] Byrde, O., 1997. Massively parallel flow computation with application to fluid mixing. Ph.D. thesis, Ecole Polytechnique Federale de Lausanne, Switzerland.

[19] Campbell, I., and J. Turner, 1986. The influence of viscosity on fountains in magma chambers. Journal of Petrology 27, 1–30.

[20] Campbell, I., and J. Turner, 1989. Fountains in magma chambers. Journal of Petrology 30, 885–923.

[21] Chakraborty, S., 1995. Diffusion in silicate melts. Reviews in Mineralogy and Geochemistry 32, 411–504.

[22] Chandrasekhar, S., 1961. Hydrodynamic and Hydromagnetic Stability. Oxford Univ. Press.

[23] Chella, R., and J. Viñals, Apr 1996. Mixing of a two-phase fluid by cavity flow. Physical Review E 53 (4), 3832–3840.

[24] Clanet, C., 1998. On large-amplitude pulsating fountains. Journal of Fluid Mechanics 366, 333–350.

[25] Costa, F., and B. Singer, 2002. Evolution of Holocene dacite and compositionally zoned magma, Volcan San Pedro, Southern Volcanic Zone, Chile. Journal of Petrology 43, 1571–1593.

[26] Cresswell, R., and R. Szczepura, 1993. Experimental investigation into a turbulent jet with negative buoyancy. Physics of Fluids 5, 2865–2878.

[27] Daly, B., 1967. Numerical study of two fluid Rayleigh-Taylor instability. Physics of Fluids 10, 297–307.

[28] DeVahl Davis, G., 1983. Natural convection of air in a square cavity: a benchmark numerical solution. International Journal for Numerical Methods in Fluids 3, 249–264.

[29] DeVahl Davis, G., and I. Jones, 1983. Natural convection in a square cavity: a comparison exercise. International Journal for Numerical Methods in Fluids 3, 227–248.

[30] Dobran, F., 2001. Volcanic processes. Mechanisms in material transport. Kluwer Academic.

[31] Dufek, J., and G. W. Bergantz, 2007. Dynamics and deposits generated by the Kos Plateau Tuff eruption: Controls of basal particle loss on pyroclastic flow transport. Geochemistry Geophysics Geosystems 8, Q12007.

[32] Dungan, M., and J. Rhodes, 1978. Residual glasses and melt inclusions in basalts from DSDP Leg 45 and 46: evidence for magma mixing. Contributions to Mineralogy and Petrology 67, 417–431.

[33] Friedman, P., 2006. Oscillation in height of a negatively buoyant jet. Journal of Fluids Engineering 128, 880–883.

[34] Friedman, P., and J. Katz, 1999. The flow and mixing mechanisms caused by the impingement of an immiscible interface with a vertical jet. Physics of fluids 11.

[35] Friedman, P., W. Meyer, and S. Carey, 2006. Experimental simulation of phase mingling in a subaqueous lava fountain. Journal of Geophysical Research 111, B07201.

[36] Friedman, P., D. Vadakoot, W. Meyer, and S. Carey, 2007. Instability threshold of a negatively buoyant fountain. Experiments in Fluids 42, 751–759.

[37] Geyer, A., J. Phillips, and M. Mier-Torrecilla, submitted. Flow behaviour of negatively buoyant jets in immiscible ambient fluid. Experiments in Fluids.

[38] Ghiorso, M., and R. Sack, 1995. Chemical mass transfer in magmatic processes iv. a revised and internally consistent thermodynamic model for the interpolation and extrapolation of liquid-solide quilibria in magmatic systems at elevated temperature and pressure. Contributions to Mineralogy and Petrology 119, 197–212.

[39] Giordano, D., J. Russell, and D. Dingwell, 2008. Viscosity of magmatic liquids: A model. Earth and Planetary Science Letters 271, 123–134.

[40] Gray, D., and A. Giorgini, 1976. The validity of the Boussinesq approximation for liquids and gases. International Journal of Heat and Mass Transfer 19, 545–551.

[41] Guermond, J.-L., and L. Quartapelle, 2000. A projection FEM for variable density incompressible flows. Journal of Computational Physics 165, 167–188.

[42] Hamblin, E., W.K.and Christiansen, 2000. Earth's dynamic systems. Prentice Hall.

[43] Harlow, A., F.H.and Amsden, 1971. A numerical fluid dynamics calculation method for all flow speeds. Journal of Computational Physics 8, 197–213.

[44] Houghton, B., H. Rymer, J. Stix, S. McNutt, and H. Sigurdsson, 1999. Encyclopedia of volcanoes. Academic Press.

[45] Idelsohn, S., M. Mier-Torrecilla, and E. Oñate, 2009. Multi-fluid flows with the Particle Finite Element Method. Computer Methods in Applied Mechanics and Engineering 198, 2750–2767.

[46] Jaupart, C., and S. Tait, 1995. Dynamics of differentiation in magma reservoirs. Journal of Geophysical Research 100, 17615–17636.

[47] Jellinek, A., R. Kerr, and R. Griffiths, 1999. Mixing and composicional stratification produced by natural convection. 1. Experiments and their application to Earth's core and mantle. Journal of Geophysical Research 104, 7183–7201.

[48] Jellinek, A., R. Kerr, and R. Griffiths, 1999. Mixing and composicional stratification produced by natural convection. 2. Applications to the differentiation of basaltic and silicic magma chambers and komatiite lava flows. Journal of Geophysical Research 104, 7203–7218.

[49] Kaye, N., and G. Hunt, 2006. Weak fountains. Journal of Fluid Mechanics 558, 319–328.

[50] Kim, H., and A. Beskok, 2007. Quantification of chaotic strength and mixing in a microfluidic system. Journal of Micromechanics and Microengineering 17, 2197–2210.

[51] Kokelaar, P., 1986. Magma-water interactions in subaqueous and emergent basaltic volcanism. Bulletin of Volcanology 48, 275–289.

[52] Lange, R., 1994. Volatiles in magmas. Mineralogical Society of America, Ch. The effect of H2O, CO2 and F on the density and viscosity of silicate melts, pp. 331–369.

[53] Lange, R., and I. Carmichael, 1990. Modern methods of igneous petrology. Mineralogical Society of America, Ch. Thermodynamic properties of silicate liquids with an emphasis on density, thermal expansion and compressibility, pp. 25–64.

[54] Le-Quere, P., C. Weisman, H. Paillere, J. Veierendeels, E. Dick, R. Becker, M. Braack, and J. Locke, 2005. Modelling of natural convection flows with large temperature differences: a benchmark problem for low mach number

solvers. ESAIM: Mathematical Modelling and Numerical Analysis 39, 609–616.

[55] Lesher, C., 1994. Kinetics of Sr and Nd exchange in silicate liquids: theory, experiments, and applications to uphill diffusion, isotopic equilibration, and irreversible mixing of magmas. Journal of Geophysical Research 99, 9585–9604.

[56] Lin, W., and S. Armfield, 2000. Direct simulation of weak axisymmetric fountains in a homogeneous fluid. Journal of Fluid Mechanics 403, 67–88.

[57] Lin, W., and S. Armfield, 2000. Direct simulation of weak laminar plane fountains in a homogeneous fluid. International Journal of Heat and Mass Transfer 43, 3013–3026.

[58] Lin, W., and S. Armfield, 2000. Very weak fountains in a homogeneous fluid. Numerical Heat Transfer, Part A 38, 377–396.

[59] Lin, W., and S. Armfield, 2003. The reynolds and prandtl number dependence of weak fountains. Computational Mechanics 31, 379–389.

[60] Lin, W., and S. Armfield, 2004. Direct simulation of fountains with intermediate Froude and Reynolds number. ANZIAM Journal 45, C66–77.

[61] Lin, W., and S. Armfield, 2008. Onset of entrainment in transitional round fountains. International Journal of Heat and Mass Transfer 51, 5226–5237.

[62] List, E., 1982. Turbulent jets and plumes. Annual Review of Fluid Mechanics 14, 189–212.

[63] Longo, A., M. Vassalli, P. Papale, and M. Barsanti, 2006. Numerical simulation of convection and mixing in magma chambers replenished with CO2-rich magma. Geophysical Research Letters 33.

[64] Marsh, B., 1984. Explosive volcanism: inception, evolution and hazards. National Academy Press, Ch. Mechanics and energetics of magma formation and ascension, pp. 67–83.

[65] Marsh, B., 1989. On convective style and vigor in sheet-like magma chambers. Journal of Petrology 30, 479–530.

[66] Marti, J., and A. Folch, 2005. Volcano and the environment. Cambridge University Press, Ch. Anticipating volcanic eruptions, pp. 90–120.

[67] McBirney, A., and T. Murase, 1984. Rheological properties of magmas. Annual Review of Earth and Planetary Sciences 12, 337–357.

[68] Mizushina, T., T. Ogino, H. Takeuchi, and H. Ikawa, 1982. An experimental study of vertical turbulent jet with negative buoyancy. Waerme- und Stoffuebertragung 16, 15–21.

[69] Morton, B., 1959. Forced plumes. Journal of Fluid Mechanics 5, 152–163.

[70] Murase, T., and A. McBirney, 1973. Properties of some common igneous rocks and their melts at high-temperatures. Geological Society of America Bulletin 84, 3563–3592.

[71] Mysen, B., and P. Richet, 2005. Silicate glasses and melts: properties and structure. Elsevier.

[72] Nagata, S., 1975. Mixing: Principles and Applications. Wiley.

[73] Oldenburg, C., F. Spera, D. Yuen, and G. Sewel, 1989. Dynamic mixing in magma bodies: theory, simulations and implications. Journal of Geophysical Research 94 (B7), 9215–9236.

[74] Oran, E., and J. Boris, 1987. Numerical simulation of reactive flow. Elsevier.

[75] Ottino, J., 1997. The kinematics of mixing: stretching, chaos, and transport. Cambridge University Press.

[76] Paillere, H., et al., 2005. Modelling of natural convection flows with large temperature differences: a benchmark problem for low mach number solvers. ESAIM: Mathematical Modelling and Numerical Analysis 39, 617–621.

[77] Paillere, H., C. Viozat, A. Kumbaro, and I. Toumi, 2000. Comparison of low mach number models for natural convection problems. Heat and Mass Transfer Journal 36, 567–573.

[78] Paolucci, S., 1982. On the filtering of sound from the Navier-Stokes equations. Tech. Rep. SAND82-8257, Sandia National Laboratories.

[79] Parfitt, E., and L. Wilson, 2008. Fundamentals of physical volcanology. Blackwell.

[80] Patnaik, G., R. Guirguis, J. Boris, and E. S. Oran, 1987. A Barely Implicit Correction for Flux-Corrected Transport. Journal of Computational Physics 71, 1–20.

[81] Perugini, D., G. Ventura, M. Petrelli, and G. Poli, 2004. Kinematic significance of morphological structures generated by mixing of magmas: a case study from salina island (southern italy). Earth and Planetary Science Letters 222, 1051–1066.

[82] Philippe, P., C. Raufaste, P. Kurowski, and P. Petitjeans, 2005. Penetration of a negatively buoyant jet in a miscible liquid. Physics of Fluids 17, 17.

[83] Philpotts, A., 1979. Silicate liquid immiscibility in tholeiitic basalts. Journal of Petrology 20, 99–118.

[84] Principe, J., 2008. Subgrid scale stabilized finite elements for low speed flows. Ph.D. thesis, Technical University of Catalonia.

[85] Puckett, E., A. Almgren, J. Bell, D. Marcus, and W. Rider, 1997. A high-order projection method for tracking fluid interfaces in variable density incompressible flows. Journal of Computational Physics 130, 269–282.

[86] Rayleigh, L., 1883. Investigation of the character of the equilibrium of an incompressible heavy fluid of variable density. Proceedings of the London Mathematical Society 14, 170–177.

[87] Rayleigh, L., 1916. On convection currents in a horizontal layer of fluid when the higher temperature is on the under side. Philosophical Magazine VI, 529–546.

[88] Rehm, R., and H. Baum, 1978. The equations of motion for thermally driven, buoyant flows. Journal of Research of the National Bureau of Standards 83, 297–308.

[89] Roedder, E., 1979. The evolution of the igneous rocks: fiftieth anniversary perspectives. Princeton University Press, Ch. Silicate liquid immiscibility in magmas, pp. 15–57.

[90] Rubin, A., 1998. Dike ascent in partially molten rock. Journal of Geophysical Research 103, 20901–20919.

[91] Ruprecht, P., G. Bergantz, and J. Dufek, 2008. Modeling of gas-driving magmatic overturn: Tracking of phenocryst dispersal and gathering during magma mixing. Geochemistry Geophysics Geosystems 9, Q07017.

[92] Sharp, D., 1984. An overview of Rayleigh-Taylor instability. Physica D 12, 3–18.

[93] Smolianski, A., 2005. Finite-Element/Level-Set/Operator-Splitting (FELSOS) approach for computing two-fluid unsteady flows with free moving interfaces. International Journal for Numerical Methods in Fluids 48, 231–269.

[94] Snyder, D., 2000. Thermal effects of the intrusion of basaltic magma into a more silicic magma chamber and implications for eruption triggering. Earth and Planetary Science Letters 175, 257–273.

[95] Sparks, R., H. Huppert, and J. Turner, 1984. The fluid dynamics of evolving magma chambers. Philosophical Transactions of the Royal Society of London, Series A 310, 511–534.

[96] Sparks, R., H. Sigurdsson, and L. Wilson, 1977. Magma mixing: a mechanism for triggering acid explosive eruptions. Nature 267, 315–318.

[97] Sparks, R. S. J., and L. Marshall, 1986. Thermal and mechanical constraints on mixing between mafic and silicic magmas. Journal of Volcanology and Geothermal Research 29, 99–124.

[98] Srinarayana, N., G. McBain, S. Armfield, and W. Lin, 2008. Height and stability of laminar plane fountains in a homogeneous fluid. International Journal of Heat and Mass Transfer 51, 4717–4727.

[99] Taylor, G., 1950. The instability of liquid surfaces when accelerated in a direction perpendicular to their planes. Proceedings of the Royal Society of London. Series A, Mathematical and Physical Sciences 201 (1065), 192–196.

[100] Thomas, N., S. Tait, and T. Koyaguchi, 1993. Mixing of stratified liquids by the motion of gas bubbles: application to magma mixing. Earth and Planetary Science Letters 115, 161–175.

[101] Tritton, D. J., 1977. Physical Fluid Dynamics. Oxford University Press.

[102] Tryggvason, G., 1988. Numerical simulation of Rayleigh-Taylor instability. Journal of Computational Physics 75.

[103] Turner, J., 1973. Buoyancy effects in fluids. Cambridge Univ.

[104] Turner, J., and I. Campbell, 1986. Convection and mixing in magma chambers. Earth-Science Reviews 23, 255–352.

[105] Turner, J. S., 1966. Jets and plumes with negative or reversing buoyancy. Journal of Fluid Mechanics 26, 779–792.

[106] Uhl, V., and J. Gray (Eds.), 1966. Mixing: theory and practice. Academic Press.

[107] Valentine, G., D. Zhang, and B. Robinson, 2002. Modeling complex, nonlinear geological processes. Annual Review of Earth and Planetary Sciences 30, 35–64.

[108] Valentini, L., and K. Moore, 2009. Numerical modeling of the development of small-scale magmatic emulsions by Korteweg stress driven flow. Journal of Volcanology and Geothermal Research 179, 87–95.

[109] Veksler, I., A. Dorfman, A. Borisov, R. Wirth, and D. Dingwell, 2007. Liquid immiscibility and the evolution of basaltic magma. Journal of Petrology 48, 2187–2210.

[110] Wiebe, R., 1996. Mafic-silicic layered intrusions: the role of basaltic injections on magmatic processes and the evolution of silicic magma chambers. Trans. Roy. Soc. Edinb. Earth Sci. 87, 233–242.

[111] Wiggins, S., and J. Ottino, 2004. Foundations of chaotic mixing. Philosophical Transactions of the Royal Society of London, Series A 362, 937–970.

[112] Williamson, N., N. Srinarayana, S. Armfield, G. McBain, and W. Lin, 2008. Low-Reynolds-number fountain behaviour. Journal of Fluid Mechanics 608, 297–319.

[113] Wohletz, K., 1986. Explosive water-magma interactions: Thermodynamics, explosion mechanisms and field studies. Bulletin of Volcanology 48, 245–264.